To the Graduate Council:

I am submitting herewith a dissertation written by Robert Michael Wham entitled "Mass Transfer To and From and Hydrodynamics In and Around a Single Drop." I have examined the final copy of this dissertation for form and content and recommend that it be accepted in partial fulfillment of the requirements for the degree of Doctor of Philosophy, with a major in Chemical Engineering.

Dr. Osman Basaran, Major Professor

We have read this dissertation
and recommend its acceptance:

Accepted for the Council:

Associate Vice Chancellor and
Dean of The Graduate School

MASS TRANSFER TO AND FROM AND HYDRODYNAMICS IN AND AROUND A SINGLE DROP

A Dissertation

Presented for the

Doctor of Philosophy

Degree

University of Tennessee, Knoxville

Robert Michael Wham

May 1996

DEDICATION

This dissertation is dedicated to my parents ,
the late Robert M. Wham and Marcia E. Wham,
who provided me with the support and encouragement
necessary to promote my education.

ACKNOWLEDGEMENTS

I would like to thank my major advisor Dr. Osman A. Basaran, for encouragement and helpful suggestions. I would like to thank Dr. Charles H. Byers for his assistance and suggestions in the early portion of this work. The interest and support of my committee, Dr. Charles P. Moore, Dr. Leonard J. Gray, Dr. Robert M. Counce, and Dr. Jack S. Watson are also greatly appreciated. I would like to thank Randy Gibson for his asssistance during the experimental

portion of the work. I would like to thank Manfred Koop for helpful suggestions on the application of electric fields to drops. I would like to thank Darryl Downing for assistance in the use use of SAS to analyze the computational data. I would like to thank Fred Wohlhuter for his assistance in contour plotting and Sam Clinton for his insight into the analysis of his experimental work. I would also like to thank Connie Atkins, and Sonia Lay for their invaluable assistance. I would like to give special recognition to Dr. Timothy C. Scott, co-inventor of the emulsion phase contactor, for his work on technology transfer. The author also wishes to acknowledge the services provided by the Oak Ridge National Laboratory, managed by Martin Marietta Energy Systems, Inc., for the Department of Energy. The work was supported by the Office of Basic Energy Sciences, U.S. Department of Energy under contract DE-AC05-84OR21400. Finally, I would like to give a special thanks to my wife, Dana Wham, for her patience and encouragement.

ABSTRACT

Fluid flow in and around and mass transfer to and from single drops that are either falling in a tube (the falling drop problem) or fluidized by an up-flowing ambient fluid in a tube (the fluidized drop problem) are analyzed both experimentally and theoretically. An experimental system has been developed to study the enhancement of mass transfer to and from a drop by forcing it to undergo oscillations by the application of a pulsed d.c. electric field. With millimeter-size drops immersed in organic solvents, mass tranfer enhancement on the order of 35% has been achieved. Previous theories based on the concept of surface stretch are unable to account for the observed increases in mass transfer rates and coefficients. First, the change in drop surface area that occur in the experiments is too small to account for the observed enhancement in mass transfer. Moreover, these previous theories also assume that the fluid inside the drops is well mixed. The validity of this assumption has been tested by flow visualization studies which has revealed that the flow inside the drops is laminar and not turbulent. Such experimental observations, which agree with recent theories of drop oscillations, point to the need to develop a better understanding of the fluid mechanics in and around drops and the implications of the flow to transient conjugate mass transfer.

In this thesis, computational techniques based on the Galerkin/ finite element method (G/FEM) are used to solve both the fluid mechanics and mass transfer problems. The solution of the fluid mechanics part of the problem is expedited by using a highly efficient penalty formulation of the Navier-Stokes equations, which eliminates the need for explicitly solving for the pressure field.

The problem of the axisymmetric flow past a solid sphere in a tube is solved first to verify the correctness of the G/FEM algorithm and computer code developed for determining flow fields. Notwithstanding that this is a much studied and classical problem in fluid mechanics, two new correlations accounting for wall effects on drag for falling and fluidized solid spheres are presented that are valid over a range of Reynolds numbers and ratios of the radius of the tube to that of the sphere. The new computations and correlations evaluate the validity of correlations and approximations of others that have lurked around in the literature, often untested, for nearly a half century. Moreover, conditions are identified for which recirculating wakes form behind the spheres. It is shown that as the ratio of the tube radius to that of the sphere decreases, the Reynolds number for the onset of wake formation increases and the length of the wake decreases. Computations are also carried out that determine for the first time the effect of thin wire that has often been used in past experiments in measuring drag.

Attention is next turned to flow past a falling and fluidized fluid spheres in tubes. By way of example, the flow field inside and outside a fluid sphere that is falling in a tube undergoes remarkable transitions when the ratio of the viscosity of the drop to that of the ambient fluid, κ, varies over a narrow range. When κ is small enough, no wake forms behind the sphere. When κ lies between about 3 and 10, a wake that is wholly detached from the drop forms behind the sphere at a Reynolds number less than 100 and disappears as Reynolds number exceeds a certain amount. When $\kappa \geq 10$, it is shown for the first time that detached wakes can attach to the drop when Reynolds number becomes sufficiently large. Additionally, two new correlations are developed and reported that account for the effects of a tube wall and finite fluid inertia on drag for fluidized and falling droplets. Moreover, in contrast to related correlations of others for fluid spheres that are placed in an infinite expanse of ambient fluid, the new correlations are valid over the entire range of Reynolds numbers considered.

A fully implicit, transient algorithm and a computer code are developed for calculating mass transfer to or from a fluid sphere in a tube using velocity fields from solutions to the aforementioned Navier-Stokes problems. In contrast to most existing models in the literature that rely on some sort of drastic simplification or another, rigorous results computed in this thesis indicate that significant differences in rates of mass transfer from one situation to another can be attributed to whether or not a recirculating eddy is present in the continuous phase at the downstream face of the drop. Such zones of fluid recirculation are of course due to fluid convection at finite Reynolds number and cannot be predicted by such *ad hoc* models as surface stretch or approximating the real flow field by creeping flow solutions which are often available in analytical form.

TABLE OF CONTENTS

PAGE

LIST OF TABLES

LIST OF FIGURES

FIGURE PAGE

FIGURE PAGE

FIGURE PAGE

FIGURE PAGE

FIGURE PAGE

FIGURE PAGE

FIGURE PAGE

FIGURE PAGE

FIGURE PAGE

FIGURE PAGE

LIST OF SYMBOLS

a	Sphere radius
$\tilde{c}^{(i)}\|_{\tau=\infty}$	Equilibrium concentration of solute in the drop
$\tilde{c}^{(o)}_{\tau=\infty}$	Equilibrium concentration of solute in the continuous fluid
C_A	Drag coefficient for sphere in an infinite fluid
C_D	Drag coefficient for sphere in tube flow
C_S	Drag coefficient for sphere in creeping flow(Stokes law regime, $\frac{12}{Re}$)
d	Tube radius
D	Dimensionless tube radius, $\frac{d}{a}$
$\mathcal{D}$	Diffusivity
dS	Element of area on sphere surface
e	Eccentricity of an ellisoidal drop
$\underline{\mathbf{e}}_k$	Represents one of the following $\underline{\mathbf{e}}_x$, $\underline{\mathbf{e}}_z$, $\underline{\mathbf{e}}_r$, $\underline{\mathbf{e}}_\theta$
$\underline{\mathbf{e}}_r$	Unit vector in $r-$direction
$\underline{\mathbf{e}}_x$	Unit vector in $x-$direction
$\underline{\mathbf{e}}_z$	Unit vector in $z-$direction
$\underline{\mathbf{e}}_\theta$	Unit vector in $\theta-$direction
E	Electric field strength
F	Fractional extraction defined by equation 5.1
F_B	Buoyant force on a sphere
F_D	Drag on a sphere in tube flow
F_K	Kinetic force on a sphere $(\frac{1}{2}\rho v^2)(\pi a^2)$
F_S	Stokes drag
F_T	Total force exerted by fluid on a sphere

f_n	Normal stress , $\underline{\underline{\mathbf{T}}} : \underline{\mathbf{nn}}$
f_t	Tangential stress , $\underline{\underline{\mathbf{T}}} : \underline{\mathbf{nt}}$
g	Gravitational constant
$\underline{\underline{\mathbf{I}}}$	Identity tensor
H	Distribution coefficient
K	Term in drag expression
$\mathcal{K}$	Mass transfer coefficient
$\mathcal{K}_{oscillating}$	Mass transfer coefficient for an oscillating drop
$\mathcal{K}_{spherical}$	Mass transfer coefficient for a spherical drop
$\mathcal{K}_{stretched}$	Mass transfer coefficient for a stretched drop
L_1	Dimensionless distance from tube inlet to center of sphere , $\frac{l_1}{a}$
L_2	Dimensionless distance from tube outlet to center of sphere , $\frac{l_2}{a}$
$\underline{\mathbf{n}}$	Unit normal to a surface
N	Flux of water into organic continuous phase
N_r	Number of elements in $r-$direction
N_x	Number of elements in $x-$direction
N_θ	Number of elements in $\theta-$direction
N_z	Number of elements in $z-$direction
p	Pressure
Pe	Peclet number
$\mathcal{R}^l$	ratio of diffusivity coefficients
R'	correction factor used by Boyzadheiv (1969)
Re	Reynolds number , $\frac{\rho U_\infty a}{\mu}$
$Re_c^{(1)}$	Reynolds number at which a detached wake first appears

$Re_c^{(2)}$	Reynolds number at which a detached wake disappears
$Re_c^{(*)}$	Reynolds number at which a detached wake attaches to the sphere
R	Dimensionless radial coordinate , $\frac{x}{a}$
S_d	Surface of sphere
S_e	Surface at tube exit
S_i	Surface at tube inlet
S_s	Surface of symmetry (centerline)
S_w	Surface at tube wall
Sh	Sherwood number, $\frac{Ka}{D}$
St	Stokes number, $\frac{\rho a^2 g}{\mu U_\infty}$
$\underline{\underline{\mathbf{T}}}$	Total stress tensor
$\underline{\mathbf{t}}$	Unit tangent to a surface
U_∞	Characteristic approach velocity-
V	Problem domain
$\underline{\mathbf{v}}$	Velocity vector
v_r	Radial velocity, spherical coordinate system
v_x	Radial velocity, cylindrical coordinate system
v_θ	Azimuthal velocity, spherical coordinate system
v_z	Axial velocity
y_1	Dimensionless velocity potential
y_2	Dimensionless streamfunction
z	Axial coordinate
z_c	Axial location along the tube centerline where $v_z = 0$
α	minor axis of prolate ellipsoid

β	major axis of prolate ellipsoid
$\frac{1}{\epsilon}$	Penalty parameter, $\mathcal{O}(10^6)$
κ	Viscosity ratio of viscosity of inner fluid to the viscosity of the outer fluid
ρ	Density
$\rho^{(i)}$	Density of fluid inside sphere
$\rho^{(o)}$	Density of fluid surrounding sphere
$\rho^{(s)}$	Density of solid sphere
μ	Viscosity
$\mu^{(i)}$	Viscosity of fluid inside sphere
$\mu^{(o)}$	Viscosity of fluid surrounding sphere
β_1	Coefficient in equation (5.9)
β_2	Coefficient in equation (5.9)
γ	Dimensionless density difference
ϕ^i	Biquadratic basis functions
ψ^j	Linear basis functions for pressure
$\underline{\underline{\tau}}$	Viscous stress tensor, $\nabla\underline{\mathbf{v}} + (\nabla\underline{\mathbf{v}})^T$
τ	Dimensionless time
σ	Interfacial tension
ω	Vorticity
ω_s	Vorticity evaluated at the sphere surface
λ, $\frac{1}{\lambda}$	Ratio of diameter of tube to that of sphere and visa versa
ψ	Dimensionless streamfunction

CHAPTER 1

INTRODUCTION

Separations processes are focal points in the science of chemical engineering and the practice of chemical processing. Perry and Chilton (1973), among others, devote a large fraction of their handbook to the discussion of such separation processes as liquid extraction, distillation, ion exchange, and absorption. Among these, solvent extraction and distillation rely on the generation and manipulation of large numbers of drops and bubbles to create large amounts of interfacial area and to promote convection with the goal of developing energy efficient devices having high rates of throughput of products.

Solvent extraction is used to separate and purify chemicals used in industries as diverse as the refining of petroleum, the manufacture of chemicals, the processing of metals, and the reprocessing of nuclear fuels. In practice, for solvent extraction to be chosen as the method to be used to carry out a given separation among several other alternatives, the process must exhibit high rates of mass transfer, consume little energy, and keep product losses low. Indeed, the process of solvent extraction would be extremely attractive if the mechanism that enhances rates of mass transfer could also lower consumption of energy. Both of these goals can be achieved by using an externally applied electric field in the unit operation of solvent extraction to increase transfer rates and lower energy usage. Therefore, a goal of this work is to carry out an experimental study of the augmentation of mass transfer by electric fields. A second goal of this dissertation is to apply modern computational methods to study mass transfer to and from the basic building block of the solvent extraction process, viz. a single liquid drop immersed in an ambient fluid. Of special interest to this author is the analysis of the effects of fluid mechanics on mass transfer to and from drops.

1.1 BACKGROUND AND ORIGINS OF THIS WORK

When a highly conducting fluid, e.g. an aqueous liquid, is brought into contact with a highly insulating fluid, e.g. an organic liquid, in the presence of an electric field, the force due to the electric field vanishes even inside the insulating fluid (the field strength equals zero inside the conducting fluid) when the fluids have constant physical properties (Melcher and Taylor, 1969; Basaran, 1984). In this situation, the force due to the electric field acts solely on the interface between the two fluids. Therefore, in contrast to familiar methods of contacting that are often based on mechanical agitation, the advantage of an electric field in multiphase separation processes such as solvent extraction is that it can focus the energy being input into the system directly on the interface rather than into the bulk of the two liquid phases. This is the underlying theme of the use of electric fields for the enhancement of mass transfer.

The so-called science of electrohydrodynamics was born when Lord Rayleigh (1882) presented an analysis of the influence of electric charge on drop stability. By means of a linearized energy stability analysis, Lord Rayleigh showed that an isolated, charged conducting drop placed in an insulating fluid becomes unstable with respect to a disturbance proportional to a Legendre polynomial of order two when the amount of surface charge that it bears exceeds a certain amount. Through his analysis and experimental observations, Lord Rayleigh demonstrated that electric fields can destabilize liquid drops and cause them to disintegrate.

Macky (1926) and Nolan (1931) experimentally studied the deformation of conducting liquid drops in the presence of an externally applied electric field. These authors demonstrated that the drops became unstable and emitted charged jets from their conical tips when the field strength exceeded a critical value. The problem of the deformation of liquid drops in an externally applied electric field was finally correctly analyzed by the famous fluid mechanician G. I. Taylor (1964).

A few years later Taylor (1966) also resolved a long-standing controversy in drop deformation under an applied electric field. Taylor showed that depending on the electrical properties of the drop and the continuous phases, the drops can be deformed either into prolate spheroids along the direction of the applied field or into oblate spheroids in the direction perpendicular to it. In this landmark paper, Taylor also demonstrated that electric fields can set fluids into convection even in the absence of any drop deformation. With the publication of this paper and some related ones by Melcher and coworkers at MIT, the modern science of electrohydrodynamics was born (Melcher and Taylor 1969).

Although Rayleigh (1882) determined the effect of surface charge on the eigenfrequencies of oscillation of liquid drops, the effect of an externally applied electric field on the oscillations of liquid drops was theoretically analyzed much later by Brazier-Smith (1971). Because Brazier-Smith made numerous assumptions in carrying out his analysis, however, the problem of the oscillations of a liquid drop in an externally applied electric field has remained an unsolved problem until recently (see Basaran *et al.* 1995).

Cottrell and Speed (1911) carried out an experimental study to develop an apparatus that used an alternating current (AC) electric field to promote the coalescence of water drops in crude oil-water emulsions. The electric field caused the drops to polarize and enhanced their rate of coalescence.

From these pioneering works and certain others on the effects of electric fields on liquid drops (Bailes and Larkai, 1982; Stewart and Thornton, 1967), it follows that chemical engineers can take advantage of these highly beneficial effects of electric fields by incorporating them in solvent extraction as qualitatively depicted in Figure 1.1. Here a downflowing conducting liquid phase is brought into countercurrent contact with an upflowing insulating phase by dispersing the former into the latter from a suitable nozzle. A simple way of applying an electric field would be to connect the nozzle to a source of high voltage and to place a pair of parallel, grounded electrodes downstream of the nozzle. As reviewed by Zhang and Basaran (1995), electric fields can drastically reduce the volume of drops being formed from a nozzle. Therefore, an applied field ought to increase the rate of mass transfer between the phases during the dispersion stage. As the drops fall through the ambient liquid, the electric field can also be used to increase the rate of mass transfer between the phases by forcing the drops to oscillate (see, e.g., Wham and Byers, 1985) or causing surface area generation through further breakup of the translating drops if the field strength is sufficiently high. Finally, the process of phase separation can be completed by using an electric field to enhance the coalescence of the liquid drops at the bottom of the unit, as discussed earlier in this chapter.

Moreover, not only can electric fields enhance the processes of drop formation and dispersion, drop oscillation, fluid convection, and drop coalescence, but the electric field-aided solvent extraction operation depicted in Figure 1.1 also makes plain that an adequate understanding of its underlying principles and further

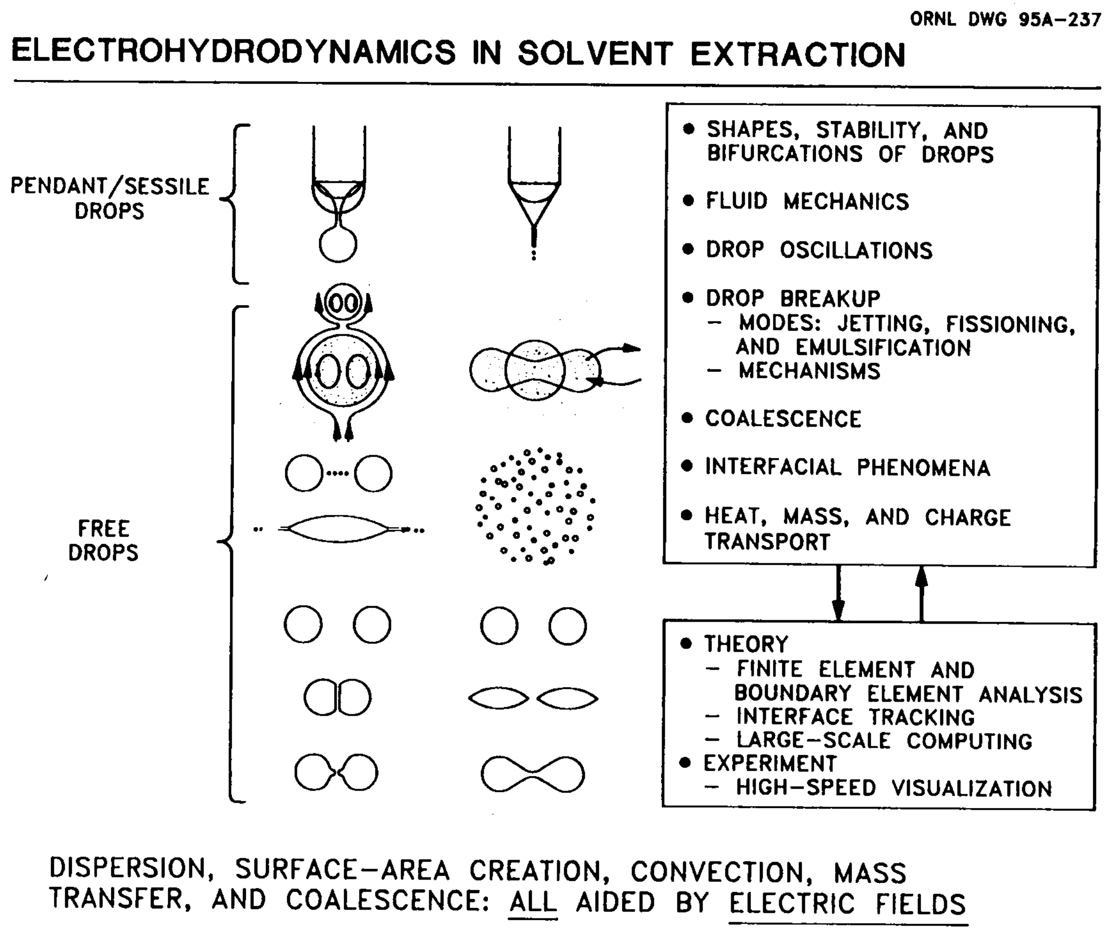

Figure 1.1. Electrohydrodynamics in solvent extraction.

improvements in its practice requires theoretical and experimental analysis of a class of problems referred to as free surface flows (see, e.g., Kistler and Scriven 1983, Kheshgi and Scriven 1983, Christodoulou and Scriven 1992, Basaran 1992). This dissertation focuses primarily on certain problems that arise as the drops are falling through the continuous phase (cf. Figure 1.1).

1.2 DISSERTATION SCOPE

The initial focus of the dissertation research was to develop an experimental system to study drop oscillations and mass transfer in the presence of an applied electric field (Part I). A single fluidized drop was chosen as being representative of the fundamental building block of mass transfer in solvent extraction. Moreover, attention was focused on systems in which the dispersed phase is highly conducting and the continuous phase is highly insulating.

A second and dominant focus of the dissertation research was the analysis of flow and mass transfer in and around fluidized and falling solid spheres and drops in tubes where both inertial and wall effects are important (Part II). Both the drop fluid and the continuous phase were taken to be Newtonian fluids with constant density and constant viscosity. The fluid mechanics problem entailed the solution of the governing continuity and momentum equations — the so-called Navier-Stokes system — by Galerkin/finite element analysis. When a solute was present that transfers between the droplet and the continuous phases, the velocity fields that were available from the solution of the aforementioned flow problem were used to expedite the solution of the mass transfer problem in which both convection and diffusion can be important.

During the course of Part I of this research work, a new device, which is called the emulsion phase contactor (EPC) and shown in Figure 1.2, that uses electric fields for drop dispersion, drop oscillation, fluid convection, and drop coalescence was developed jointly with Dr. T. C. Scott (Scott and Wham, 1988,1989). Over the past several years, not only was this technology licensed to several companies, but it has to resulted in the development of several new techniques and devices with applications ranging from electrospraying to synthesis of ceramic precursor powders. For example, Scott and Harris (1993) have extended the EPC concept so that each droplet acts as a microreactor inside which chemical reactions take place. This so-called electric dispersion reactor (EDR) concept can produce particles having homogeneity on a scale not readily achievable by other techniques.

Although the flows studied in this dissertation are steady and axisymmetric *and* the fluids are isothermal and Newtonian, the finite element methods used here can be readily extended to analyze transient, fully three-dimensional flows. Although the flow codes developed as part of this dissertation have built into them subroutines to compute transient flows, this capability was not exploited here. Moreover, flows past spherical drops studied in this work can serve as starting points for the computation of flows past deformable drops in tubes as in a continuation or a homotopy approach to solving the Navier-Stokes system.

Furthermore, finite element methods used here to compute transient mass transfer to and from drops can be extrapolated to study nonisothermal flows past liquid drops in tubes and in a variety of other situations as well. Indeed, the mass transfer equations solved in this dissertation reduce to their heat transfer counterparts when the distribution coefficient for mass transfer is set equal to unity *and* concentration is replaced by temperature, the ratio of diffusivities is

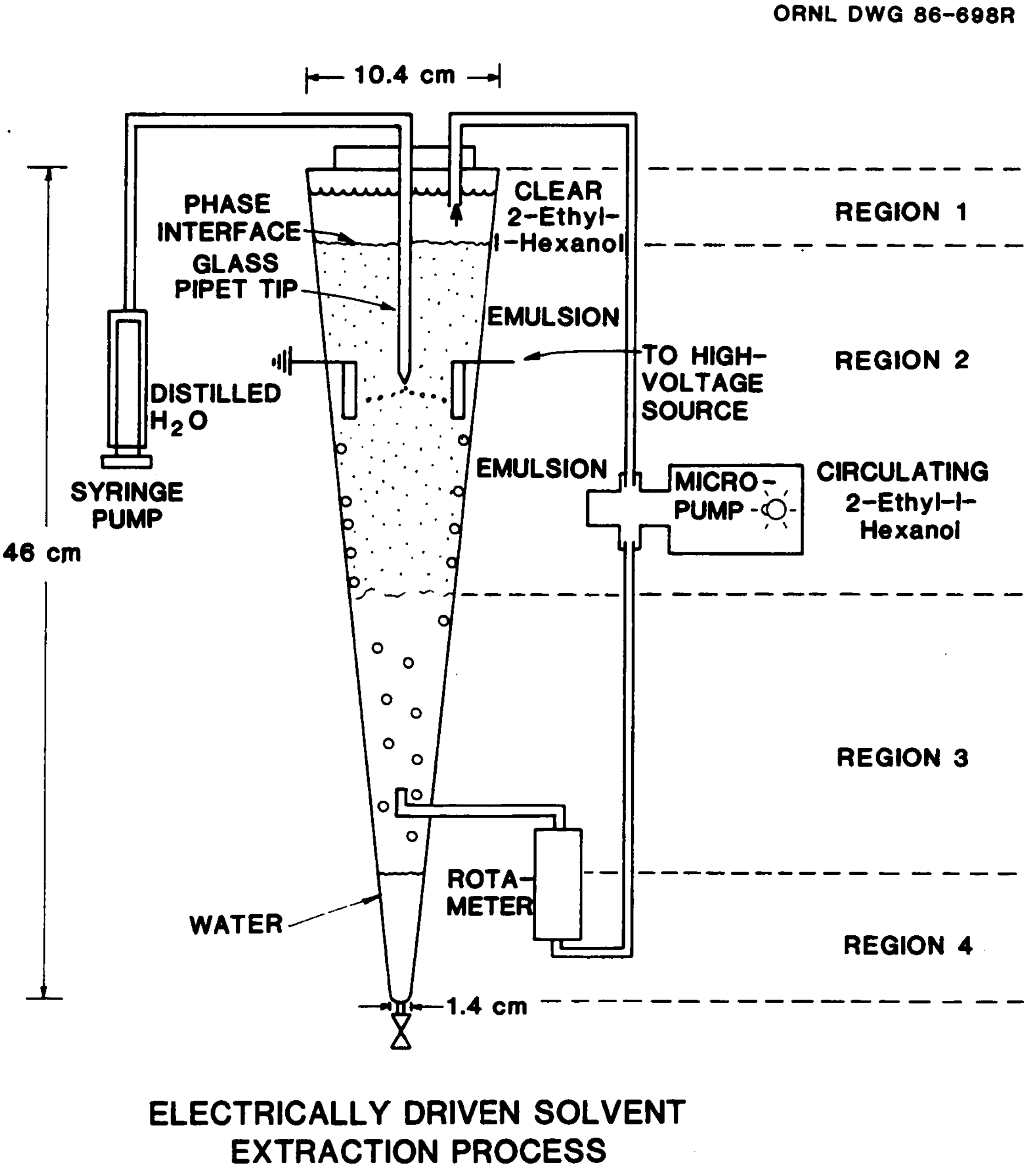

Figure 1.2. The emulsion phase contactor.

replaced by that of conductivities, and the Peclet number is replaced by the Nusselt number for heat transfer.

The computer code contains the necessary programming in order to do unsteady axisymmetric as well as steady and unsteady two dimensional flow.

1.3 DISSERTATION SYNOPSIS

1.3.1 Experimental work

Chapter 2 examines mass transfer from a fluidized water drop into an organic continuous phase. To minimize the amount of organic solvent used in the experiments, a drop is suspended in a narrow tapered column as shown in Figure 1.3. Since oscillation frequencies on the order of 1 to 100 Hz are anticipated for the aqueous-organic pairs of liquids considered (Miller and Scriven 1968), a high speed video camera and associated video hardware is used to capture images of drops during their oscillation cycles.

It is shown in Chapter 2 that mass transfer enhancement on the order of 35% can be achieved by causing the aqueous drops to undergo forced oscillations. Previous approximate theories by Angelo *et al.* (1966) and Rose and Kintner (1966) had surmised that the enhancement in mass transfer is due to the increase in surface area experienced by the drops during their oscillations. These earlier studies have also assumed, albeit without proof, that the interior of the drops are well mixed due to a turbulent core that is brought about by the forced oscillations. Experimental results reported in Chapter 2 show that changes in average surface area experienced by the drops are minimal and do not explain the observed increase in mass transfer coefficient. Flow visualization studies carried

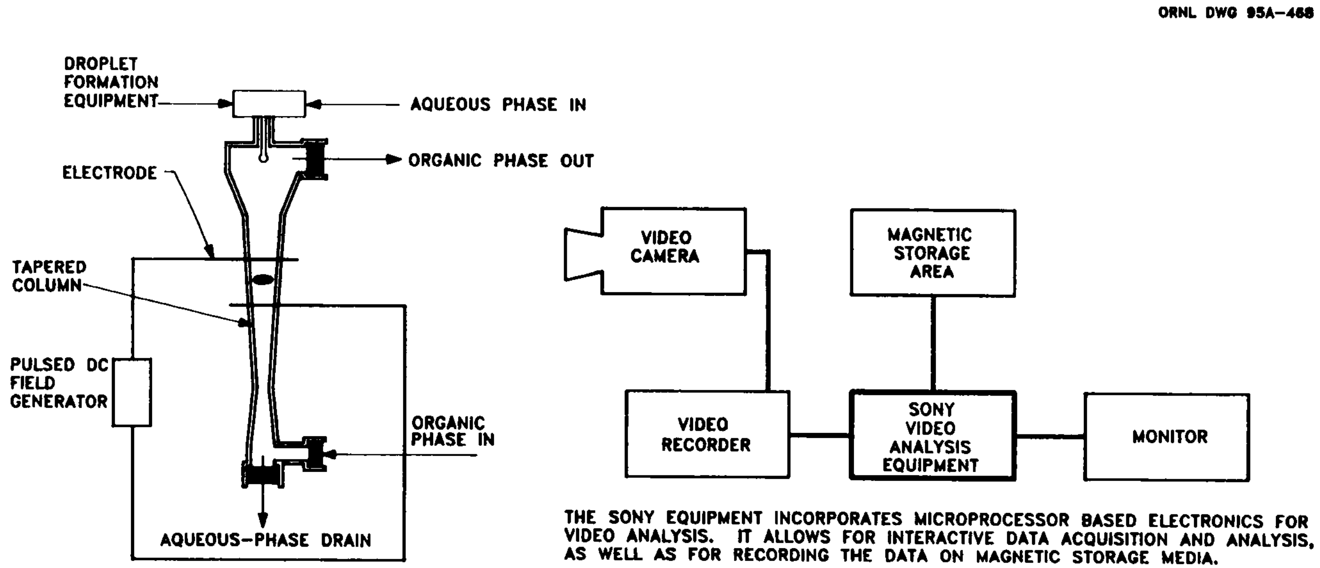

Figure 1.3. Schematic diagram of experimental equipment for single drop oscillation studies.

out by placing neutrally buoyant particles inside the drops show that the streak lines correspond to those that are expected were the flow inside the oscillating drops laminar. Although these findings are in direct contradiction with the commonly held assumptions of surface area stretch for oscillating drops and turbulent mixing inside them, they are in accord with modern computational theories for oscillating drops (see, e.g., Basaran, 1992; Basaran and DePaoli, 1994). The results of this chapter point to the need for better theories of mass transfer that account for the influence of fluid mechanics on mass transfer to and from liquid drops in the presence and absence of drop oscillations. This point is returned to in what follows and in much greater detail in Chapter 5.

1.3.2 Wall effects on flow past solid spheres

Chapter 3 determines the axisymmetric, steady flow of a Newtonian fluid past a solid sphere that is either suspended in a tube by an upflowing liquid (*the fluidized sphere problem*) or falling in a tube (*the falling sphere problem*) by finite element analysis using a consistent penalty formulation (Engelman *et al.*, 1982). To verify the correctness of the computer code developed to solve the flow problem, the computational results are compared to several well-known results from the literature, in particular in the case of the fluidized sphere problem to the experimental results of Fayon and Happel (1960) and analytical results of Haberman and Sayre (1958). The new results show that the correlation for drag presented by Fayon and Happel is inaccurate (i) for any value of the ratio of the diameter of the tube to that of the sphere, $\frac{1}{\lambda}$, when inertial effects, characterized by a Reynolds number, Re, are moderate ($Re \geq 30$) and (ii) for $\frac{1}{\lambda} < 3.3$ when Re is small. Haberman and Sayre's results are restricted to creeping flow ($Re = 0$)

and are shown to hold so long as $\frac{1}{\lambda} > 2$.

Two new correlations accounting for wall effects on drag for fluidized and falling spheres are presented that are valid when $0 \leq Re \leq 100$ and $12.5 \geq \frac{1}{\lambda} \geq 1.42$. The comparison of the predictions of the new correlation for fluidized spheres with the computational predictions and those due to Fayon and Happel is presented in Figure 1.4. A similar comparison for falling spheres is presented in Figure 1.5. Moreover, the effect of λ on the onset of wake formation with increasing Re and the effects of λ and Re on wake characteristics are studied in detail, important issues which past flow visualization experiments have left unresolved. The results show that as $\frac{1}{\lambda}$ decreases, the Re for the onset of wake formation increases, whereas the length of the wake decreases. Finally, calculations have been carried out to simulate the effect of a wire that has been used in some experiments to support fluidized spheres; such results assess for the first time errors that might have been incurred in measuring drag coefficients.

1.3.3 Wall effects on flow past fluid spheres

Once the algorithm and the computer code to model flow past a solid sphere have been developed and verified, the model is extended in Chapter 4 to predict the flow past a fluid sphere. Following the pioneering works of Leal and coworkers (Dandy and Leal, 1986; Leal, 1989; Dandy and Leal, 1989), a detailed report is made on the dynamics of recirculating wakes that form at finite Reynolds number Re due to vorticity accumulation at the rear of a fluid sphere that is either suspended in a tube by an upflowing fluid (*the fluidized drop problem*) or falling in a tube (*the falling drop problem*). The axisymmetric, steady flow of a Newtonian fluid past the fluid sphere is also determined by finite element

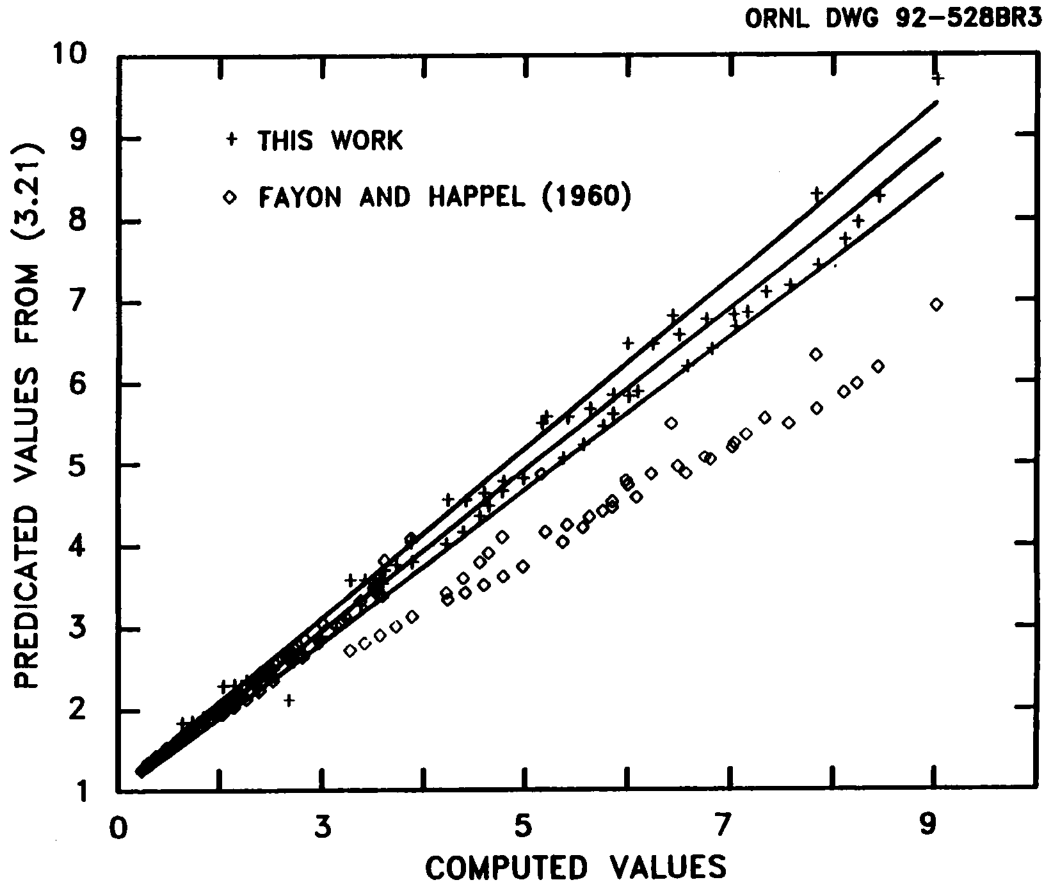

Figure 1.4. Comparison of Galerkin/finite element predictions of drag for falling spheres to the new correlation (3.19) and the correlation due to Fayon and Happel (1960).

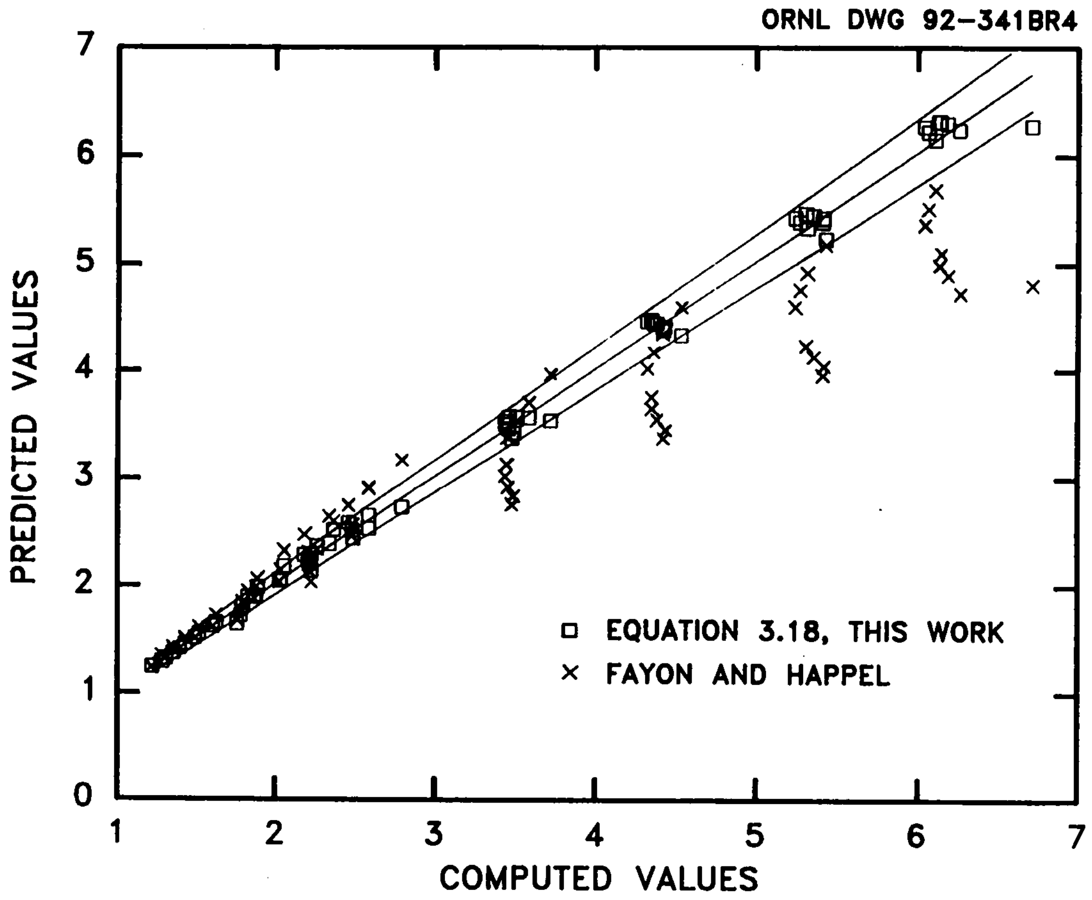

Figure 1.5. Comparison of Galerkin/finite element predictions of drag to the new correlation (3.18) and the correlation due to Fayon and Happel (1960).

analysis using a consistent penalty formulation.

By way of example, the flow past a fluid sphere that is falling in a tube for which the ratio of the tube radius to the drop radius $1/\lambda = 5$ undergoes remarkable transitions when the ratio of the viscosity of the drop to that of the ambient fluid, κ, varies over a narrow range. When $\kappa \leq 2.75$, no wake forms behind the sphere as Re increases. When $3 \leq \kappa < 10$, an eddy that is detached from the drop forms at a critical value of $Re = Re_c^{(1)}$, grows, and eventually disappears as Re rises above a certain amount $Re_c^{(2)}$. Remarkably, when $\kappa = 3$, these critical Reynolds numbers are as low as $Re_c^{(1)} = 51 \pm 1$ and $Re_c^{(2)} = 77 \pm 1$. Figure 1.6 shows the dependence of $Re_c^{(1)}$ and $Re_c^{(2)}$ on the viscosity ratio. When $\kappa \geq 10$, it is shown by using as many as 46,000 velocity degrees of freedom that the detached eddy attaches to the drop when Re exceeds a critical value, $Re \geq Re_c^*$, which was heretofore unknown. Whereas only a single, large — primary — eddy is present inside the drop when $Re < Re_c^*$, a second but much smaller — secondary — eddy also forms inside the drop upon attachment. Figure 1.7 depicts the evolution of the flow field with viscosity ratio when the Reynolds number is held fixed at 100 and the ratio of the tube radius to the sphere radius equals 5.

Two new correlations are developed and reported in Chapter 4 that account for the effects of a tube wall and finite fluid inertia on drag for fluidized and falling droplets. Moreover, in contrast to related correlations of others for fluid spheres that are placed in an infinite expanse of ambient fluid, the new correlations are valid over the entire range of Reynolds numbers considered.

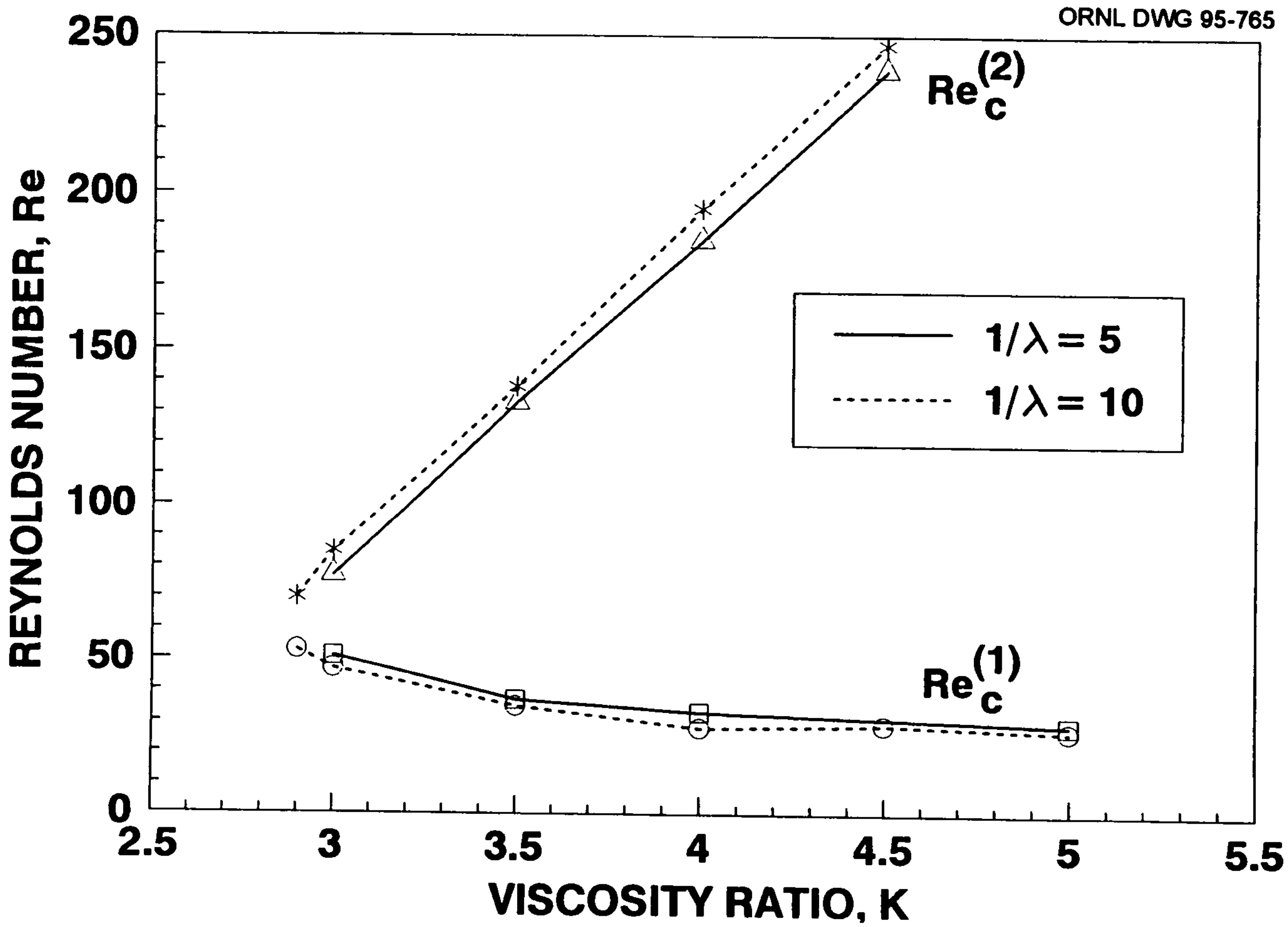

Figure 1.6. Effect of viscosity ratio and ratio of tube radius to sphere radius on the value of Re at which a detached wake first appears, $Re_c^{(1)}$, and that at which the wake disappears, $Re_c^{(2)}$.

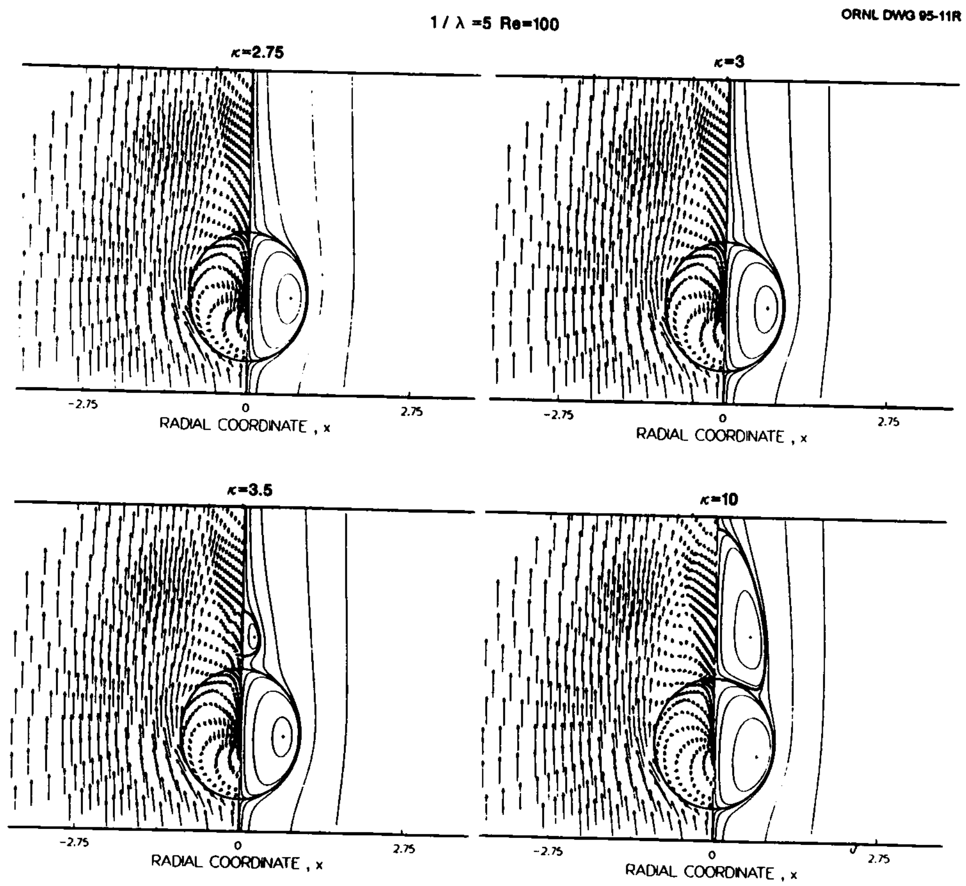

Figure 1.7. Velocity profiles as a function of κ for a falling sphere. Here $Re = 100$ and $\frac{1}{\lambda} = 5$.

ORNL DWG 95-12R

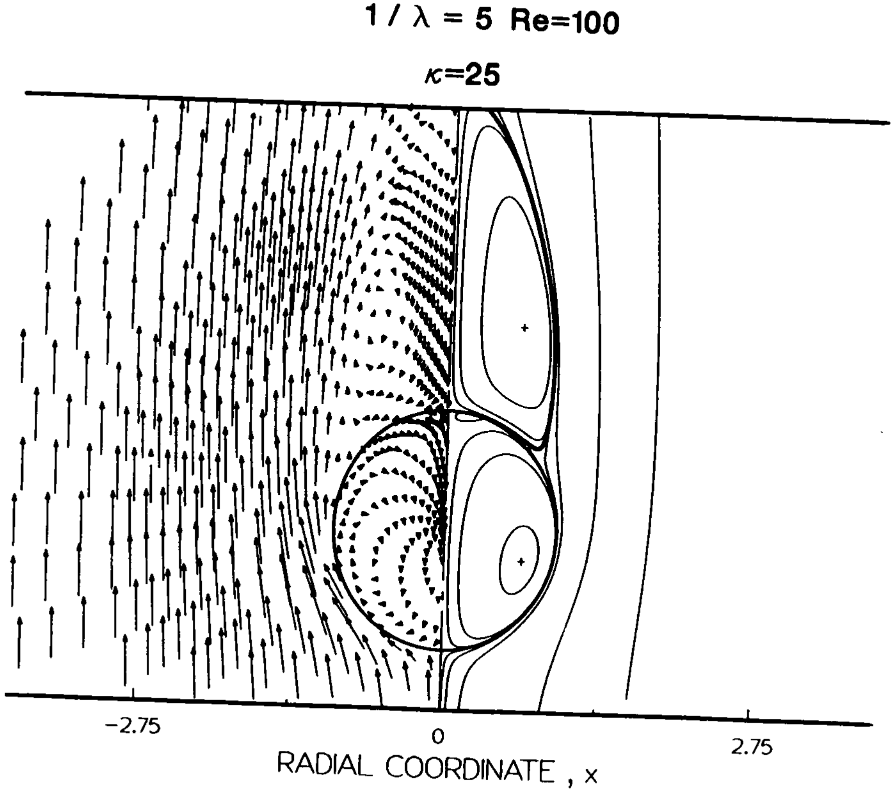

Figure 1.7. (continued)

1.3.4 Flow field effects on mass transfer to drops

Chapter 5 presents a transient algorithm and a computer code for calculating mass transfer to or from a fluid sphere in a tube using velocity fields that are available from solving the Navier-Stokes system in Chapters 3 and 4. In contrast to most existing models in the literature that rely on some sort of drastic simplification or another, rigorous results computed in Chapter 5 indicate that significant differences in rates of mass transfer from one situation to another can be attributed to whether or not a recirculating eddy is present in the continuous phase at the downstream face of the drop (cf. Chapters 3 and 4). Such zones of fluid recirculation are of course due to fluid convection at finite Reynolds number and cannot be predicted by such *ad hoc* models as surface stretch or approximating the real flow field by the creeping flow solution of Hadamard (1911) and Rybczynski (1911).

Figure 1.8 shows velocity fields and lines of constant values of concentration — concentration contours — inside and outside drops of four different values of the viscosity ratio at a Reynolds number of 60 and a Peclet number of 100. In the four cases shown in Figure 1.8, initially all the solute is distributed uniformly inside the drops at a dimensionless concentration of unity and its concentration outside the drops is zero. When $\kappa = 1$, there is of course no wake in the continuous phase at the rear of the drop (cf. Chapter 4). In this case, the concentration contours indicate that the solute diffuses across the interface, is swept to the rear of the drop, and is then advected downstream with no interference from the wake. Figure 1.8 makes plain that the formation of a wake results in a decrease in the rate of mass transfer as evidenced by the movement of the

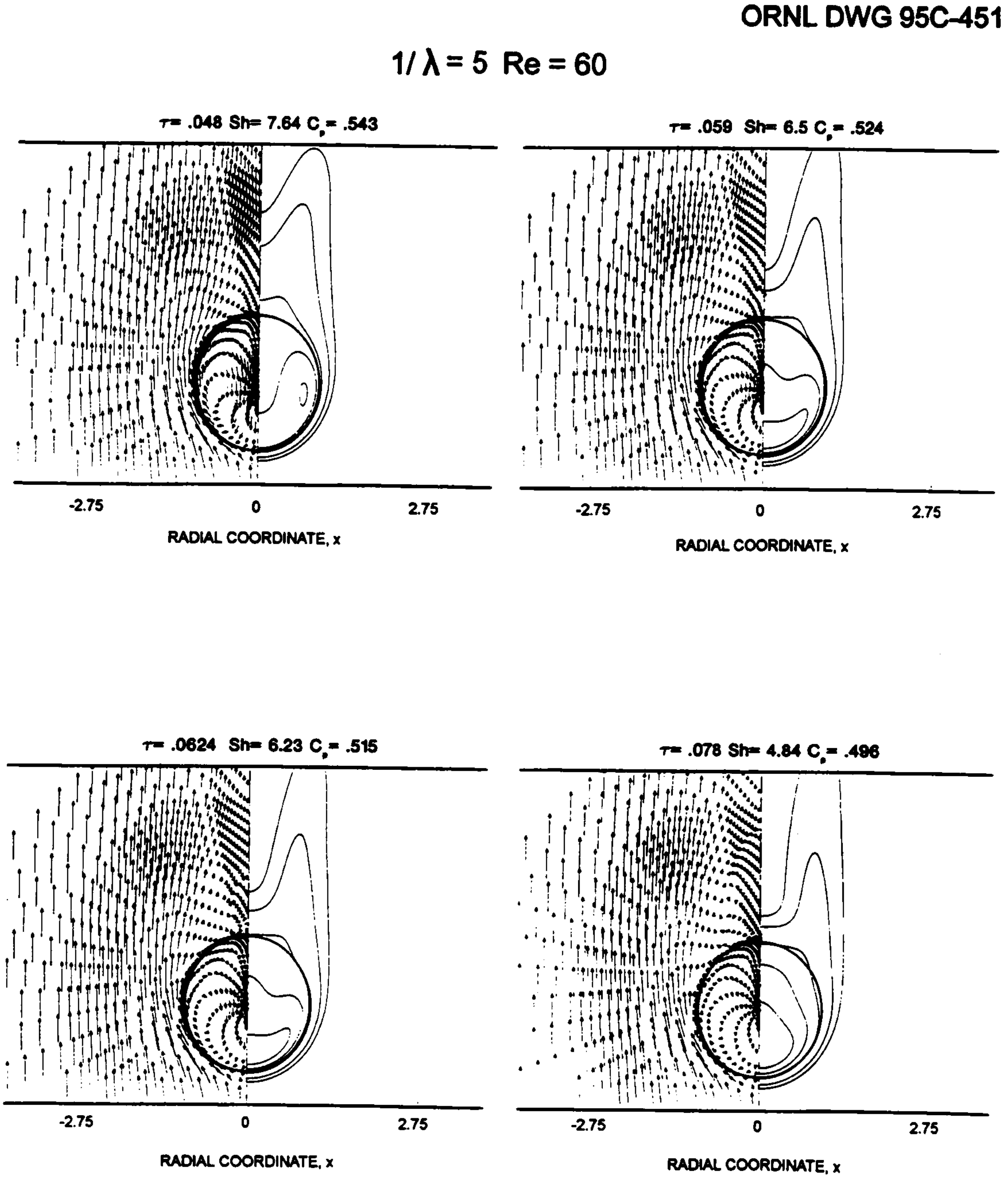

Figure 1.8. Concentration contours as a function of viscosity ratio. Here Re = 60 and Pe = 100.

concentration contours closer to the drop when κ = 3, 3.5, and 10. This decrease can be visualized by noting that regardless of whether a wake is present, the flux of solute out of the drop is solely due to diffusion because the radial component of the velocity vanishes at the spherical interface. When an eddy is present in the continuous phase, its presence essentially acts like a second barrier to the transport of solute out of the drop: this is because there can be no velocity component normal to the streamline enclosing the wake. The solute that transfers out of the drop and into the wake can only be swept past the drop by the free stream once it diffuses out of the wake, a slow process compared to the convective one at work outside the surface of the drop on its upstream side.

The aforementioned result when coupled to the dominant role played by fluid convection over diffusion at finite Peclet numbers point to the utility of causing the wake to shed to enhance rates of mass transfer. Wake shedding can of course be caused by forcing the drop to undergo oscillations, as in Chapter 2. Therefore, it is the combination of fluid convection and wake shedding that can account for the enhancement of mass transfer recorded in the experiments reported in Chapter 2, and not the surface stretch phenomena surmised by some authors.

1.4 CONCLUSIONS AND OUTLOOK

The use of electric fields to enhance rates of mass transfer to and from drops by oscillating them and the concept of creating and manipulating emulsions by externally applied electric fields has had a big impact on research underway not only at the Oak Ridge National Laboratory (ORNL) and the University of Tennessee but around the world as well. Examples of spinoffs that have resulted from early portions of this dissertation include the Ph.D. dissertation of F. K.

Wohlhuter (1992) on the use of electric fields for controlling bubbles and films in distillation, the Ph.D. dissertation of D. W. DePaoli (1994) on experimental studies of free and forced oscillations of pendant drops with application to multiphase separation processes, and the ongoing Ph.D. dissertation work of E. D. Wilkes on theoretical and experimental studies of forced oscillations of pendant drops. Davis and colleagues (1994) at the University of Colorado are studying counterparts of certain problems reported in this dissertation and under investigation at ORNL albeit in aqueous-aqueous systems. In Holland, Kerkhof and colleagues (1990; see, also, Ptasinski and Kerkhof, 1992) are studying the enhancement of multiphase separations by the application of electric fields.

The results presented in this dissertation can be extended in several directions. First, it is unknown at this time whether detached eddies can attach to deformable drops over certain regions of the parameter space. It needs to be investigated whether Dandy and Leal's (1989) inability to find attached eddies outside deformed drops is a physical result or due to the use of too few unknowns in their numerical discretization. The present author and colleagues plan to tackle this problem in the near future by means of a two-pronged attack. The first entails studying the flow past nondeformable fluid ellipsoids of increasing eccentricity to determine if there is critical value of the drop eccentricity above which attachment does not take place. The second approach involves solving the full free boundary problem by Galerkin/finite element analysis (cf. Basaran, 1992; Basaran and DePaoli, 1994; Feng and Basaran, 1994).

Computationally challenging problems involving fully three-dimensional flows past liquid drops are also of interest to the present author and coworkers and can now be tackled owing to the increase in computer power made possible by the availability of massively parallel computers. A fascinating avenue of future research entails extension of the results reported in Chapter 3 of this dissertation and the work of Tavener (1994) to investigate the three-dimensional flow structure that develops upon the loss of stability of the axisymmetric solutions computed here. The transition from the steady three-dimensional flow to the transient one involving vortex shedding is not understood at the present time.

To date, fundamental studies of drop oscillations (Tsamopoulos and Brown, 1983; Lundgren and Mansour, 1988; Patzek *et al.*, 1991; Basaran, 1992; Basaran and DePaoli, 1994) have all considered fluid mechanics in the absence of mass transfer. By combining computational methods described in Chapter 5 of this dissertation with the analyses reported in these previous works on drop oscillations it should now be possible to analyze the enhancement of mass transfer to and from oscillating drops by means of externally applied electric fields.

CHAPTER 2

ELECTRIC FIELD-INDUCED OSCILLATIONS OF FLUIDIZED DROPS IN TUBES

The scientific study of the effects of electric charges and fields on drop oscillations was inaugurated by Rayleigh's (1882) now celebrated analysis of the infinitesimal-amplitude oscillations of an isolated, conducting, inviscid drop bearing surface charge. Although a far cry from a rain-drop, Rayleigh's analysis of this prototypical problem in electrohydrodynamics lead to a flurry of activity in the 20th century that has continued to the present day. An up to date review of the literature in this area is provided in the paper by Basaran *et al.* (1995) commemorating the 35th anniversary of the publication of the classic text on transport phenomena by Bird *et al.* (1960).

Because electric charges and fields can deform fluid interfaces and drops *and* change frequencies of oscillations of them, the goals of this chapter are to explore experimentally the effects of electric fields

(i) on finite-amplitude oscillations of a liquid drop that is immersed in another liquid and

(ii) in modifying mass transfer to and from *and* fluid flow in and around such a drop.

Unfortunately, theoretical understanding of finite-amplitude oscillations of drops is incomplete. Tsamopoulos and Brown (1983), Lundgren and Mansour (1988), and Patzek *et al.* (1991) have analyzed the moderate- to large-amplitude oscillations of inviscid drops immersed in a gas in the absence of an electric field. Basaran (1992) has analyzed the large-amplitude oscillations of a viscous liquid drop but his drops are surrounded by a gas and he too does not consider the effects of an electric field. Miller and Scriven (1968) were first to analyze correctly the oscillations of drops in liquid-liquid systems but their analysis considered neither the effect of finite-amplitude excursions from the spherical base state nor that of an electric field. Feng and Beard (1990) and Basaran *et al.* (1995) have considered the effect of an electric field on the oscillations of moderate amplitude and large amplitude, respectively, of liquid drops but restricted their drops to be inviscid liquids and surrounded them by a gas phase. Recently, Kang (1993) considered the forced oscillations of liquid drops induced by a time-periodic electric field but restricted his *inviscid* drops to remain spheroidal in shape and surrounded them by a gas phase. Sherwood (1988) and Haywood *et al.* (1991) have considered the dynamics of a liquid drop that is surrounded by another viscous liquid in the presence of an electric field. However, these authors did not study drop oscillations but analyzed the deformation of such drops under a d.c. electric field.

In this chapter, an experimental system is described that is designed to force drops that are immersed in a second viscous liquid to undergo oscillations by subjecting them to a time-dependent electric field. The goal here is to exploit the electric field-induced oscillations of drops in liquid-liquid systems to enhance mass transfer to and from the drops. Section 2.1 discusses the experimental apparatus that has been designed and built for studying the forced oscillations of liquid drops and measuring mass transfer. Section 2.2 outlines the experimental procedures used in studying the oscillations of drops and in quantifying mass transfer from drops to an ambient liquid. Section 2.3 presents results on the oscillatory response of drops set into motion by a transient electric field and the effects of the oscillations on mass transfer from the drops. Section 2.4 discusses the nature of flow fields inside the drops. Section 2.5 describes a new device for carrying out solvent extraction that has resulted from the research on drop oscillations and mass transfer enhancement in the presence of an electric field described in the previous sections. Concluding remarks are the subject of Section 2.6.

2.1 EXPERIMENTAL APPARATUS FOR DROP OSCILLATIONS AND MASS TRANSFER ENHANCEMENT IN AN ELECTRIC FIELD

In the experiments, a single water drop is fluidized by an upflowing continuous organic liquid. A schematic diagram of the experimental apparatus is shown in Figure 2.1 and a photograph of the entire apparatus is shown in Figure 2.2. The experimental system consists of the following essential elements.

(1) A vessel for containing the dispersed and continuous phases and associated equipment for delivering, metering, and monitoring the flow of the two phases.

(2) Equipment for subjecting the drop to an electric field.

(3) Video recording and playback equipment for monitoring certain features of the drop so that its shape and mass transfer to or from it can be inferred.

The continuous phase is delivered by a laboratory pump, its flow rate is controlled by a rotameter, and a purged reservoir is available to hold the necessary inventory of the continuous phase. The continuous phase enters the column at the bottom and exits it at the top. In the experiments, a drop is placed in a

ORNL DWG 86-200

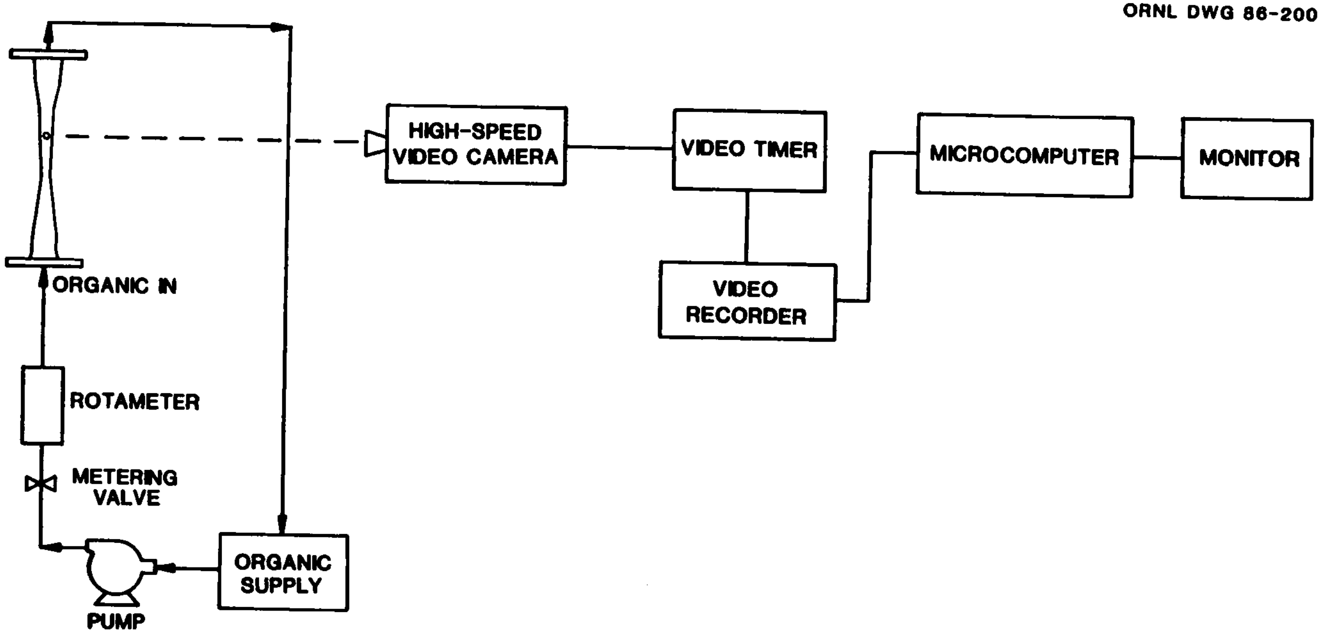

Figure 2.1. The experiment centers around a fluidized water drop in a continuous phase of upflowing organic.

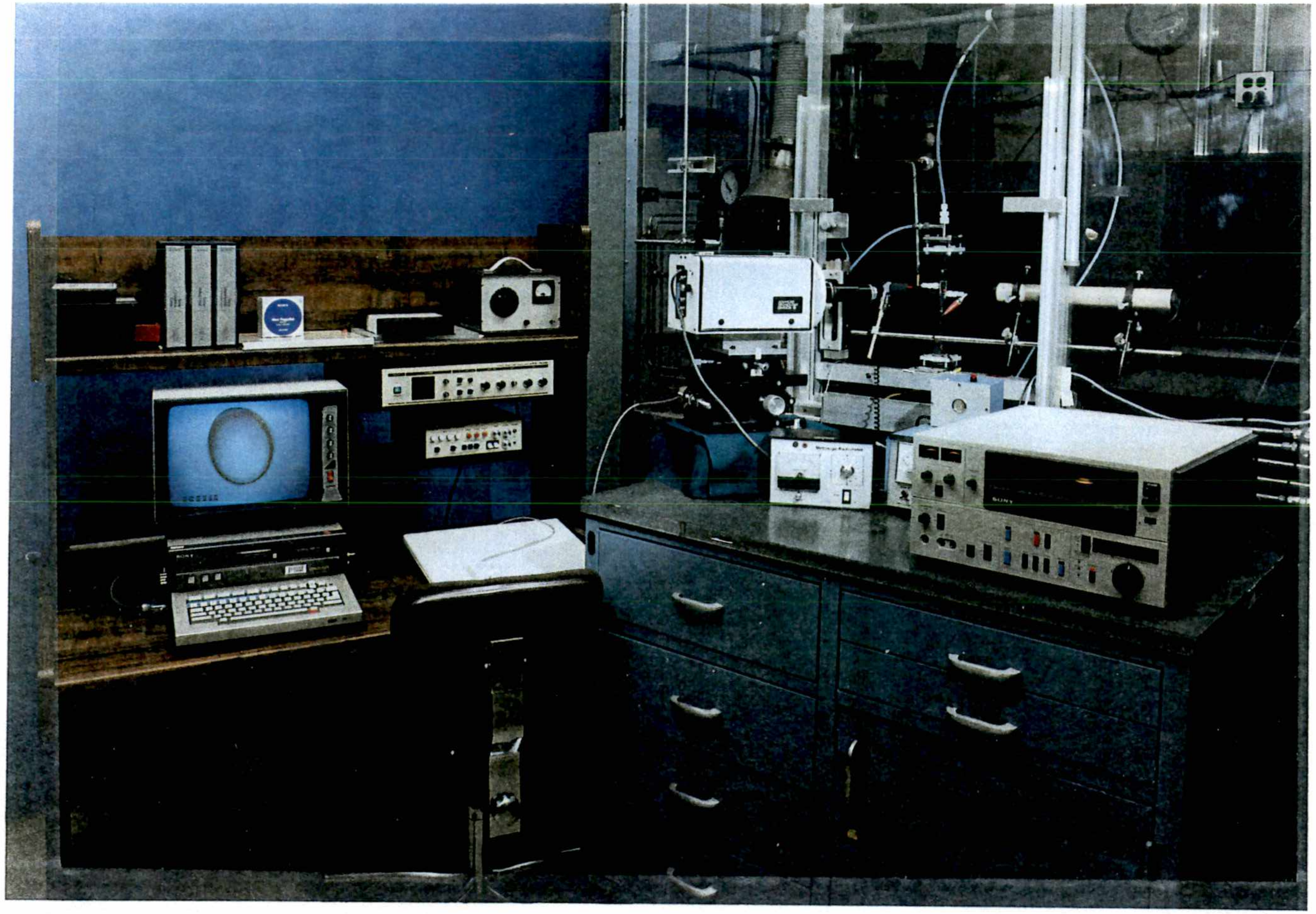

Figure 2.2. A photograph of the experimental equipment used for this work.

tapered column, as shown in Figure 2.1 and in a closeup in Figure 2.3, to stably fluidize it for extended periods of time, e.g. on the order of several minutes. The column is fabricated from glass tubing and polished to assure smoothness (see below). Drops are introduced into the tapered column through a hole in the top of the column and are allowed to fall through the ambient liquid to a location where the diameter of the tapered column is smallest. The narrowest point of the column is also sandwiched between two electrodes which allows the drops to be subjected to an electric field. Once the drops reach this point, they are stably fluidized, or levitated, by adjusting the flow rate of the continuous phase.

In the experiments, the drops are subjected to both static d.c. and pulsed (transient) d.c. electric fields by connecting the electrodes to appropriate power supplies. In this work, the electrodes are made of stainless steel and they too have been polished to ensure smoothness. Drops were subjected to electric fields using electrodes inserted into the tube as depicted in Figure 2.3. The electrodes are 0.32 cm in diameter stainless steel rods and are positioned 2.5 cm apart. The top electrode was retracted when a drop was introduced into the column and was put back into position when the drop was at the appropriate location between the electrodes.

Three modes of operation are of interest in this work. The first mode is one in which a drop is fluidized without an applied electric field. The second mode of operation is that in which a static d.c. electric field is applied to deform an initially spherical drop into a prolate ellipsoid. This is accomplished using a Hipotronics d.c. power supply with a range of 0-20 kV. The third mode of operation is one in which a drop is forced to oscillate by using a pulsed

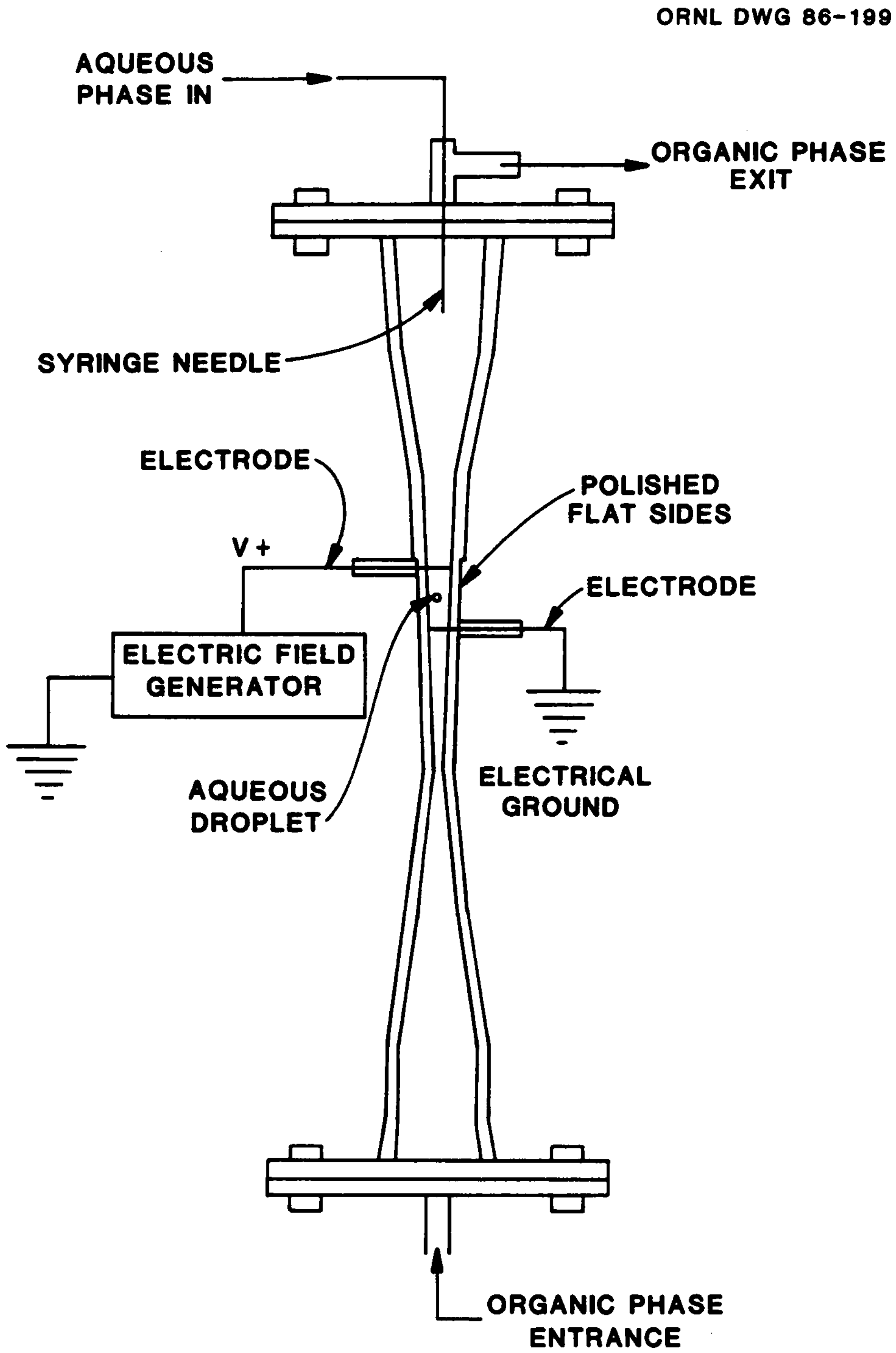

Figure 2.3. A diagram of the tapered column used in this study depicting the location of the electrodes.

d.c. electric field. Pulsing the field allows a drop to tend to a nearly prolate ellipsoidal profile when the field is on and return to a spherical and sometimes an oblate ellipsoidal profile when the field is off, as shown in Figure 2.4. Since pulsed field generators capable of achieving the high voltages needed in this work are not available commercially, the pulsed electric field is produced here by an automotive distributor and ignition coil. Power to the coil is supplied by a low voltage, $0 - 12$ volt, variable power supply. The amplitude of deformation of the drop is then maintained by controlling the amplitude of the applied field by regulating the input voltage to the coil. The frequency of the pulsed electric field is set by turning the distributor using a variable speed motor. The arrangement allows pulses to be generated with a frequency in the range of 0-150 Hz and a duration of about 4 msec for each pulse. The electric potential difference between the electrodes is typically approximately 10 kV but often varies between 5 and 20 kV. A Digistrobe strobe light/tachometer is used to measure the frequency of the electric pulse. A Tektronix model 504 oscilloscope is also deployed to check the voltage being delivered to the high voltage electrode and to further confirm the pulse frequency.

In addition to the two essential sets of equipment described above, an equally important part of the experimental apparatus is the high speed video camera and associated equipment for recording, analyzing, and playing back experimental results. A Tritronics model PC5600 video camera with a high speed shutter is used to monitor the profiles of the drop during the experiments. Shutter speed can be varied from 4 msec to 0.1 msec with framing rates of 60-300 frames per second. A Sony V0-5800 video recorder is used for recording the video image as well as playing back the results for subsequent analysis. A FOR.A video timer,

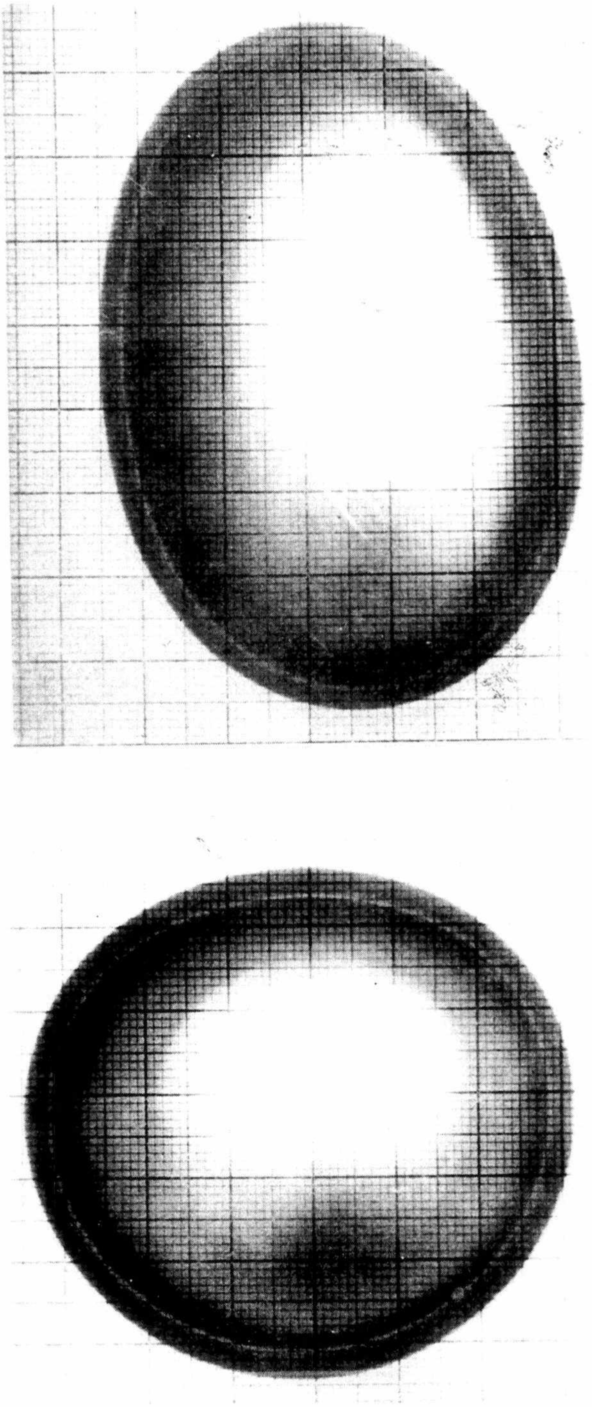

Figure 2.4. Photographs of a water drop as a prolate spheroid and as an oblate spheroid. The water drop is fluidized by an upflowing stream of 2-ethyl-hexanol in the equipment depicted in Figure 2.1. These photographs were taken while the drop was oscillating due to an imposed DC electric field.

model VTG-33, is used to record the date and time on the video tape during each experiment. A VPA-100 position analyzer is used for determination of drop size from the video image. A Sony microcomputer is then used to digitize the video images obtained to determine drop volume, drop surface area, and drop aspect ratio, $\frac{\alpha}{\beta}$, defined as the ratio of the length of the half semi-major axis of the virtually ellipsoidal drop, α, to that of the half semi-minor axis of the drop, β.

As discussed in subsequent sections, the nature of the flow inside the drops is also of interest. To visualize flow fields inside the drops, neutrally buoyant particles of $1 - 10$ micron have been placed inside the drops in a small number of experiments. The flow inside the drop is then visualized by illuminating the vicinity of the narrow portion of the tapered tube where the drop is located with a 5 milliwatt He-Ne laser (Melles Griot), as shown in Figure 2.5. The particles following the motion of the fluid particles inside the drop scatters the laser light. The image created by the scattered light can be recorded and analyzed in the same way as the drop profile (see above). Furthermore, this image is then videotaped for subsequent review.

2.2 EXPERIMENTAL PROCEDURES

In the experiments, a cleaned reservoir is charged with about 400 ml of organic solvent used as the continuous phase. The flow rate of the continuous phase is adjusted using the rotameter. The video camera is started just prior to introduction of the drop into the column. When the drop of water that is introduced into the column reached the region between the two electrodes, the flow rate of the continuous phase is adjusted to keep the drop fluidized between the

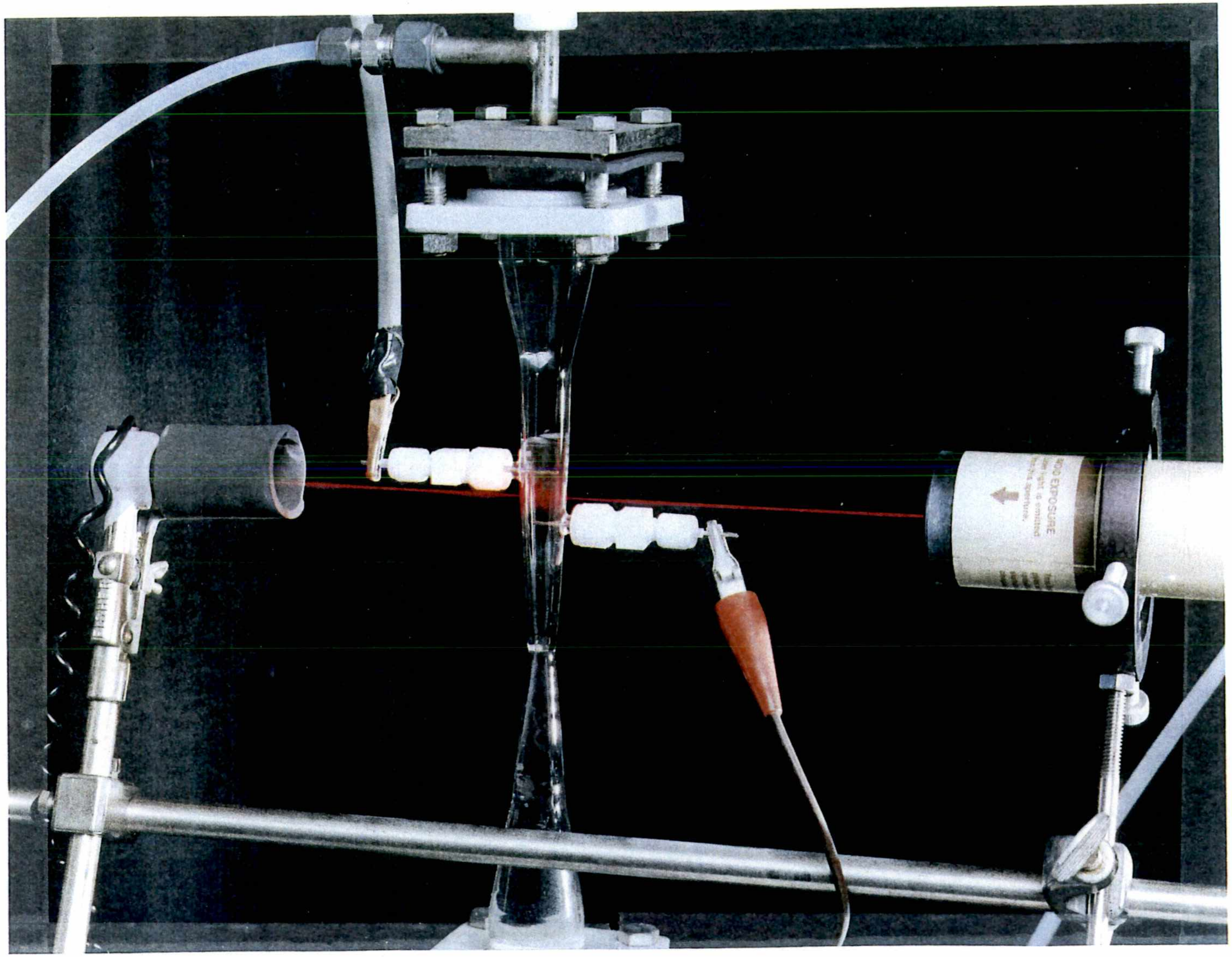

Figure 2.5. Experimental equipment used for flow visualization studies.

electrodes. Thereafter, the electric field is applied as required for the particular experiment. Observations of the size and oscillations of the drops continue for up to 10 min.

Mass transfer data is obtained by measuring the time rate of change in the volume of an axisymmetric drop. The measured drop volume and surface area, when plotted versus time, yield the needed mass transfer data. The flux of water from the drop to the continuous phase is calculated from

$$N = -\frac{1}{A}\frac{\mathrm{d}(\rho^{(i)}V)}{\mathrm{d}t} = K\left(c^{(o)}|_{r=a} - c^{(o)}|_{r=\infty}\right) \tag{2.1}$$

where N is the flux of water from the drop into the organic phase, K is the mass transfer coefficient, A is the drop surface area, $\rho^{(i)}$ is the density of the drop, t is time, $c^{(o)}|_{r=a}$ is the concentration of water at the interface (taken to be the equilibrium concentration), $c^{(o)}|_{r=\infty}$ is the bulk concentration in the continuous phase. Initially, many experiments involving several drop sizes have been run to confirm the accuracy of the present setup and technique for acquiring data to previous experiments by Clinton (1972) who studied the dissolution of water drops in organic media in the absence of electric fields. Figure 2.6 shows that the present results agree well with those of Clinton. The change in slope of the curves after about 10 min can be attributed to the unavoidable accumulation of surfactants at the drop/continuous phase interface (cf. Clinton, 1972).

2.3 EXPERIMENTAL RESULTS

Figure 2.7 shows results of experiments that have been carried out to determine the variation of drop deformation, or aspect ratio, with the applied field strength. In the experiments of Figure 2.7, the continuous phase is 2-ethyl-1-hexanol (2EH). Evidently, up to an electric field strength of approximately 1

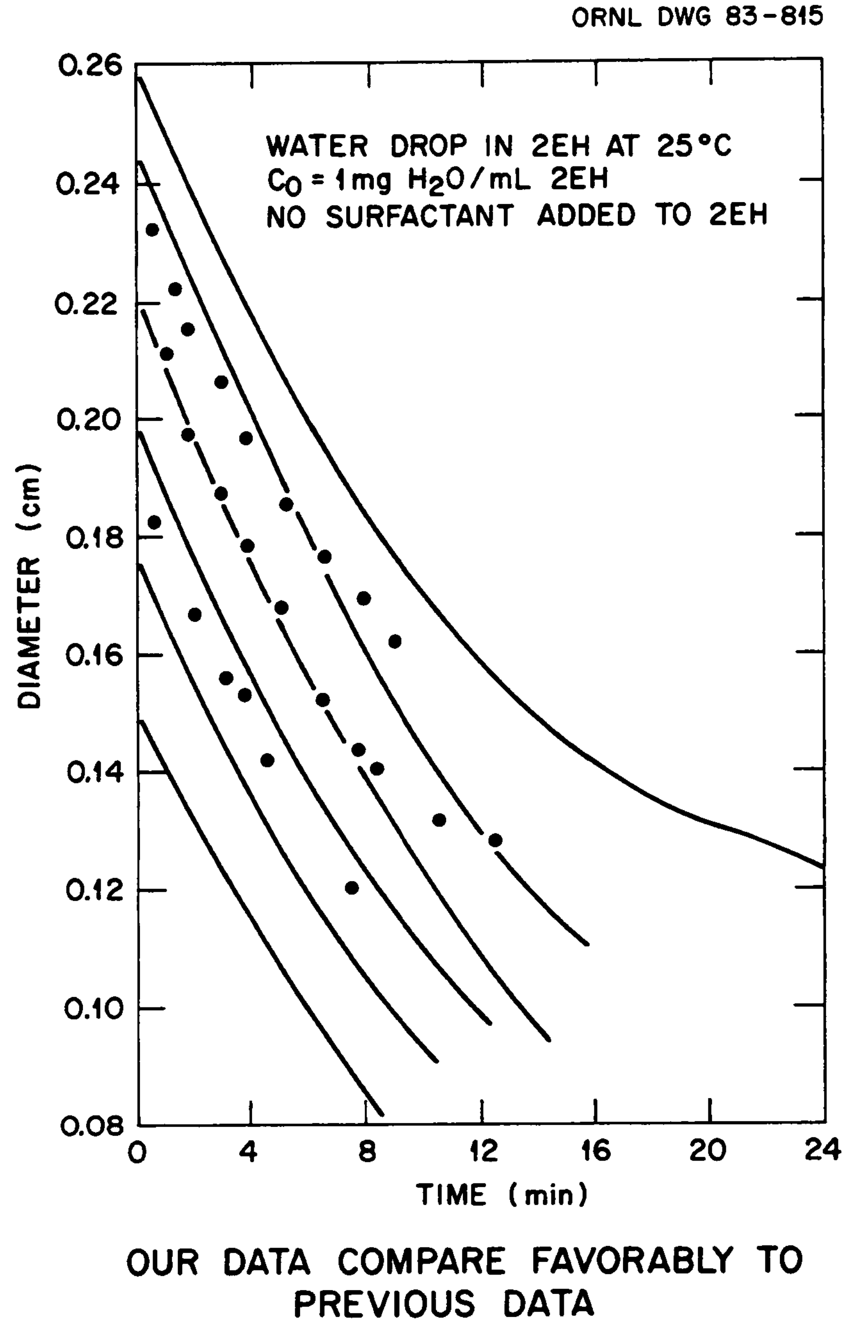

Figure 2.6. Comparison of experimental data from this work to that of Clinton(1972) for a drop of water fluidized in an upflowing stream of 2-ethyl-hexanol.

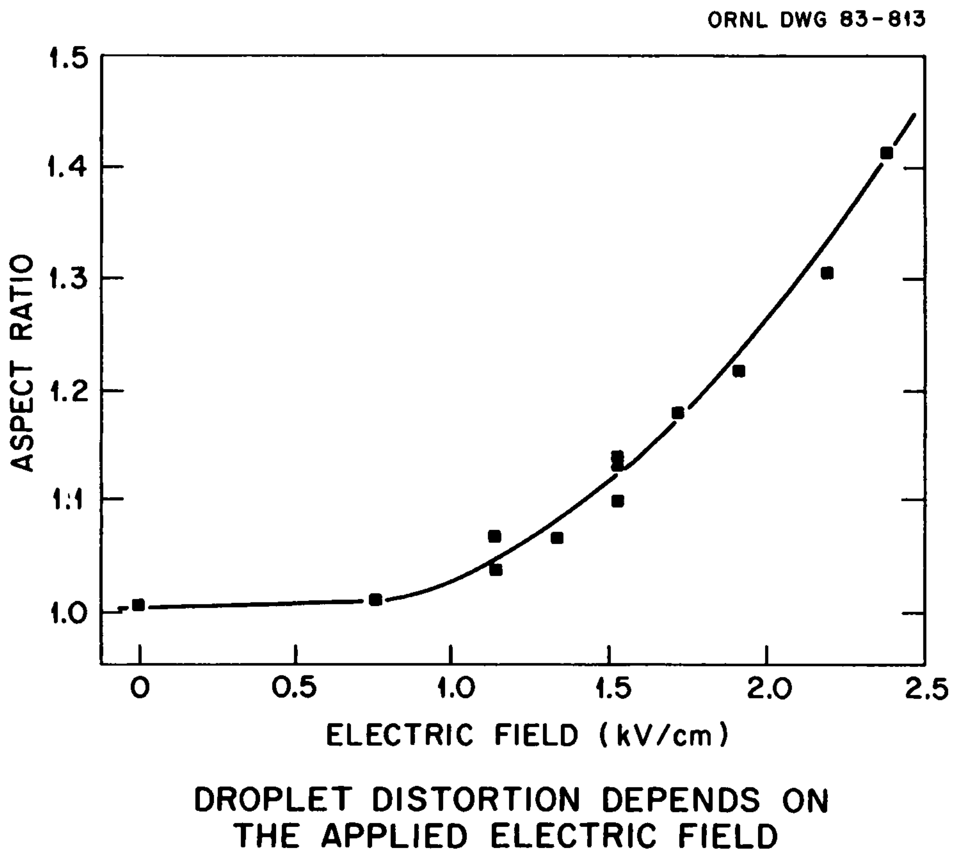

Figure 2.7. Drop aspect ratio as a function of the applied electric field strength for a water drop fluidized in an upflowing stream of 2-ethyl-hexanol.

kV/cm, the drops are not deformed to any significant extent while at 2.5 kV/cm the aspect ratio is about 1.4. The experimental measurements reported in Figure 2.7 also accord with the spheroidal approximation of Taylor (1964) and the more exact finite element computations of Basaran and Scriven (1989)

Aside from their usefulness in their own right, these results also indicate that an electric field generator for forcing drops having an undeformed radius of 0.3 cm to undergo oscillations must be capable of imposing a field strength of approximately 3 kV/cm. Moreover, the pulsed field generator must also be able to reduce quickly enough to less than 1 kV/cm in order to induce the drop to undergo oscillations. This process can then be repeated rapidly to force the drop to oscillate at a predetermined frequency.

In systems with fluid interfaces, the application of an electric field may affect interfacial tension either directly (see, e.g., Adamson, 1982) or indirectly by accelerating the accumulation of surfactants at the drop-ambient fluid interface. Simple scaling arguments (see, e.g., Basaran and Scriven, 1989) and an analysis due to O'Konski and Harris (1957) as well as other show that the eccentricity of a drop, which is defined as $e \equiv \sqrt{1 - (\frac{\beta}{\alpha})^2}$, that is placed in an electric field is proportional to $E\sqrt{\frac{a}{\sigma}}$, where E is the strength of the applied electric field, σ is the interfacial tension, and a is the equivalent radius of the drop, when the interfacial tension is a constant. Figure 2.8 shows the same data as Figure 2.7 but depicts how the eccentricity varies as a function of the product of the applied field strength by the square root of the undeformed radius of the drop. Figure 2.8 shows that e varies linearly with $E\sqrt{a}$, which implies that the interfacial tension remains constant during the course of the present experiments. Figures 2.9 and 2.10 show the variation of e with $E\sqrt{a}$ is also linear for water drops in

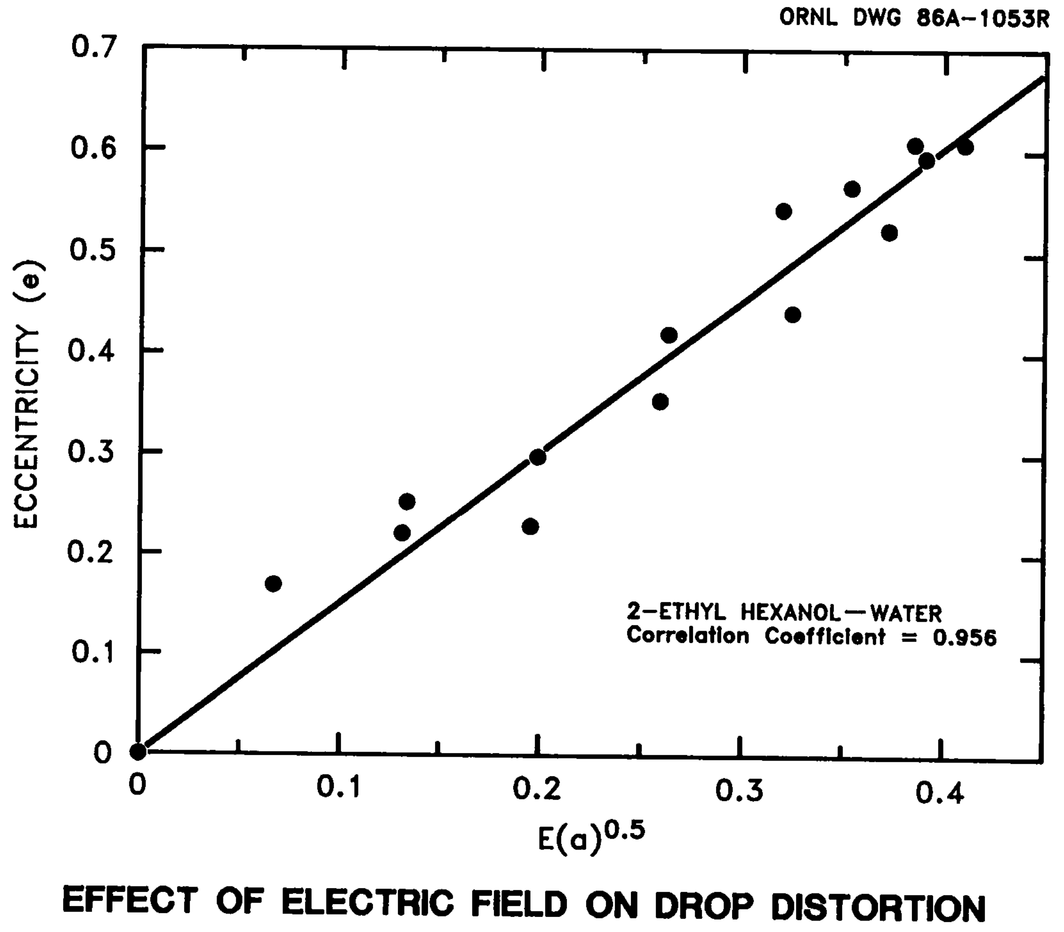

Figure 2.8. Droplet eccentricity as a function of the product of applied electric field strength times the square root of the drop radius based on equivalent volume. In this case the drop is water and the organic phase is 2-ethyl-hexanol.

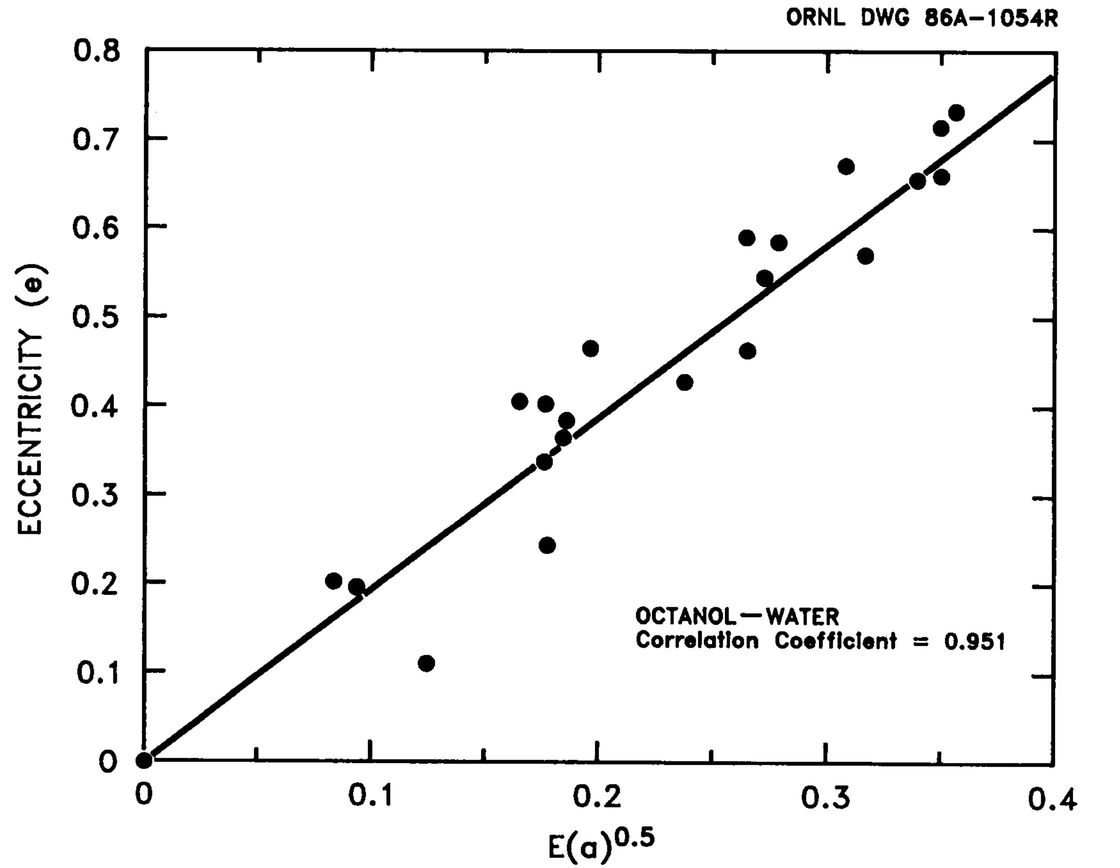

EFFECT OF ELECTRIC FIELD STRENGTH ON DROP DISTORTION

Figure 2.9. Droplet eccentricity as a function of the product of applied electric field strength times the square root of the drop radius based on equivalent volume. In this case the drop is water and the organic phase is octanol.

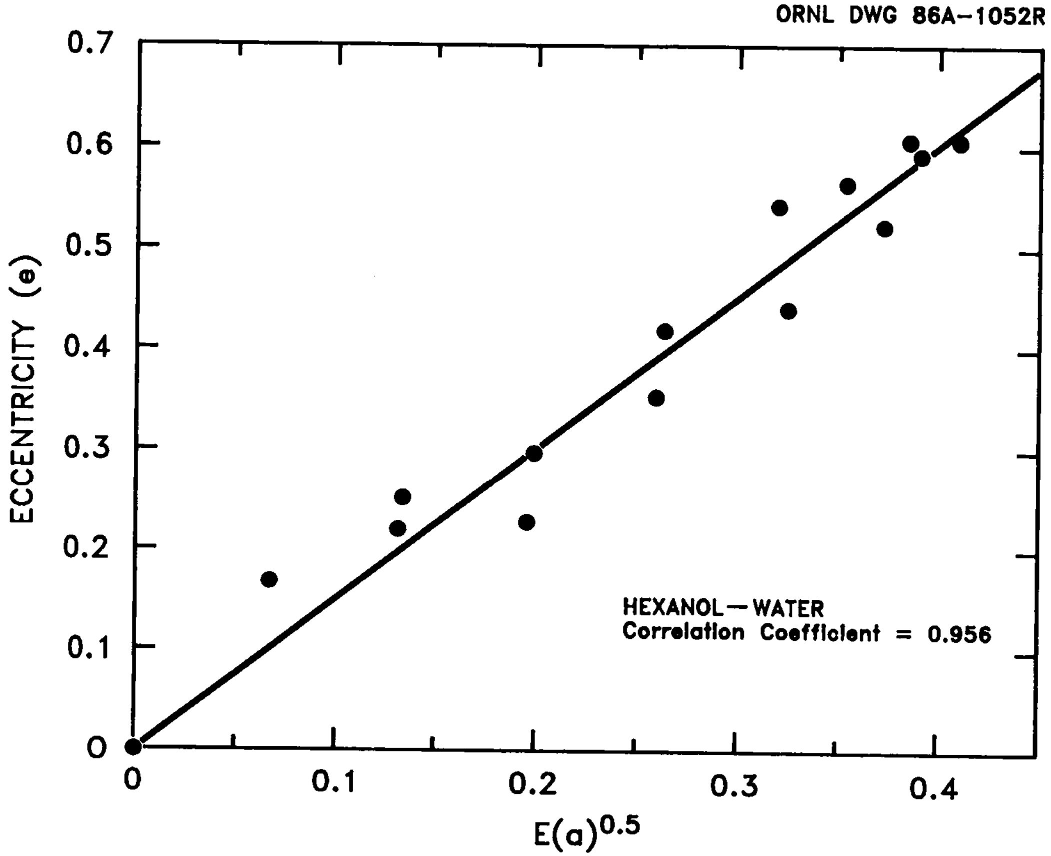

EFFECT OF ELECTRIC FIELD ON DROP DISTORTION

Figure 2.10. Droplet eccentricity as a function of the product of applied electric field strength times the square root of the drop radius based on equivalent volume. In this case the drop is water and the organic phase is hexanol.

octanol and water drops in hexanol, respectively. Therefore, for all three systems considered the interfacial tension should remain independent of the applied field strength during the oscillating drop experiments to be described in what follows.

Figure 2.11 compares the amount of mass remaining in water drops from which mass is transferring out of and into a 2EH continuous phase in three situations: (1) the drop is simply fluidized but the electric field strength is zero, i.e. the drop is neither deformed (by the field) nor oscillating; (2) the drop is deformed by a static d.c. electric field; and (3) the drop is forced to undergo oscillations by a pulsed d.c. electric field. In all three cases, the experiments are started from the same set of initial conditions. Of course, the slope of the drop mass versus time curves are directly proportional to the mass transfer rates. Figure 2.11 makes plain that $\mathcal{K}_{\text{oscillating drop}} > \mathcal{K}_{\text{stretched drop}} > \mathcal{K}_{\text{spherical drop}}$.

Figure 2.12 shows the variation of the average drop mass transfer coefficient with the frequency of the pulsing field. Here again the dispersed phase is water and the continuous phase is 2EH. All the drops used in the experiments depicted in Figure 2.12 have initial diameters of 0.3 cm. Moreover, the data presented in Figure 2.12 correspond to the rate computed over the first three minutes of the experiment (see below). Based on previous experiments, it is expected that surfactant accumulation should not cause the curves of amount of mass remaining in the drop versus time to deviate from linearity for the first 6 to 10 minutes. Thus, collecting and presenting the data for the first three minutes of the experiment should ensure that surfactant effects are negligible in the results presented in Figure 2.12. The natural oscillation frequency of such drops can be estimated from Lamb's (1945) theory to be 100 Hz. As can be seen from Figure 2.12, there is very little change in mass transfer coefficient at low

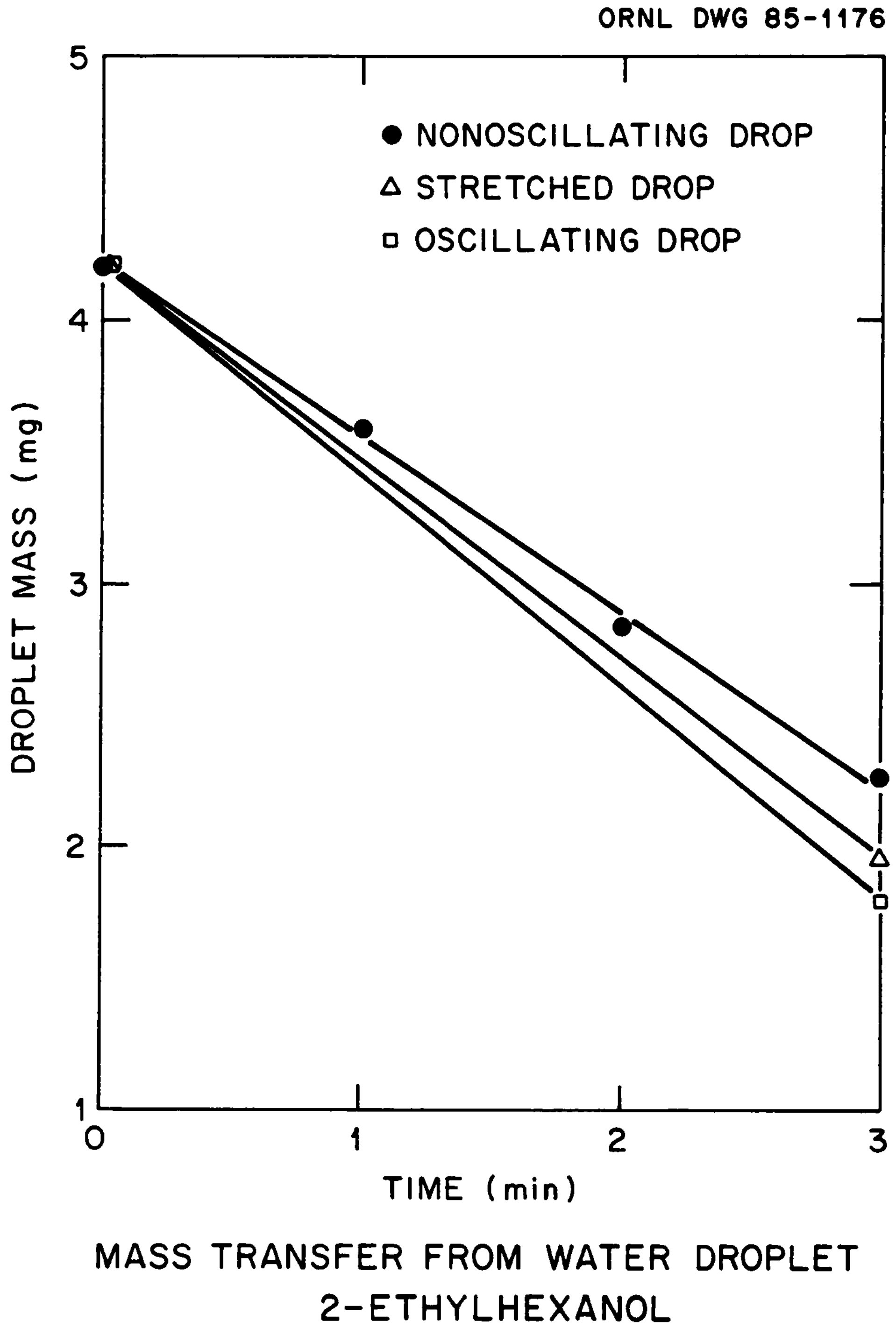

Figure 2.11. Change in droplet mass vs time for a circulating drop, a stretched circulating drop and an oscillating drop. Here the drops are water and the upflowing phase is 2–ethylhexanol.

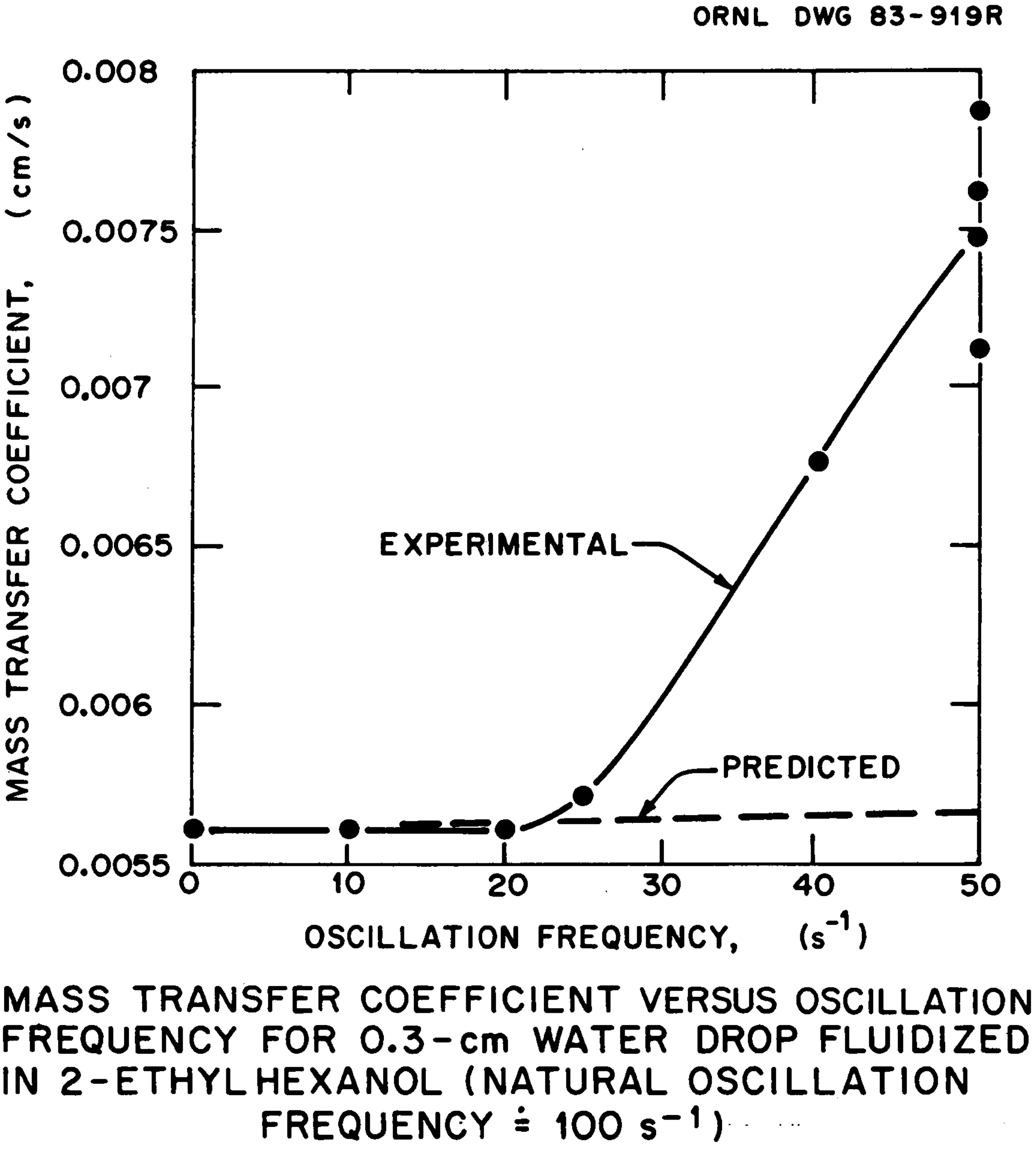

Figure 2.12. Mass transfer coefficient as a function of oscillation frequency for 0.3-cm water drop fluidized in 2-ethylhexanol.

frequencies of 10-30 Hz, but a 35% increase occurs at 50 Hz. Evidently, the mass transfer coefficient increases as the driver frequency approaches the resonance frequency of the drop. Also shown in Figure 2.12 is a mass transfer coefficient that has been calculated based on a time averaged surface area that is available for mass transfer. The time averaged values of drop surface area are computed from experimental measurements of drop shape. Evidently, the prediction of the mass transfer coefficient by this surface stretch theory does not match the experimental data. As discussed in Chapter 1, such surface stretch models have been proposed by Angelo *et al.* (1966) and others.

Since the surface stretch model does not match the experimental results, additional experiments have been conducted by placing water drops in a continuous phase consisting of 2EH saturated with water so that no mass transfers from the dispersed to the continuous phase. In these experiments, the pulsing frequency has been varied over a range to determine the change in drop surface area as a function of the forcing frequency. Figure 2.13 shows the variation of the ratio of the surface area of the drop to that of a sphere of equivalent volume with the forcing frequency. In these experiments, the drops are subjected to forcing frequencies of 10-120 Hz and a field strength of 2.5 kV/cm. Figure 2.13 shows that surface area changes by less than 1% over the entire range of frequencies considered. Because the surface area changes so little during these finite-amplitude oscillations (see below), it is not too surprising that surface stretch model cannot account for the increase in the mass transfer coefficient observed in Figure 2.12.

The aforementioned results are further reinforced by plotting the variation of the surface area ratio with the drop aspect ratio, as shown in Figure 2.14. In most experiments, the drop aspect ratio ranges between 0.7 and 1.3. It is

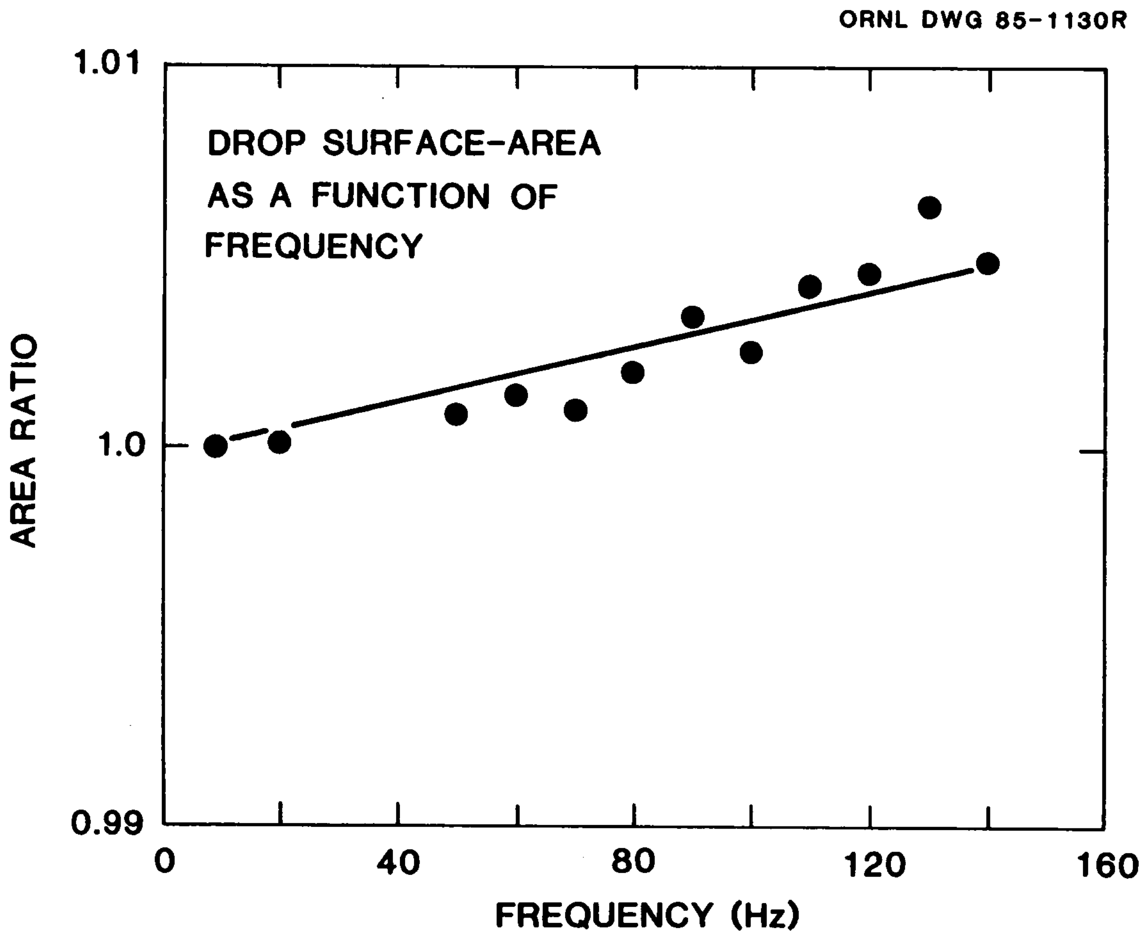

Figure 2.13. The ratio of the surface area of an oscillating drop to a sphere of equivalent volume vs frequency oscillation. Here the drop size has been kept constant. The drop is water fluidized by 2-ethyl-hexanol.

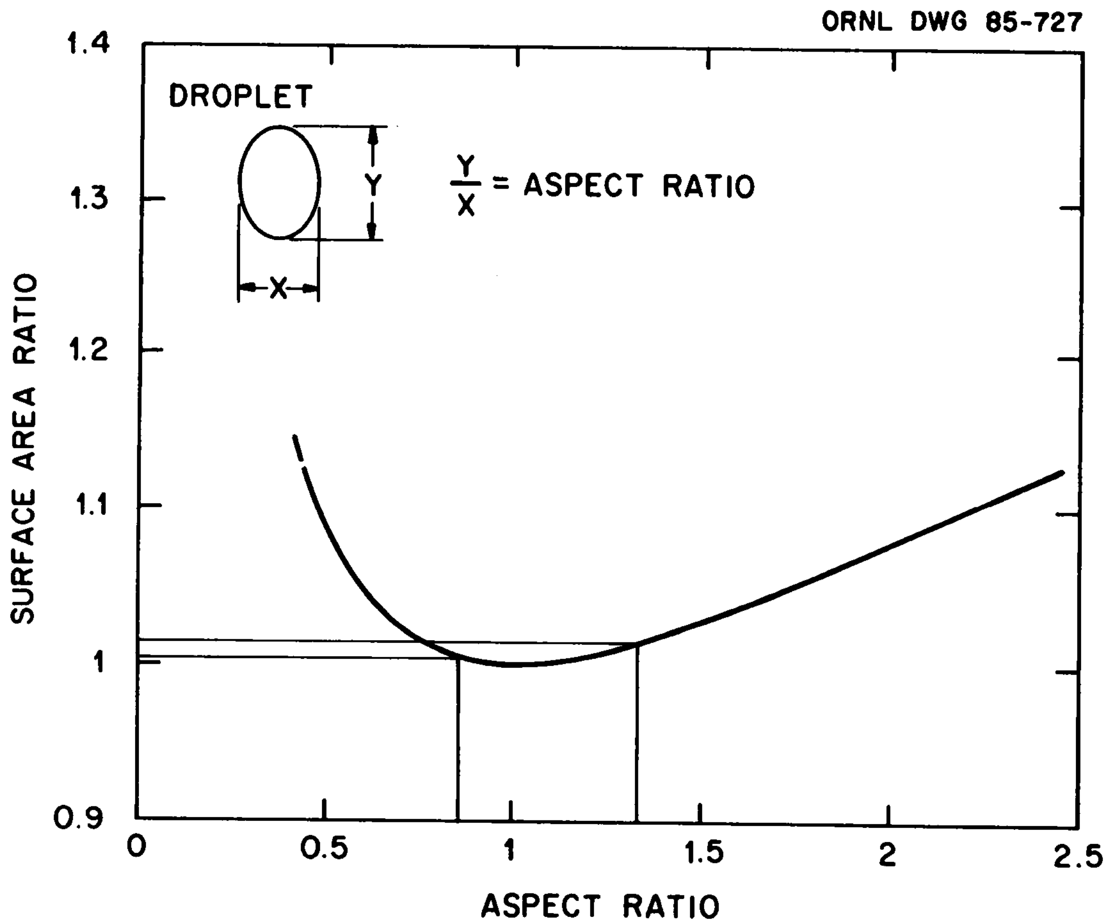

Figure 2.14. The ratio of surface area of an elliptical drop to a sphere of equivalent volume versus the aspect ratio of the elliptical drop. The area indicated by the lines represents the range for a typical drop in this work.

noteworthy that a drop having an aspect ratio larger than 1.85 cannot exist in static equilibrium in an externally applied electric field. Therefore, were the drops allowed to deform to the highest aspect ratio accessible to them, the change in surface area would still be too small to account for the increase in mass transfer rates observed in this work.

2.4 FLOW VISUALIZATION

A second major assumption of the surface stretch theories of Angelo *et al.* (1966) and Rose and Kintner (1966) is that a well-mixed turbulent core exists inside the drops. This assumption is put to test here by directly observing the flow fields inside the drops by tracking the motion of neutrally buoyant particles as outlined earlier. A turbulent core would of course be well mixed and the particles inside such a core would appear to move randomly and not undergo regular motions.

In these experiments, 2EH is used as the continuous phase. The 2EH, however, is saturated with water to eliminate mass transfer from the drop. Figure 2.15 shows the flow field inside a fluidized drop: the path lines of the fluid particles are toroidal and regular. Figure 2.16 shows the flow field inside an oscillating drop: the path lines are again regular in nature. Complete mixing would be manifested as uniformly distributed particles moving in a random fashion. However, Figure 2.16 makes plain that the path lines inside the oscillating drops are merely a superposition of circulatory motion due to the fluidization and the radial motion due to drop oscillation.

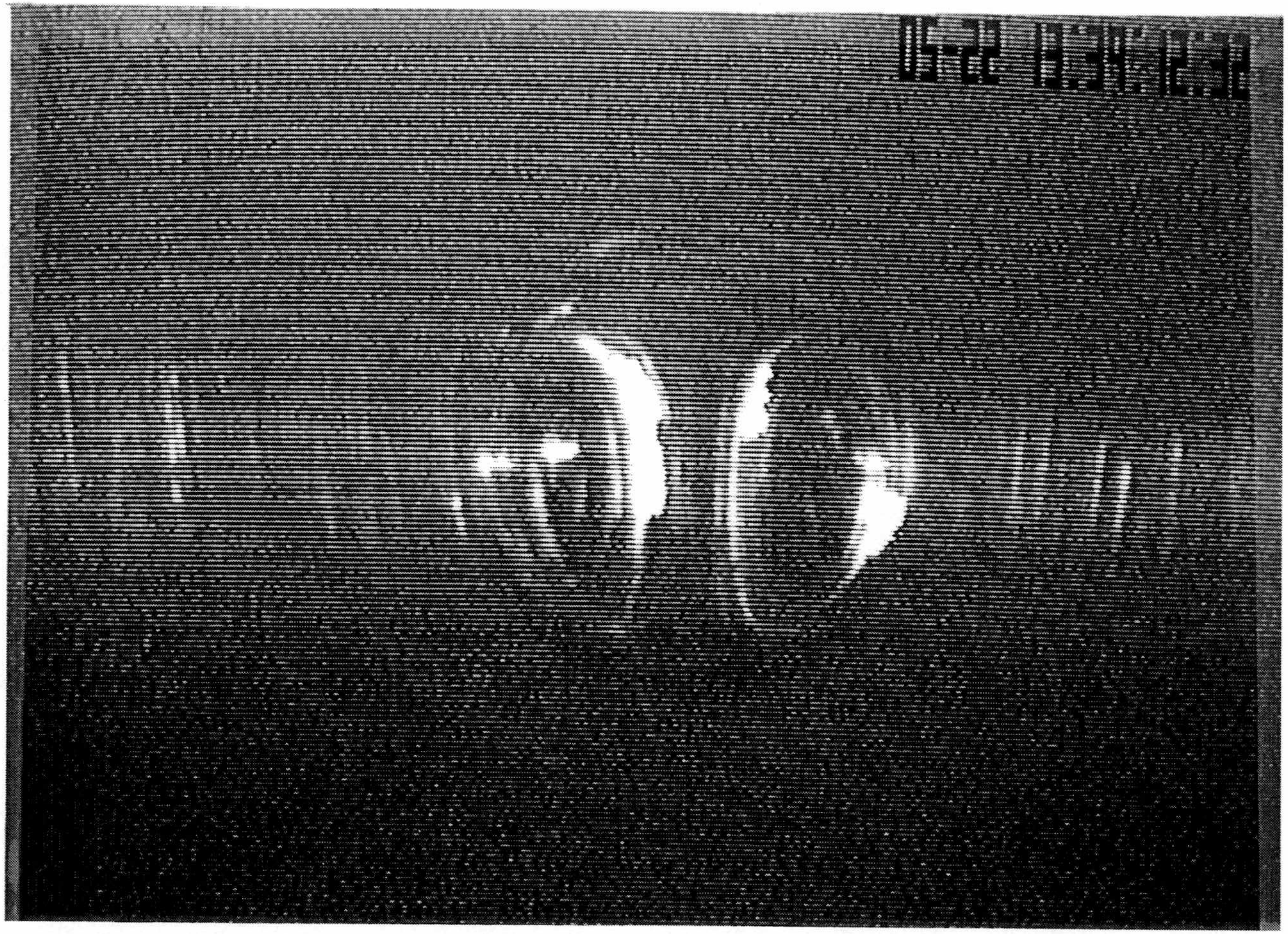

Figure 2.15. Laser illumination of a circulating drop. The drop is water which is fluidized by 2-ethyl-hexanol.

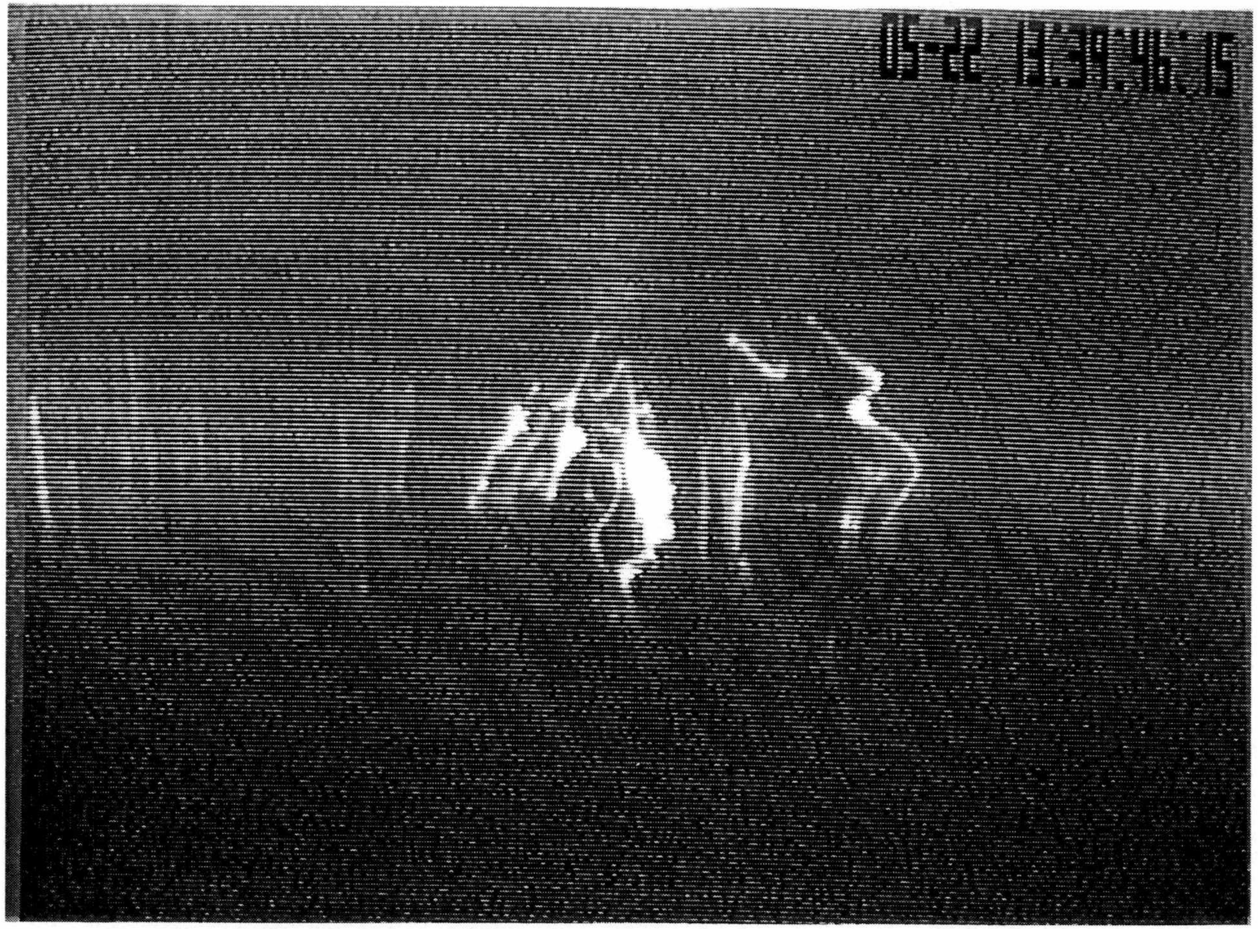

Figure 2.16. Laser illumination of an oscillating drop. The drop is water which is fluidized by 2-ethyl-hexanol.

2.5 AN ELECTRICALLY-ENHANCED DEVICE FOR SOLVENT EXTRACTION

As mentioned previously in Chapter 1, one of the goals of this work was to look at the application of electric fields to solvent extraction. Work by pioneers in electrohydrodynamics such as Rayleigh(1882), Macky(1926), and Nolan (1931) showed that application of electric fields of appropriate strength will cause drop disintegration leading to formation of many small droplets. Experimental studies presented in Section 2.4 showed that drop oscillations will increase mass transfer rates. A patent by Cottrell and Speed (1911) showed that application of electric fields enhanced coalescence of aqueous drops and application of this technology has been used for oil/water separators by the petroleum industry (Waterman, 1965). These three consequences of the application of electric fields have been applied to solvent extraction with the outcome being an extraction device based on use of electric fields.

An experimental apparatus was assembled to study the electrically driven emulsification with subsequent coalescence of the drops. Figure 2.17 presents the range of electric field strengths examined to determine appropriate ranges for operation. Figure 2.17 shows plainly that the range of electric field strengths used for dispersion falls close to the range of electric field strengths necessary for coalescence. Based on the information presented in Figure 2.17, a prototype solvent extraction unit was built and is shown in Figure 2.18, This unit was designed to take advantage of the narrow change in electric field occurring between coalescence and emulsification. The prototype used a pulsed electric field to control droplet formation, emulsification, and coalescence. The unit depicted in Figure 2.18 operates with counter current flow of the aqueous stream and

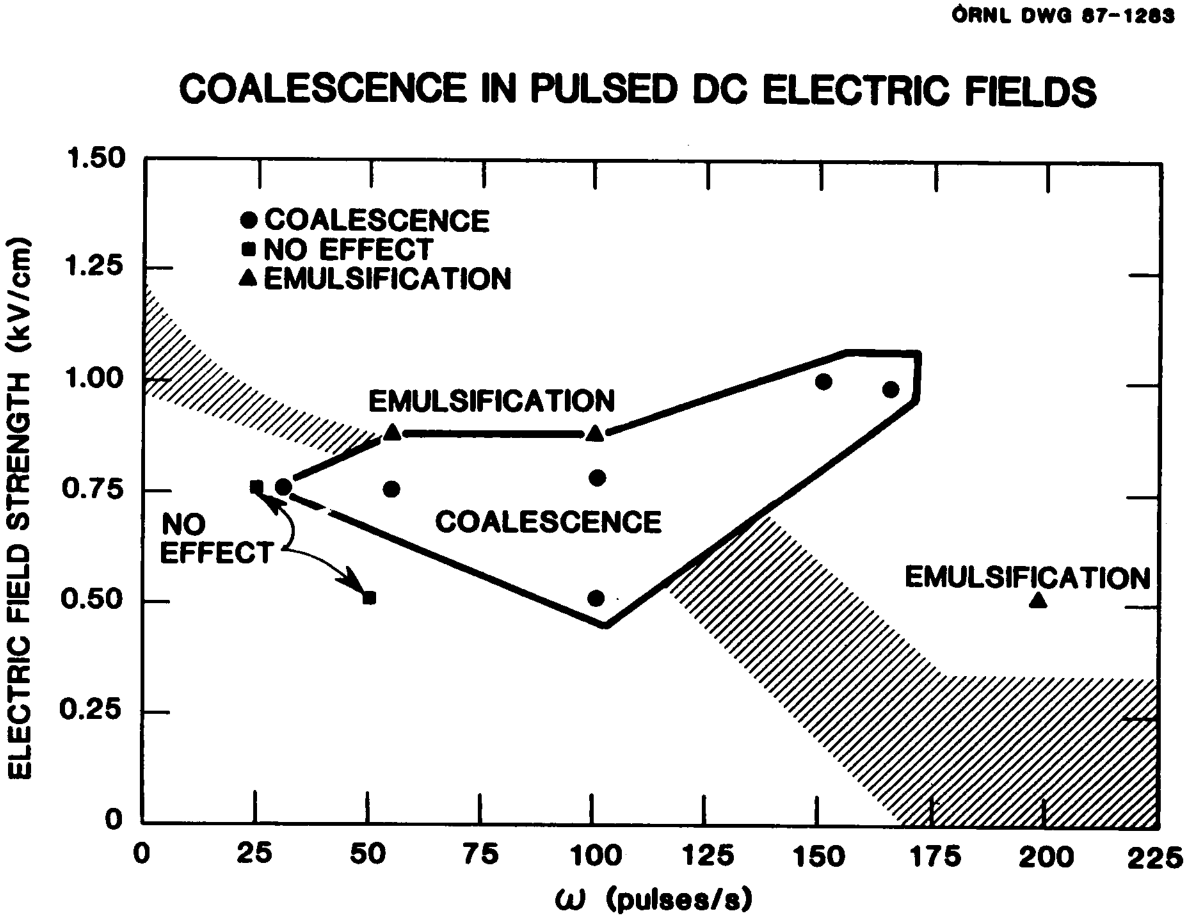

Figure 2.17. Behavior of drops in an applied electric field. The drops are water in 2-ethyl-hexanol.

ORNL DWG 86-698R

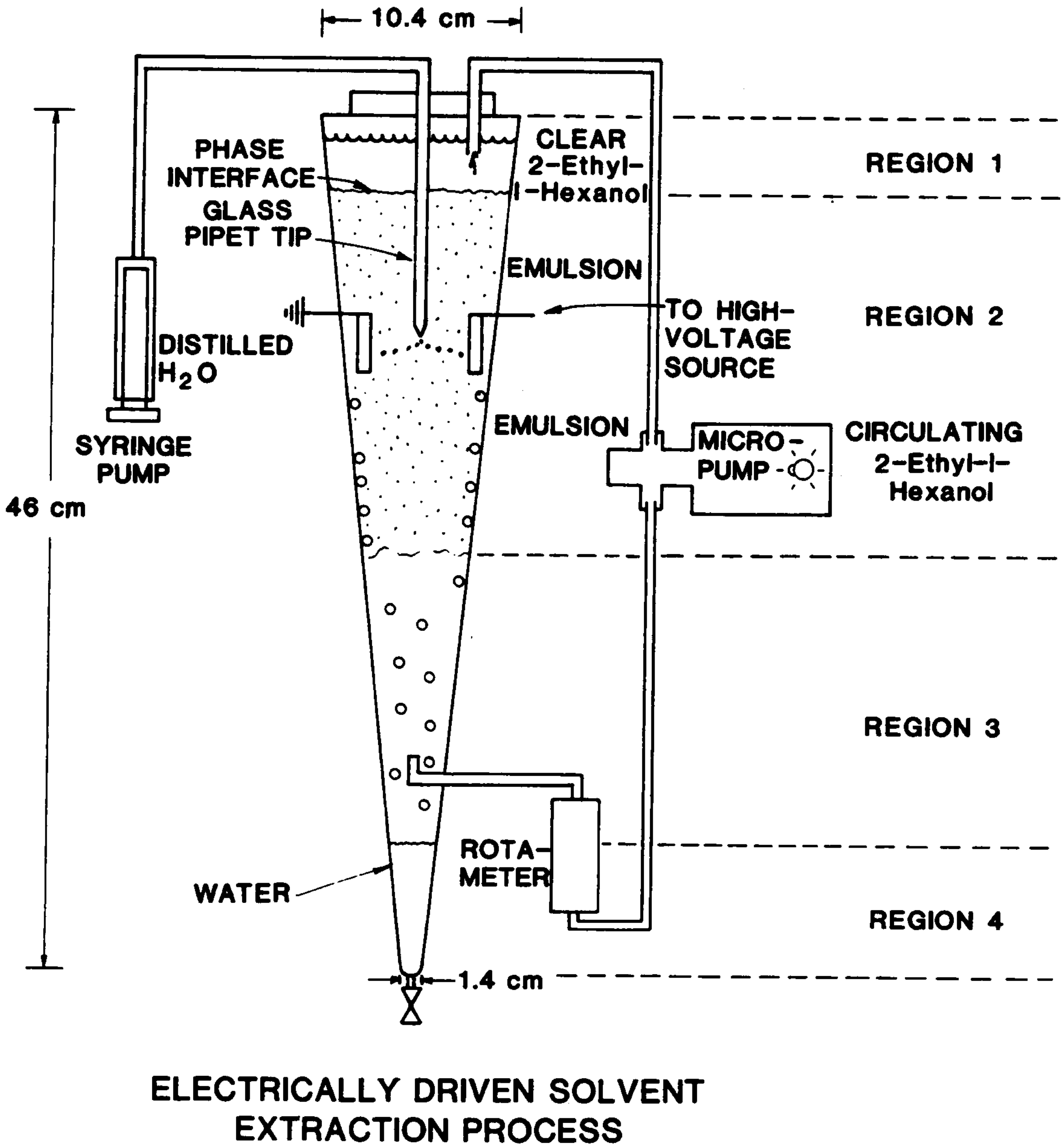

Figure 2.18. The emulsion phase contactor

organic stream. Organic flows into the column near the bottom of the column, up through the emulsion and then out the top of the device. The aqueous phase enters at the top of the unit through a nozzle placed between the electrodes. The electrodes were used to impose an electric field on the nozzle tip. The drops were broken into small drops in the device and a cloud of emulsion formed. The small aqueous drops comprising the emulsion coalesced and fell through the organic into the bottom of the column where the aqueous phase was then withdrawn. Imposition of both AC and DC electric fields was shown to create small droplets with a high surface area to volume ratio and coalesce the droplets. A patent for the device shown in Figure 2.18 was granted (U.S. Patent 4,767,515; Scott and Wham, 1988). The unit was later tested for mass transfer rates and found to yield favorable mass transfer rates as compared to more traditional contacting equipment (Scott and Wham, 1989).

Subsequent to this invention, a study of drop coalescence has been conducted by Zhang, *et al.*(1995). Recognizing that enhancement of drop coalescence occurs when the electric field induces charges of the opposite sign on the closest faces of two nearby drops(Davis, 1964), Zhang, *et al.* conducted a trajectory analysis which included both gravitational and electric field effects. The trajectory analysis of drop coalescence was used to predict pairwise collision and coalescence rates. Zhang, *et al.* found that enhancement of drop collision was found to be more pronounced when the imposed electric field acted in a direction perpendicular to gravity.

2.6 RESULTS/CONCLUSIONS FROM EXPERIMENTAL WORK.

An experimental system has been developed to study the enhancement of mass transfer to and from a drop by forcing it to undergo oscillations by the application of a pulsed d.c. electric field. With millimeter-size drops immersed in organic solvents, increases in mass transfer coefficients on the order of 35% has been achieved. Previous theories based on the concept of surface stretch are unable to account for the observed increases in mass transfer rates and coefficients. First, the change in drop surface area that occur in the experiments is too small to account for the observed enhancement in mass transfer. Moreover, these previous theories also assume that the fluid inside the drops is well mixed. The validity of this assumption has been tested by flow visualization studies which has revealed that the flow inside the drops is laminar and not turbulent. Such experimental observations, which agree with recent theories of drop oscillations(e.g., Basaran, 1992; Basaran and DePaoli, 1994), point to the need to develop a better understanding of the fluid mechanics in and around drops and the implications of the flow to transient conjugate mass transfer.

A device for solvent extraction based on the use of electrohydrodynamics was developed and patented. This device has seen application in industry. Further work on the device has focused on understanding the theoretical basis for electric field enhanced coalescence (Zhang, *et al.*, 1995)

The next step in understanding mass transfer from oscillating drops is to develop appropriate computational models to facilitate understanding the complex hydrodynamics. Chapter 3 describes the work on modelling flow around solid spheres. Chapter 4 describes modelling work on fluid spheres. Chapter 5 describes the use of fluid sphere flow fields in analyzing conjugate mass transfer problem for fluid drops.

CHAPTER 3

WALL EFFECTS OF FLOW PAST SOLID SPHERES AT FINITE REYNOLDS NUMBER

The flow past both solid and fluid spheres and spheroids *and* deformable drops or bubbles, even when the fluids are simple Newtonian ones, is important in a number of fields of science and technology. For example, such flows play a central role in areas as diverse as chemical processing (Bird *et al.*, 1960; Sherwood *et al.*, 1975) and meteorology (Beard *et al.*, 1989). Despite the importance of such flows, however, a fundamentals-based and detailed understanding of the apparently simple problem of the steady flow past a solid sphere in an unbounded fluid (Fornberg, 1988) and its stability (Kim and Pearlstein, 1990; Natarajan and Acrivos, 1993) was not available until recently. The closely related problem of flow past a solid sphere that is either suspended in a tube of *finite radius* by an upflowing liquid (the fluidized sphere problem) or falling in a tube of *finite radius* (the falling sphere problem) is of even greater technological interest. An adequate understanding of the bounded flow case has heretofore been lacking and is the goal of this work.

There has been a resurgence in the study of flow past noncolloidal solid and fluid particles in the last few years. One major driving force for this renewed interest is the need to understand at a fundamental level recent innovations that utilize electric fields to enhance transport phenomena and separations in multiphase systems (see, e.g., Kaji *et al.*, 1980; Scott and Wham, 1988; Ptasinski and Kerkhof, 1992). The problem of flow in and/or around solid and fluid particles in a tube is a central issue in these efforts and is fundamental to understanding the role of electric fields in enhancing heat and mass transfer to or from solid and fluid particles.

Flow past and drag coefficients for fluidized spheres are likely to see additional renewed interest if recent research on containerless processing on earth (see, e.g., Dagani, 1992) can provide contaminant free materials as claimed. Fluidizing the product minimizes the contaminants introduced by the container walls and can also produce a perfect sphere as the end product. The new containerless processing concept aims to provide a lower cost alternative to space-based, zero-gravity processing (see, e.g., Carruthers and Testardi, 1983).

There are numerous works in the literature which either present or analyze experimental data on drag coefficients for spheres in an infinite expanse of ambient fluid (e.g., Clift *et al.*, 1978; Flemmer and Banks, 1986; and Turton and Levenspiel, 1986). There are also numerous computational studies of flow past spheres in an unbounded fluid (e.g., Dennis and Walker, 1971; Rivkind *et al.*, 1976; Fornberg, 1988). Unfortunately, there are no numerical (but see below) results available for the corresponding problem of a sphere in a tube and there is significant disagreement concerning which correlations provide the best estimate of drag for flow past a solid sphere in a finite tube.

Hartman *et al.* (1989) devote the majority of their paper to modifying literature correlations for spheres in an unbounded expanse of ambient fluid to fit their data on drag for spheres falling in a tube without acknowledging wall effects. Wall effects are expected to be important in the experiments they describe over the range of values of the ratio of the diameter of the sphere to that of the tube, λ , presented in their paper of 0.022 to 0.0804. For example, in Section 3.4 of this work, it is shown that when $\lambda = 0.08$, not accounting for wall effects can introduce an error of 20% in drag coefficient even when the Reynolds number, which measures the relative importance of inertial to viscous forces, is small.

The presence of a finite-size physical container also raises concerns about wall effects on drag coefficients for fluidized spheres. Another complicating factor here is the use of a wire to suspend the sphere for the experimental measurement of drag (see below). The error introduced by the wire was heretofore not known and is also evaluated here for the first time.

Furthermore, there are very few experimental studies of flow past solid spheres in tubes in the range of low to moderate Reynolds numbers as evidenced by the scarceness of data in the literature when $1 < Re < 100$.

(a) Drag correlations for fluidized spheres

Fayon and Happel (1960) carried out experiments with both fluidized and falling spheres under conditions of low Reynolds number flow. They made partial use of their own experimental data in developing a correlation for drag since they did not allow the correction factor that accounts for the presence of the tube to depend on Re. The correlation they gave that relates the ratio of the drag coefficient for a fluidized sphere in a tube to that predicted by the Stokes equation for a sphere in an unbounded fluid is:

$$\frac{F_D}{F_S} = \frac{C_D}{C_S} = \left[\frac{1 - \frac{2}{3}\lambda^2}{1 - K\lambda + 2.087\lambda^3} + \left(\frac{C_A}{C_S} - 1\right)\right] \quad , \tag{3.1}$$

where F_D is the actual drag on a sphere in tube flow, F_S is the Stokes drag on a sphere in an infinite expanse of fluid, C_D is the actual drag coefficient for a sphere in tube flow, C_A is the actual drag coefficient for a sphere in an unbounded fluid given by Perry (1950), C_S is the drag coefficient based on Stokes law ($\frac{12}{Re}$), and K is set equal to 2.105 to agree with a theoretical analysis of Brenner and Happel (1958). Here the wording actual, as in the definition of F_D, C_D, and C_A, means that these quantities are evaluated at the Reynolds number appropriate to the flow. The correlation assumes that the correction due to the presence of the tube wall is additive to that due to inertia. However, Fayon and Happel (1960) also acknowledged that K is a function of Reynolds number as first postulated by Faxen (1923) and, in fact, that a K value of 1.96 actually provides a better fit to their data over the range $0 \leq Re \leq 30$. Brenner and Happel (1958) arrived at the value of $K = 2.105$ by analyzing by the method of reflections the problem of a sphere suspended in a tube in the creeping flow regime. Therefore, by forcing their correlation to agree with Brenner and Happel in the limit as $Re \to 0$, Fayon and Happel arrived at a correlation that becomes increasingly more inaccurate as Re increases.

Wakiya (1957) presented a modification to the Faxen result that is similar to the Fayon and Happel correlation in the creeping flow limit by incorporating higher order terms in λ

$$\frac{F_D}{F_S} = \frac{1 - \frac{2}{3}\lambda^2}{1 - 2.105\lambda + 2.09\lambda^3 - 1.11\lambda^5} \quad . \tag{3.2}$$

Haberman and Sayre (1958) developed an analytical solution based on a truncated polynomial series that satisfy the Stokes equations and the appropriate boundary conditions. They thereby obtained the following result in the creeping flow limit:

$$\frac{F_D}{F_S} = \frac{1 - \frac{2}{3}\lambda^2 - 0.20217\lambda^5}{1 - 2.105\lambda + 2.0865\lambda^3 - 1.0768\lambda^5 + 0.72603\lambda^6} \quad . \tag{3.3}$$

(b) Drag correlations for falling spheres

Several correlations that predict the variation of drag with λ are available for the case of a falling sphere. Ladenburg (1907) gave the following linear approximation in the creeping flow limit:

$$\frac{F_D}{F_S} = 1 + 2.105\lambda \quad . \tag{3.4}$$

Francis (1933) developed an empirical formula based on data available in the literature. This formula too is restricted to the creeping flow limit and is given by:

$$\frac{F_D}{F_S} = \left(\frac{1 - 0.475\lambda}{1 - 4.75\lambda}\right)^4 \quad . \tag{3.5}$$

For falling spheres, the counterpart of (3.1) obtained by Fayon and Happel (1960) is:

$$\frac{C_D}{C_S} = \frac{F_D}{F_S} = \left[\frac{1}{1 - K\lambda + 2.087\lambda^3} + \left(\frac{C_A}{C_S} - 1\right)\right] \quad . \tag{3.6}$$

As in (3.1), the coefficient that appears in (3.6) is given by $K = 2.105$.

The Haberman and Sayre (1958) result for a falling sphere under conditions of creeping flow is

$$\frac{F_D}{F_S} = \frac{1 - 0.75857\lambda^5}{1 - 2.105\lambda + 2.0865\lambda^3 - 1.7068\lambda^5 + 0.72603\lambda^6} \quad . \tag{3.7}$$

Comparison of (3.7) to (3.3) for fluidized spheres shows that the two drag expressions differ only in their numerators.

(c) Goals and outline

There are no correlations in the literature for the fluidized sphere problem or the falling sphere problem which properly account for the effects of both λ and Re. In order to solve the problem and obtain drag coefficients, an approach based on numerical simulation is adopted in this work.

Section 3.1 presents the equations and boundary conditions that govern the flow past a solid sphere in a tube of finite radius. Section 3.2 outlines the Galerkin/finite element formulation used for calculation of velocity profiles. Section 3.3 presents results for three situations: a fluidized sphere, a falling sphere, and a fluidized sphere attached to the end of a wire. Also, new drag coefficients for falling and fluidized spheres are presented that are valid for $0 \leq Re \leq 100$ and $0.08 \leq \lambda \leq 0.7$. Moreover, the onset of wake formation and wake characteristics are investigated as functions of λ and Re and the computational predictions are compared to experiments of Nakamura (1976) and others. Section 3.4 discusses the relevance and relationship of this work to certain others and lays the groundwork for future studies based on the present analysis.

3.1. GOVERNING EQUATIONS AND BOUNDARY CONDITIONS

A solid sphere is centrally located and is either fluidized or falling in a vertical circular tube. The fluid exterior to the sphere is Newtonian and has constant viscosity μ and constant density ρ. Therefore, the axisymmetric, steady, incompressible flow in both the fluidized sphere and falling sphere problems is governed by the Navier-Stokes equations and the continuity equation:

$$Re\,\underline{\mathbf{v}} \cdot \nabla \underline{\mathbf{v}} - \nabla \cdot \underline{\underline{\mathbf{T}}} + St\,\underline{\mathbf{e}}_z = \underline{0} \quad ,$$
$$\nabla \cdot \underline{\mathbf{v}} = 0 \quad . \tag{3.8}$$

Equation (3.8) is already dimensionless because length is measured in units of a, the sphere radius, and velocity is measured in units of U_∞, a characteristic velocity. In the case of a fluidized sphere, the flow approaches a fully-developed Poiseuille flow sufficiently far upstream and downstream of the sphere and U_∞ is the (maximum) value of the velocity along the axis of symmetry of the tube which has radius d. In the case of a falling sphere, the flow is quiescent sufficiently far upstream and downstream of the sphere, and U_∞ is the steady translational velocity of the falling sphere. In (3.8), $Re \equiv \frac{\rho U_\infty a}{\mu}$ is the Reynolds number; $\underline{\mathbf{v}}$ is the velocity vector with components v_x and v_z in a cylindrical coordinate system (x, z) based at the center of the sphere where z denotes distance measured along the axis of symmetry or the centerline of the tube and x that perpendicular to it; $\underline{\underline{\mathbf{T}}}$ is the total stress tensor; $\underline{\mathbf{e}}_z$ is a unit vector in the z-direction; and $St \equiv \frac{\rho g a^2}{\mu U_\infty}$ is the Stokes number, where g is the magnitude of the gravitational acceleration which points in the negative z-direction. The total stress tensor $\underline{\underline{\mathbf{T}}} = -p\underline{\underline{\mathbf{I}}} + \underline{\underline{\tau}}$, where p is the pressure, $\underline{\underline{\mathbf{I}}}$ the identity tensor, and the viscous stress tensor of a Newtonian fluid $\underline{\underline{\tau}} = \nabla \underline{\mathbf{v}} + (\nabla \underline{\mathbf{v}})^T$. Figure 3.1 shows the physical domain for the falling sphere and the fluidized sphere problems.

Boundary conditions for the fluidized sphere problem are fully developed flow at the inlet S_i and outlet S_e, symmetry about the centerline S_s, and no penetration and zero slip at the tube walls S_w and sphere surface S_d:

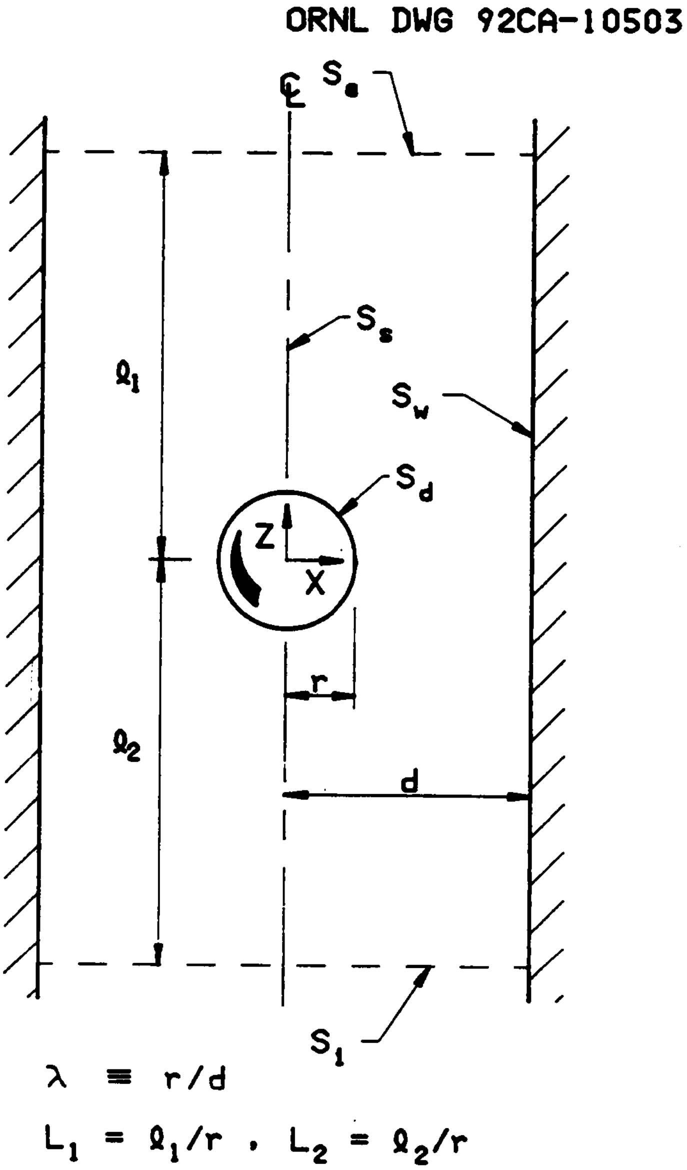

Figure 3.1. A solid sphere in tube flow: definition sketch.

$$
\begin{aligned}
S_i :&\quad v_x = 0, \quad v_z = 1 - (x\lambda)^2 \\
S_w :&\quad v_x = v_z = 0 \\
S_e :&\quad v_x = 0, \quad f_n \equiv \underline{\underline{\mathbf{T}}} : \underline{\mathbf{n}}\,\underline{\mathbf{n}} = 0 \\
S_d :&\quad v_x = v_z = 0 \\
S_s :&\quad v_x = 0, \quad f_t \equiv \underline{\underline{\mathbf{T}}} : \underline{\mathbf{n}}\,\underline{\mathbf{t}} = 0 \quad .
\end{aligned}
\tag{3.9}
$$

In (3.9), and also in (3.10) below, $\underline{\mathbf{n}}$ and $\underline{\mathbf{t}}$ are unit vectors normal and tangent to the surfaces bounding the flow domain. In the case of the falling sphere, the problem is recast to a coordinate system in which the sphere is at rest. In the recast coordinate system, the governing equations (3.8) are unchanged, but the boundary conditions become:

$$
\begin{aligned}
S_i :&\quad v_x = 0, \quad v_z = 1 \\
S_w :&\quad v_x = 0, \quad v_z = 1 \\
S_e :&\quad v_x = 0, \quad f_n \equiv \underline{\underline{\mathbf{T}}} : \underline{\mathbf{n}}\,\underline{\mathbf{n}} = 0 \\
S_d :&\quad v_x = v_z = 0 \\
S_s :&\quad v_x = 0, \quad f_t \equiv \underline{\underline{\mathbf{T}}} : \underline{\mathbf{n}}\,\underline{\mathbf{t}} = 0 \quad .
\end{aligned}
\tag{3.10}
$$

Note that in both (3.9) and (3.10), the condition of fully developed flow is expressed by a natural boundary condition along the outlet plane from the flow domain. This traction-free form is not only more accurate than prescribing both components of the velocity field by essential boundary conditions (see, e.g., Gresho, 1991), but also sets the level of the pressure inside the liquid in the tube.

A force balance on the sphere is next used to compute the dimensional drag, $\tilde{F}_D$, on it. This is done by equating the total force exerted by the fluid on the sphere, $\tilde{F}_T$, which is the sum of the viscous and pressure forces on the sphere, to the gravitational force on it, which in turn is equal to the sum of the buoyancy force on the sphere , $\tilde{F}_B$, and the force due to fluid movement (kinetic force), $\tilde{F}_D$, viz.:

$$\tilde{F}_T = \int \underline{\mathbf{e}}_z \cdot \underline{\underline{\tilde{\mathbf{T}}}} \cdot \underline{\mathbf{n}}\, d\tilde{S} = \frac{4}{3}\pi a^3 \rho_s g = \tilde{F}_B + \tilde{F}_D \quad , \tag{3.11}$$

where ρ_s is the density of the sphere. In (3.11) and in what follows, a variable with a tilde over it is dimensional and the same variable without a tilde is dimensionless. The drag coefficient is then calculated by subtracting $\tilde{F}_B$ from the total force and dividing the result — the drag force — by the product of a characteristic area (πa^2) with kinetic energy per unit volume ($\frac{1}{2}\rho U_\infty^2$). Using dimensionless variables

$$C_D \equiv \frac{\tilde{F}_D}{(\pi a^2)(\frac{1}{2}\rho U_\infty^2)} = (F_T - F_B)\frac{4}{Re} \tag{3.12}$$

where F_T and F_B are measured in units of $2\pi a \mu U_\infty$. (The coefficient 4 in (3.12) is often replaced by 8 in the literature because the Reynolds number is defined in terms of the sphere diameter rather than its radius as in this work.) An additional piece of information obtained from the force balance is the ratio of the density difference between the sphere and that of the fluid to the fluid density, $\gamma \equiv \frac{\rho_s - \rho}{\rho}$. Once a numerical solution is available so that the total force exerted by the fluid on the sphere can be computed, γ can be determined by rearranging Equation (3.11) as:

$$F_T = \frac{2}{3}(\gamma + 1)St \quad . \tag{3.13}$$

3.2. GALERKIN/FINITE ELEMENT ANALYSIS

In this work, the Navier-Stokes system (3.8) is solved everywhere within the region $V = \{(x,z) : 0 \leq x \leq D, -L_1 \leq z \leq L_2\}$ excluding the sphere. Here $D \equiv \frac{d}{a} = \frac{1}{\lambda}$ is the dimensionless tube radius, $L_1 = \frac{l_1}{a}$ is the dimensionless distance from the tube inlet to the center of the sphere, and $L_2 = \frac{l_2}{a}$ is the dimensionless distance from the tube outlet to the center of the sphere. The problem domain is tessellated into a set of N_z times N_x quadrilateral elements, where N_z is the number of elements in the z-direction and N_x is the number of elements in the x-direction.

The location of node points is chosen to yield a so-called boundary conforming mesh. This approach to mesh generation avoids errors due to element angles grossly deviating from 90^o and also controls the rate at which element sizes change. In general, a set of elliptic partial differential equations must be solved to compute the locations of mesh points for a boundary conforming mesh (e.g., Christodoulou and Scriven, 1992). However, in this case, determination of a boundary conforming mesh is relatively straightforward due to the domain shape being fixed and because of the availability of a potential flow solution for flow past a solid sphere. Lines of constant velocity potential, or equipotential lines, and streamlines of the potential flow solution form a family of orthogonal curves which can be used to generate the desired mesh (cf. Conner and Elghobashi, 1987).

Following Conner and Elgobashi (1987) the dimensionless stream function, y_2, and the dimensionless velocity potential, y_1, are written in terms of spherical coordinates (R, θ) based at the center of the sphere. Next, the angular dependence between the two equations is eliminated yielding an equation that involves a ninth order polynomial in R. This equation is solved for R by Newton's method. The value of the angle is then calculated to yield the (R, θ) coordinates of the grid points. Finally, the locations of the grid points are transformed back to the cylindrical coordinate system (x, z). We add in passing that Equation A-24 of the paper by Conner and Elgobashi is incorrect and should state:

$$R^9 - (y_1^2 + 2y_2^2)R^7 + (y_1^2 - 2y_2)R^4 - \frac{3}{4}R^3 - \frac{1}{2}y_2 R - \frac{1}{4} = 0 \quad . \tag{3.14}$$

Figure 3.2 shows the sample grids or tessellations used in this paper. The grids shown in Figure 3.2 are (a) a coarse grid with 492 elements, (b) a medium grid with 672 elements, and (c) a fine grid with 957 elements.

The unknown velocity field is expanded in a standard set of biquadratic basis functions (Strang and Fix, 1973) ϕ^i as :

$$v_x(\underline{x}) = \sum_{i=1}^{I} v_{x,i}\, \phi^i(\underline{x}) \quad , \quad v_z(\underline{x}) = \sum_{i=1}^{I} v_{z,i}\, \phi^i(\underline{x}) \quad , \tag{3.15a}$$

and the unknown pressure field is expanded in a standard set of discontinuous linear basis functions ψ^j:

$$p(\underline{x}) = \sum_{j=1}^{J} p_j \psi^j(\underline{x}) \quad . \tag{3.15b}$$

In (3.15a) and (3.15b) $\underline{x} \in V$is the position vector of a point with coordinates $(x, z), I \equiv (2N_x + 1)(2N_z + 1)$ is the total number of nodes in the finite element

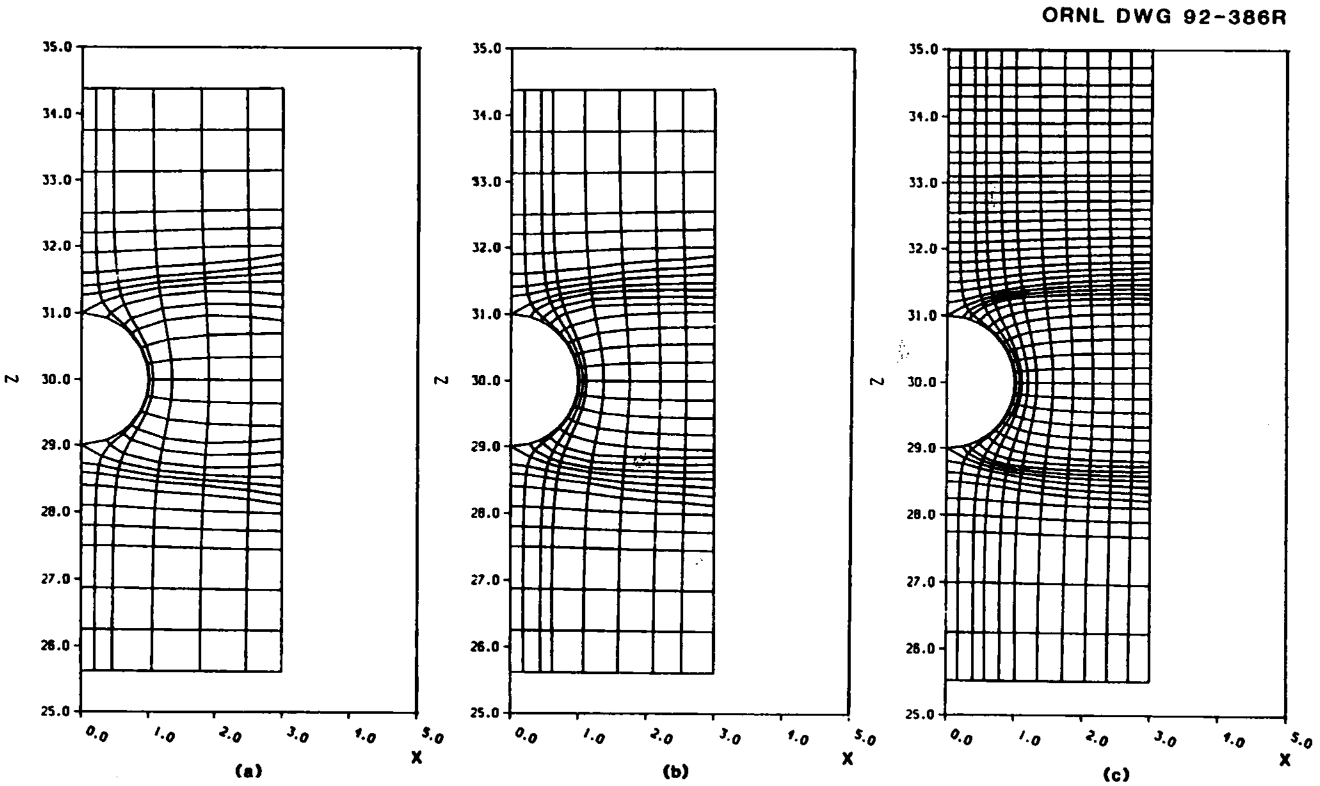

Figure 3.2. Computational grids: (a) a coarse mesh, (b) a coarse to fine, or a medium mesh, and (c) a fine mesh.

mesh, and $J \equiv 3(N_x \times N_z)$ is the total number of pressure unknowns. The coefficients $v_{x,i}$ and $v_{z,i}$ are the values of the velocity components at the nodes and p_j are the unknown coefficients in the finite element approximation of the pressure and $v_x = (v_{x,1}, v_{x,2}, \ldots, v_{x,I}), v_z = (v_{z,1}, v_{z,2}, \ldots, v_{z,I})$, and $p = (p_1, p_2, \ldots, p_J)$ are vectors representing all the unknowns. With the choice of basis functions adopted, the three grids used had 2145, 2873, and 4025 nodes, respectively.

The continuity equation is eliminated by introducing the variable penalty constraint described by Kheshgi and Scriven (1983),

$$\pm\frac{1}{\epsilon}\nabla \cdot \underline{\mathbf{v}} = p, \quad \frac{1}{\epsilon} \equiv O(10^6)\,, \tag{3.16}$$

where quantity $\frac{1}{\epsilon}$ is the penalty parameter.

The Galerkin weighted residuals of the Navier-Stokes equation after integrating the stress term by parts is :

$$\begin{aligned}\underline{\mathbf{R}}^i_M = \int \phi^i \underline{\mathbf{e}}_k \cdot Re\, \underline{\mathbf{v}} \cdot \nabla \underline{\mathbf{v}}\, dV + \int \underline{\underline{\mathbf{T}}} : \nabla \phi^i \underline{\mathbf{e}}_k\, dV - \\ \int \phi^i \underline{\mathbf{e}}_k \cdot \underline{\underline{\mathbf{T}}} \cdot \underline{\mathbf{n}}\, dS + St \int \underline{\mathbf{e}}_k \cdot \underline{\mathbf{e}}_z \phi^i\, dV = \underline{0}\,,\ i = 1, \ldots, I,\end{aligned} \tag{3.17a}$$

where $\underline{\mathbf{e}}_k = \underline{\mathbf{e}}_x$ or $\underline{\mathbf{e}}_z$ stands for the unit vector in the x- or z-direction. The Galerkin weighted residual of the penalized continuity equation is :

$$R^i_C = \int \psi^i (\pm\frac{1}{\epsilon}\nabla \cdot \underline{\mathbf{v}} - p)\, dV = 0\,,\ i = 1, \ldots, J \quad . \tag{3.17b}$$

The penalty constraint allows the continuity equation and the pressure nodes to be algebraically eliminated from the system of equations. The consistent penalty method described by Engelman et al. (1982), Kheshgi and Scriven (1983), and

Eaton (1983) is used in this work. The set of nonlinear algebraic equations is solved using Newton's method and zeroth-order continuation in Reynolds number.

The coarse, medium, and fine grids described above were used to check the sensitivity of computed solutions to mesh refinement. A particular grid was judged to be acceptable when further systematic grid refinement produced less than 0.2% change in the solution under conditions of creeping flow ($Re \rightarrow 0$). The results that are reported in Section 3.4 were obtained with $L \equiv L_1 = L_2$. The distance L, i.e., the location of the inflow and outflow boundaries, was varied until further changes in L produced less than 0.2% change in the solution as $Re \rightarrow 0$.

The algorithm was written in FORTRAN and the calculations were carried out on an IBM RS 6000/320H workstation at the Oak Ridge National Laboratory and a CRAY Y-MP/4 at Florida State University Supercomputer Center.

3.3 RESULTS

Computations for both a fluidized sphere and a falling sphere were carried out for various combinations of $(\frac{1}{\lambda}, Re)$. In each case, approximately 350 solutions were generated. Among other things, the data were used together with a SAS program (SAS Language and Procedures, 1989) to develop correlations which fit the computational data over the range of parameters $0 \leq Re \leq 100$ and $12.5 \geq \frac{1}{\lambda} \geq 1.42$.

3.3.1 Fluidized sphere

Figure 3.3 compares the value of the drag correction for a fluidized sphere in creeping flow computed by finite element analysis in this work to the analytical solutions of Fayon and Happel (1960), equation (3.1), Haberman and Sayre (1958), equation (3.3), and Wakiya (1957), equation (3.2). The computed results and the three approximations agree well when $\lambda \leq 0.3$, i.e., when the radius of the tube is larger than 3.3 times that of the sphere. However, the Fayon and Happel correlation deteriorates significantly when $\lambda > 0.3$. This deterioration is due to the fact that the Fayon and Happel solution is based on the method of reflections, which works well when the sphere and tube walls are far apart. By including higher order terms in λ in the denominator of equation (3.2), the Wakiya solution tends to follow the computed results better than that of Fayon and Happel. Nevertheless, Figure 3.3 shows that the Wakiya solution still underestimates the drag for narrow tubes ($\lambda \rightarrow 1$). The Haberman and Sayre solution shows good agreement with the computed results up to $\lambda = 0.5$ where it begins to deviate slightly from the computed values. This deterioration of the solution of Haberman and Sayre as λ increases is attributed to not retaining enough terms in their solution. By contrast, when the number of unknowns is held fixed, the finite element solution becomes more accurate as the tube radius approaches the sphere radius ($\lambda \rightarrow 1$) because the average element size in the mesh decreases.

Figure 3.4 shows how the actual drag, F_D, normalized by the Stokes drag, $F_S = \frac{12}{Re}$, varies with Reynolds number when inertial effects are weak compared to viscous ones, $0 \leq Re \leq 1$. If the drag were insignificantly affected by Re

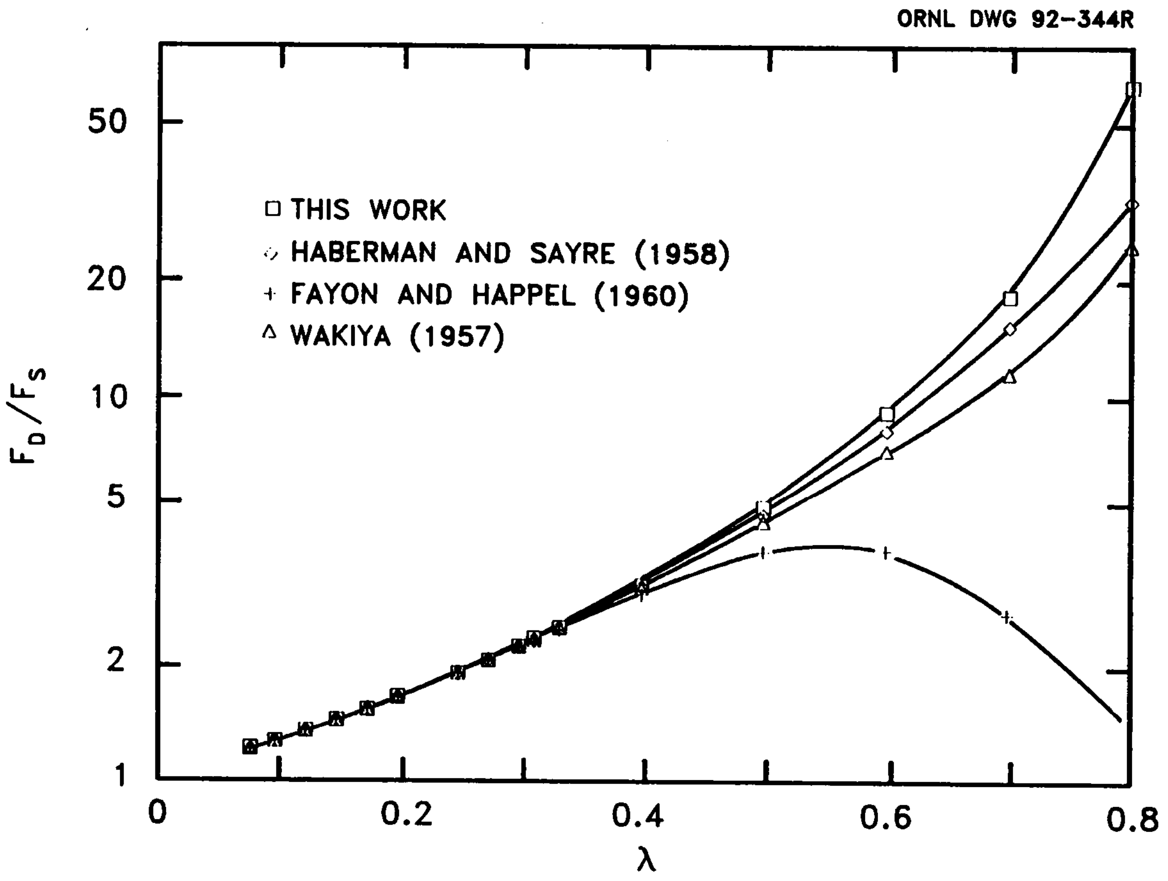

Figure 3.3. Drag correction for a fluidized sphere in creeping flow: ratio of the actual drag to the Stokes drag of a sphere in an unbounded fluid as a function of the ratio of the radius of the sphere to that of the tube.

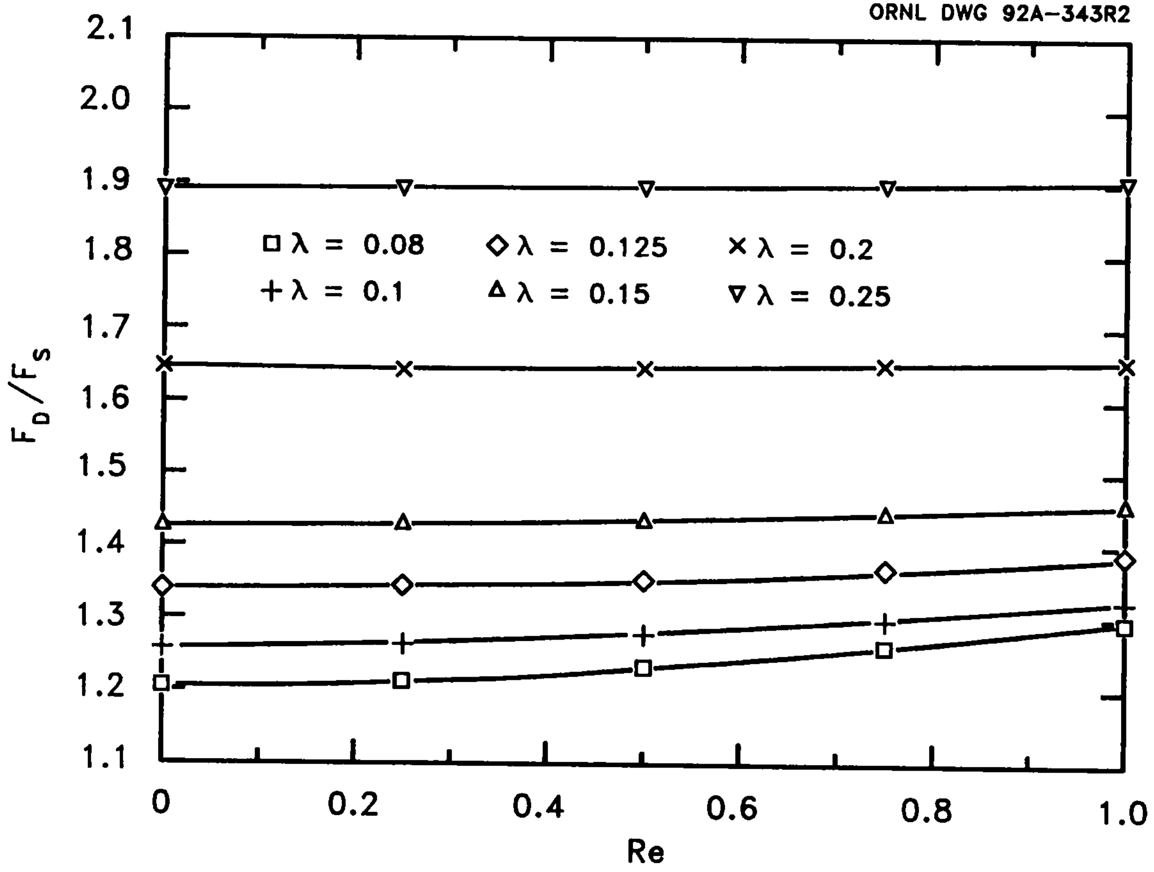

Figure 3.4. Drag correction for a fluidized sphere at low Reynolds numbers as a function of Reynolds number for several selected values of the ratio of radius of the sphere to that of the tube.

when $0 \leq Re \leq 1$, the curves of $\frac{F_D}{F_S}$ versus Re for a fixed value of λ would be straight lines with zero slope. Figure 3.4 shows for the first time that as $\lambda \rightarrow 1$, the drag is little affected by Reynolds number when $0 \leq Re \leq 1$. However, as $\lambda \rightarrow 0$, the drag is affected by inertia at increasingly smaller values of Re. These results indicate that for narrow tubes ($\lambda \rightarrow 1$) the creeping flow assumptions hold for a larger range of Reynolds numbers than for wide tubes. Also, in the limit of $Re \rightarrow 0$, that the computed value of the drag increases as the tube radius decreases accords with extremum principles well known in Stokes flow (Kim and Karrila, 1991).

Figure 3.5 shows computed values of the drag correction over the range $0 \leq Re \leq 100$ for several values of λ. Figure 3.5 makes plain that the drag in very narrow tubes ($\lambda \rightarrow 1$) changes little with Reynolds number. By contrast, the drag in tubes of moderate to large radii changes rapidly for low to moderate values of the Reynolds number. The rate of change of drag with Re in such tubes approaches that in narrow tubes as Reynolds number exceeds about 40.

Figure 3.6 compares the experimental data found in the paper by Fayon and Happel (1960) to the new computations. Aside from the suspicious and abrupt change in the slope of the experimental drag data between $15 \leq Re \leq 30$ (which is also evident in Figure 1 of Fayon and Happel's paper), the computations and experimental data are in excellent agreement for Re as high as 40. This good agreement is another testimony to the accuracy of the computed results reported in this paper. Although the experiments were restricted to $Re \leq 40$, computations of this work extend to $Re = 100$ (cf. Figure 3.5).

Based on the calculations reported in this paper, a new correlation for drag on a fluidized sphere is developed:

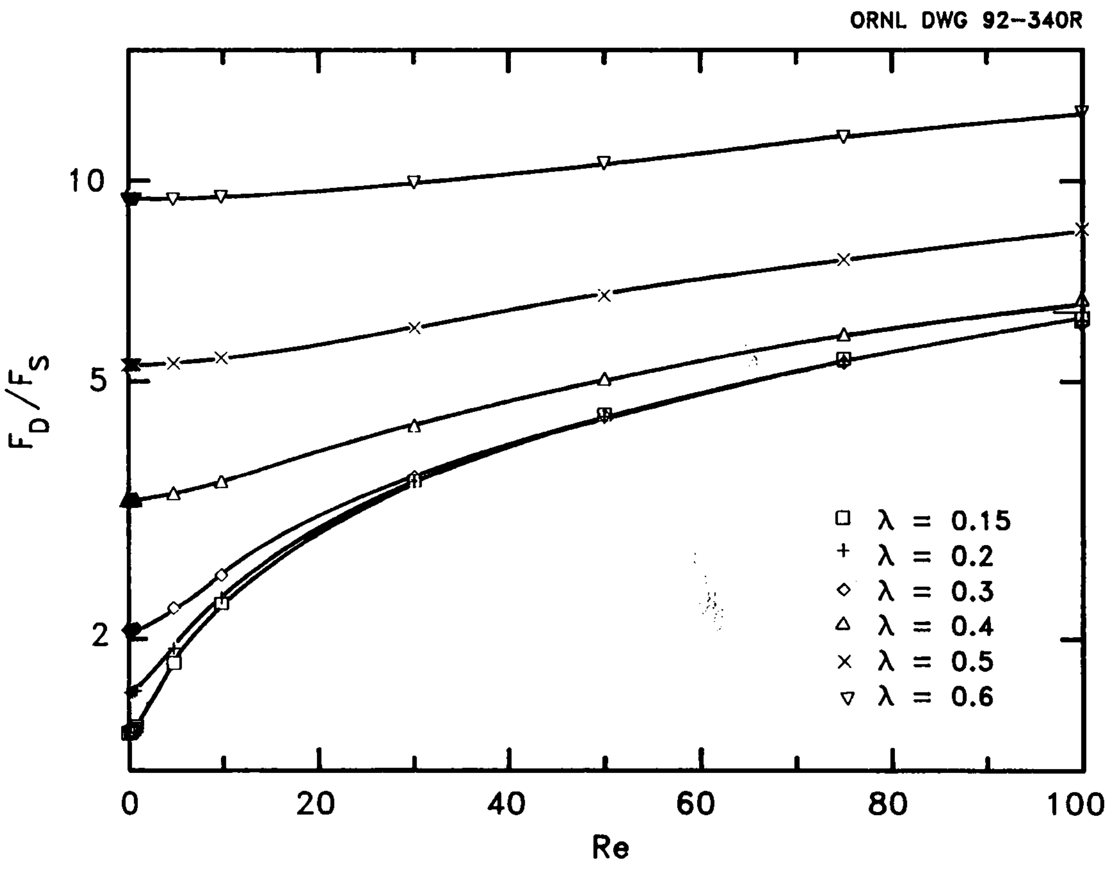

Figure 3.5. Drag correction for fluidized spheres as a function of *Re*.

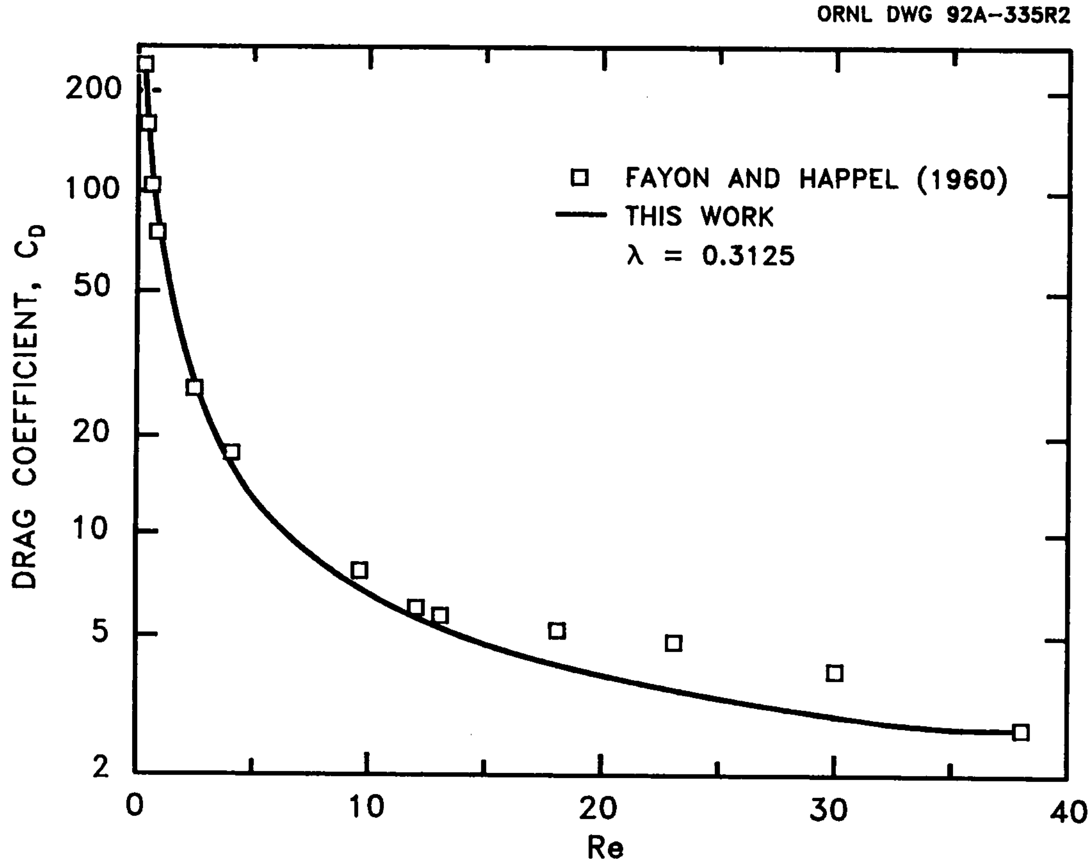

Figure 3.6. Comparison of the computed value of the drag coefficient for fluidized spheres to the experimental data of Fayon and Happel (1960) as a function of Re. Here $\lambda = 0.3125$.

$$\frac{F_D}{F_S} = (1 + 0.05488 Re^{(1.2905 - 0.07529 \ln Re)}) \left[\frac{1 - \frac{2}{3}\lambda^2 - 0.20217\lambda^5}{1 - K\lambda + 2.0865\lambda^3 - 1.0768\lambda^5 + 0.72603\lambda^6}\right] , \tag{3.18}$$

where $K = 1.358 + 0.7486e^{-0.07836Re}$.

The results of drag calculations from parametric studies in Re for all values of $\frac{1}{\lambda}$, $0.08 \leq \frac{1}{\lambda} \leq 0.4$ and $0 \leq Re \leq 100$, are plotted in Figure 3.7 along with the predictions of the correlation (3.18) and the correlation of Fayon and Happel (1960). The diagonal (ordinate = abscissa) represents perfect agreement between the new correlation and the computed results. The lines on either side of the diagonal indicate $\pm 5\%$ deviation between the computations and values predicted by equation (3.18).

The boxes represent computational results from this work, while the crosses represent values obtained from Fayon and Happel's correlation (equation 3.1). Low values of drag are indicative of large diameter tubes and/or low values of Reynolds number. Figure 3.7 shows that the accuracy of the Fayon and Happel correlation deteriorates significantly as the drag increases.

In Figure 3.8 (and also in Figure 3.17 below), velocity vectors and streamlines are plotted side by side to gain insight into how the flow field develops as Reynolds number increases. Three values of $\frac{1}{\lambda}$ were chosen in order to emphasize differences between tubes of large and small radii. As the Reynolds number increases, flow separation occurs and a wake or an eddy, i.e. a zone of fluid recirculation, forms downstream of the sphere. The so-called center of the wake, which corresponds to the point where the stream function has its minimum value, is indicated by a cross. At a fixed value of λ, increasing the Reynolds

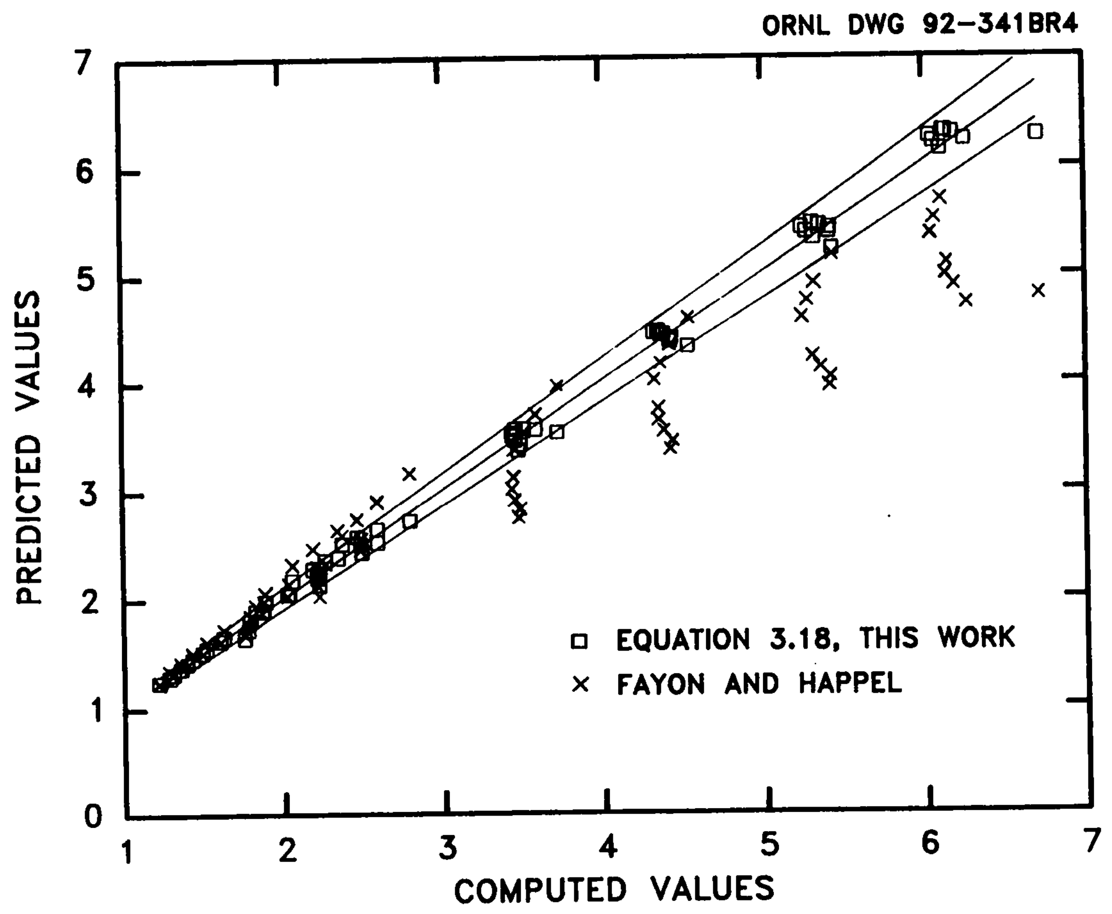

Figure 3.7. Comparison of Galerkin/finite element predictions of drag to the new correlation (3.18) and the correlation due to Fayon and Happel (1960).

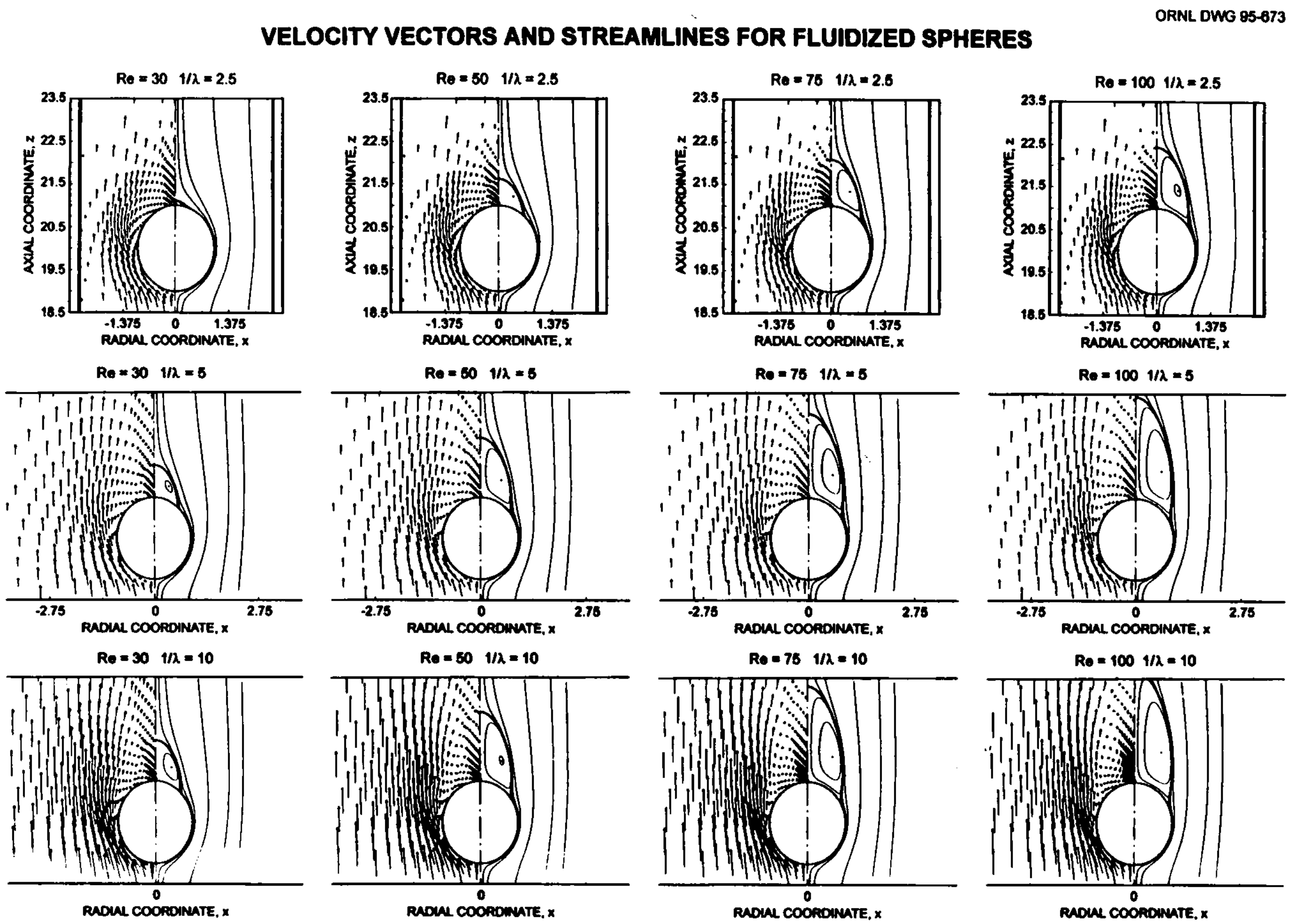

Figure 3.8. Velocity profiles as a function of Re and $1/\lambda$ for fluidized spheres. In each panel of Figure 3.8 (and Figure 3.17 below), streamlines are plotted to the right of the centerline and velocity vectors to the left of it. Each velocity vector shown belongs to its basepoint.

number causes the wake to grow, as can be seen by looking from left to right in Figure 3.8. At a fixed value of Re, increasing the radius of the tube relative to that of the sphere also causes the wake to grow, as can be seen by looking from top to bottom in Figure 3.8.

The angle measured from the north pole, or the rear stagnation point, to the point on the sphere surface where the wake detaches from it — the wake angle — is plotted as a function of Reynolds number in Figure 3.9. Evidently, the presence of a tube wall at a finite distance from the sphere suppresses wake formation: at a fixed value of Re, the wake angle decreases as λ increases. The latter effect is quite significant for tubes of small radii ($\lambda \rightarrow 1$) but becomes less important as $\lambda \rightarrow 0$. Moreover, Figure 3.9 shows that the critical Reynolds number for the onset of wake formation increases as the ratio of the tube radius to the sphere radius decreases ($\lambda \rightarrow 1$). Also, for all values of λ, wake angles appear to approach an asymptotic value for large Re indicating that the effect of the tube size on wake angle diminishes as Re increases.

Figure 3.10 shows how the wake length, $z_c - 1$, measured along the centerline varies as a function of Re for several values of λ. Here z_c is the location along the centerline downstream of the sphere where the axial velocity vanishes. At a fixed value of Re, the wake length increases as $\frac{1}{\lambda}$ increases, which agrees with the finding that the presence of the tube inhibits the formation and growth of the wake.

Figure 3.11 shows the location of the wake center, i.e., the location at which the stream function attains its lowest value, for several combinations of Re and λ. Evidently, the wake center moves virtually at a 45^o angle from the north pole of the sphere ($x = 0, z = 1$) as Re increases when the value of λ is held fixed.

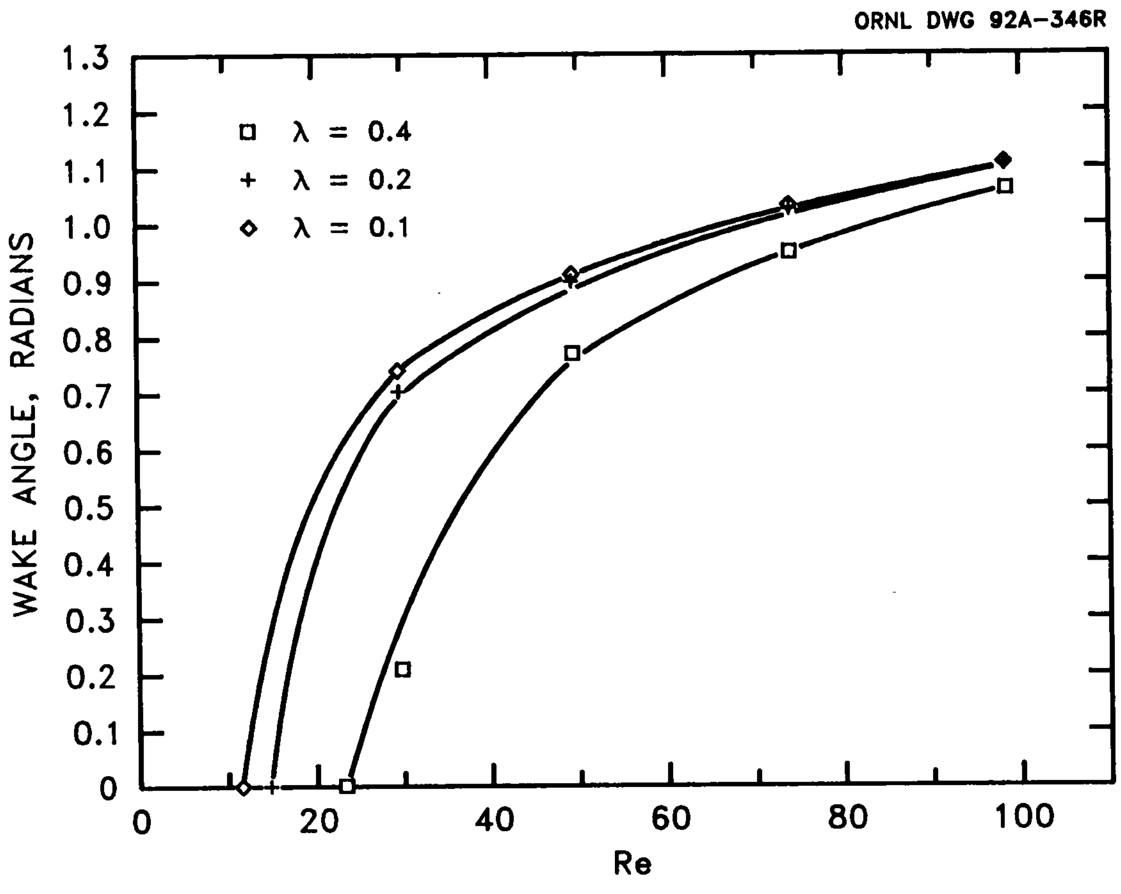

Figure 3.9. Wake angle as a function of *Re* and λ for a fluidized sphere.

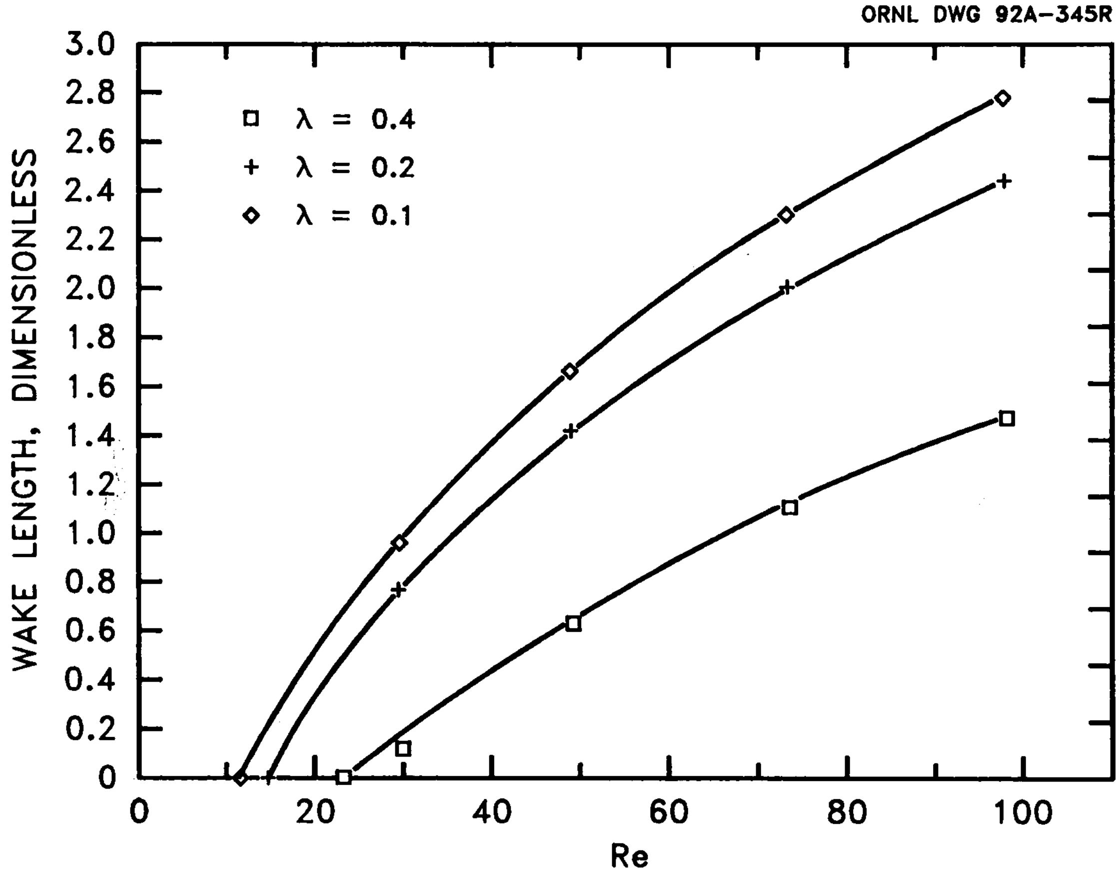

Figure 3.10. Wake length as a function of *Re* and λ for a fluidized sphere.

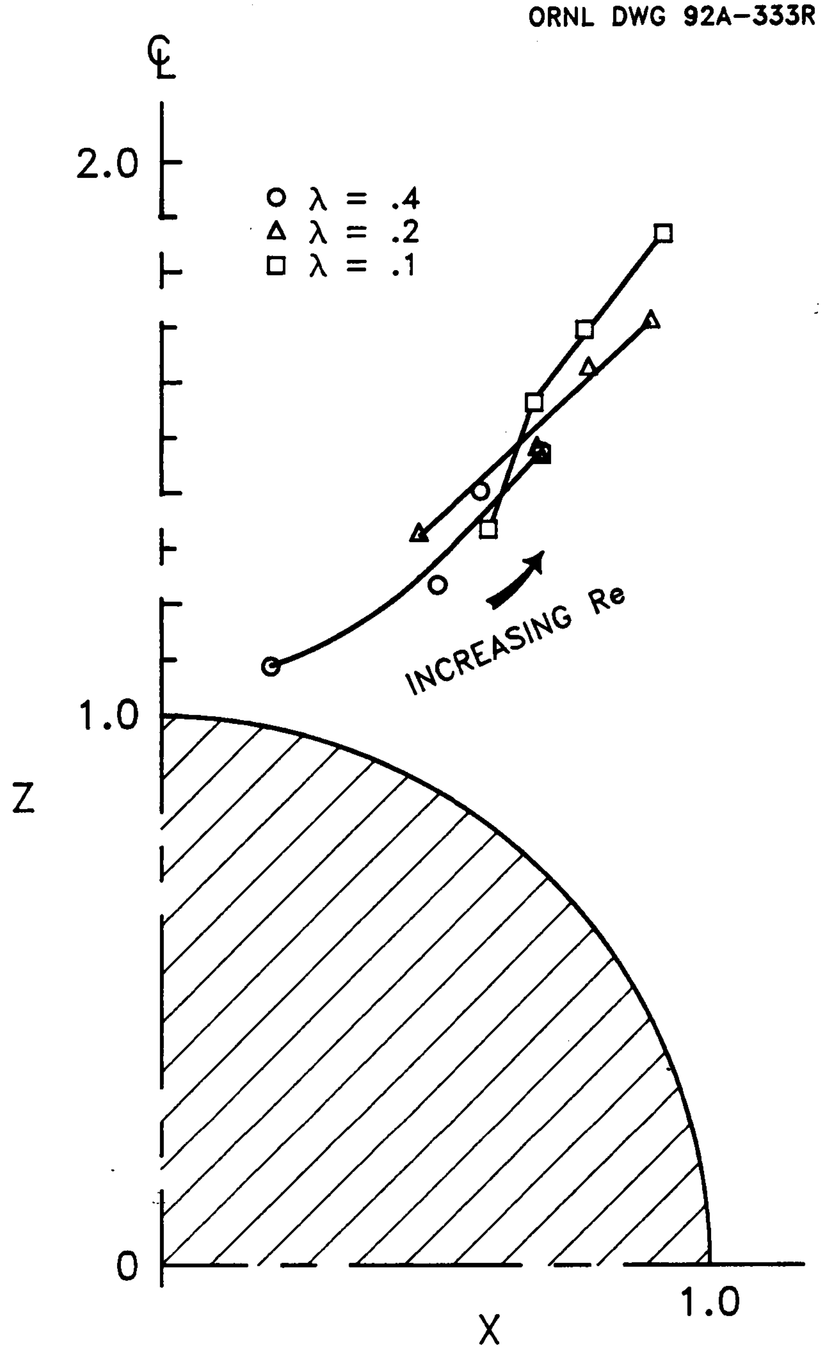

Figure 3.11. Location of wake center or stream function minimum as a function of *Re* and λ for a fluidized sphere.

3.3.2 Falling sphere

Figure 3.12 compares the value of the drag correction for a falling sphere in creeping flow computed in this paper by Galerkin/finite element analysis to predictions due to Fayon and Happel (1960), equation 3.6; Faxen (1923); Ladenburg (1907), equation 3.4; Francis (1933), equation 3.5; and Haberman and Sayre (1958), equation 3.7. The Ladenburg correlation given by (3.4) varies linearly with λ and, not too surprisingly, is inaccurate when $\lambda \geq 0.1$. The correlation of Fayon and Happel (3.6) does better than that of Ladenburg but deteriorates for values of $\lambda > 0.3$. The correlation of Francis, (3.5), is an empirical correlation which is an improvement over those of Ladenburg and Fayon and Happel, but starts to break down when $\lambda > 0.5$. Evidently, the best correlation among this lot is that due to Haberman and Sayre (3.7). However, it too breaks down when $\lambda > 0.7$, i.e., for very narrow tubes.

Figure 3.13 shows the variation of drag with Re in low but non-zero Reynolds number flow. As in the case of fluidized spheres, Figure 3.13 illustrates that the creeping flow assumption holds over a larger range of Re for flow past spheres in narrow tubes than for flow past spheres in an infinite expanse of fluid. Were Stokes flow conditions to hold at small but finite Re, the slope of the $\frac{F_D}{F_S}$ versus λ curves would be zero in Figure 3.13. Remarkably, the deviation from Stokes law at low Re is greater for a fluidized sphere than for a falling sphere (cf. Figures 3.4 and 3.13).

Figure 3.14 compares the predictions made here by Galerkin/finite element analysis to the experimental data found in the paper of McNown et al. (1948). Figure 3.14 shows that good agreement exists between the new computational

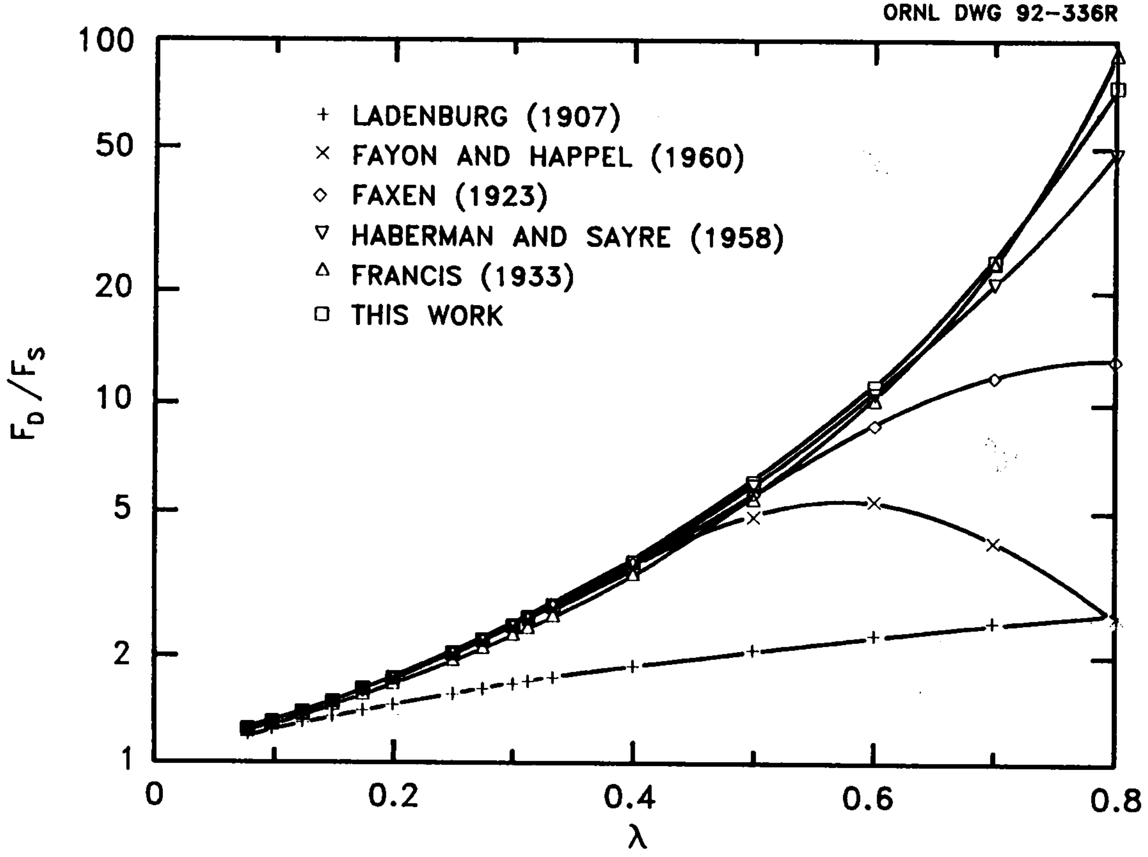

Figure 3.12. Drag correction for a falling sphere in creeping flow: ratio of the actual drag to the Stokes drag of a sphere in an unbounded fluid as a function of the ratio of the radius of the sphere to that of the tube.

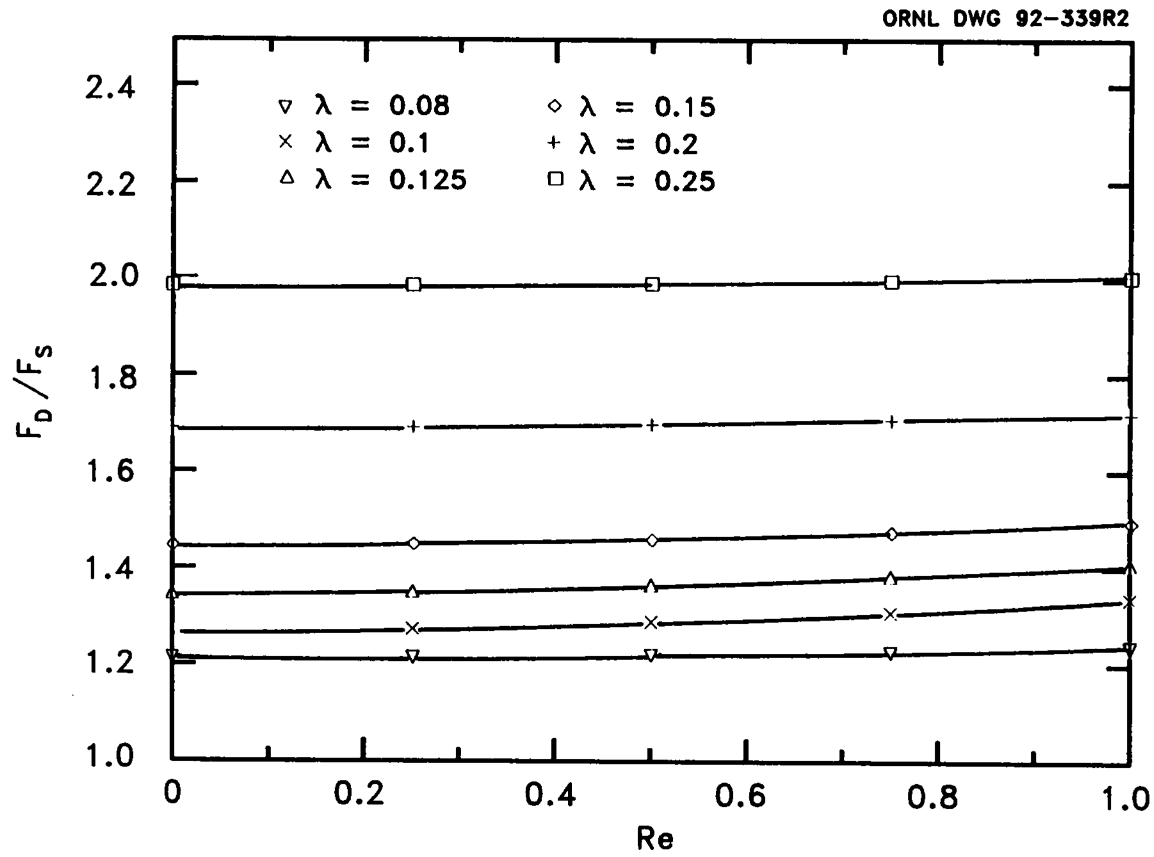

Figure 3.13. Drag correction for a falling sphere at low Reynolds numbers as a function of Reynolds number for several selected values of the ratio of radius of the sphere to that of the tube.

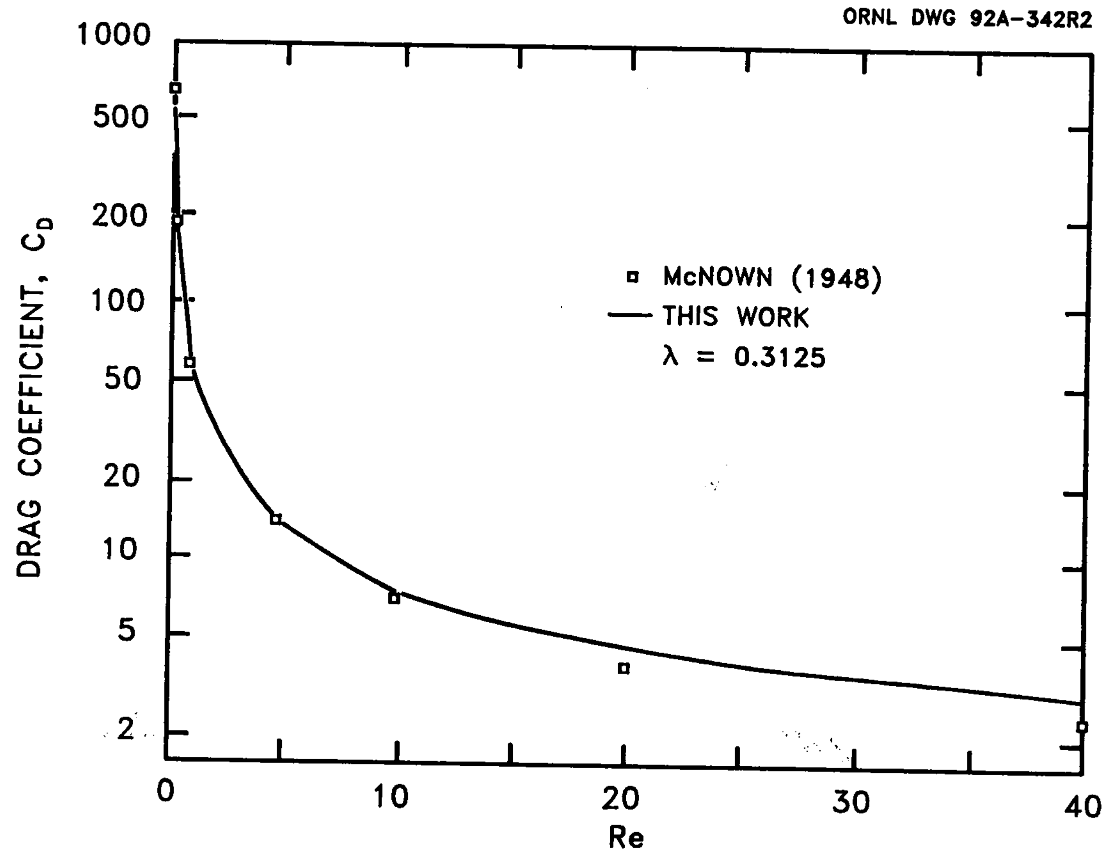

Figure 3.14. Comparison of the Galerkin/finite element predictions of the drag for falling spheres to the experimental measurements of McNown et al. (1948) as a function of Re. Here $\lambda = 0.3125$.

results and the experimental data of McNown et. al. However, a weakness of the comparison is that experimental results are restricted to $Re < 40$ and to a single value of λ , $\lambda = 0.3125$.

Figure 3.15 shows the variation of the ratio $\frac{F_D}{F_S}$ with Re for several values of λ. Figure 3.15 shows that for falling spheres, the difference in drag for different values of λ increases as the Reynolds number increases, a result that is in contrast to that for fluidized spheres (cf. Figure 3.5).

Once the accuracy of the Galerkin/finite element calculations was demonstrated for (a) low Re flow by comparison of calculated results to previously published results in the literature and (b) moderate Re flow by establishing that the results were insensitive to further mesh refinement, calculations were made for $12.5 \geq \frac{1}{\lambda} \geq 1.42$ and $0 \leq Re \leq 100$ to develop a correlation for drag as a function of Re and λ. The new correlation for falling spheres is:

$$\frac{F_D}{F_S} = (1 + 0.03708Re^{(1.514-0.1016\ln Re)}) \left[\frac{1 - 0.75857\lambda^5}{1 - K\lambda + 2.0865\lambda^3 - 1.7068\lambda^5 + 0.72603\lambda^6}\right] , \qquad (3.19)$$

where $K = 0.6628 + 1.458e^{-0.05635Re}$.

The results of drag calculations are plotted in Figure 3.16 along with the predictions of correlation (3.19) and the correlation of Fayon and Happel (1960) for $0.08 \leq \lambda \leq 0.7$ and $0 \leq Re \leq 100$. The diagonal represents perfect agreement between the new correlation and the computational results. The lines on either side of the centerline indicate $\pm 5\%$ variation between computational results and values computed from the new correlation. As expected and similar to the case of a fluidized sphere, the correlation of Fayon and Happel is found to break down

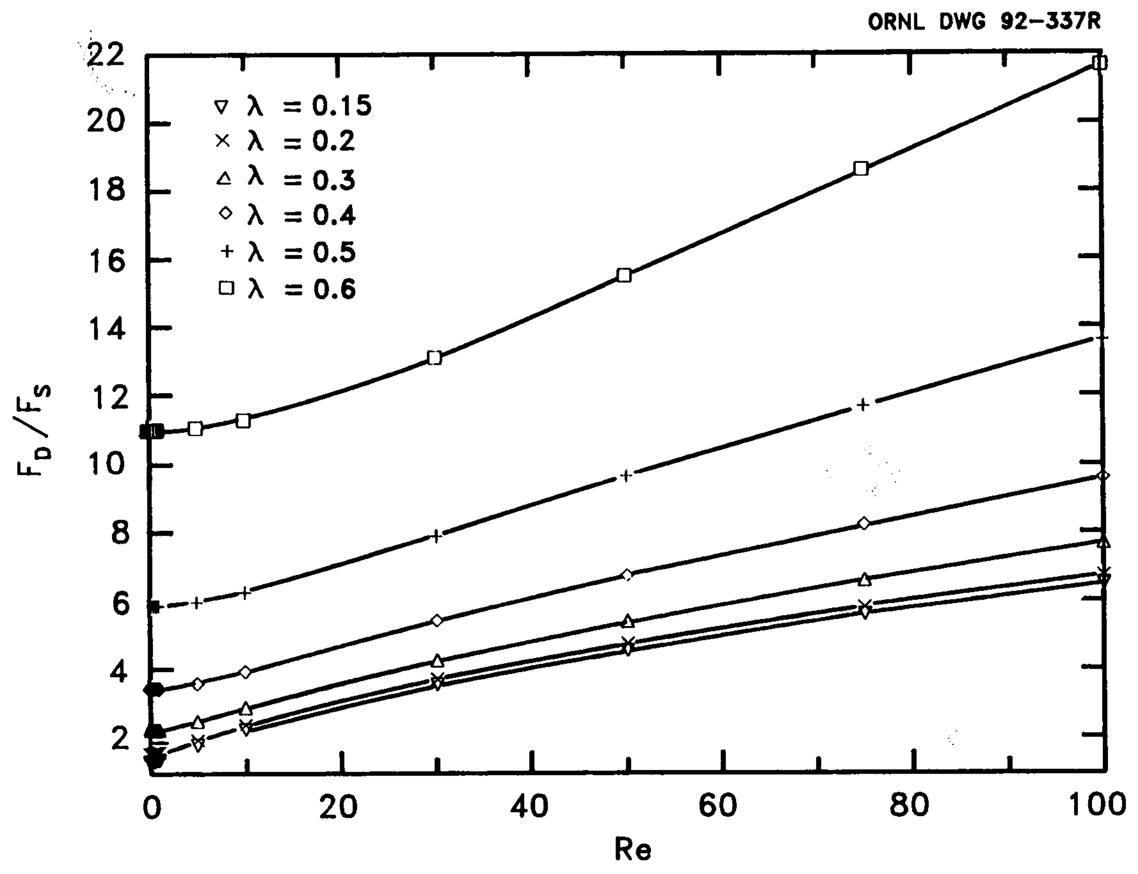

Figure 3.15. Drag correction for falling spheres as a function of *Re*.

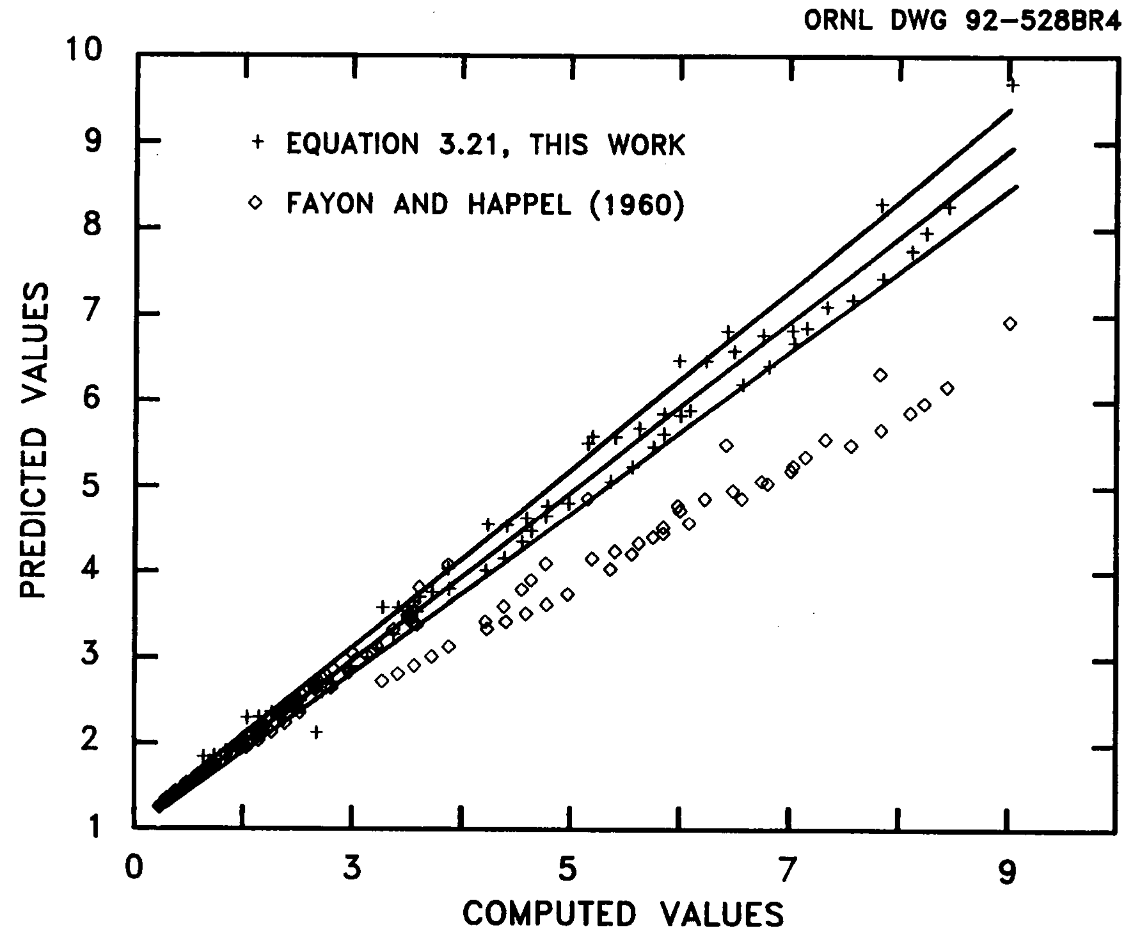

Figure 3.16. Comparison of Galerkin/finite element predictions of drag for falling spheres to the new correlation (3.19) and the correlation due to Fayon and Happel (1960).

of a fluidized sphere, the correlation of Fayon and Happel is found to break down as the drag increases.

Details of flow fields around falling spheres that are of interest but are difficult to obtain quantitatively from experiments are shown in Figures 3.17-3.20. Figure 3.17 shows velocity vectors and streamlines outside falling spheres. Comparison of Figures 3.17 and 3.8 shows that wake formation is more suppressed in small tubes in which a sphere is fluidized than in ones in which a sphere is falling. This finding is further reinforced by Figures 3.18 and 3.19, which show the evolution with Reynolds number of the wake angle and the wake length, respectively. Figure 3.20 shows that the center of a wake downstream of a falling sphere migrates a shorter distance than that of a fluidized sphere and tends to move a larger distance in the z-direction than in the x-direction.

3.3.3 Sphere on the end of a wire

The case of a sphere suspended by a wire of infinitesimal thickness was analyzed by replacing the symmetry boundary conditions along the centerline of the tube downstream of the sphere by conditions of no-slip and no penetration. Figure 3.21 compares the variation of drag with Reynolds number for several values of λ for a fluidized sphere and a sphere suspended from a wire. The difference in drag for the two cases is seen to be small, a remarkable but reassuring finding. Figure 3.22 shows how the fractional difference between the drag on a fluidized sphere and the drag on a sphere at the end of a wire varies with Re. Plainly, the fractional difference is a function of λ and Re. Figure 3.22 shows that the fractional difference decreases as the tube radius decreases. This is due to the fact that the velocity profile downstream of a sphere at the end of a wire

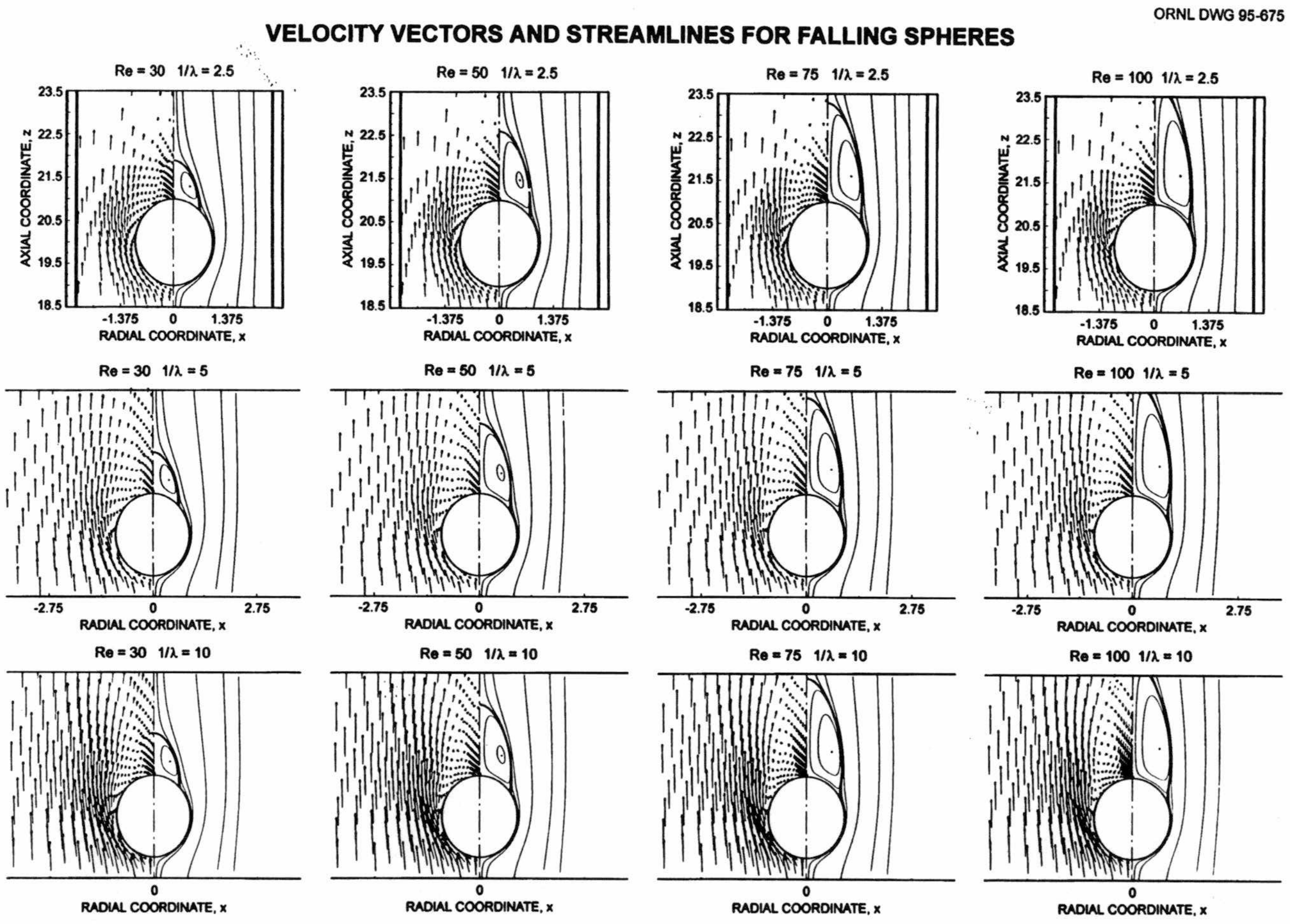

Figure 3.17. Velocity profiles as a function of Re and $1/\lambda$ for falling spheres

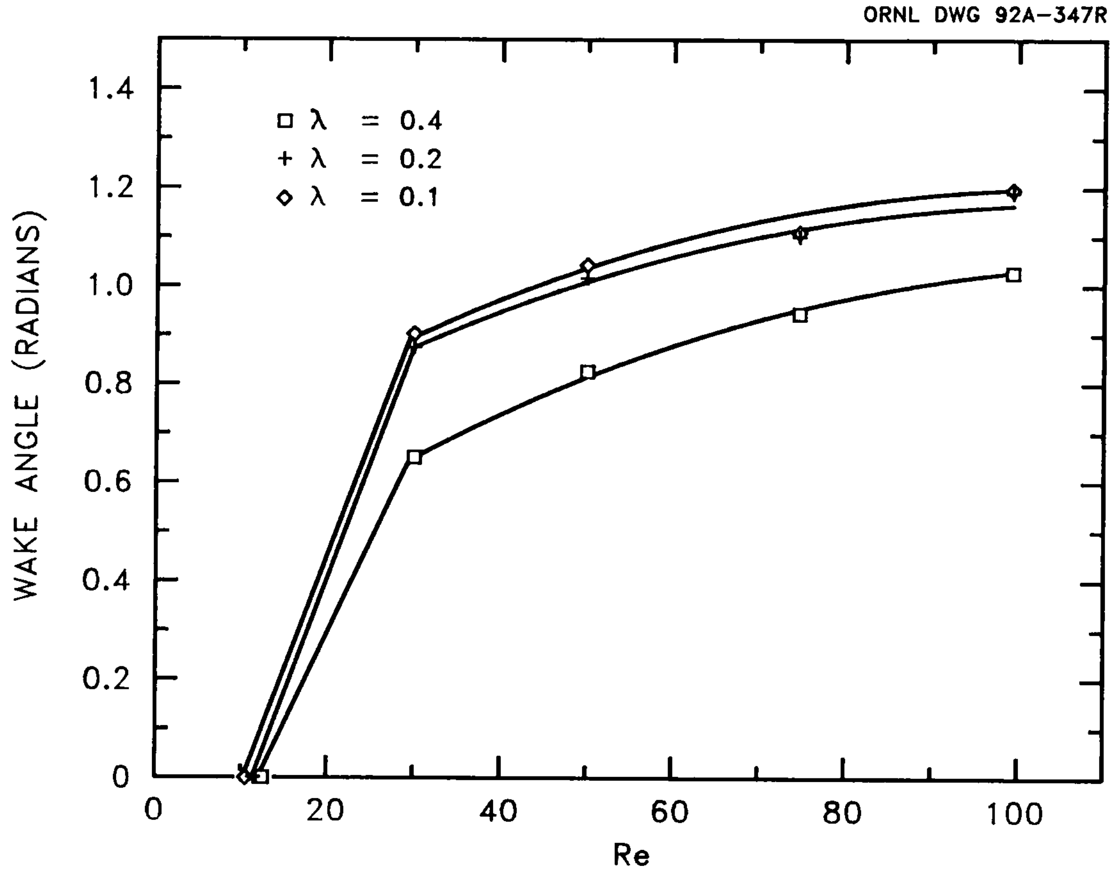

Figure 3.18. Wake angle as a function of *Re* and λ for a falling sphere.

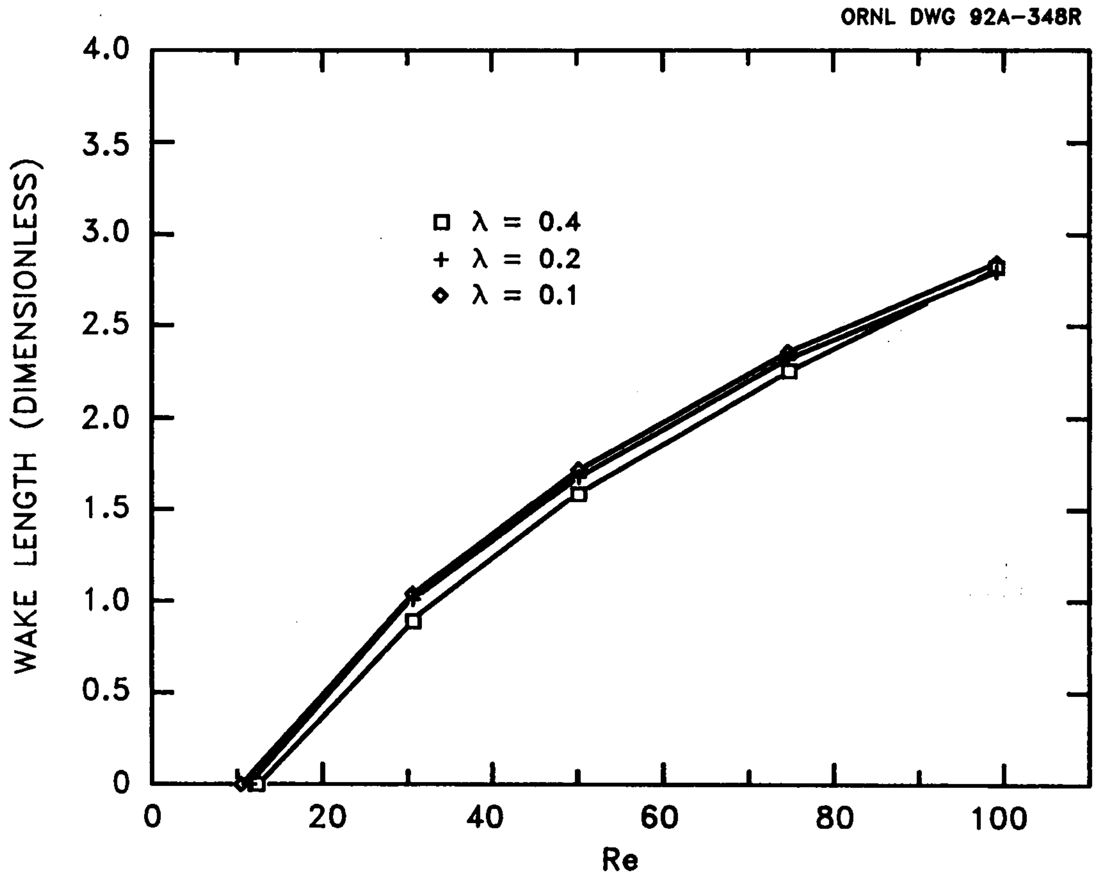

Figure 3.19. Wake length as a function of *Re* and λ for a falling sphere.

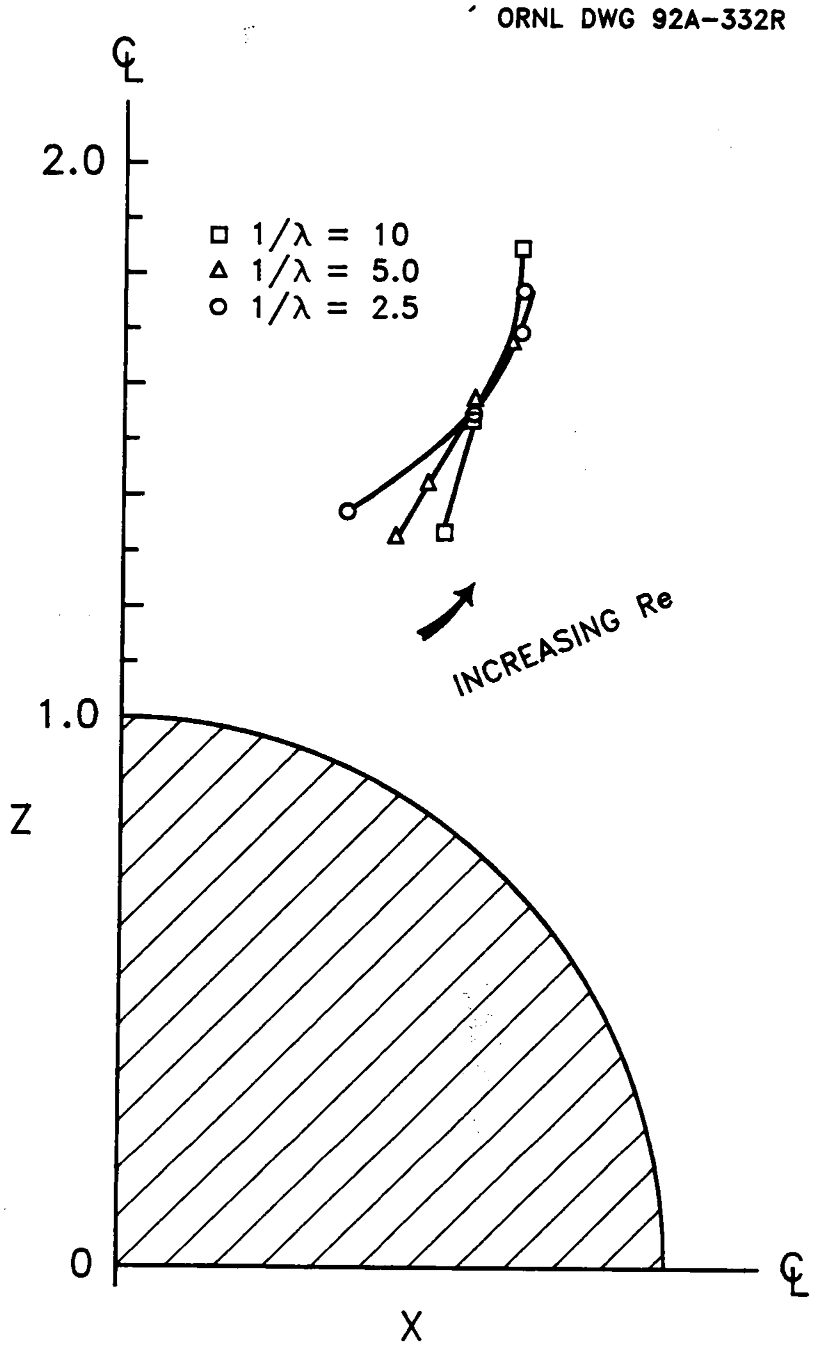

Figure 3.20. Location of wake center or stream function minimum as a function of *Re* and $1/\lambda$ for a falling sphere.

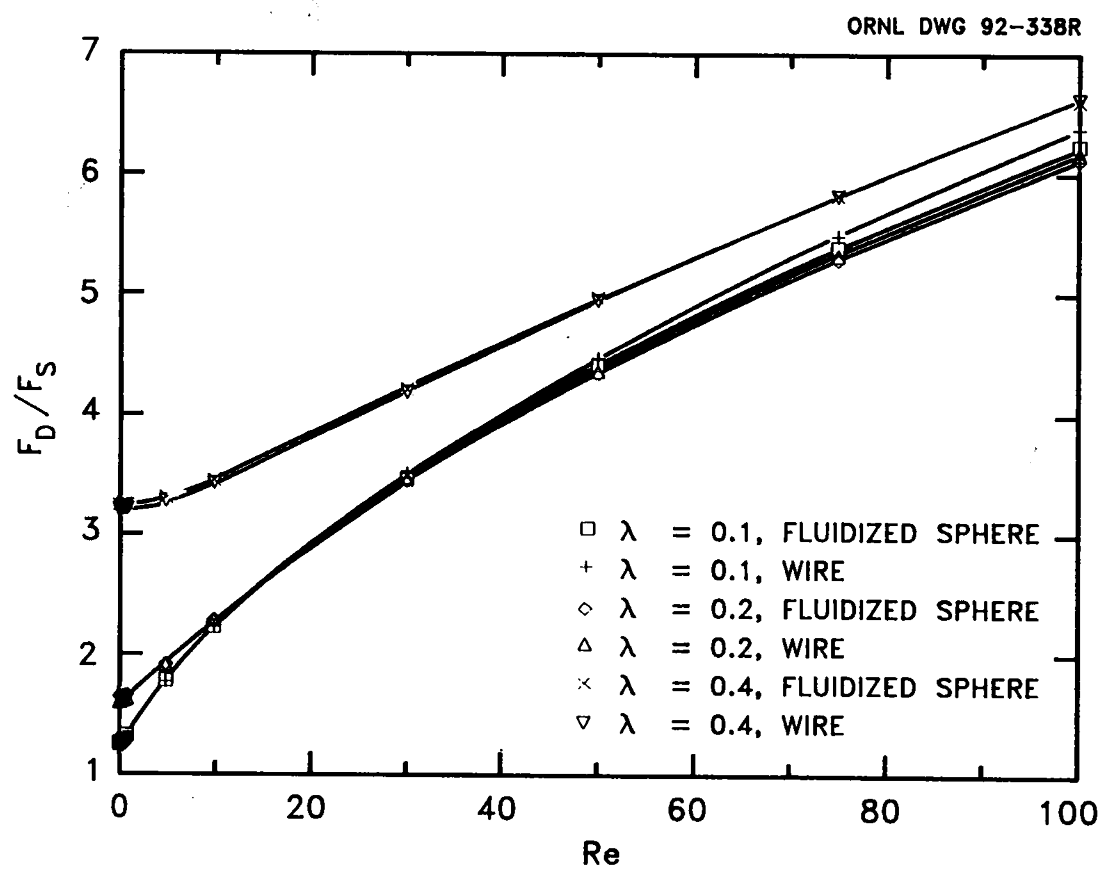

Figure 3.21. Variation with *Re* of the drag on a fluidized sphere and the drag on a sphere held by a wire for several values of λ.

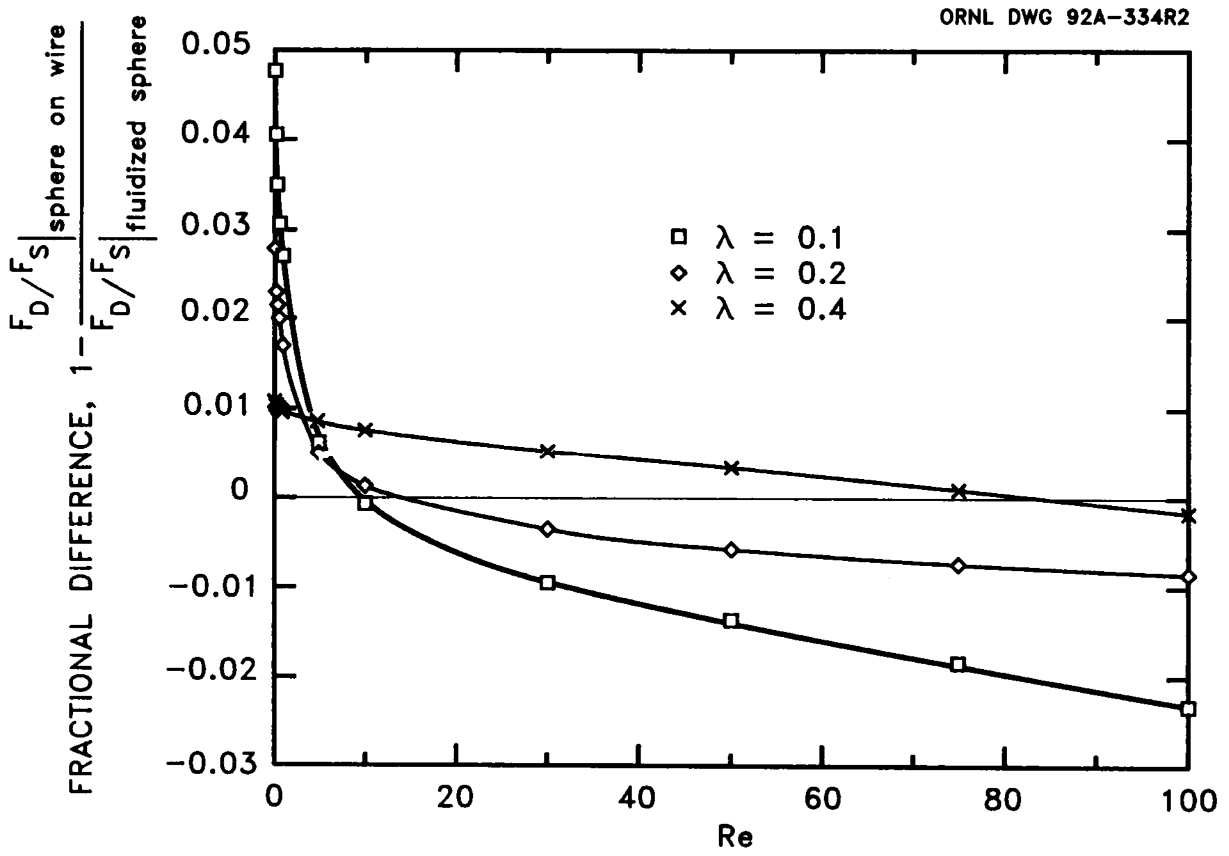

Figure 3.22. Variation with *Re* of the fractional difference between the drag on a fluidized sphere and the drag on a sphere held by a wire for several values of λ.

becomes more similar to the parabolic profile downstream of a fluidized sphere, except near the centerline, as $\lambda \rightarrow 1$ (see Figure 3.23). Although the error in drag measurement introduced by the wire is larger the larger the tube radius, the error quickly drops and varies slowly as Re increases.

Figure 3.23 shows that the axial velocity v_z varies rapidly with the radial coordinate x in the vicinity of the wire, which leads to large values of the shear stress τ_{xz} along the wire. However, the contribution of the wire to the drag force would be calculated by integrating τ_{xz} over the surface area of the wire. Since the surface area of the wire is vanishingly small, the contribution of the wire to the drag force should therefore be small, as confirmed by the results of finite element computations reported in Figures 3.21 and 3.22.

3.4. CONCLUSIONS

Rigorous finite element calculations that account for the effect of finite inertia and presence of tube walls in flows past fluidized and falling spheres have allowed scrutiny of drag correlations that have been around, often untested, in the literature for more than a half century. According to the foregoing results, Faxen's (1923) postulate that the coefficient K in equations (3.1) and (3.6) should be a function of Reynolds number is indeed correct. Furthermore, the assumption that the effects of finite inertia and finite tube radius are additive is equally restrictive. Indeed, as shown in Figures 3.7 and 3.16, the consequences of treating K as a constant and assuming that inertia and wall effects are additive are inaccurate prediction of drag as Reynolds number increases and/or tube radius decreases. Moreover, it has been shown that correlations that are specifically

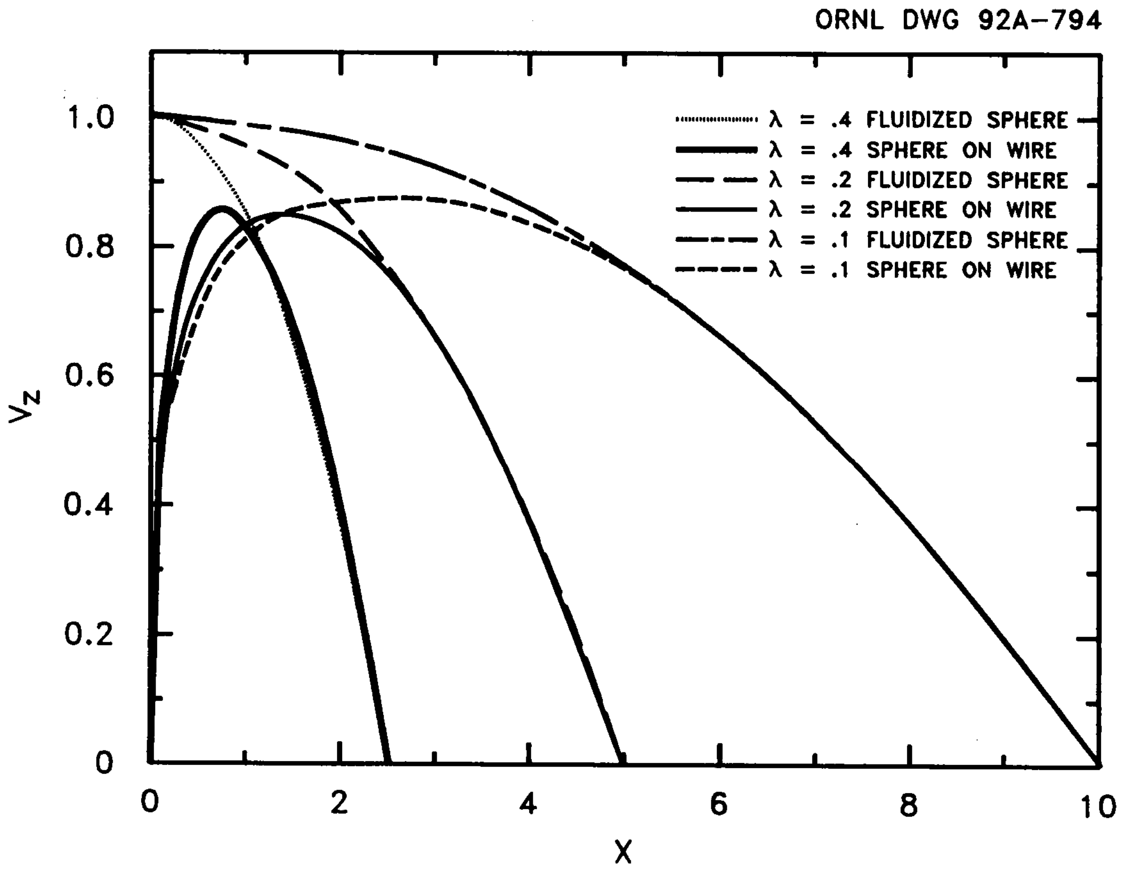

Figure 3.23. Outflow velocity profiles along S_e for flow past a fluidized sphere and flow past a sphere held by a wire for several values of $\frac{1}{\lambda}$. Here $Re = 100$.

designed to be accurate in situations in which inertial effects are small fail when the tube radius is less than or equal to twice the sphere radius.

The new results resolve at last the long-standing controversy on the value of the critical value of the Reynolds number for the onset of flow separation or wake formation in flow past solid spheres. For example, Taneda (1956) and others have claimed that wake formation is delayed until $Re = 20$. However, in accordance with the experimental observations of Nakamura (1976), the calculations reported in this paper show that wake formation in flow past a solid sphere can occur at a Reynolds number as low as about 10. Careful reading of the experimental papers devoted to studies of wake characteristics reveal the difficulty of determining accurately the critical Reynolds number for wake formation and the evolution of wake characteristics with increasing Reynolds number. By contrast, these important details of the flow field are readily and unambiguously determined in a post-processing step once the velocity field has been computed by Galerkin/finite element analysis.

The new calculations have also allowed quantifying the effect on the drag of a wire that is sometimes used in experiments to support a solid sphere. The results of this paper show conclusively that the perturbation introduced by the wire on the drag is well within experimental error.

Recent research on transient flows past solid spheres in which the flow rate is varied sinusoidally in time has revealed that under certain conditions the wake can migrate to the upstream face of the sphere, a remarkable fact (see, e.g., Chang and Maxey, 1991). The implications of this fascinating effect for flow past solid spheres in tubes of small enough radius is unknown and is currently under study.

As the Reynolds number continues to increase, the axisymmetric, steady base flow becomes unstable to non-axisymmetric perturbations having infinitesimal amplitude when *Re* reaches a critical value. The instability of the base flow has been studied experimentally by Nakamura (1976) and others. More recently, by means of a linear stability analysis of the base flow computed by the Galerkin/finite element method, Tavener (1994) has shown that the flow past a fluidized solid sphere in a tube becomes unstable with respect to a *steady* non-axisymmetric disturbance at a critical value of *Re*. This result is in qualitative agreement with the finding of Natarajan and Acrivos (1993) for flow past a solid sphere in an infinite expanse of fluid but contradicts the result of Kim and Pearlstein (1991) who contended that the bifurcation between the axisymmetric and three-dimensional solutions is of the Hopf type and that the ensuing flow is transient. The stability of the base flow past a sphere falling in a tube or that past a fluidized sphere supported by a wire in a tube are not known and are left open as problems for future studies.

Accurate knowledge of flow fields outside solid spheres and that inside and outside fluid spheres are essential for quantifying mass transfer to and from such particles. Detailed information on mass transfer to and from liquid drops suspended in tubes under conditions of finite Reynolds number, for example, is required for further advances in solvent extraction and related separation processes.

CHAPTER 4

WALL EFFECTS ON FLOW PAST FLUID SPHERES AT FINITE REYNOLDS NUMBERS: WAKE STRUCTURE AND DRAG CORRELATIONS

A central issue in solvent extraction is the transfer of solute into or out of drops. In solvent extraction, diffusion and convection compete to determine the rate of mass transfer to and from the drops. Knowledge of flow fields in and around fluid drops is critical to development of appropriate models for mass transfer since mass transfer is often dominated by convection in commercial solvent extraction units (Treybal, 1963).

When the right combination of physical and geometric parameters is met, the flow around drops can exhibit a wake at the rear of the drops, which can affect mass transfer rates. The goals of this study are to develop a better understanding of the flow in and around drops, obtain velocity fields for later use in mass transfer calculations, and develop new correlations for drag for fluid drops at low to moderate Reynolds numbers all in the limit in which the fluid drop is constrained to remain spherical in shape.

In a series of papers, Leal and coworkers (see below) have shown that recirculating wakes form at finite Reynolds number Re downstream of bluff bodies due to vorticity accumulation. The generation of vorticity in such flows is especially easy to understand if one considers the axisymmetric flow of an ambient Newtonian fluid past a spherical *particle* — a bubble or a void, a Newtonian fluid, or a solid — of radius a. Using the fact that at the spherical interface the shear stress is $\tilde{\tau}_{\tilde{r}\theta} = \mu\left(\frac{\partial \tilde{v}_\theta}{\partial \tilde{r}} - \frac{\tilde{v}_\theta}{\tilde{r}}\right)$ at $\tilde{r} = a$ and the surface vorticity is $\tilde{\omega}_s = \frac{\partial \tilde{v}_\theta}{\partial \tilde{r}} + \frac{\tilde{v}_\theta}{\tilde{r}}$ at $\tilde{r} = a$, where μ is viscosity, $(\tilde{r}, \theta, \phi)$ are spherical coordinates based at the center of the sphere and the flow is invariant in the ϕ-direction, $(\tilde{v}_{\tilde{r}}, \tilde{v}_\theta, \tilde{v}_\phi = 0)$ are the velocity components in the coordinate directions, and here and elsewhere in this work variables with a tilde are dimensional counterparts of those without a tilde. When the sphere is an inertialess gas bubble that exerts no viscous stress, i.e. a void, the appropriate expression for the surface vorticity $\tilde{\omega}_s$, which is shown in (T4.1.1) in Table 4.1, follows from the definition given above after making use of the condition of vanishing shear stress along the interface $\tilde{\tau}_{\tilde{r}\theta} = 0$ at $\tilde{r} = a$. In Table 4.1 and in the remainder of this work, superscripts "$^{(o)}$" and "$^{(i)}$" stand for the ambient fluid and the sphere, respectively. When the sphere encloses a fluid, the continuity of stress and no slip along it demand, respectively, that

$$\mu^{(i)}\Big(\frac{\partial \tilde{v}_\theta^{(i)}}{\partial \tilde{r}} - \frac{\tilde{v}_\theta^{(i)}}{\tilde{r}}\Big) = \mu^{(o)}\Big(\frac{\partial \tilde{v}_\theta^{(o)}}{\partial \tilde{r}} - \frac{\tilde{v}_\theta^{(o)}}{\tilde{r}}\Big) \quad \text{at } \tilde{r} = a\,, \tag{4.1}$$

$$\tilde{v}_\theta^{(i)} = \tilde{v}_\theta^{(o)} \quad \text{at } \tilde{r} = a\,. \tag{4.2}$$

Equation (T4.1.2) presents the expression for the surface vorticity appropriate for this situation, which is obtained from the definition of $\tilde{\omega}_s$ given above using (4.1)-(4.2) and denoting by κ the viscosity ratio of the two fluids, viz. $\kappa \equiv \mu^{(i)}/\mu^{(o)}$. When the sphere is a solid, with the no slip condition $\tilde{v}_\theta^{(o)} = 0$, $\tilde{\omega}_s$ reduces to (T4.1.3). Generalizations of the formulae presented in Table 4.1 to nonspherical *particles* can be found in the papers by Leal (1989) and Dandy and Leal (1989).

Thus, as summarized by Leal (1989) and as shown by (T4.1.1), vorticity can be generated at a perfect slip boundary if it is not flat, i.e. its radius of curvature $\tilde{r}$ is not infinite. At a no-slip boundary, the mechanism of vorticity generation is quite different, as shown for example by Tritton (1988) and by (T4.1.3). For

Table 4.1

Expressions for surface vorticity at a spherical interface.
(These are to be evaluated at $\tilde{r} = a$.)

Sphere/Ambient Fluid	Surface vorticity or jump in surface vorticity	
Void/Fluid	$\tilde{\omega}_s^{(o)} = \frac{2\tilde{v}_\theta^{(o)}}{\tilde{r}}$	$(T4.1.1)$
Drop/Fluid	$\kappa\tilde{\omega}_s^{(i)} - \tilde{\omega}_s^{(o)} = \frac{2\tilde{v}_\theta^{(o)}}{\tilde{r}}(\kappa - 1)$	$(T4.1.2)$
Solid/Fluid	$\tilde{\omega}_s^{(o)} = \frac{\partial\tilde{v}_\theta^{(o)}}{\partial\tilde{r}}$	$(T4.1.3)$

a fluid drop, vorticity is generated by a combination of these two mechanisms, as shown by (T4.1.2). Moreover, whereas for a perfect slip boundary of fixed curvature $\tilde{\omega}_s \approx \mathcal{O}(1)$ for $Re \gg 1$, where Re is the Reynolds number, for a no-slip surface $\tilde{\omega}_s \approx \mathcal{O}(Re^{1/2})$ for $Re \gg 1$. Among the many interesting questions that arise in studying such flows, three have occupied particularly central positions. One of these has been whether sufficient vorticity can be generated and accumulate immediately downstream of the body to result in a recirculating wake at a finite value of the Reynolds number. The second one has been whether as Re increases, sufficient vorticity can accumulate immediately downstream of the body to compensate for the increasingly more effective convection of vorticity so that a wake remains even as $Re \rightarrow \infty$. The third question has been whether these zones of fluid recirculation manifest themselves as eddies that are attached to or wholly detached from these bodies.

By numerically solving the Navier-Stokes equations, Brabston and Keller (1975) showed that a wake does not form downstream of a spherical void/bubble for Reynolds numbers up to 60 (see also Section 4.4). However, real bubbles do deform significantly with increasing Re and Ryskin and Leal (1984) showed that a large eddy appears over a range of Reynolds numbers provided that the Weber number, which measures the relative importance of inertial to surface tension forces, exceeds some critical value, as shown schematically in Figure 4.1(a). The difference between these two results is that as the bubble deforms, there exist regions of large enough curvature on its surface to create sufficient amounts of vorticity to produce a recirculating wake. To prove the validity of this hypothesis, Dandy and Leal (1986) studied the flow past axisymmetric bubbles or voids that are constrained to be oblate spheroids and showed that recirculating wakes

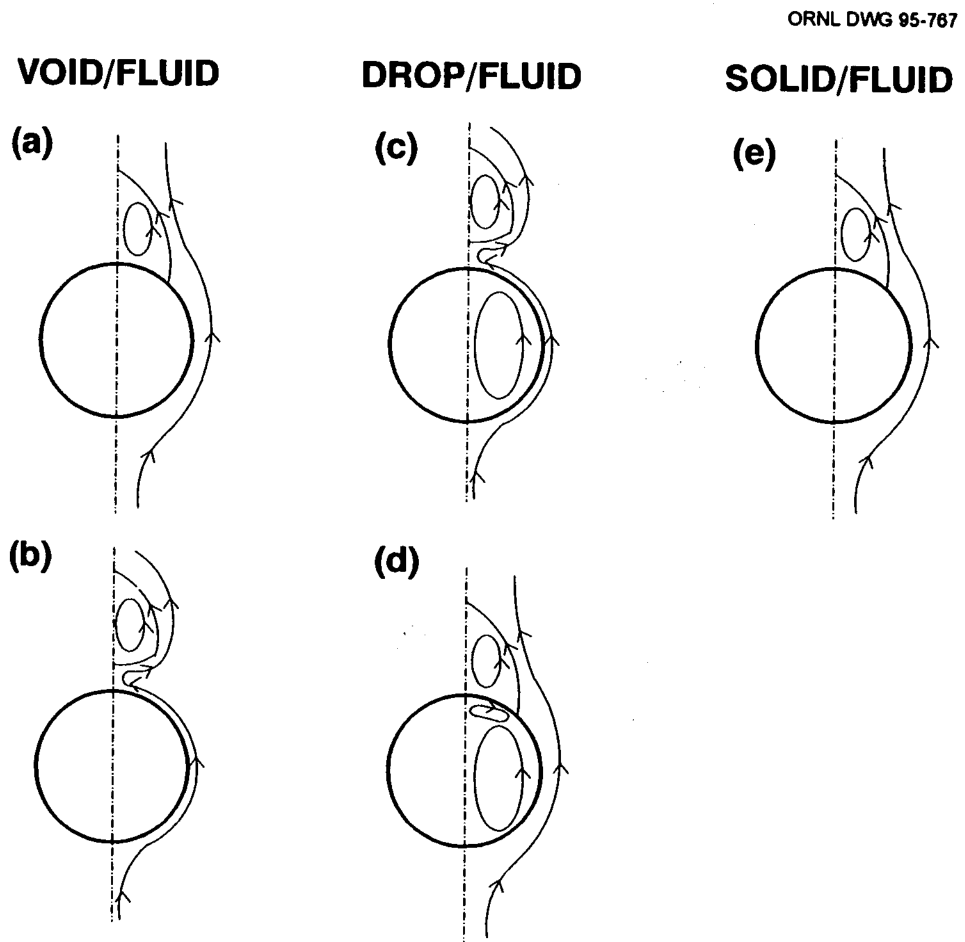

Figure 4.1. Axisymmetric flow past a particle — a void, a drop, or a solid. When the particle is a deformable body in this figure, its profile has been mapped onto a sphere by a suitable transformation. In (a)-(e), the continuous phase is a fluid. In (a) and (b), the dispersed phase is a void. In (c) and (d), the dispersed phase is a drop. In (e), the dispersed phase is a solid.

result when the oblate aspect ratio of the spheroids are sufficiently large. The wakes in both Ryskin and Leal's (1984) and Dandy and Leal's (1986) works were attached eddies, as shown in Figure 4.1(a), although there is no a priori reason to rule out detached eddies, as shown in Figure 4.1(b), in these situations. Also noteworthy in Dandy and Leal's (1986) work was that the eddy initially increased in size with Re but eventually decreased in size and disappeared when Re exceeded a certain value.

Although there have been dozens of papers that have addressed the problem of flow past a spherical fluid drop, three of these are especially relevant to the present work. Rivkind and Ryskin (1976) used a finite difference method to study flow at moderate Re and found three drastically different types of streamline patterns depending on the value of the parameters. These authors showed that sometimes there was no recirculation in the ambient fluid, under other conditions there was a detached wake downstream of the sphere as shown in Figure 4.1(c), and under yet other conditions the wake was attached to the sphere as shown in Figure 4.1(d). Rivkind and Ryskin were able to find an attached wake only under conditions approximating a mercury drop falling in air. Moreover, these authors neither determined precisely conditions for onset and termination of recirculations or the relationship, if any, in parameter space between solutions with detached and attached wakes. Oliver and Chung (1985) used a series truncation method coupled with a finite difference technique and Oliver and Chung (1987) used a series truncation method coupled with a finite element method to study flow at low Reynolds numbers and low to moderate Reynolds numbers, respectively. Although Oliver and Chung have provided an exhaustive review of the previous works in this area and have pointed out various inaccuracies contained in these previous publications, their works too have not been as definitive as one would like. For example, Oliver and Chung (1987) report solutions only up to a Reynolds number of 50 whereas, as shown in Section 4.4 of this work, much interesting fluid mechanics occurs at higher values of Re. Furthermore, the majority of Oliver and Chung's (1987) calculations were over very narrow regions of the parameter space and these authors devoted virtually no attention to the physics of recirculating wakes.

Dandy and Leal (1989) studied the buoyancy–driven motion of a deformable drop through a quiescent ambient fluid. They found that recirculating wakes can arise behind deformable drops over certain regions of the parameter space. However, they showed that these eddies are always detached, as shown in Figure 4.1(c), regardless of the ratio of the drop viscosity to that of the continuous phase and disappear as Re is increased beyond a certain value. Thus, Dandy and Leal postulated that the solid sphere with an attached wake as shown in Figure 4.1(e) is a singular limit and is only attained when the viscosity ratio equals infinity.

Therefore, the goals of this work are to determine more precisely than has been done to date the parameter ranges over which recirculating wakes form and disappear in flows past fluid drops and explore the relationship between wholly detached and attached wakes that have been reported in previous publications. In order to focus on these two issues and to achieve these goals in a computationally efficient manner, attention is restricted here to situations in which the drops are constrained to remain spherical in shape. In doing so, the computationally intensive free boundary nature of the problem is set aside and the analysis is focused strictly on the mechanics of the wakes, much in the spirit of the related study of Dandy and Leal (1986) on flow past spheroidal bubbles of fixed shape. Moreover, because most experiments in solvent extraction are often carried out in circular tubes of *finite* radii rather than in an infinite expanse of ambient fluid, the spherical drops in the present work are either suspended in a tube by an upflowing fluid (*the fluidized drop problem*) or falling in a tube (*the falling drop problem*). The equations and boundary conditions that govern the flow inside and outside the drops in these two situations are presented in Section 4.1. Section 4.2 summarizes the numerical approach based on the Galerkin/finite element method to solve the governing equations. Computational results and analyses of the findings are the subjects of Sections 4.3 and 4.4. In Section 4.3 also, two new correlations are presented for drag coefficients that, in contrast to other works that have appeared in the literature, are valid over the entire range of Reynolds numbers considered and also account for the combined effects of the presence of the tube wall and fluid inertia.

4.1. GOVERNING EQUATIONS AND BOUNDARY CONDITIONS

A fluid sphere is located centrally in a vertical circular cylindrical tube. The fluid exterior to the sphere is Newtonian and has constant viscosity $\mu^{(o)}$ and constant density $\rho^{(o)}$. The fluid interior to the sphere is also Newtonian and has constant viscosity $\mu^{(i)}$ and constant density $\rho^{(i)}$. Therefore, the flow inside and outside the drop in both the fluidized sphere and falling sphere problems is governed by the steady, incompressible Navier-Stokes equations and the continuity equation:

$$Re^{(l)}\underline{\mathbf{v}}^{(l)} \cdot \nabla\underline{\mathbf{v}}^{(l)} - \nabla \cdot \underline{\underline{\mathbf{T}}}^{(l)} + St^{(l)}\underline{\mathbf{e}}_z = \underline{0} \quad , \tag{4.3}$$

$$\nabla \cdot \underline{\mathbf{v}}^{(l)} = 0 \tag{4.4}$$

where "l" stands for either "i" or "o." Equations (4.3) and (4.4) are already dimensionless because length is measured in units of a and velocity is measured in units of U_∞, a characteristic velocity. In the case of a fluidized sphere, the flow approaches a fully-developed Poiseuille flow sufficiently far upstream and downstream of the sphere and U_∞ is the maximum value of the velocity along the axis of symmetry of the tube which has radius d. In the case of a falling sphere, the flow is quiescent sufficiently far upstream and downstream of the sphere, and U_∞ is the steady translational velocity of the falling sphere. In (4.3), $Re^{(l)} \equiv \frac{\rho^{(l)} U_\infty a}{\mu^{(l)}}$ is the Reynolds number; $\underline{\mathbf{v}}^{(l)}$ is the velocity vector with components $v_r{}^{(l)}$ and $v_\theta{}^{(l)}$ in a spherical coordinate system (r, θ) based at the center of the sphere; $\underline{\underline{\mathbf{T}}}^{(l)}$ is the total stress tensor; $\underline{\mathbf{e}}_z$ is a unit vector in the z-direction which lies along the tube axis and in the direction opposite to gravity; and $St^{(l)} \equiv \frac{\rho^{(l)} g a^2}{\mu^{(l)} U_\infty}$ is the Stokes number, where g is the magnitude of the gravitational acceleration. The total stress tensor $\underline{\underline{\mathbf{T}}}^{(l)} = -p\underline{\underline{\mathbf{I}}} + \underline{\underline{\tau}}^{(l)}$, where p is the pressure, $\underline{\underline{\mathbf{I}}}$ the identity tensor, and $\underline{\underline{\tau}}^{(l)} \equiv \nabla\underline{\mathbf{v}}^{(l)} + (\nabla\underline{\mathbf{v}}^{(l)})^T$ is the viscous stress tensor of a Newtonian fluid. Figure 4.2 shows the physical domain for the falling sphere and the fluidized sphere problems.

In this work, the Reynolds and Stokes numbers of the drop fluid are expressed in terms of the corresponding dimensionless groups based on the properties of the continuous fluid, viz. $Re^{(i)} = Re^{(o)}\frac{(\gamma+1)}{\kappa}$ and $St^{(i)} = St^{(o)}\frac{(\gamma+1)}{\kappa}$, where $\gamma \equiv \frac{\rho^{(i)} - \rho^{(o)}}{\rho^{(o)}}$. Because the sphere is placed inside a tube of finite radius, another dimensionless group arises that expresses the ratio of the sphere and tube diameters, viz. $\lambda \equiv 1/D \equiv a/d$.

Boundary conditions for the fluidized sphere problem are fully developed flow at the inlet S_i and outlet S_e, symmetry about the centerline S_s, no penetration

ORNL DWG 94A-423

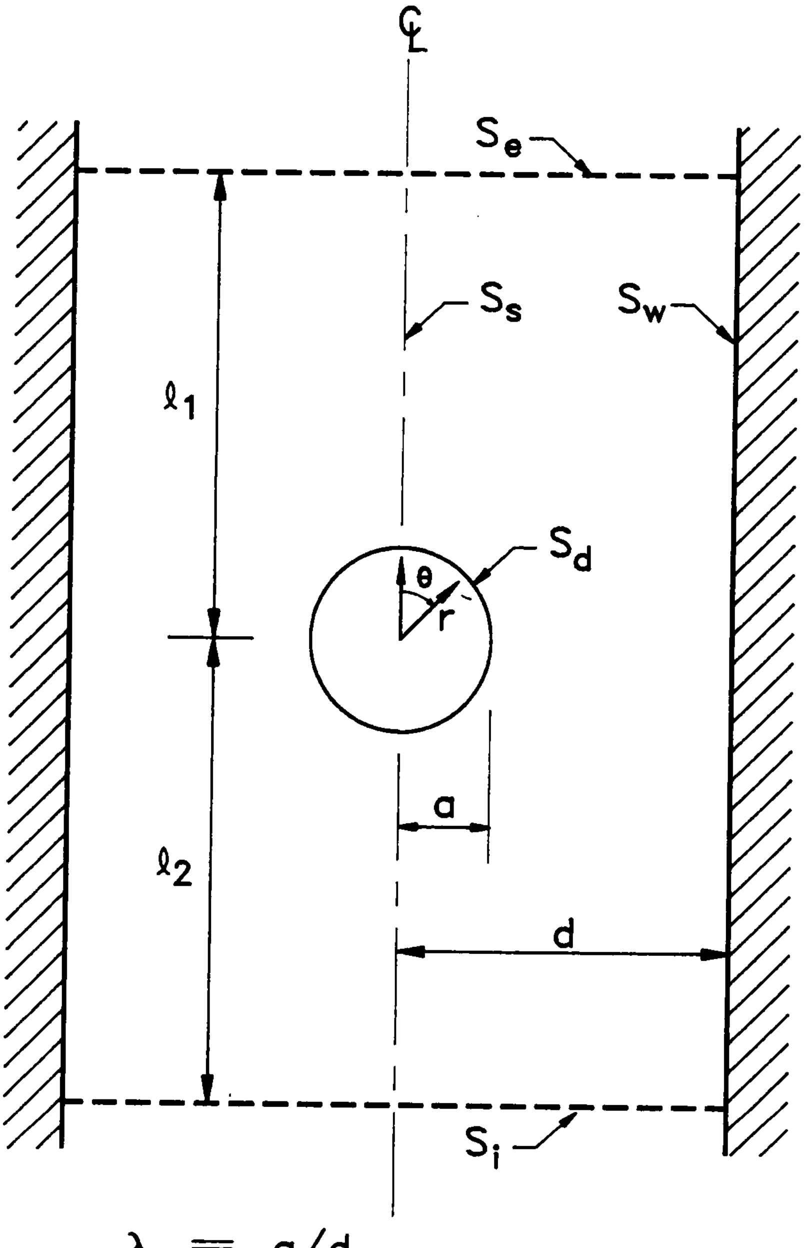

$$\lambda \equiv a/d$$

$$L_1 = \ell_1/a, \; L_2 = \ell_2/a$$

Figure 4.2. A fluid sphere that is centrally located in a tube: definition sketch.

and zero slip at the tube walls S_w, and no penetration, no slip, and continuity of tangential stress on the sphere surface S_d:

$$
\begin{aligned}
S_i: &\quad \underline{\mathbf{t}} \cdot \underline{\mathbf{v}}^{(o)} = 0, \quad \underline{\mathbf{n}} \cdot \underline{\mathbf{v}}^{(o)} = 1 - (\lambda r \sin\theta)^2 \\
S_w: &\quad v_r^{(o)} = v_\theta^{(o)} = 0 \\
S_e: &\quad \underline{\mathbf{t}} \cdot \underline{\mathbf{v}}^{(o)} = 0, \quad f_n \equiv \underline{\underline{\mathbf{T}}}^{(o)} : \underline{\mathbf{n}}\,\underline{\mathbf{n}} = 0 \\
S_d: &\quad v_r^{(l)} = 0, \quad v_\theta^{(i)} = v_\theta^{(o)}, \quad \underline{\underline{\mathbf{T}}}^{(i)} : \underline{\mathbf{n}}\,\underline{\mathbf{t}} = \frac{1}{\kappa}\underline{\underline{\mathbf{T}}}^{(o)} : \underline{\mathbf{n}}\,\underline{\mathbf{t}} \\
S_s: &\quad v_\theta^{(l)} = 0, \quad f_t \equiv \underline{\underline{\mathbf{T}}}^{(l)} : \underline{\mathbf{n}}\,\underline{\mathbf{t}} = 0 \quad .
\end{aligned}
\tag{4.5}
$$

In (4.5), and also in (4.6) below, $\underline{\mathbf{n}}$ and $\underline{\mathbf{t}}$ are unit vectors normal and tangent to the surfaces bounding the flow domain. In the case of the falling sphere, the problem is recast to a coordinate system in which the sphere is at rest. In the recast coordinate system, the governing equations (4.3)and (4.4) are unchanged, but the boundary conditions become:

$$
\begin{aligned}
S_i: &\quad \underline{\mathbf{t}} \cdot \underline{\mathbf{v}}^{(o)} = 0, \quad \underline{\mathbf{n}} \cdot \underline{\mathbf{v}}^{(o)} = 1 \\
S_w: &\quad \underline{\mathbf{t}} \cdot \underline{\mathbf{v}}^{(o)} = 1, \quad \underline{\mathbf{n}} \cdot \underline{\mathbf{v}}^{(o)} = 0 \\
S_e: &\quad \underline{\mathbf{t}} \cdot \underline{\mathbf{v}}^{(o)} = 1, \quad f_n \equiv \underline{\underline{\mathbf{T}}}^{(o)} : \underline{\mathbf{n}}\,\underline{\mathbf{n}} = 0 \\
S_d: &\quad v_r^{(l)} = 0, \quad v_\theta^{(i)} = v_\theta^{(o)}, \quad \underline{\underline{\mathbf{T}}}^{(i)} : \underline{\mathbf{n}}\,\underline{\mathbf{t}} = \frac{1}{\kappa}\underline{\underline{\mathbf{T}}}^{(o)} : \underline{\mathbf{n}}\,\underline{\mathbf{t}} \\
S_s: &\quad v_\theta^{(l)} = 0, \quad f_t \equiv \underline{\underline{\mathbf{T}}}^{(l)} : \underline{\mathbf{n}}\,\underline{\mathbf{t}} = 0 \quad .
\end{aligned}
\tag{4.6}
$$

Note that in both (4.5) and (4.6), the condition of fully developed flow is expressed by a natural boundary condition along the outlet plane from the flow domain. This traction-free form is not only more accurate than prescribing both components of the velocity field by essential boundary conditions (see, e.g., Gresho, 1991), but also sets the level of the pressure inside the liquid in the tube.

Because at steady state the sphere is not accelerated, a macroscopic force balance is written that equates the dimensional total force exerted by the ambient fluid on the sphere, $\tilde{F}_T$, which is the sum of the viscous and pressure forces, to the gravitational force acting on it

$$\tilde{F}_T = \int_{S_d} \underline{\mathbf{e}}_{\tilde{z}} \cdot \underline{\underline{\tilde{\mathbf{T}}}}^{(o)} \cdot \underline{\mathbf{n}} \, d\tilde{S} = \frac{4}{3}\pi a^3 \rho^{(i)} g = \frac{4}{3}\pi a^3 \rho^{(o)} g(\gamma + 1) \quad . \tag{4.7}$$

Therefore, all the dimensional parameters among the set composed of $\rho^{(o)}$, $\rho^{(i)}$, $\mu^{(o)}$, $\mu^{(i)}$, U_∞, a, and d or all the dimensionless parameters among the set $Re^{(o)}$, $St^{(o)}$, κ, γ, and λ (or D) cannot be assigned values independently. Here, the force balance (4.7) is used to augment the Navier-Stokes system (4.3-4.4) and γ is added to the list of unknowns.

It is customary to write the total force as the sum of the buoyancy force on the sphere (static force), $\tilde{F}_B$, and the force due to fluid movement (kinetic force), $\tilde{F}_D$, viz. $\tilde{F}_T = \tilde{F}_B + \tilde{F}_D$. The kinetic contribution to the total force is henceforward referred to as the drag force. The drag coefficient C_D is then calculated by subtracting $\tilde{F}_B$ from $\tilde{F}_T$ and dividing the result by the product of a characteristic area (πa^2) with kinetic energy per unit volume ($\frac{1}{2}\rho^{(o)} U_\infty^2$). Using dimensionless variables

$$C_D \equiv \frac{\tilde{F}_D}{(\pi a^2)(\frac{1}{2}\rho^{(o)} U_\infty^2)} = (F_T - F_B)\frac{4}{Re^{(o)}} \tag{4.8}$$

where F_T and F_B are the dimensionless counterparts of $\tilde{F}_T$ and $\tilde{F}_B$ and are measured in units of $2\pi a \mu^{(o)} U_\infty$. (The coefficient 4 in (4.8) is often replaced by 8 in the literature because the Reynolds number is defined in terms of the sphere diameter rather than its radius as in this work.)

4.2. GALERKIN/FINITE ELEMENT ANALYSIS

The conditions of fully developed flow given in (4.5) and (4.6) at the inlet and outlet planes are approached asymptotically as one moves indefinitely far from the sphere center-of-mass. Because it is impracticable to solve a problem on an infinite domain on a computer, here the outlet and inlet planes are placed at distances $L_1 \equiv l_1/a$ and $L_2 \equiv l_2/a$ downstream and upstream of the sphere. In this work, the axisymmetric Navier-Stokes system (4.3-4.4) is then solved everywhere within the rectangular region $V = \{(x,z) : 0 \le x \le D\,,\, L_1 \le z \le -L_2\}$ where $z \equiv r\cos\theta$, $x \equiv r\sin\theta$, and $0 \le \theta \le \pi$ (see Figure 4.2). The problem domain is tessellated into a set of N_r times N_θ nonuniformly spaced quadrilateral elements, where N_r is the number of elements in the r-direction and N_θ is the number of elements in the θ-direction. Figure 4.3 shows a sample grid or tessellation used in this work.

The unknown velocity field is expanded in a standard set of biquadratic basis functions (Strang and Fix 1973) ϕ^i as :

$$v_r^{(l)}(\underline{\mathbf{r}}) = \sum_{i=1}^{I} v_{r,i}^{(l)}\,\phi^i(\underline{\mathbf{r}})\,, \quad v_\theta^{(l)}(\underline{\mathbf{r}}) = \sum_{i=1}^{I} v_{\theta,i}^{(l)}\,\phi^i(\underline{\mathbf{r}})\,, \tag{4.9a}$$

and the unknown pressure field is expanded in a standard set of discontinuous linear basis functions ψ^j:

$$p^{(l)}(\underline{\mathbf{r}}) = \sum_{j=1}^{J} p_j^{(l)}\psi^j(\underline{\mathbf{r}})\,. \tag{4.9b}$$

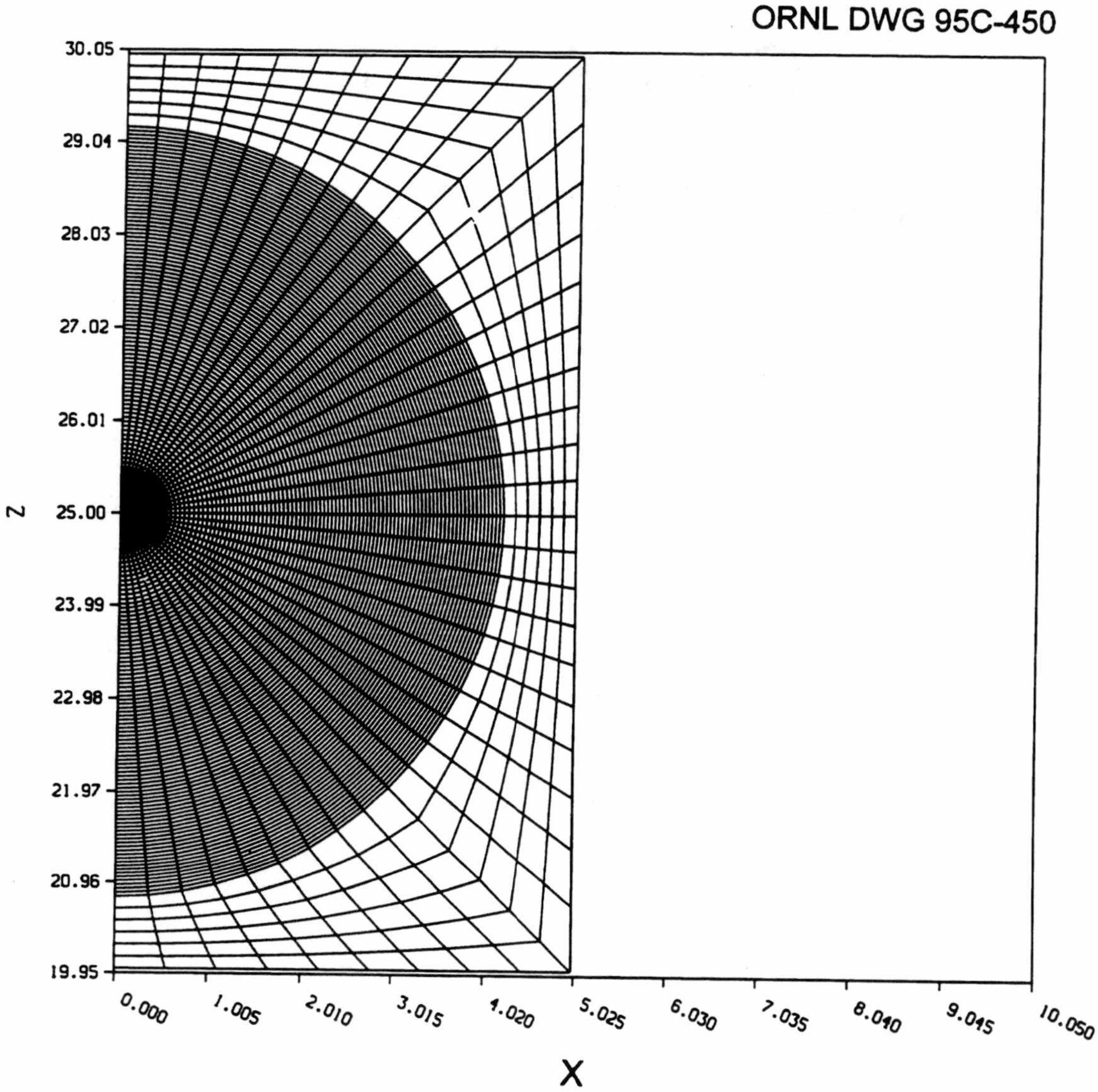

Figure 4.3. Example of a computational grid used in this work.

In (4.9a) and (4.9b), $\underline{r} \in V$ is the position vector of a point with coordinates (r,θ), $I \equiv (2N_r+1)(2N_\theta+1)$ is the total number of nodes in the finite element mesh, and $J \equiv 3(N_r \times N_\theta)$ is the total number of pressure unknowns. The coefficients $v_{r,i}^{(l)}$ and $v_{\theta,i}^{(l)}$ are the values of the velocity components at the nodes and $p_j^{(l)}$ are the unknown coefficients in the finite element approximation of the pressure and $v_r^{(l)} = (v_{r,1}^{(l)}, v_{r,2}^{(l)}, \ldots, v_{r,I}^{(l)})$, $v_\theta^{(l)} = (v_{\theta,1}^{(l)}, v_{\theta,2}^{(l)}, \ldots, v_{\theta,I}^{(l)})$, and $p^{(l)} = (p_1^{(l)}, p_2^{(l)}, \ldots, p_J^{(l)})$ are vectors representing all the unknowns.

The continuity equation is eliminated by introducing the variable penalty constraint described by Kheshgi and Scriven (1983),

$$\pm\frac{1}{\epsilon}\nabla \cdot \underline{v}^{(l)} = p, \quad \frac{1}{\epsilon} \equiv \mathcal{O}(10^6), \tag{4.10}$$

where the quantity $\frac{1}{\epsilon}$ is the penalty parameter.

The Galerkin weighted residuals of the Navier-Stokes equation after integrating the stress term by parts are:

$$R_{M,k}^i = \int\limits_{V^{(l)}} \left[\phi^i \underline{e}_k \cdot Re^{(l)} \underline{v}^{(l)} \cdot \nabla \underline{v}^{(l)} + \underline{\underline{T}}^{(l)} : \nabla \phi^i \underline{e}_k + St^{(l)}\, \underline{e}_k \cdot \underline{e}_z\, \phi^i \right] dV -$$
$$\int\limits_{S^{(l)}} \phi^i \underline{e}_k \cdot \underline{\underline{T}}^{(l)} \cdot \underline{n}\, dS = 0, \quad i = 1, \ldots, I, \tag{4.11}$$

where $\underline{e}_k = \underline{e}_r$ or $\underline{e}_\theta$ stands for the unit vector in the r- or θ-direction, $V^{(l)}$ stands for the region inside or outside the drop, and $S^{(l)}$ stands for the surfaces bounding these regions.

Special care must be taken for those nodes that lie along the interface, i.e. the drop surface. The boundary conditions on the radial and meridional components of the velocity along the drop surface in (4.5) and (4.6) imply that the velocity is continuous along the interface, viz. $\underline{\mathbf{v}}^{(i)} = \underline{\mathbf{v}}^{(o)}$. Therefore, it suffices to use a single velocity node at each mesh point along the interface. The radial component of the velocity is set equal to zero at each of these interface nodes. The equation appropriate for the meridional component of the velocity at each interface node is obtained by adding $\frac{1}{\kappa}$ times the θ-component of the momentum equation for the outer fluid to the θ-component of the momentum equation for the inner fluid:

$$R^i_{M,\theta} = \frac{1}{\kappa}\Bigg\{ \int_{V^{(o)}} \Big[\phi^i \underline{\mathbf{e}}_\theta \cdot Re^{(o)} \underline{\mathbf{v}}^{(o)} \cdot \nabla \underline{\mathbf{v}}^{(o)} + \underline{\underline{\mathbf{T}}}^{(o)} : \nabla \phi^i \underline{\mathbf{e}}_\theta +$$

$$St^{(o)} \underline{\mathbf{e}}_\theta \cdot \underline{\mathbf{e}}_z \phi^i \Big] \, dV - \int_{S^{(o)}-S_d} \phi^i \underline{\mathbf{e}}_k \cdot \underline{\underline{\mathbf{T}}}^{(o)} \cdot \underline{\mathbf{n}} \, dS \Bigg\} +$$

$$\int_{V^{(i)}} \Big[\phi^i \underline{\mathbf{e}}_\theta \cdot \frac{1}{\kappa}(\gamma+1) Re^{(o)} \underline{\mathbf{v}}^{(i)} \cdot \nabla \underline{\mathbf{v}}^{(i)} + \underline{\underline{\mathbf{T}}}^{(i)} : \nabla \phi^i \underline{\mathbf{e}}_\theta +$$

$$\frac{1}{\kappa}(\gamma+1) St^{(o)} \underline{\mathbf{e}}_\theta \cdot \underline{\mathbf{e}}_z \phi^i \Big] \, dV - \int_{S^{(i)}-S_d} \phi^i \underline{\mathbf{e}}_\theta \cdot \underline{\underline{\mathbf{T}}}^{(i)} \cdot \underline{\mathbf{n}} \, dS = 0 \, . \tag{4.12}$$

In (4.12), the surface integrals over the drop surface S_d have canceled out on account of the continuity of the tangential stress at the fluid-fluid interface (cf. (4.5) and (4.6)).

The Galerkin weighted residuals of the penalized continuity equation are:

$$R^i_C = \int \psi^i (\pm \frac{1}{\epsilon} \nabla \cdot \underline{\mathbf{v}}^{(l)} - p^{(l)}) dV = 0 \, , i = 1, \ldots , J \, . \tag{4.13}$$

The penalty constraint allows the continuity equation and the pressure nodes to be algebraically eliminated from the system of equations. The consistent penalty method described by Engelman et al. (1982), Kheshgi and Scriven (1983), and Eaton (1983) is used in this work.

Additionally, another residual equation is written to enforce the force balance (4.7):

$$R_{2I+1} = \frac{1}{2\pi} \int\limits_{S_d} \underline{\mathbf{e}}_z \cdot \underline{\underline{\mathbf{T}}}^{(o)} \cdot \underline{\mathbf{n}}\, dS - \frac{2}{3} St^{(o)}(\gamma + 1) = 0\,. \tag{4.14}$$

An interesting feature of the continuous problem stated in the previous section and its discretized counterpart formulated in this section is the role played by the Stokes number. The Stokes number can be eliminated from the momentum equations by defining a modified pressure as $p^{(l)'} \equiv p^{(l)} + St^{(l)}\, z$. Then the force balance (4.7) or its finite element counterpart (4.14) rewritten in terms of a modified total stress $\underline{\underline{\mathbf{T}}}^{(o)'} \equiv -p^{(o)'}\underline{\underline{\mathbf{I}}} + \underline{\underline{\tau}}^{(o)}$ shows that the force exerted by the fluid on the drop depends not on $St^{(o)}$ or γ alone but on their product. Therefore, values of $St^{(o)}$ can be assigned arbitrarily with no effect on calculated velocity fields and drag forces or coefficients.

The set of $2I+1$ nonlinear algebraic equations is solved for the unknown values of the velocity and γ using Newton's method. Because of the constraint (4.14), the Jacobian matrix that arises at each Newton iteration is arrow-shaped, i.e. it is banded except for a densely populated row and column as γ enters all the momentum residuals. At each iteration, the linearized system of equations is efficiently solved by the arrow solver developed by Thomas and Brown (1987). In marching across parameter space, the initial estimate to Newton's method is generated by zeroth-order continuation in Reynolds number $Re^{(o)}$. Because of the elimination of the Stokes number $St^{(o)}$ from the list of parameters, the task of exploring the parameter space is reduced to varying only the three parameters $Re^{(o)}$, κ, and $1/\lambda$. In what follows, whenever the notation Re is used, it is to be understood that reference is being made to the Reynolds number based on the properties of the outer fluid, viz. $Re \equiv Re^{(o)}$.

The correctness of the computer algorithm and the code was established by running the code with $Re = 0$ and demonstrating that the numerical predictions were in excellent agreement with the well known correlations of Haberman and Sayre (1958) for both fluidized and falling spheres in tubes. Quantitative comparisons between the computed predictions and the correlations of Haberman and Sayre are presented in Sections 4.2 and 4.3.

Moreover, several grids were used to check the sensitivity of computed solutions to mesh refinement. A particular grid was judged to be acceptable when further systematic grid refinement produced less than 0.2% change in the solution under conditions of creeping flow ($Re \to 0$). The results that are reported in Section 4.3 were obtained with $L \equiv L_1 = L_2$. The distance L, i.e., the location of the inflow and outflow boundaries, was varied until further changes in L produced less than 0.2% change in the solution as $Re \to 0$.

The algorithm was written in FORTRAN and the calculations were carried out on IBM RS6000/320H and /390 workstations at the Oak Ridge National Laboratory and a CRAY Y-MP/4 supercomputer at Florida State University Supercomputer Center.

4.3. RESULTS

In obtaining the results reported in this section, computations were carried out for values of $\kappa = 0.1$ to 10^7 and $\frac{1}{\lambda} = 5, 10, 20$ over a range of Reynolds numbers $0 \leq Re \leq 250$ in the falling sphere and fluidized sphere problems. In subsection 4.3.1, a detailed discussion is provided on the evolution of the flow field with Re and κ in the falling sphere problem. In subsections 4.3.2 and 4.3.3, new correlations are presented for drag coefficients in both the fluidized sphere and falling sphere problems.

4.3.1 Flow fields and wake structure

Because the Navier-Stokes equation was solved in the so-called primitive variable formulation, streamfunction ψ and vorticity values were subsequently obtained during postprocessing of the computed velocity fields. It was observed that plots of constant values of the streamfunction — streamlines — were much more sensitive to the number of nodal points in the mesh than other measures of solution sensitivity, e.g. drag coefficient. Table 4.2 shows that the computed value of the drag coefficient up to $Re = 200$ varied by less than 0.2% when the number of nodes was changed from 6,885 to 18,961. By contrast, whereas the streamline plots obtained with a mesh of 6,885 nodes exhibited kinks in the wake region downstream of the sphere, the streamlines obtained with a mesh of 18,961 nodes were smooth. Therefore, the majority of the plots depicting flow fields in this work were obtained with meshes containing 18,961 nodes or 37,922 unknowns. In certain cases when attached eddies occurred (see below), meshes containing approximately 23,000 nodes were used to examine details of the computed flow fields.

An important question that has not been answered definitively in the literature is the lowest value of κ at which a wake forms. The new computations have shown that in the range $0.1 \leq \kappa \leq 1.0$ the flow fields outside the sphere have virtually fore and aft symmetry for all values of the Reynolds number studied with no evidence of wake formation up to $Re = 250$. Another notable result in

Table 4.2

Effect of number of nodes in grid on drag, C_D,
for the case of $\frac{1}{\lambda} = 5$
(Here $\kappa = 10$)

Re	fine grid (18,961 nodes)	medium grid (6,885 nodes)
10	5.7169	5.724
20	3.6544	3.6577
50	2.1565	2.1578
100	1.4842	1.4861
150	1.1828	1.1864
200	0.99732	1.0037

this low κ regime is that the internal streamlines are also virtually symmetric about the equatorial midplane and the location of the center of the internal vortex remains virtually fixed for all values of Re investigated. Figure 4.4, where $\kappa = 1.0$, is typical of results obtained at low viscosity ratios. The Hadamard-Rybczynski (Hadamard 1911, Rybczynski 1911) solution for creeping flow past a fluid sphere in an infinite expanse of ambient fluid predicts that regardless of the value of the viscosity ratio, the inner vortex center is located at $r = \sqrt{2}/2 \approx 0.7071$, $\theta = \pi/2$. For $\kappa = 1$, the center of the inner vortex in Figure 4.4 is located at $r = 0.704$, $\theta = \pi/2$ in the limit of $Re \to 0$. The vortex center migrates ever so slightly as Reynolds number increases and tends to $r = 0.715$, $\theta = \pi/2$ as $Re \to 250$.

Next, the value of the viscosity ratio was systematically increased to determine the value of κ for the onset of wake formation. Figure 4.5 shows the effect of an order of magnitude increase in κ over that in Figure 4.4 to $\kappa = 10$ while keeping $\frac{1}{\lambda}$ fixed at 5. At Re=20, a slight asymmetry is observed in the streamlines just to the rear of the drop. As the Reynolds number increases, a detached wake occurs when $Re = 25 \pm 5$. As Re increases further, the detached wake moves closer to the rear of the droplet; Figure 4.5 shows a detached wake when $Re = 30$. The occurrence of such detached wakes has previously been reported by Rivkind and Ryskin (1976) and Dandy and Leal (1989) in the context of the fluid sphere and fluid drop problems, respectively. However, as the Reynolds number continues to increase, it has been uncovered here that the wake attaches to the rear of the drop at $Re = 71 \pm 1$. The attachment of a previously detached eddy with increasing Re was heretofore not known. For the set of parameters applicable to Figure 4.5, the wake is still present at the rear of the drop at $Re = 250$, which

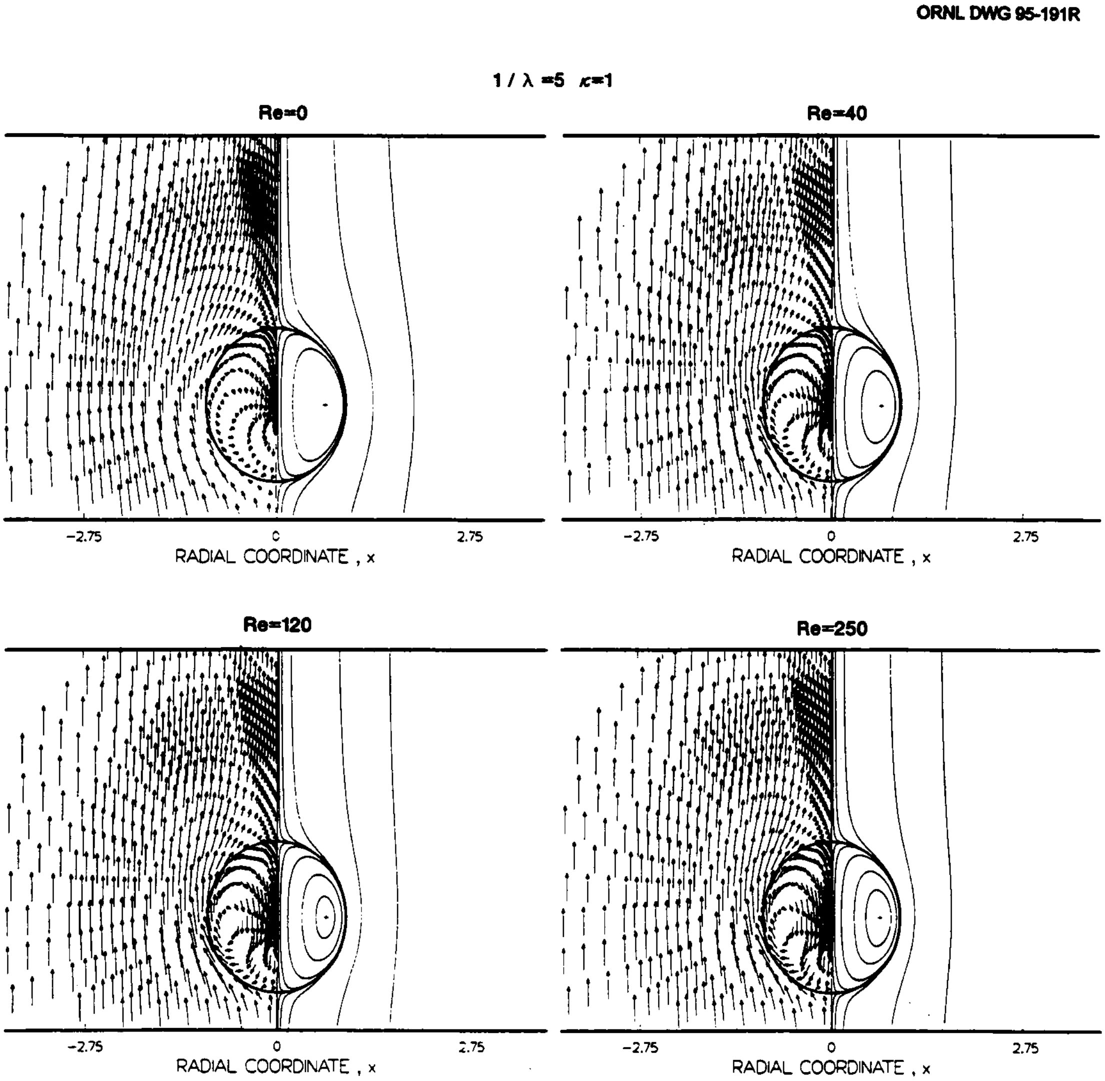

Figure 4.4. Velocity profiles as a function of Re for a falling sphere. Here $\kappa = 1$ and $\frac{1}{\lambda} = 5$. In each panel of Figure 4.4 (and Figures 4.5-4.9 below), streamlines are plotted to the right of the centerline and velocity vectors to the left of it. Each velocity vector shown belongs to its basepoint.

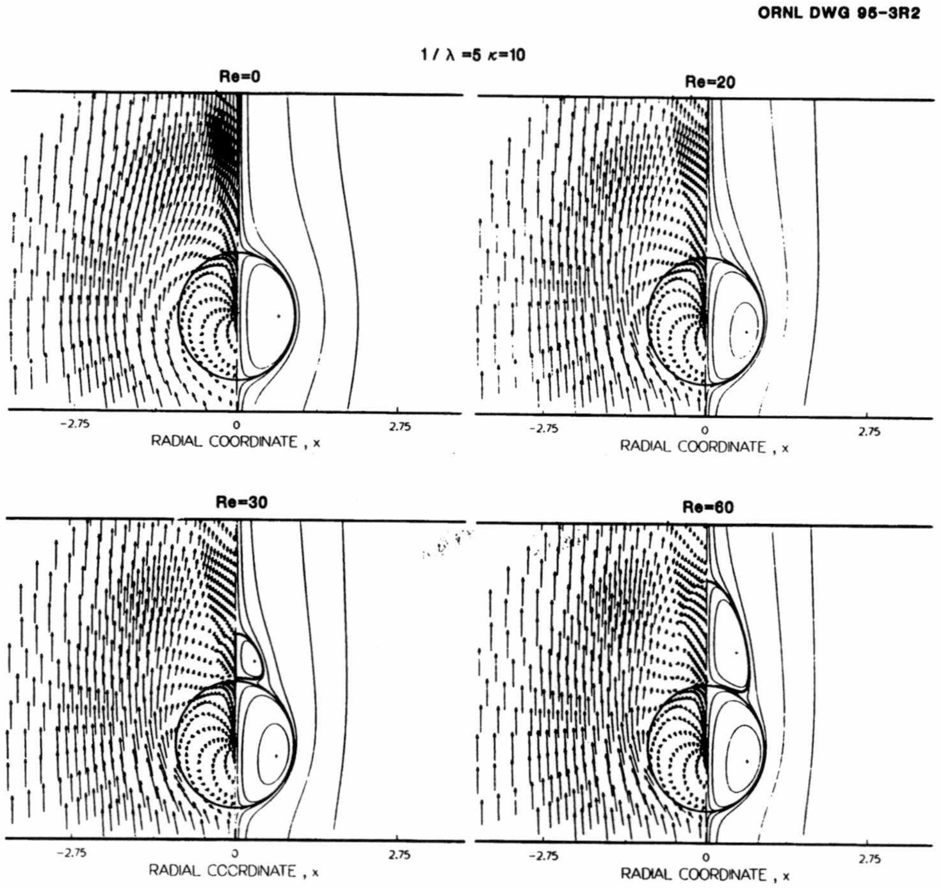

Figure 4.5. Velocity profiles as a function of Re for a falling sphere. Here $\kappa = 10$ and $\frac{1}{\lambda} = 5$.

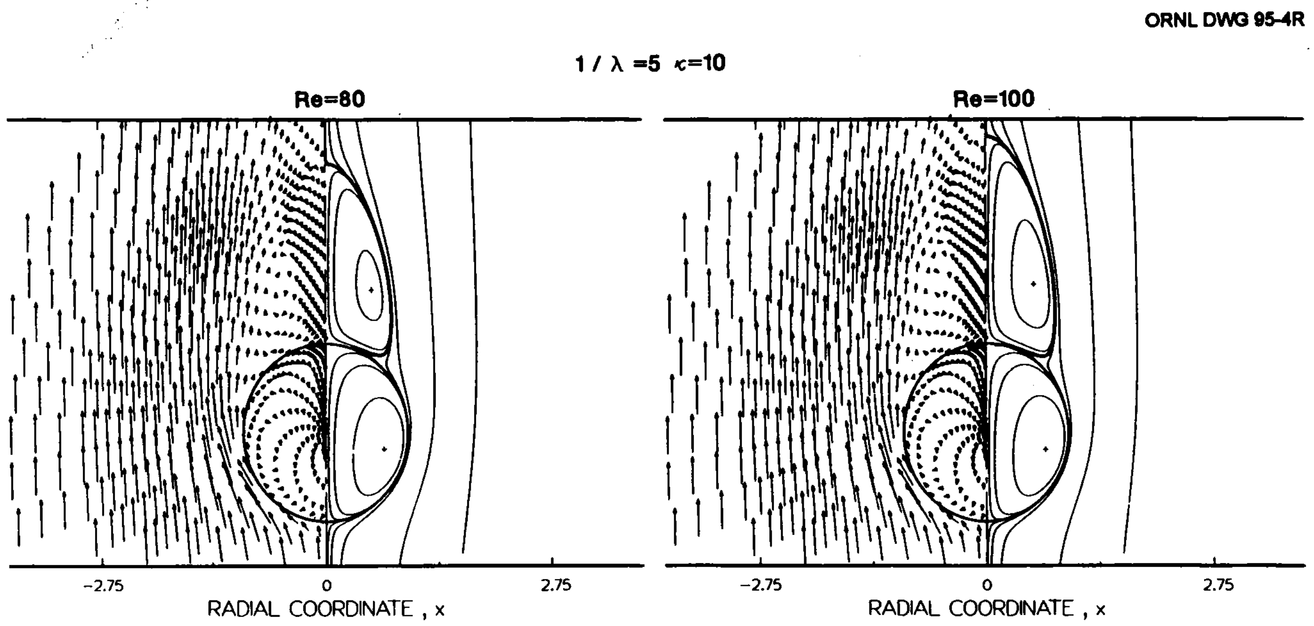

Figure 4.5. Continued

is the highest value of the Reynolds number considered in this work. Upon attachment of the exterior wake, a much smaller secondary vortex appears at the rear (downstream) face of the fluid sphere.

The appearance of this vortex is also confirmed by observing a change in sign in both (i) the tangential component of the velocity and (ii) the viscosity weighted vorticity difference between the two fluids at the interface, as expected based on equation (T4.1.2) in Table 4.1. The secondary inner vortex is weak and typically is of strength $\mathcal{O}(10^{-5})$. Meanwhile, the center of the primary inner vortex moves toward the front stagnation point as Re increases. The evolution with Re of the streamlines in and around the drop shown in Figure 4.5 is in sharp contrast to those of the lower viscosity ($\kappa = 1$) drop of Figure 4.4 where the streamlines exterior to the sphere exhibit virtually perfect fore and aft symmetry and the vortex interior to the sphere moves little for all values of Re.

Figures 4.6-4.9 depict the evolution of flow fields in and around falling fluid spheres in situations in which the Reynolds number is held fixed at four different values and the viscosity ratio is systematically increased. Figure 4.6 illustrates that when $Re = 20$, drops with viscosity ratios of $\kappa = 2.75, 3, 3.5$ exhibit streamlines having fore and aft symmetry while that with $\kappa = 10$ exhibits ones that are slightly bent at the rear of the drop. Figure 4.6 demonstrates that at a viscosity ratio of 25, a detached wake has already formed at the rear of the drop.

Figure 4.7 shows streamlines and velocity vectors in and around falling drops at the same values of the viscosity ratio as Figure 4.6 albeit at the slightly higher value of Reynolds number of 60. For this higher Re flow, slight asymmetry in the streamlines, but no wake, is already apparent at the rear of the drop at a value of the viscosity ratio as low as 2.75. In this case, a small detached wake forms

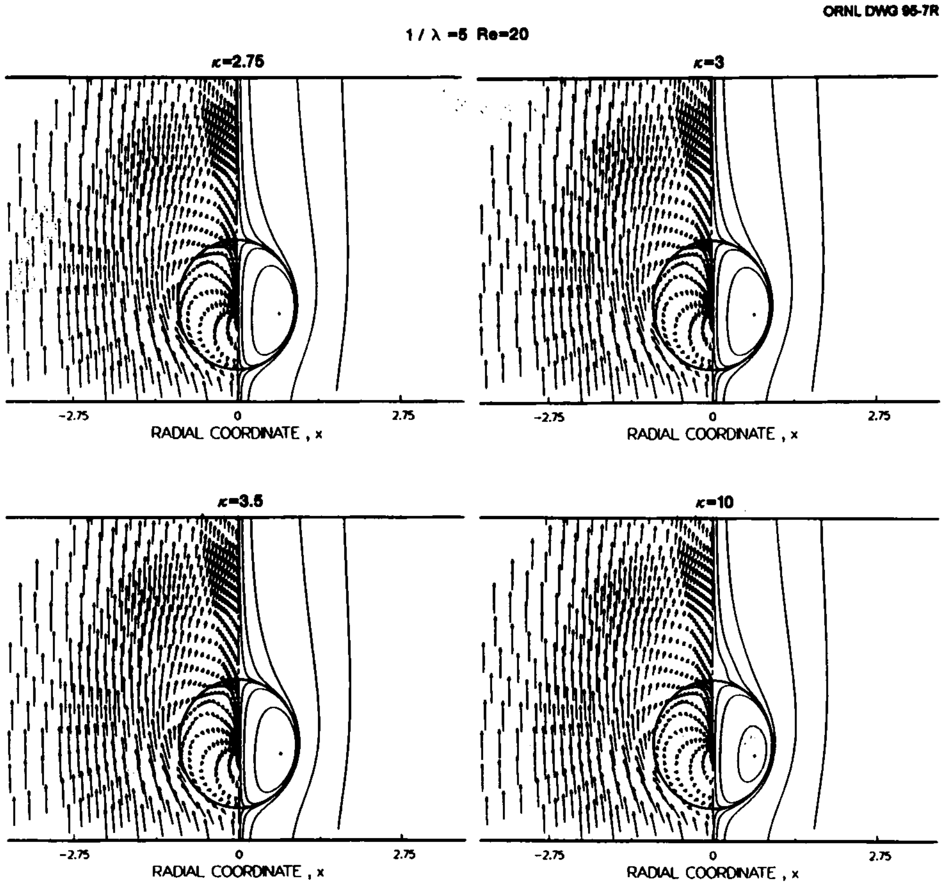

Figure 4.6. Velocity profiles as a function of κ for a falling sphere. Here $Re = 20$ and $\frac{1}{\lambda} = 5$.

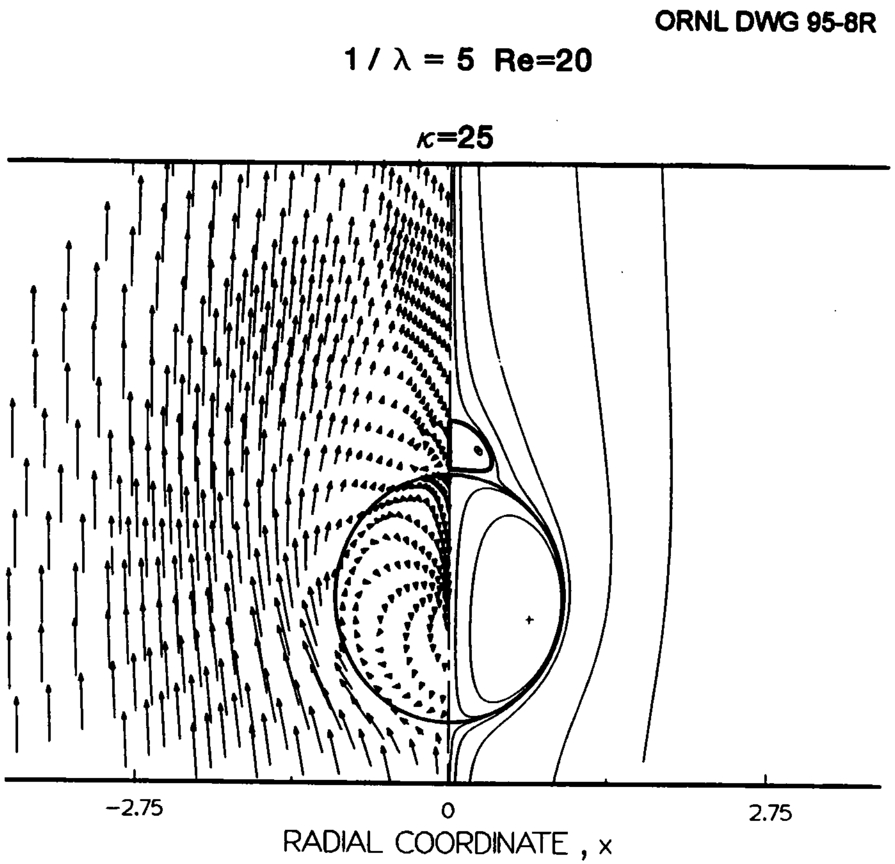

Figure 4.6. Continued

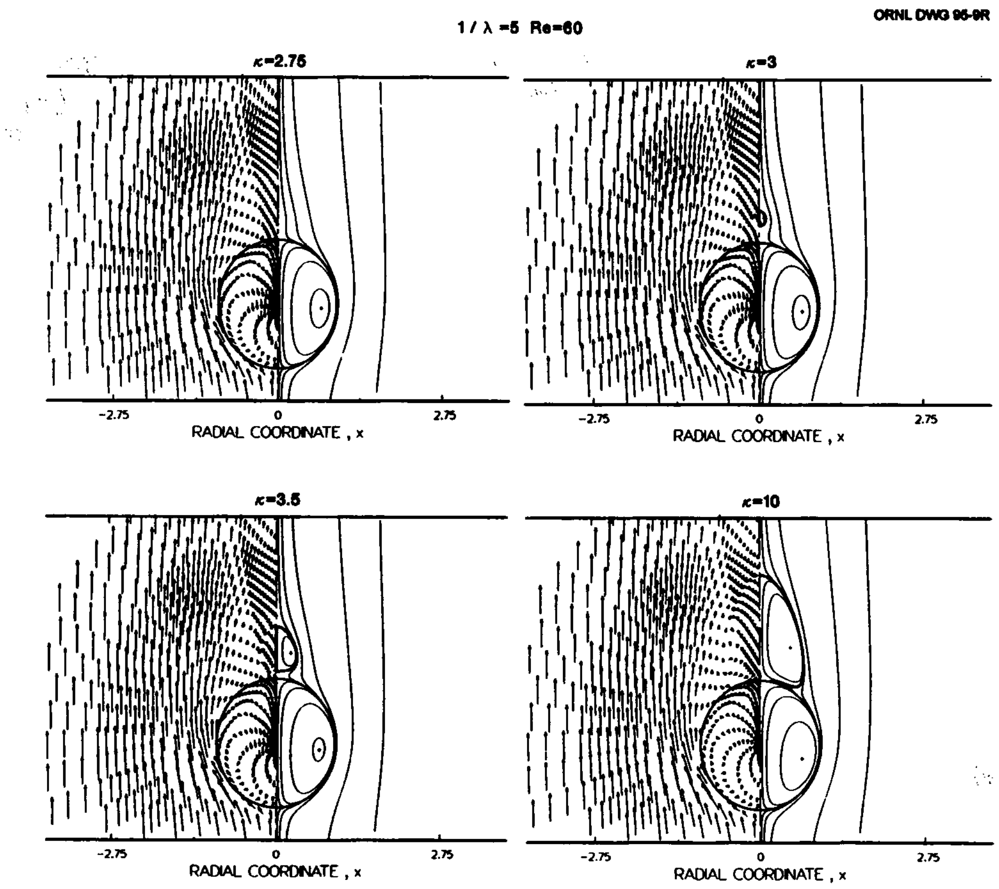

Figure 4.7. Velocity profiles as a function of κ for a falling sphere. Here $Re = 60$ and $\frac{1}{\lambda} = 5$.

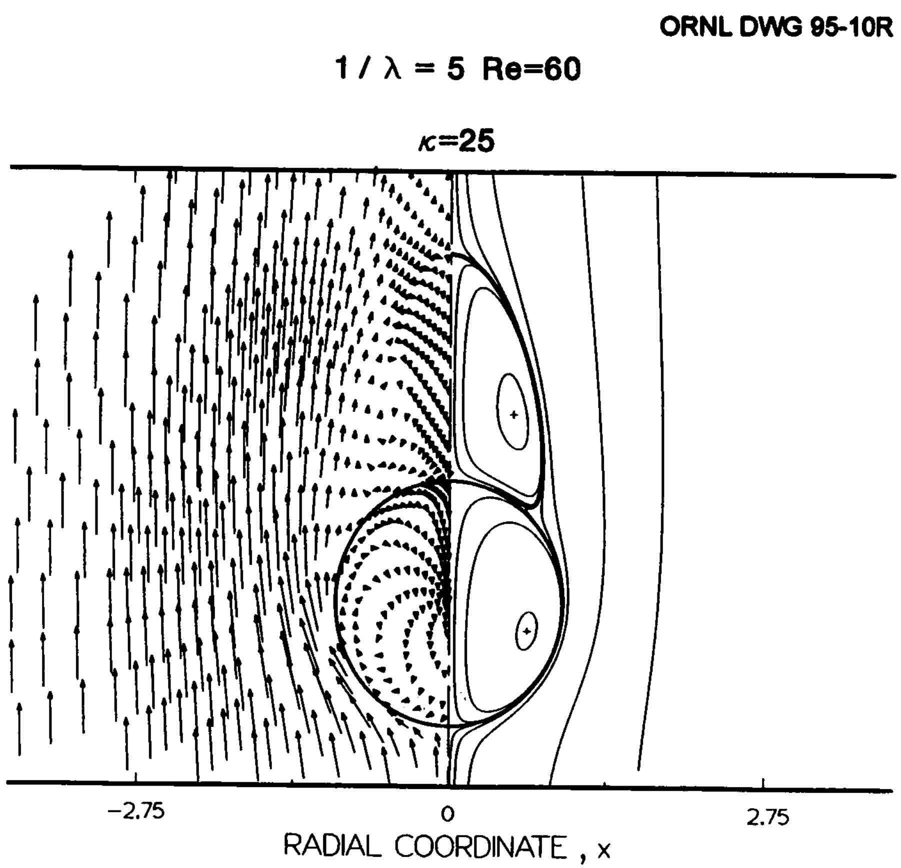

Figure 4.7. Continued

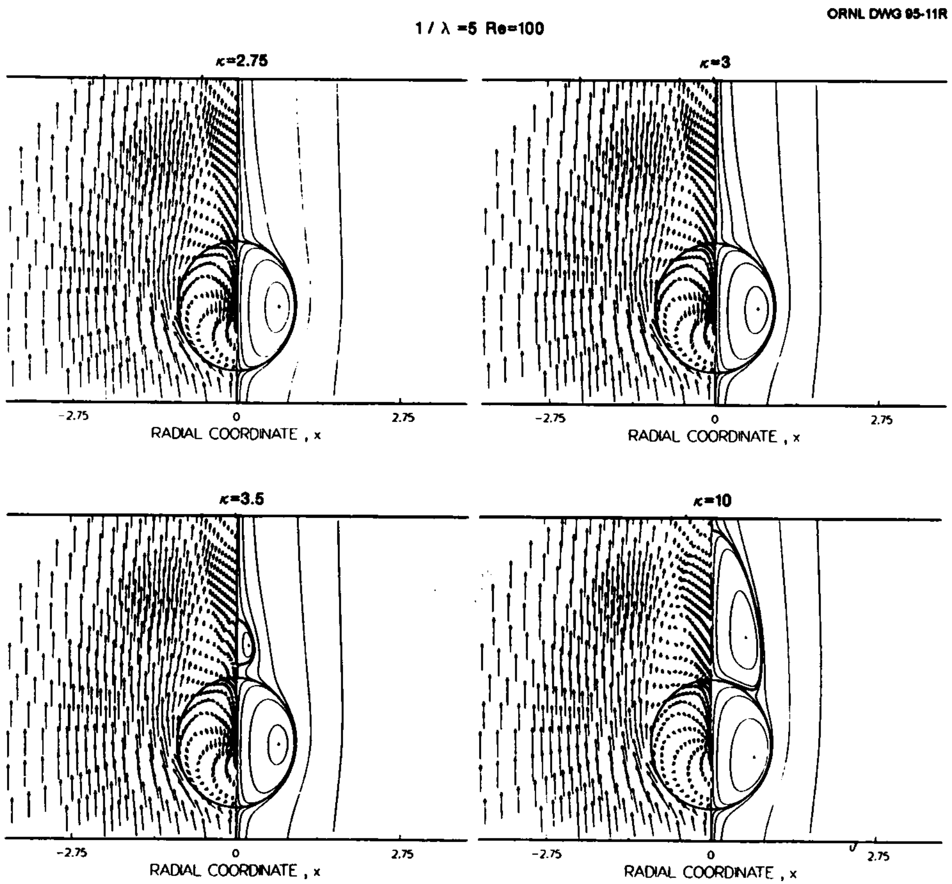

Figure 4.8. Velocity profiles as a function of κ for a falling sphere. Here $Re = 100$ and $\frac{1}{\lambda} = 5$.

ORNL DWG 95-12R

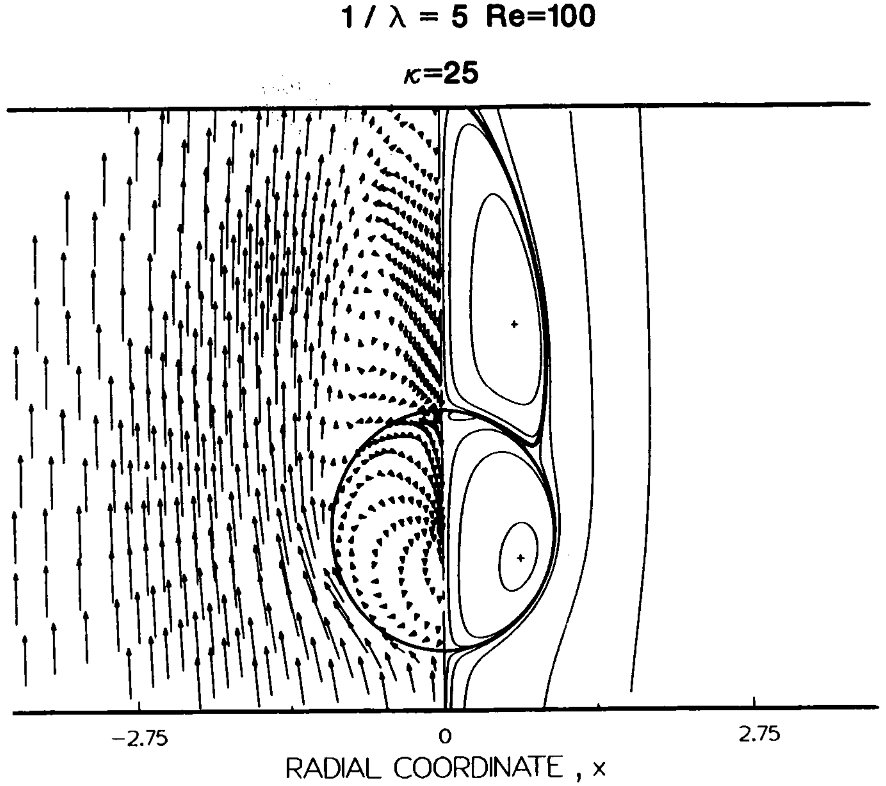

Figure 4.8. Continued

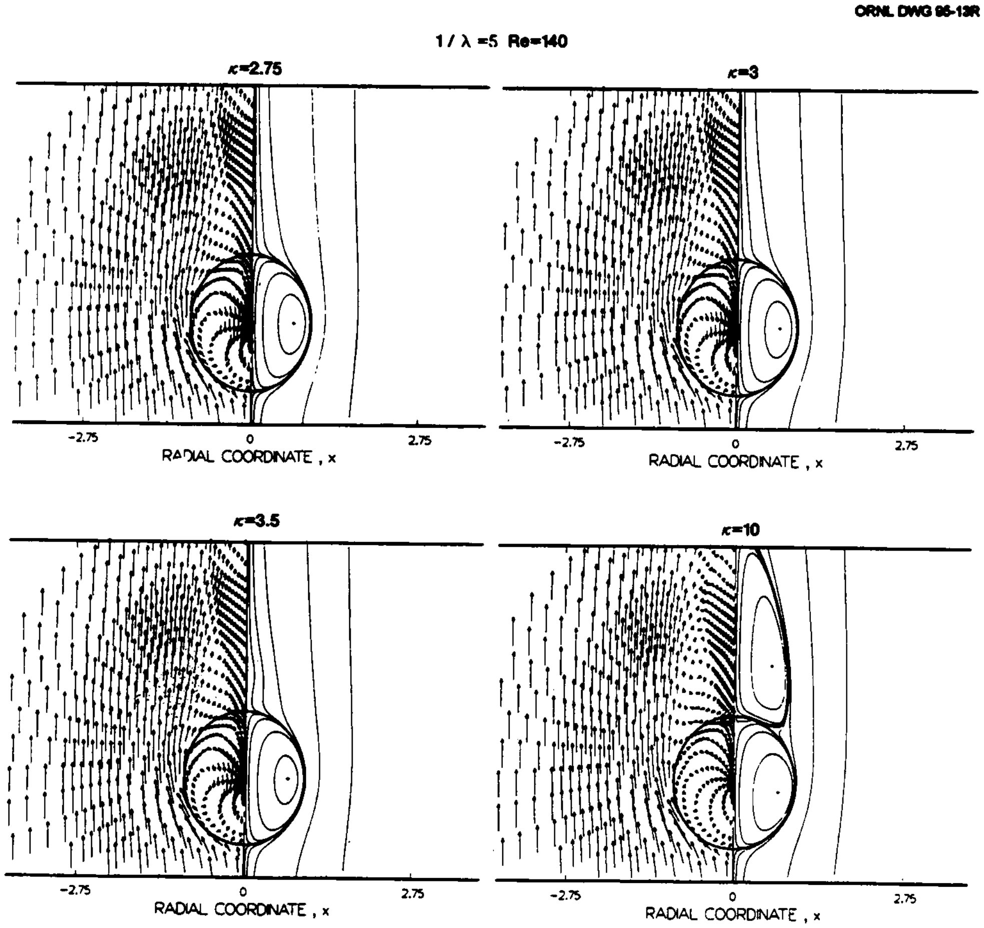

Figure 4.9. Velocity profiles as a function of κ for a falling sphere. Here $Re = 140$ and $\frac{1}{\lambda} = 5$.

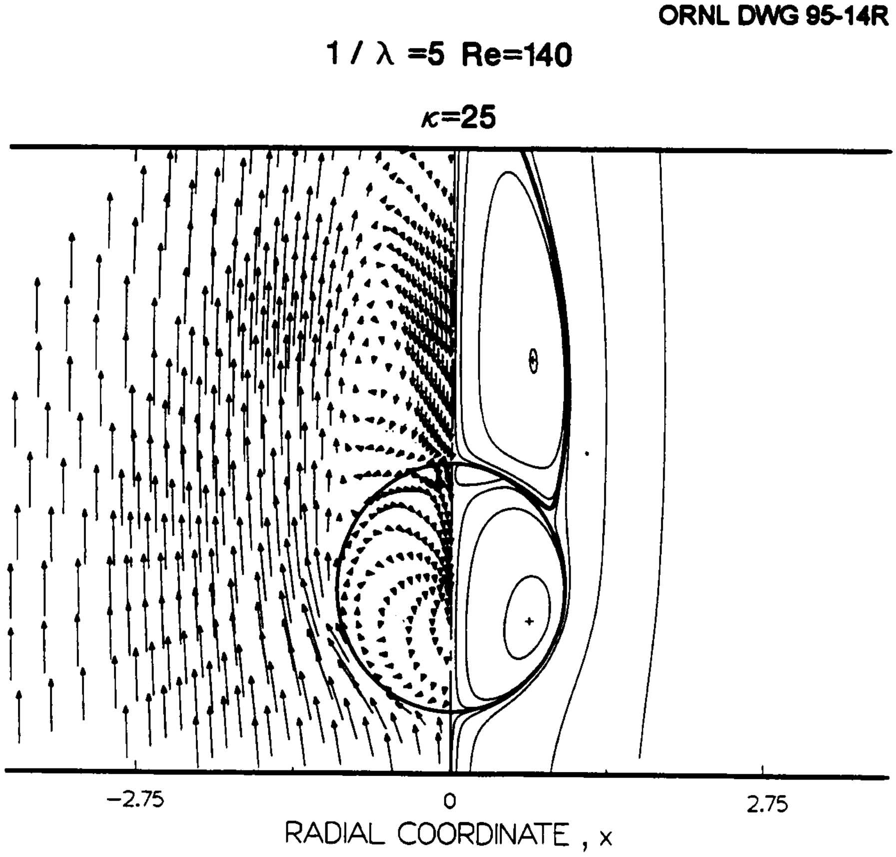

Figure 4.9. Continued

at a viscosity ratio $\kappa = 3$. Moreover, Figure 4.7 shows that a small increase in κ to 3.5 results in a significant increase in the size of the wake. Although the wake continues to grow as the viscosity ratio is increased from 3.5 to 25, it remains detached from the drop for all values of κ shown in Figure 4.7 as made evident by a lack of change in sign in both v_θ and $\kappa\omega_s^{(i)} - \omega_s^{(o)}$.

Further changes in wake behavior can be seen in Figure 4.8 which depicts the evolution of streamlines and velocity vectors in and around a falling fluid sphere at $Re = 100$. Comparison of Figures 4.7 and 4.8 reveals that the streamlines at the rear of the drop for $\kappa = 2.75$ have more fore and aft symmetry when $Re = 100$ than when $Re = 60$. Moreover, when $\kappa = 3$ the wake that is present behind the drop at $Re = 60$ is absent at $Re = 100$. Furthermore, when $\kappa = 3.5$ the wake behind the drop is reduced slightly in size and the location of the inner vortex moves toward the centerline of the tube as the Reynolds number increases from $Re = 60$ to $Re = 100$. When $Re = 100$, the wake attaches to the rear surface of the drop at the higher viscosity ratios of $\kappa = 10, 25$, as made plain by the appearance of a small secondary vortex inside the drop at its rear face. Figures 4.7 and 4.8 point to a particularly interesting competition with increasing Re between the generation and accumulation of vorticity behind the drop on the one hand and the removal of vorticity by convection on the other hand. Whereas the generation of vorticity is primarily due to the curvature of the free surface at low viscosity ratios, its generation is primarily due to the no slip mechanism at high viscosity ratios. Therefore, at low viscosity ratios vorticity generation at a spherical surface of constant curvature cannot keep up with the increasingly more effective convection of vorticity as Re increases, as made evident by the disappearance of the wake at $\kappa = 3$ and the smoothing of streamlines at $\kappa = 2.75$ when Re is increased from 60 to 100. By contrast, at high viscosity ratios, the increasingly more important role played by the no slip mechanism in vorticity generation leads to continuing accumulation of vorticity at the rear of the droplet albeit the accompanying rise in vorticity convection away from the drop as Re increases. The consequences of this rise in the accumulation of vorticity are the growth of the wake at the rear of the drops and and the eventual formation of the secondary vortex inside the drops as Re increases (cf. Figure 4.8).

Figure 4.9 depicts flow fields at the same viscosity ratios as the previous three figures albeit at the higher Reynolds number of 140. The streamlines outside the drop when $\kappa = 2.75$, 3 have now almost attained fore and aft symmetry. For $\kappa = 3.5$, the wake that was present behind the drop when $Re = 100$ has disappeared but slight bending is still apparent of those streamlines that lie near the centerline of the tube immediately downstream of the drop. Compared to the situation when $Re = 100$, the wake behind the drop for $\kappa = 10$, 25, although still attached to the rear of the drop, and the secondary vortex inside the drop are now larger in size. Whereas the center of the primary inner vortex remains virtually fixed at the location $r = 0.715, \theta = \frac{\pi}{2}$ for low values of the viscosity ratio, it moves toward the front stagnation point when $\kappa = 10$, 25.

Table 4.3 shows the effect of the ratio of the tube radius to the sphere radius on the value of Re at which a detached wake first appears, $Re_c^{(1)}$, and that at which the wake disappears, $Re_c^{(2)}$, for the situation in which $\kappa = 3$. Table 4.3 makes plain that narrow tubes suppress wake formation: the value of the Reynolds number for the first appearance of a wake, $Re_c^{(1)}$, increases but that for its disappearance, $Re_c^{(2)}$, decreases as the ratio of the tube radius to the sphere

Table 4.3

Effect of ratio of tube radius to sphere radius, $1/\lambda$, on the value of the Reynolds number at which a detached wake first appears, $Re_c^{(1)}$, and that at which the wake disappears, $Re_c^{(2)}$ (Here $\kappa = 3$)

$1/\lambda$	$Re_c^{(1)}$	$Re_c^{(2)}$
5	51 ± 1	77 ± 1
10	47 ± 1	85 ± 1
20	46 ± 1	87 ± 1

radius, $1/\lambda$, decreases. The inhibiting nature of tube walls on wake formation reported here for fluid drops accords with results previously reported for solid spheres (Wham *et al.* 1995).

Figure 4.10 shows the effect of viscosity ratio on the critical Reynolds numbers $Re_c^{(1)}$ and $Re_c^{(2)}$ for wake formation and wake disappearance, respectively. When $\kappa = 2.9$, spherical drops placed in narrow tubes having $\frac{1}{\lambda} = 5$ do not exhibit a wake over the range of Reynolds numbers $0 \leq Re \leq 250$ whereas ones placed in wider tubes having $\frac{1}{\lambda} = 10$ exhibit wakes over the range $53 \pm 1 \leq Re \leq 70 \pm 1$. Moreover, this result and others shown in Figure 4.10 further demonstrate the suppression of wakes by narrow tubes. For values of κ up to 4.5, both wake formation and wake disappearance are observed over the Reynolds number range $0 \leq Re \leq 250$. Although wakes do form for values of κ larger than 5, they persist and do not disappear for Reynolds numbers up to 250.

Figure 4.11 shows the variation with the reciprocal of the viscosity ratio, $\frac{1}{\kappa}$, of the Reynolds number at which the wake first attaches to the rear of the sphere, Re_c^* , and that at which a detached wake first appears, $Re_c^{(1)}$. Also plotted in the same figure as a horizontal line is the value of the Reynolds number at which a wake forms behind a falling *solid* sphere. If the transition from the fluid sphere to the solid sphere is to be continuous, one would expect both of the curves for Re_c^* and $Re_c^{(1)}$ to approach the solid sphere limit as $\frac{1}{\kappa} \to 0$. Figure 4.11 shows that Re_c^* decreases slightly as $\frac{1}{\kappa}$ decreases and appears to approach an asymptotic value of about 61 ± 1. Indeed, Re_c^* equals 61 ± 1 when the viscosity ratio is 10^7, a value which remains unchanged upon further systematic refinement of the mesh in and around the sphere. Similarly, Figure 4.11 shows that $Re_c^{(1)}$ too decreases slightly as $\frac{1}{\kappa}$ decreases and it appears to approach an asymptotic value of about

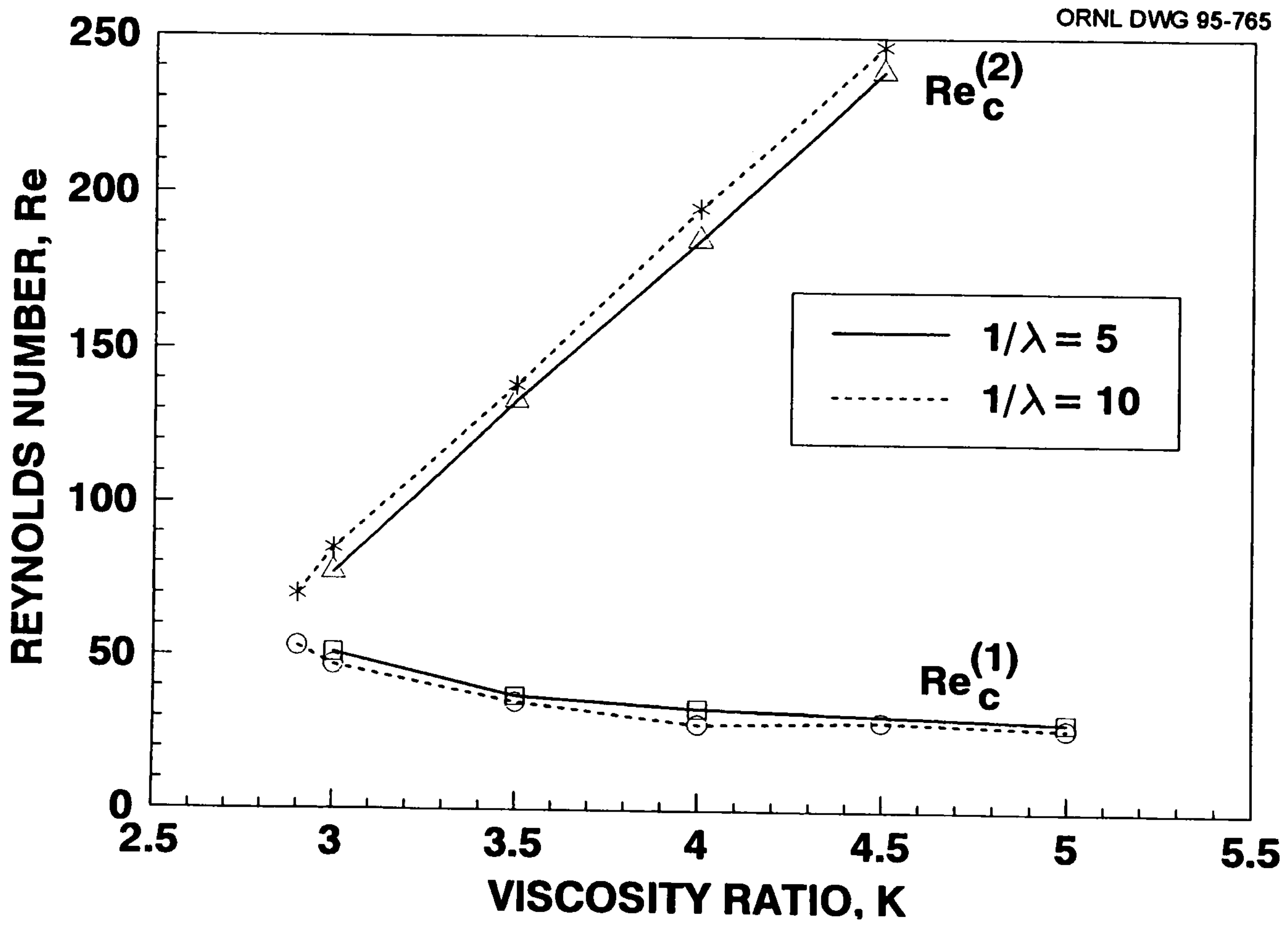

Figure 4.10. Effect of viscosity ratio and ratio of tube radius to sphere radius on the value of Re at which a detached wake first appears, $Re_c^{(1)}$, and that at which the wake disappears, $Re_c^{(2)}$.

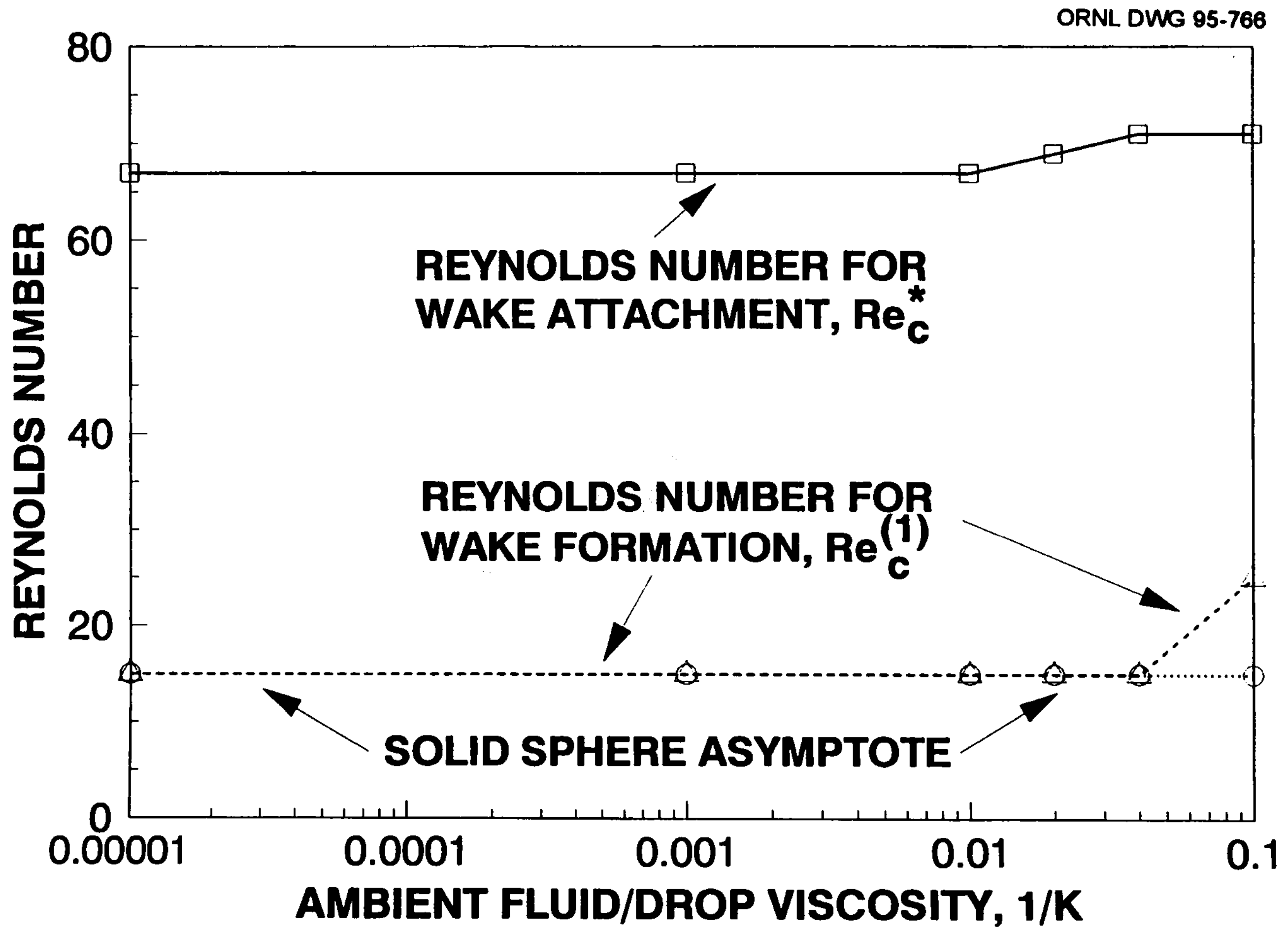

Figure 4.11. Reynolds number at which a detached wake first attaches to the drop, Re_c^*, as a function of the reciprocal of the viscosity ratio, $1/\kappa$. Also shown for comparison are the Reynolds number at which a detached wake first forms behind a fluid sphere, $Re_c^{(1)}$, and that at which a wake first forms behind a solid sphere.

15 ± 1 as $\frac{1}{\kappa} \to 0$. Therefore, the results of Figure 4.11 confirm the surmise of Dandy and Leal (1989) that the solid sphere is a singular limit in the sense that it is not approached smoothly by fluid spheres in the limit as $\frac{1}{\kappa} \to 0$.

Figure 4.12 depicts the variation with Reynolds number of the maximum value of the vorticity of the ambient fluid evaluated on the surface of the fluid sphere. Figure 4.12 shows that the magnitude of the surface vorticity increases with Re for all values of κ *and* at any value of Re both the magnitude of the surface vorticity and its rate of change with Re are larger the larger the value of κ. Furthermore, for small values of κ, it can be seen that the surface vorticity approaches an asymptotic value for Re exceeding about 200. The trends shown in Figure 4.12 accord with intuition because it is well known that the surface vorticity remains $\mathcal{O}(1)$ for a slip boundary of fixed curvature and varies as $\mathcal{O}(Re^{1/2})$ for a no slip boundary for $Re \gg 1$ (see, e.g., Leal 1989).

Figures 4.13–4.15 show the variation along the interface of the viscosity weighted vorticity difference, $\kappa\omega_s^{(i)} - \omega_s^{(o)}$, and the tangential component of the velocity, v_θ, as functions of the viscosity ratio at Reynolds numbers of 20, 60, and 100, respectively. Figures 4.13–4.15 make plain that the magnitude of the viscosity weighted vorticity difference rises and that of the tangential velocity falls as the viscosity ratio rises.

Figure 4.15 shows the viscosity weighted vorticity difference and the tangential component of the velocity when $Re = 100$. Results for the higher viscosity ratios of 10 and 25 are especially significant since both $\kappa\omega_s^{(i)} - \omega_s^{(o)}$ and v_θ exhibit a sign change near the rear of the drop. This observation of course accords with the results previously shown in Figure 4.8 that at these viscosity ratios the detached wake attaches to the sphere surface and a secondary internal vortex forms inside

ORNL DWG 95-432R

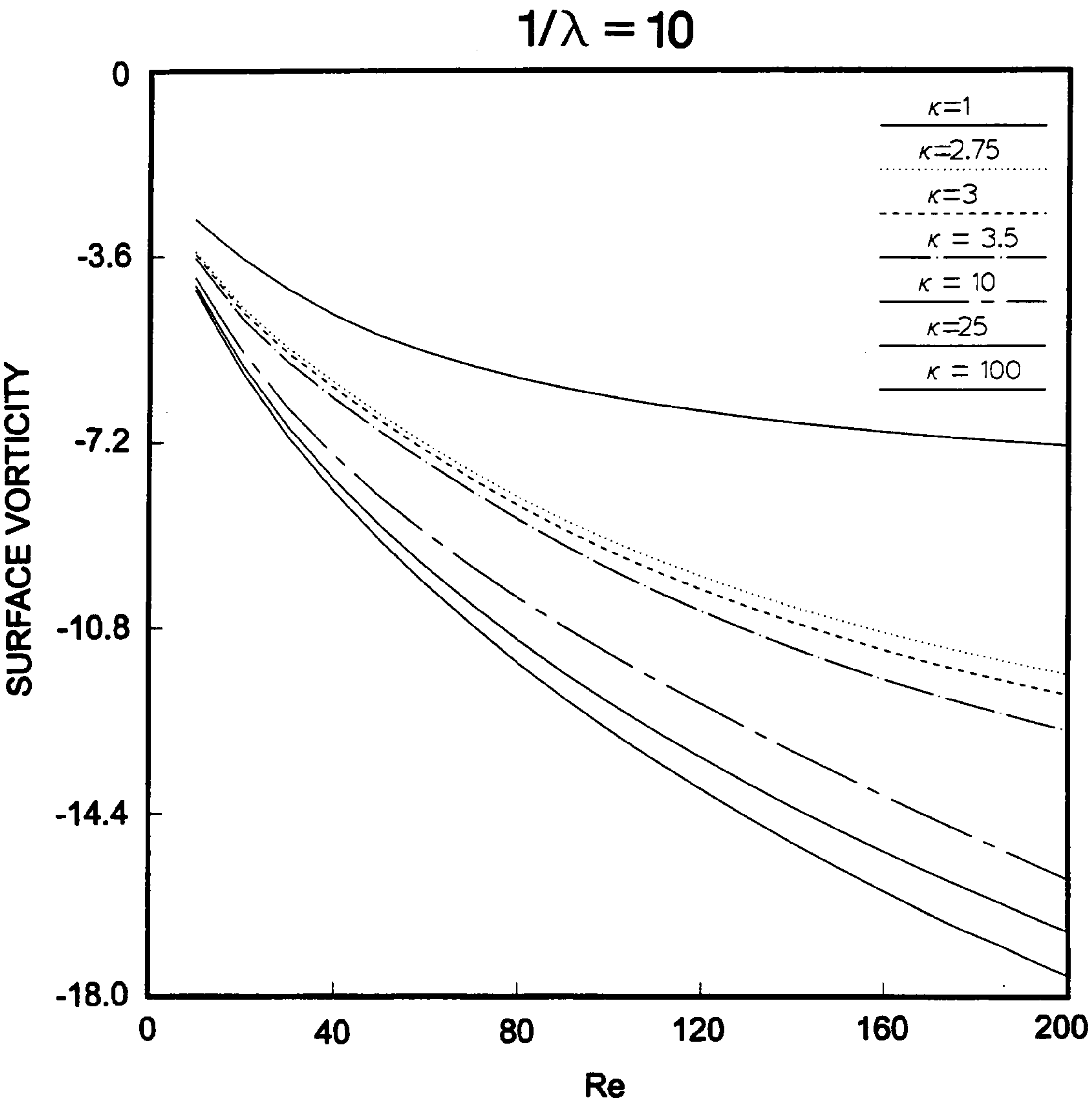

Figure 4.12. Variation of the maximum value of the vorticity of the ambient fluid on the surface of a fluid sphere with Reynolds number for several values of the viscosity ratio. Here $1/\lambda = 10$.

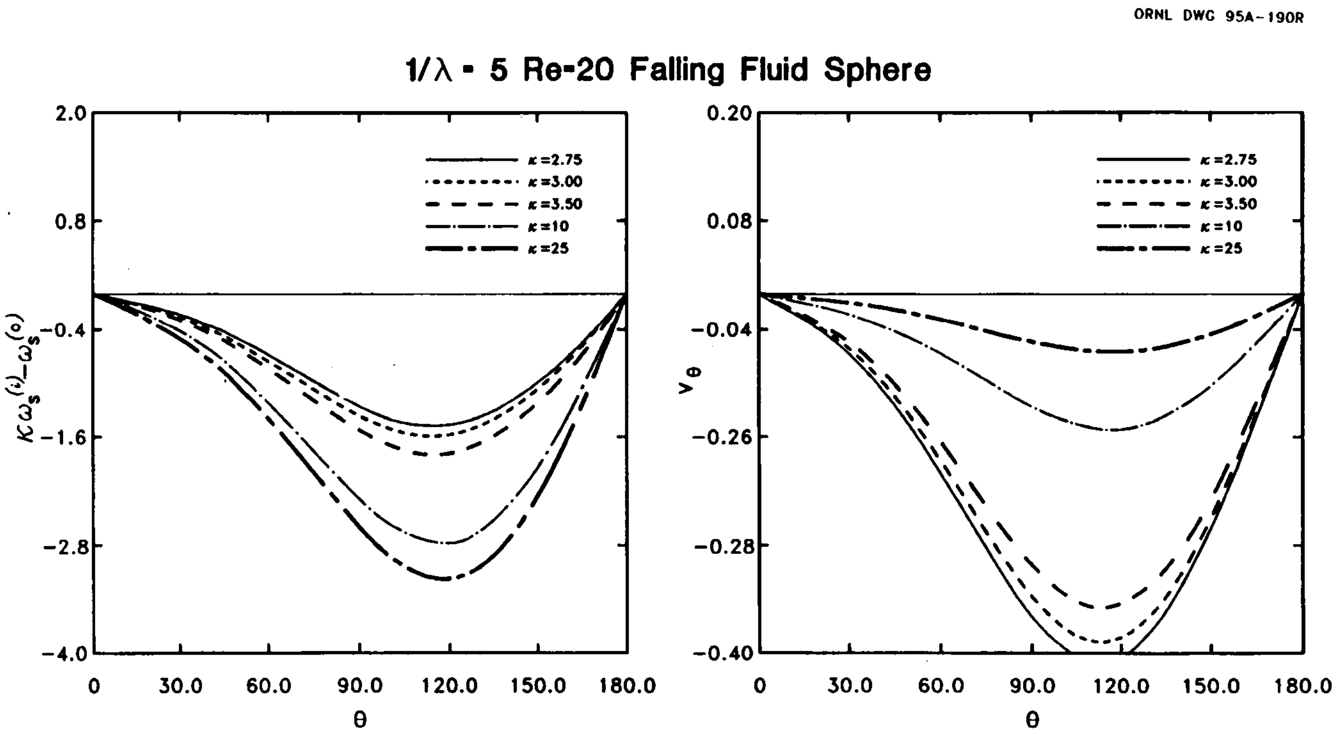

Figure 4.13. Variation of (a) the viscosity weighted vorticity difference and (b) the tangential velocity with meridional angle θ on the surface of a fluid sphere for several values of the viscosity ratio. Here $\frac{1}{\lambda} = 5$ and $Re = 20$.

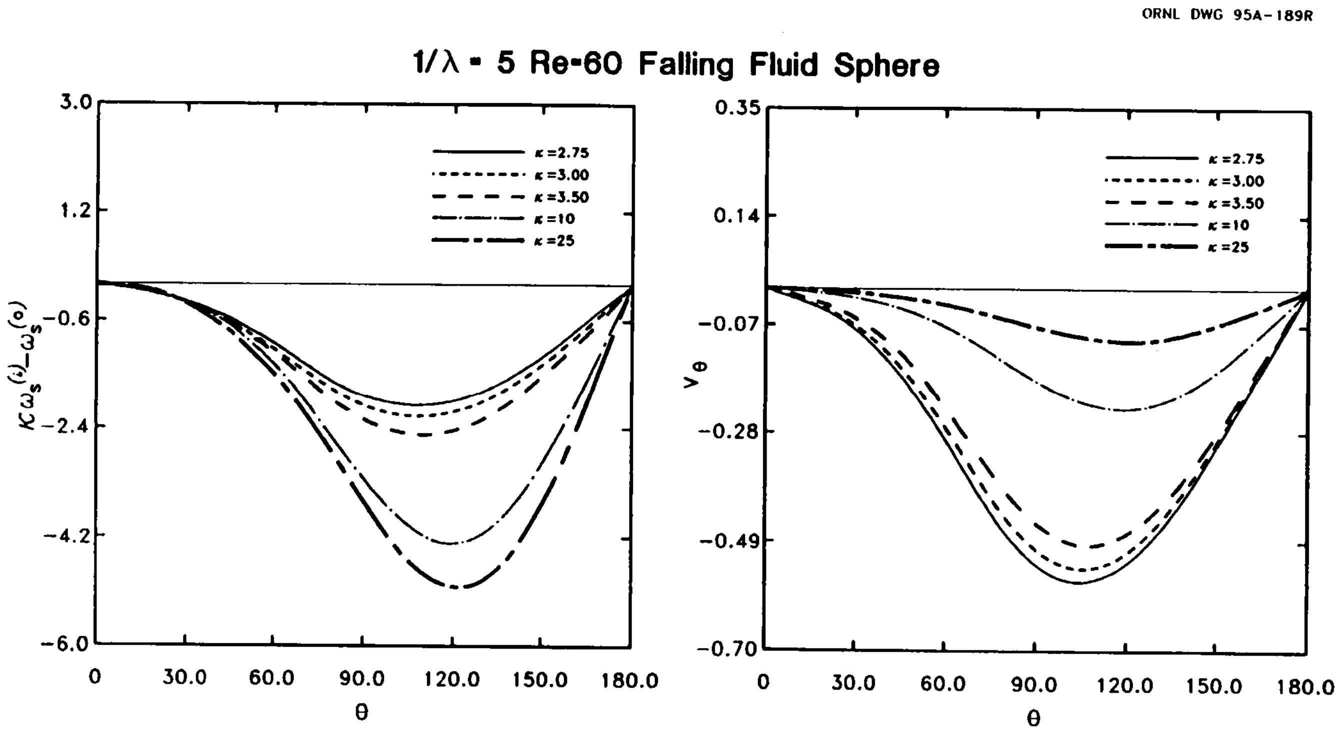

Figure 4.14. Variation of (a) the viscosity weighted vorticity difference and (b) the tangential velocity with meridional angle θ on the surface of a fluid sphere for several values of the viscosity ratio. Here $\frac{1}{\lambda} = 5$ and $Re = 60$.

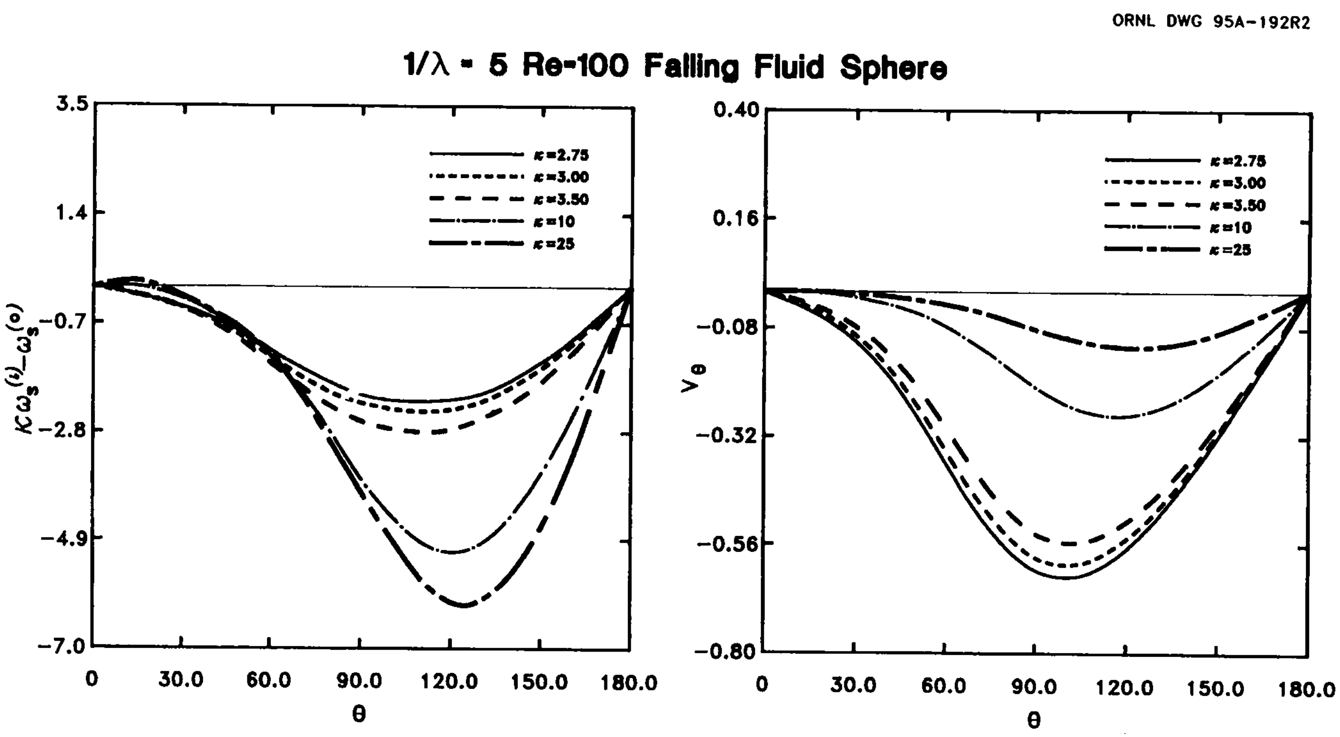

Figure 4.15. Variation of (a) the viscosity weighted vorticity difference and (b) the tangential velocity with meridional angle θ on the surface of a fluid sphere for several values of the viscosity ratio. Here $\frac{1}{\lambda} = 5$ and $Re = 100$.

the drop.

A question that has remained incompletely answered from past computational studies is the effect of $Re^{(i)}$ on the flow inside the drop. Many of these studies computational studies (see, e.g., Oliver and Chung 1985, 1987) have assumed that constant values of drag over a range of $Re^{(o)}$ and constant $Re^{(i)}$ implies that the internal flow structure remains invariant as $Re^{(o)}$ increases. To evaluate the effect of increasing fluid inertia over viscous forces on flow structure in both inside and outside the spherical drop, Figure 4.16 shows the effect of Re and κ on the magnitude of the strength of the inner and outer vortices, $|\psi^{(i)}|_{max}$ and $|\psi^{(o)}|_{max}$. Although the strength of the inner vortex increases as Re increases while holding κ fixed, $|\psi^{(i)}|_{max}$ varies insignificantly for Reynolds numbers exceeding about 40. Moreover, whereas the strength of the outer vortex increases with Re for $\kappa = 10, 100$, $|\psi^{(o)}|_{max}$ reaches a maximum and then decreases for $\kappa = 3.5, 5$. It is noteworthy that the wake disappears as Reynolds number exceeds a certain value for $\kappa = 3.5$ but it persists beyond $Re = 250$ for $\kappa = 5$. In the latter case, the wake would presumably disappear once the Reynolds number becomes large enough since wake strength is a decreasing function of Re when Re is sufficiently large.

Further insight into the behavior of the wakes is provided in Figure 4.17, which shows the variation of the length of the wake exterior to the drop as a function of Re. Figure 4.17 makes plain that at a fixed value of Re, the higher the ratio of the viscosity of the drop to that of the ambient fluid the longer is the wake outside the sphere. For the two lowest values of κ shown in Figure 4.17, that the wake length is maximized at some value of Re and decreases thereafter accords with the results of vortex strength presented in Figure 4.16.

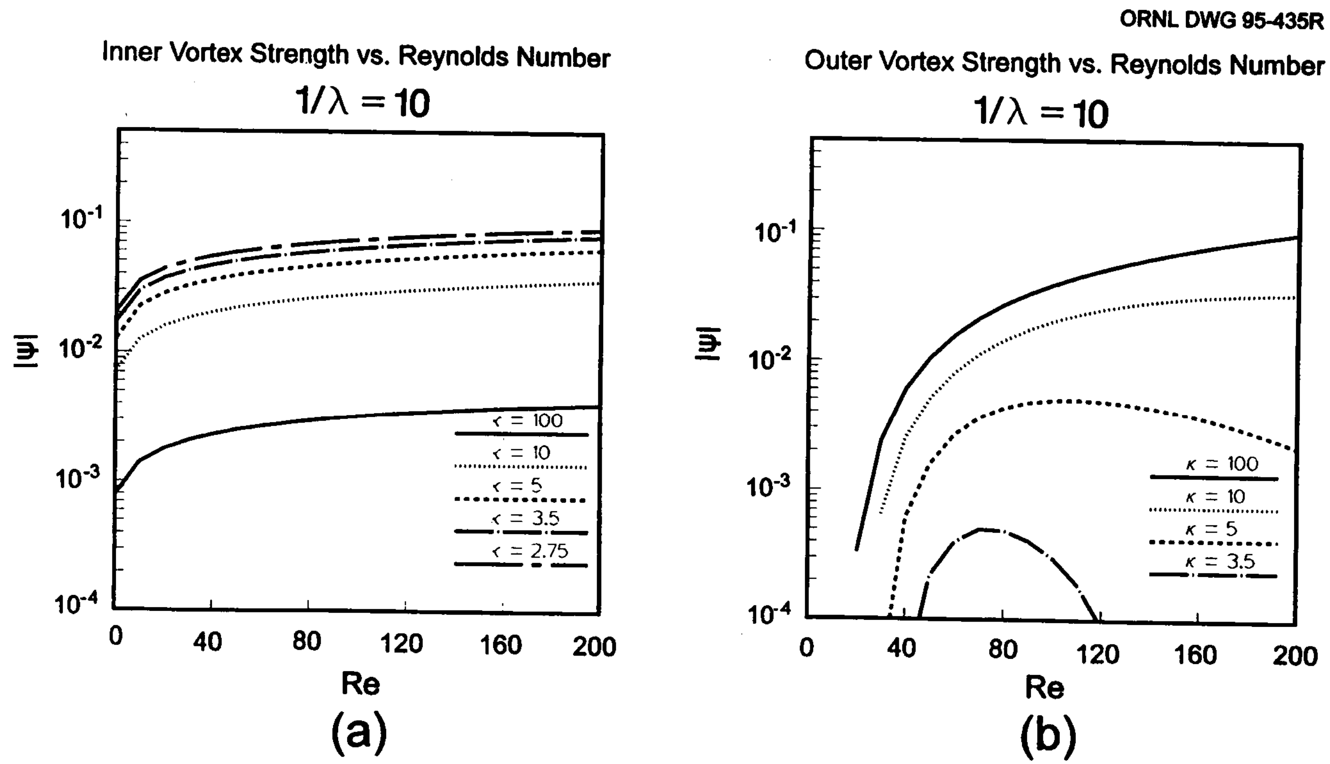

Figure 4.16. Variation of the absolute value of the streamfunction (a) inside and (b) outside the sphere with Reynolds number for several values of the viscosity ratio. Here $\frac{1}{\lambda} = 10$.

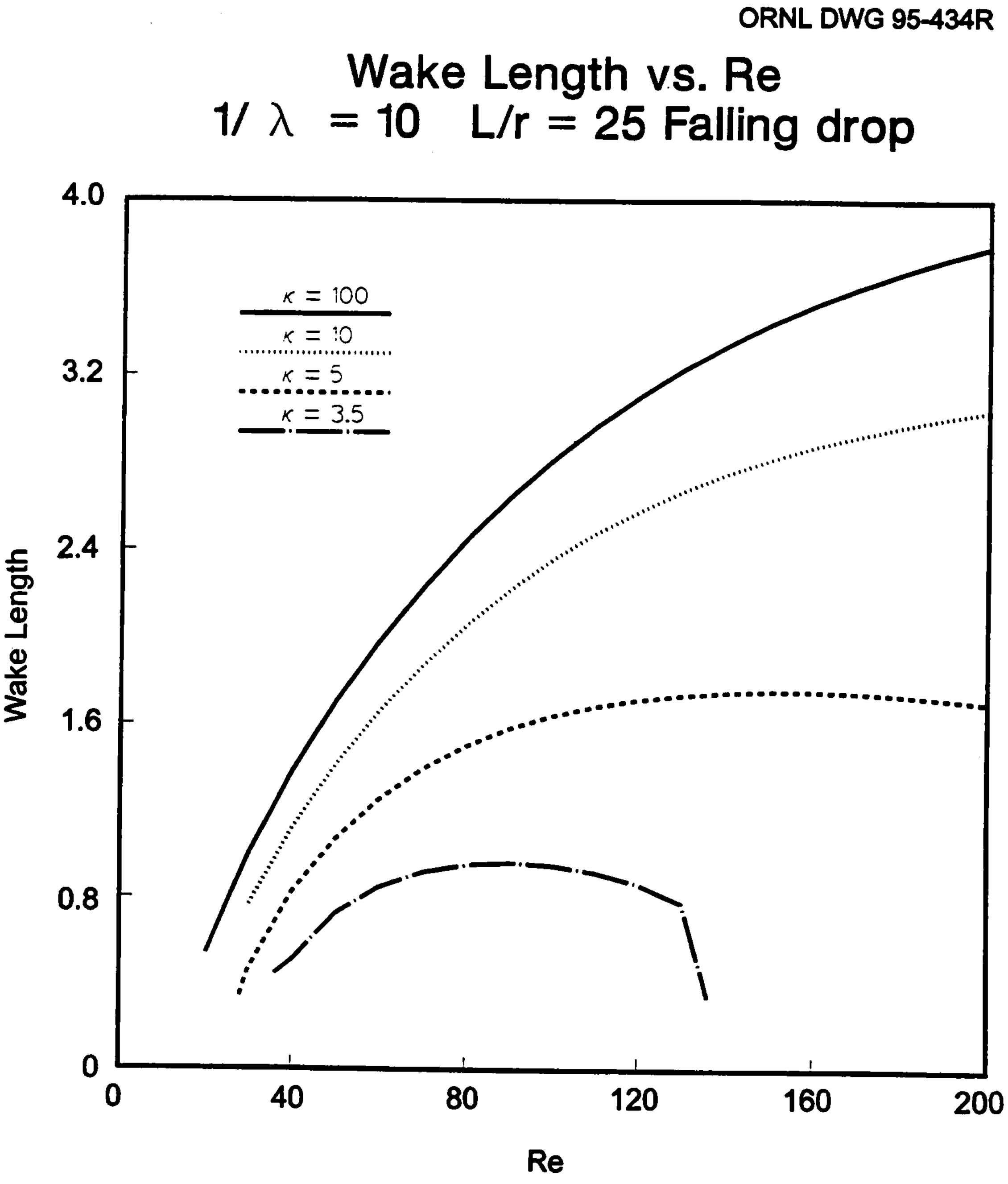

Figure 4.17. Variation of wake length with Reynolds number for several values of the viscosity ratio. Here $\frac{1}{\lambda} = 10$.

4.3.2 Drag data for a fluidized sphere

Figure 4.18 compares values of the drag force on a fluidized sphere in a tube computed by finite element analysis when $Re = 0$ with the correlation of Haberman and Sayre (1958) which is valid under conditions of creeping flow. The data points denote computational results while the continuous curves correspond to Haberman and Sayre's correlation. The excellent agreement between the computational results and Haberman and Sayre's correlation over three orders of magnitude of change in κ for several values of $\frac{1}{\lambda}$ is a testament to the accuracy of computational results reported in this work. Also, that the computed value of the drag increases as the tube radius decreases accords with extremum principles well known in Stokes flow (Kim and Karrila, 1991).

Figures 4.19 and 4.20 show the variation of the computed drag with Reynolds number for fluidized droplets in tubes of different dimensionless tube radii, $\frac{1}{\lambda}$ of 5 and 10, to examine the range of Re over which the creeping flow assumption is valid. In both figures, the computed drag has been normalized by the value of the drag on a sphere in an infinite expanse of ambient fluid under conditions of creeping flow (Hadamard 1911, Rybczynski 1911), F_{H-R}, so as to make clearer the effect of the tube radius on the drag. Of course, the drag ratio will exceed 1 for all tubes and approach 1 as $\frac{1}{\lambda} \rightarrow \infty$. Were the creeping flow assumption to hold at $Re \neq 0$, each of the curves shown in Figures 4.19 and 4.20 would be horizontal lines, i.e. have zero slope. When $\frac{1}{\lambda} = 5$, Figure 4.19 shows that the creeping flow assumption holds well up to a Reynolds number of 1 for all values of κ. When the dimensionless tube radius is increased to $\frac{1}{\lambda} = 10$, Figure 4.20 shows that the creeping flow assumption holds well up to $Re \approx 0.7$. These

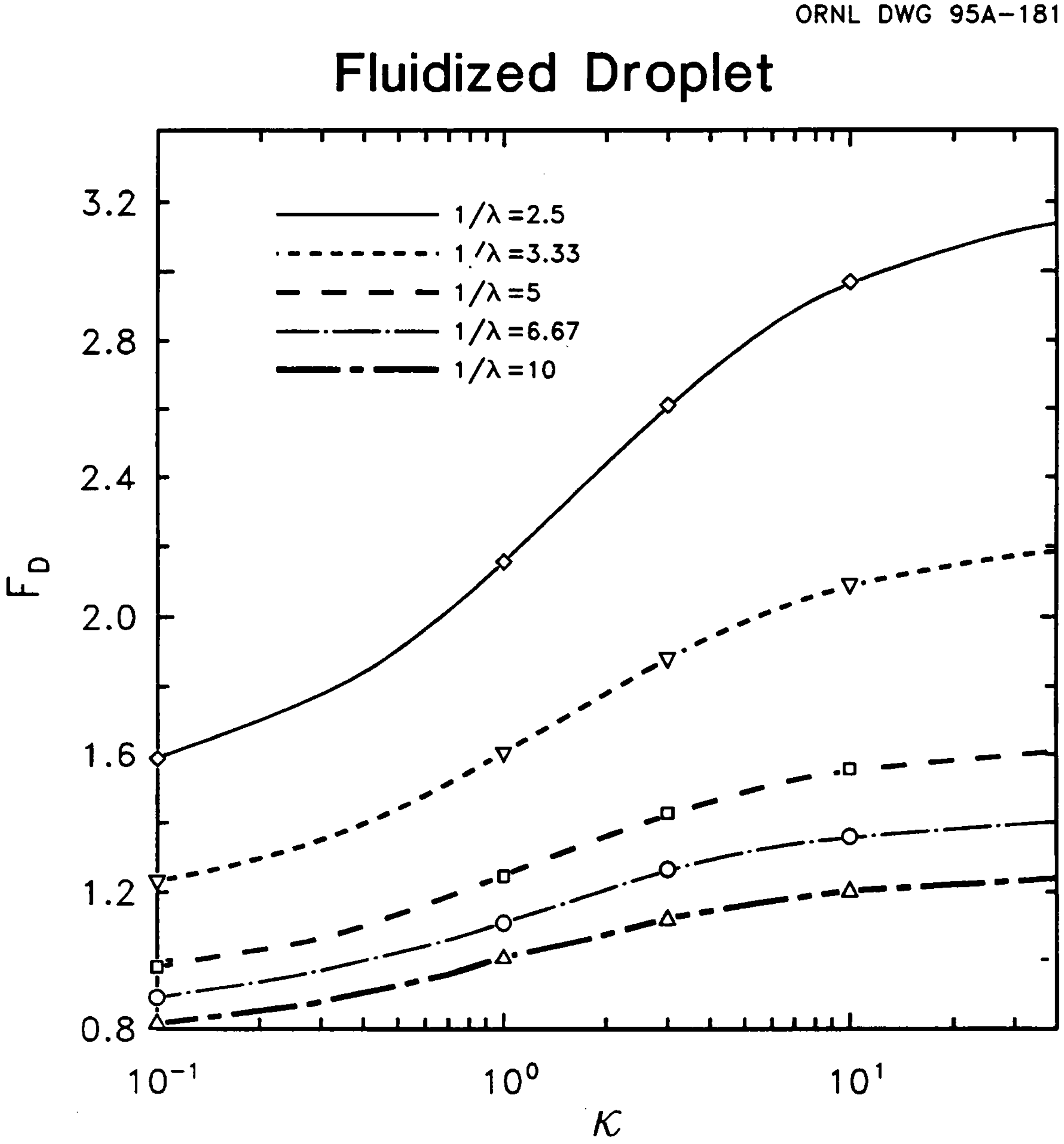

Figure 4.18. Comparison of Galerkin/finite element predictions of the drag on a fluidized droplet to the correlation due to Haberman and Sayre (1958). Here $Re = 0$.

ORNL DWG 95A-182R

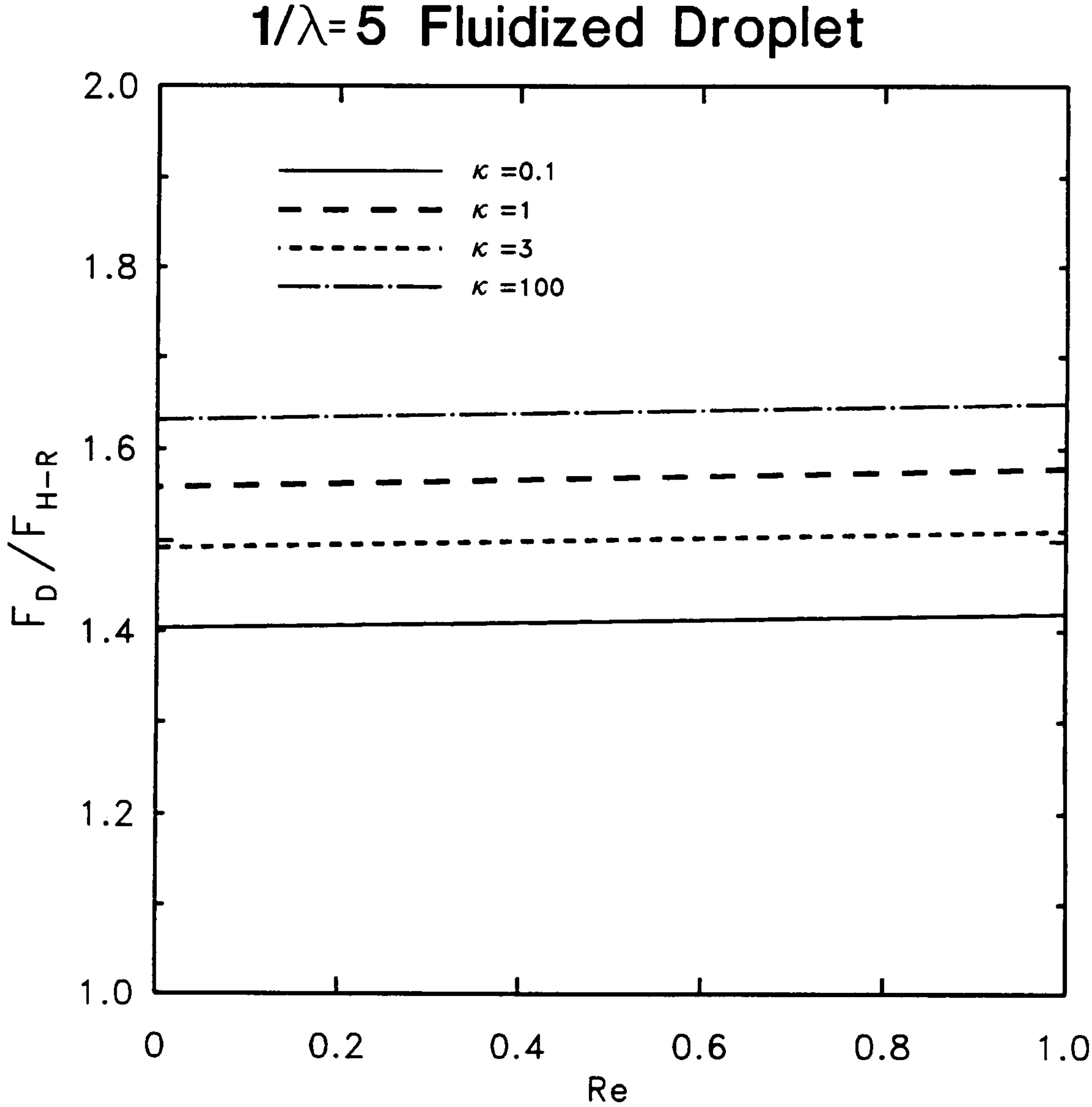

Figure 4.19. Drag correction for a fluidized drop in low Reynolds number flow: ratio of the actual drag to the drag computed from the Hadamard-Rybczynski solution (Hadamard 1911, Rybczynski 1911) for a fluid sphere in an unbounded fluid. Here $\frac{1}{\lambda} = 5$.

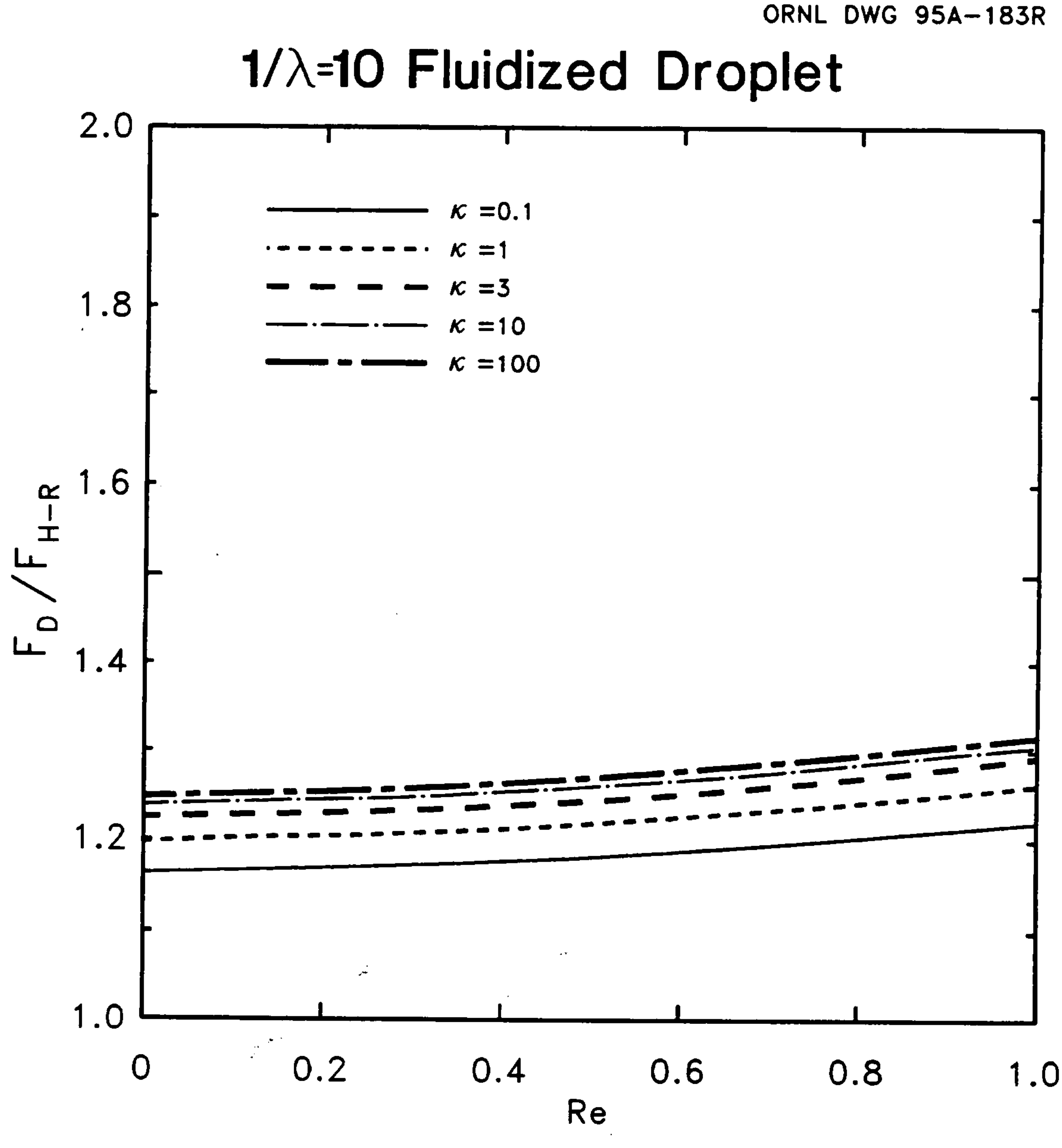

Figure 4.20. Drag correction for a fluidized drop in low Reynolds number flow: ratio of the actual drag to the drag computed from the Hadamard-Rybczynski solution (Hadamard 1911, Rybczynski 1911) for a fluid sphere in an unbounded fluid. Here $\frac{1}{\lambda} = 10$.

results accord with earlier ones reported on the role played by the tube wall in suppressing effects associated with finite inertia.

Based on the computations reported in this work and other calculations that were carried out, a new correlation for drag on a fluidized sphere has been developed which is based on modification of the Haberman and Sayre(1958) solution for creeping flow:

$$\frac{F_D}{F_{H-R}} = (1 + 0.05488 Re^{(1.2905 - 0.07529 \ln Re)})$$
$$\left[\frac{1 - \frac{2}{3}\frac{\kappa}{\kappa+\frac{2}{3}}\lambda^2 - 0.20217\frac{\kappa-1}{\kappa+\frac{2}{3}}\lambda^5}{1 - K\frac{\kappa+\frac{2}{3}}{\kappa+1}\lambda + 2.0865\frac{\kappa}{\kappa+1}\lambda^3 - 1.7068\frac{\kappa-\frac{2}{3}}{\kappa+1}\lambda^5 + 0.72603\frac{\kappa-1}{\kappa+1}\lambda^6}\right], \quad (4.15)$$

where $K = 1.358 + 0.7486 e^{-0.07836 Re}$. It is noteworthy that the form of equation (4.15) was chosen so that in the limit as $\kappa \to \infty$, it reduces to a correlation that has been proposed recently for solid spheres (Wham *et al.* 1995).

The results of drag calculations from parametric studies in Re for values of $0.1 \leq \frac{1}{\lambda} \leq 0.2$ and $0 \leq Re \leq 100$ are plotted in Figure 4.21 along with the predictions of correlation (4.15). The diagonal (ordinate = abscissa) represents perfect agreement between the new correlation and the computed results. The lines on either side of the diagonal indicate ±10% deviation between the computational values and the values predicted by (4.15). The data points are the computational results from this work. Small (large) values of drag are indicative of large (small) diameter tubes and/or low (high) values of Reynolds number.

4.3.3 Drag data for a falling sphere

Figure 4.22 compares values of the drag force on a falling sphere in a tube computed by finite element analysis when $Re = 0$ with the correlation of Haberman and Sayre (1958) which is valid under conditions of creeping flow. The data

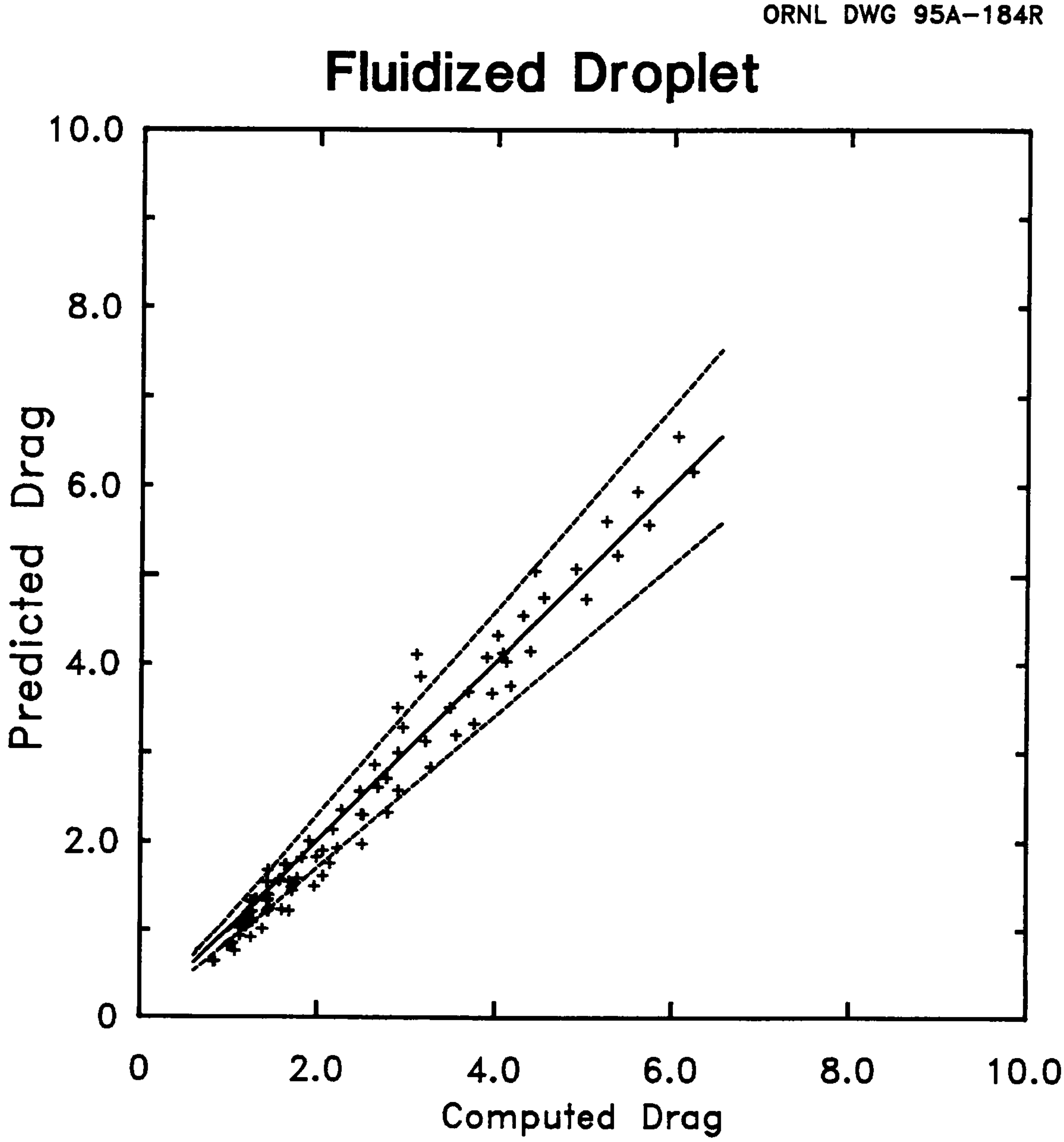

Figure 4.21. Comparison of Galerkin/finite element predictions of the drag on a fluidized sphere in a tube to those of the new correlation (4.15).

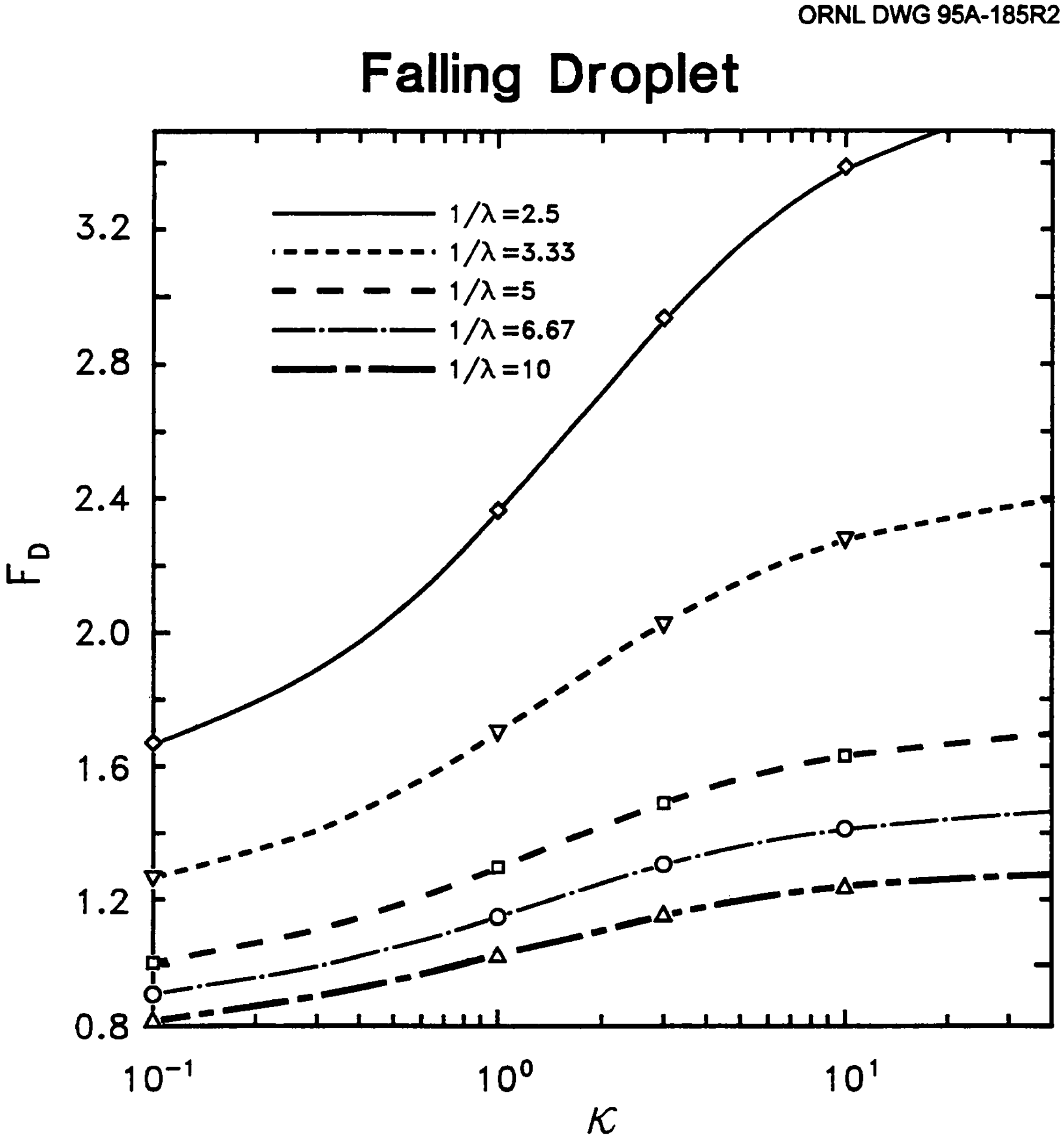

Figure 4.22. Comparison of Galerkin/finite element predictions of the drag on a falling droplet to the correlation due to Haberman and Sayre (1958). Here $Re = 0$.

points denote computational results while the continuous curves correspond to Haberman and Sayre's correlation. Once again, the excellent agreement between the computational results and Haberman and Sayre's correlation over three orders of magnitude of change in κ for several values of $\frac{1}{\lambda}$ is further evidence to the accuracy of computational results reported in this work.

Figures 4.23 and 4.24 show the variation of the computed drag with Reynolds number for falling droplets in tubes of different dimensionless tube radii, $\frac{1}{\lambda}$ of 5 and 10, to determine the range of Re over which the creeping flow assumption holds well. As in Figures 4.20 and 4.21, the computed drag in Figures 4.23 and 4.24 has been normalized by the value of the drag on a sphere in an infinite expanse of ambient fluid under conditions of creeping flow (Hadamard 1911, Rybczynski 1911). These results also demonstrate the role played by the tube wall in suppressing effects associated with finite inertia.

Based on the computations reported in this work and others, a new correlation for drag on a falling sphere has been developed which is based on modification of the Haberman and Sayre(1958) solution for creeping flow:

$$\frac{F_D}{F_{H-R}} = (1 + 0.03708Re^{(1.514-0.1016\ln Re)}) \left[\frac{1 - 0.7587\frac{\kappa-1}{\kappa+\frac{2}{3}}\lambda^5}{1 - K\frac{\kappa+\frac{2}{3}}{\kappa+1}\lambda + 2.0865\frac{\kappa}{\kappa+1}\lambda^3 - 1.7068\frac{\kappa-\frac{2}{3}}{\kappa+1}\lambda^5 + 0.72603\frac{\kappa-1}{\kappa+1}\lambda^6}\right], \quad (4.16)$$

where $K = 0.6628 + 1.458e^{-0.05635Re}$. Equation (4.16) too reduces to a correlation that has been proposed recently for solid spheres falling in a tube (Wham *et al.* 1995) in the limit as $\kappa \to \infty$.

The results of drag calculations from parametric studies in Re for values of $0.1 \leq \frac{1}{\lambda} \leq 0.2$ and $0 \leq Re \leq 100$ are plotted in Figure 4.25 along with the

ORNL DWG 95A-186R

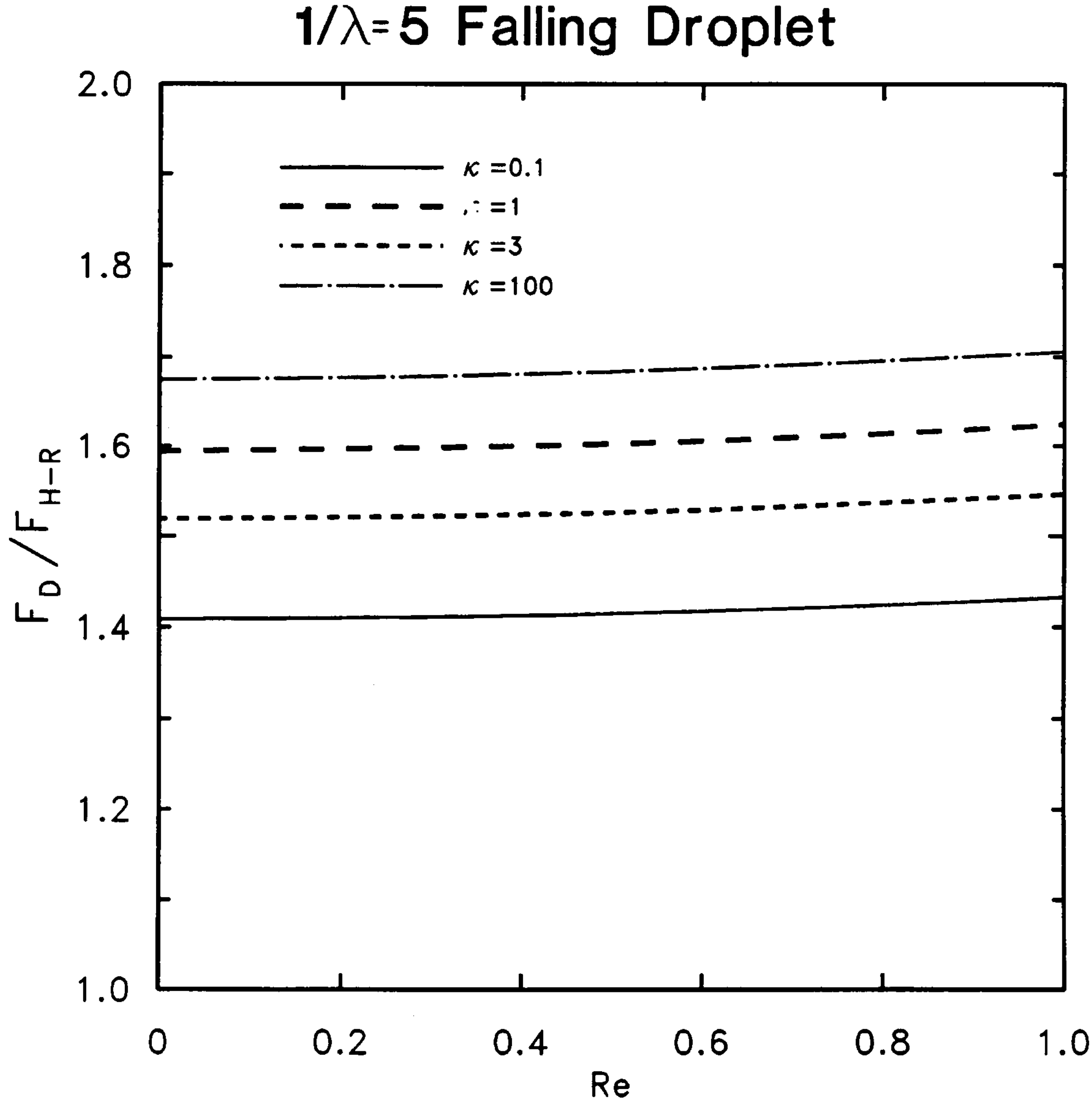

Figure 4.23. Drag correction for a falling drop in low Reynolds number flow: ratio of the actual drag to the drag computed from the Hadamard-Rybczynski solution (Hadamard 1911, Rybczynski 1911) for a fluid sphere in an unbounded fluid. Here $\frac{1}{\lambda} = 5$.

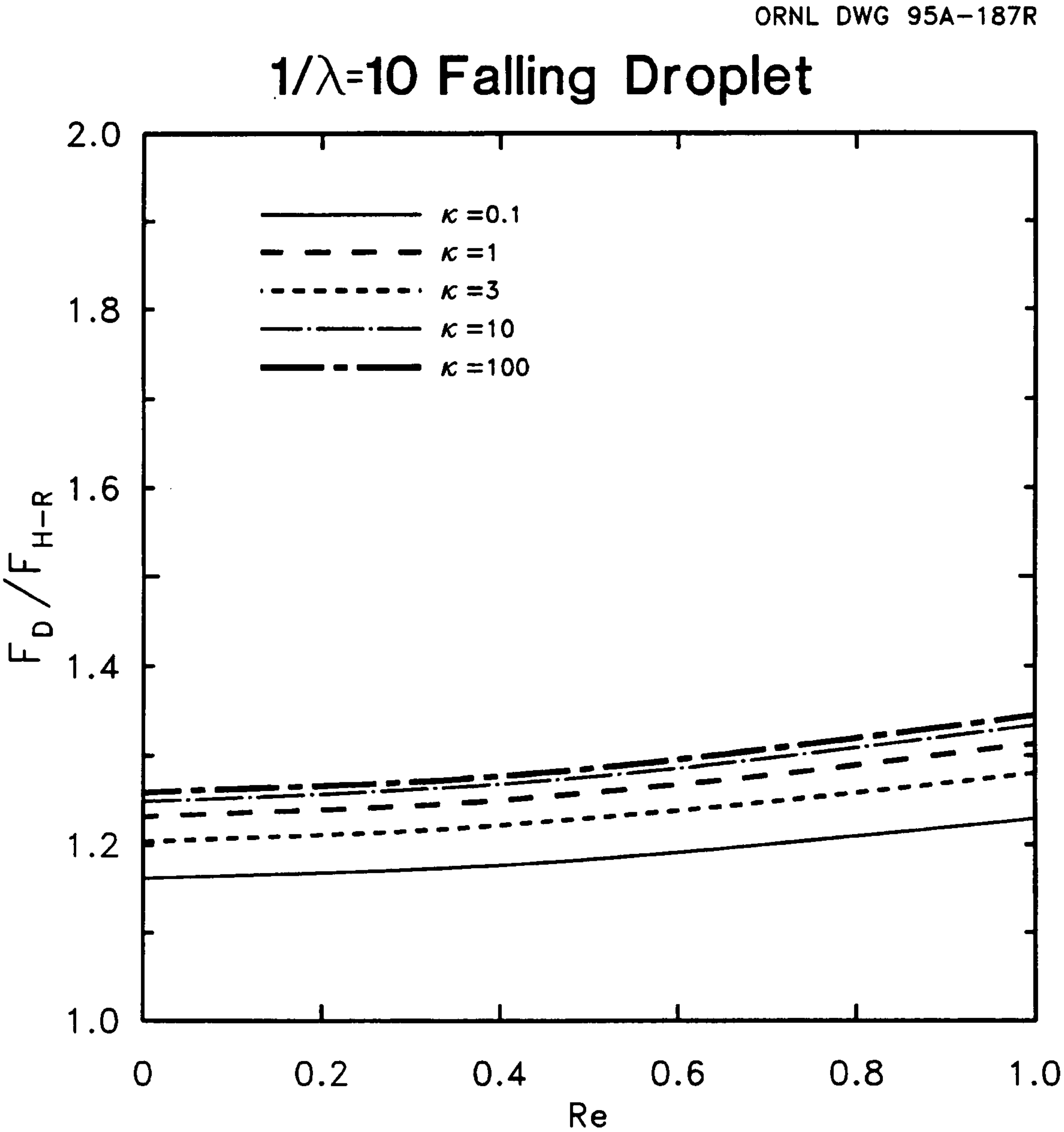

Figure 4.24. Drag correction for a falling drop in low Reynolds number flow: ratio of the actual drag to the drag computed from the Hadamard-Rybczynski solution (Hadamard 1911, Rybczynski 1911) for a fluid sphere in an unbounded fluid. Here $\frac{1}{\lambda} = 10$.

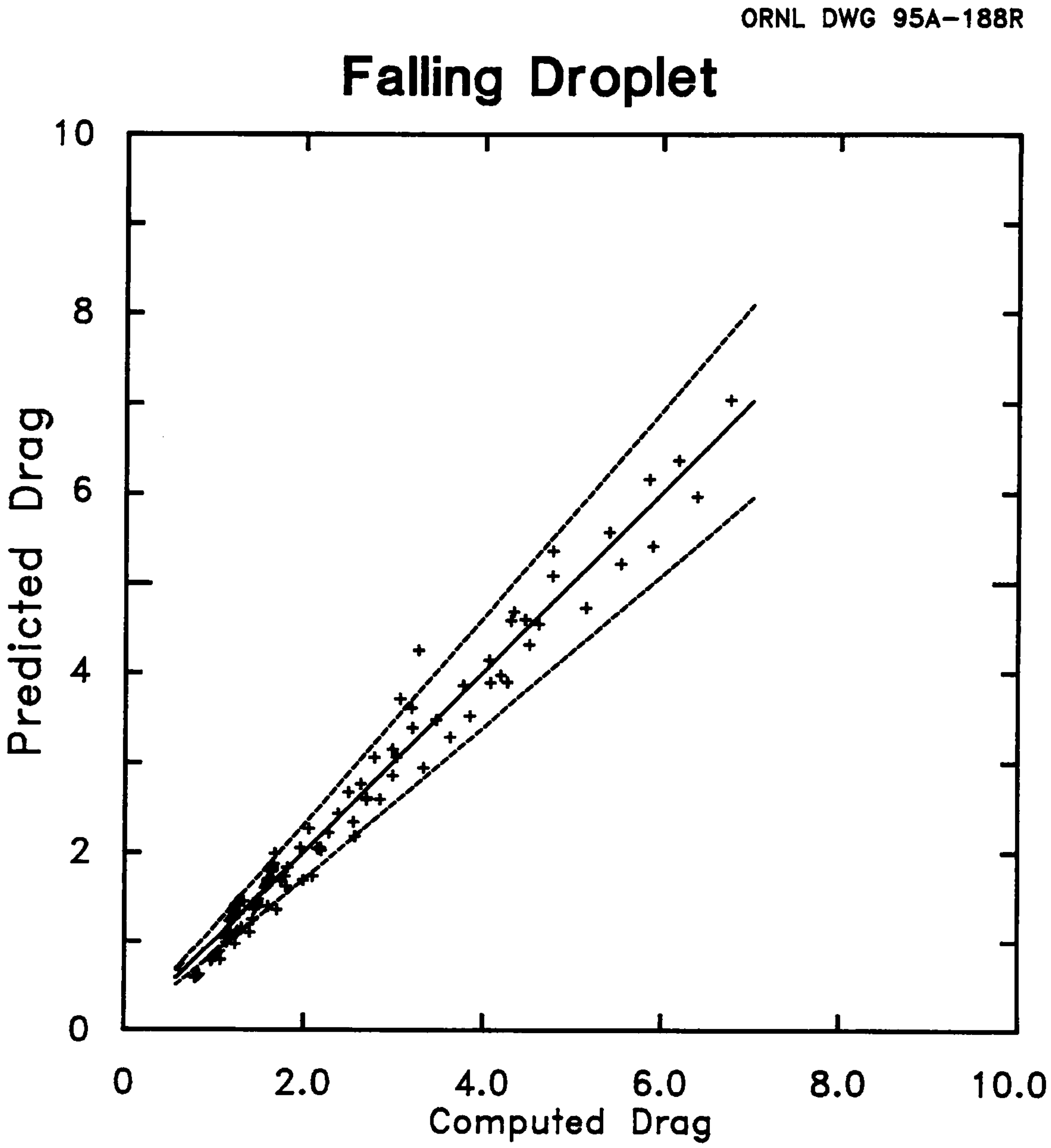

Figure 4.25. Comparison of Galerkin/finite element predictions of the drag on a falling sphere in a tube to those of the new correlation (4.16).

predictions of correlation (4.16). The diagonal represents perfect agreement between the new correlation and the computed results. The lines on either side of the diagonal indicate $\pm 10\%$ deviation between the computational values and the values predicted by (4.16). Figure 4.25 shows that good agreement exists between the computational results and the new correlation.

4.4. CONCLUSIONS

According to the foregoing results, for certain values of the ratio of the viscosity of the drop to that of the ambient fluid recirculating wakes that appear behind the drops for $Re = Re_c^{(1)} < 100$ can disappear when $Re = Re_c^{(2)} < 100$, where $Re_c^{(1)} < Re_c^{(2)}$ and the value of $Re_c^{(2)}$ is much lower than that previously reported by Dandy and Leal (1989). This finding further reinforces those of Leal and coworkers and others that such wakes have nothing to do with boundary layer separation, which is a large Reynolds number phenomenon. It has also been found that the presence of a tube wall in the fluidized and falling sphere problems can suppress the formation of recirculating wakes. Equally noteworthy is the discovery that when the viscosity ratio $\kappa \geq 10$, detached eddies can attach to the rear of the drop when the Reynolds number is sufficiently large. The attachment of a previously detached eddy was previously unknown (see, e.g., Rivkind and Ryskin 1976) and is demonstrated in this work by (i) the appearance of a third vortex inside the drop at its rear face, (ii) a change in sign in the tangential component of the velocity v_θ along the sphere surface, and (iii) a change in sign in the weighted vorticity difference $\kappa\omega_s^{(i)} - \omega_s^{(o)}$ evaluated along the sphere surface.

New correlations have also been presented in this work for drag on both fluidized and falling spheres that are applicable over a more expanded range of parameters than previously available. Moreover, these correlations account for both the presence of a tube wall and effects of finite fluid inertia.

Although the present results are important in their own right, they also provide without any adhoc approximations the velocity fields that are needed in computing mass transfer to and from fluid spheres in tubes. Unfortunately, such mass transfer studies have often been made in the past without the availability of accurate flow field data.

CHAPTER 5

EFFECT OF WAKE STRUCTURE ON MASS TRANSFER AT FINITE REYNOLDS NUMBER

Solvent extraction is a critical processing step in the recovery and purification of many products of significant commercial value. It is used in applications as widely different as the recovery of metals (Treybal, 1963; Treybal, 1968), the processing of nuclear fuels (Benedict *et al.*, 1981), and the purification of radioisotopes (Freiser, 1959; Weaver, 1974). Solvent extraction processes are generally limited by the rate at which mass is transferred from one liquid phase to a second liquid phase. Calculation of mass transfer rates is necessary for design of extraction processes and contacting devices.

An often used physical model to calculate rates of mass transfer in solvent extraction processes is that of a drop which is dispersed in a continuous liquid phase. Solute present in the drop transfers across the interface into the continuous phase or solute present in the continuous phase transfers into the drop. Developing a better understanding of this mass transfer process than that currently available is a goal of this chapter.

A key objective in the theory of mass transfer is to predict the amount of solute that transfers into or out of a drop in a given period of time. In the case of mass transfer from the drop into the continuous phase, the extraction of solute out of the drop can be quantified by the fractional extraction, F:

$$F = \frac{\tilde{c}_0^{(i)} - \overline{\tilde{c}^{(i)}}}{\tilde{c}_0^{(i)} - H\tilde{c}^{(o)}|_{\tau=\infty}} \text{ , where } H = \frac{\tilde{c}^{(i)}|_{\tau=\infty}}{\tilde{c}^{(o)}|_{\tau=\infty}} . \tag{5.1}$$

Here the initial concentration of solute in the drop is uniform and is denoted by $\tilde{c}_0^{(i)}$ while the initial concentration of solute in the continuous phase, which is also uniform, is denoted by $\tilde{c}_0^{(o)}$. In equation (5.1), $\tilde{c}^{(i)}|_{r=\infty}$ denotes the equilibrium concentration of solute in the drop while $\tilde{c}^{(o)}_{r=\infty}$ denotes the equilibrium concentration of solute in the continuous fluid. The ratio of these two quantities, H, is the distribution coefficient. Additionally, $\tilde{c}^{(o)}|_{r=\infty}$ denotes the concentration of solute at $r = \infty$ and is taken to be constant. Finally, $\overline{\tilde{c}^{(i)}}$ refers to the average concentration of solute in the drop at time t which is obtained by integrating the instantaneous concentration $\tilde{c}^{(i)}$ over the drop volume V, viz. $\overline{\tilde{c}^{(i)}} \equiv \frac{\int \tilde{c}^{(i)}\,dV}{\int dV}$. In (5.1) and elsewhere in this work, superscripts "$^{(o)}$" and "$^{(i)}$" stand for the ambient fluid and the drop, respectively.

Many correlations to estimate rates of mass transfer exist in the literature and Chapter 3 of Clift *et al.* (1978) gives a review of such correlations. Unfortunately, many of the existing correlations that can be used to estimate rates of mass transfer are based on significant simplifications such as

(1) the resistance to mass transfer is significant in one phase and that in the second phase is essentially zero, an approximation that allows the second phase to be dropped from further consideration;

(2) convection dominates diffusion or vice versa, an approximation that often allows solution by analytical techniques of 19th century mathematical physics; and

(3) velocity fields needed for determining the convective contribution to mass transport can be approximated with ones calculated on the basis of creeping flow conditions, an approximation that is without foundation.

In most practical situations, the resistance to mass transfer may be significant in both phases and the analysis must take this into account by solving the appropriate material balances in both phases. Additionally, most commercial devices rely on convection to increase the rate of mass transfer. The relative importance of convective transport to diffusive transport is measured by the Peclet number, $Pe \equiv \frac{U_\infty a}{\mathcal{D}}$, where U_∞ is a characteristic velocity, a is the undeformed radius of the drop, and $\mathcal{D}$ is the diffusivity of the solute. When mass transfer by diffusion is indefinitely large compared to that by convection, then $Pe \rightarrow 0$. If, on the other hand, the convective mode of mass transfer is indefinitely large compared to the diffusive mode, then $Pe \rightarrow \infty$. However, in most cases the Peclet number is neither 0 nor ∞. Moreover, as shown in the previous two chapters, flow fields obtained under the assumption of creeping flow cannot describe the real velocity fields in and around drops unless inertial effects are negligible. The velocity field to the rear of the drop may exhibit a recirculating eddy or a wake and the drop may periodically shed this wake if the Reynolds number is high enough or the drop is oscillating.

The experimental literature provides several examples where wake shedding from drops has been shown to significantly increase the rate of mass transfer (Garner and Tayeban, 1960; Angelo, 1966; Rose and Kinter, 1966; Brunson and Wellek, 1969). Worst of all, some past analyses of mass transfer to and from drops have adopted simultaneously two or more of the above three approximations.

There exist two approximate and simple but celebrated analyses of mass transfer from spherical drops that are placed in an infinite expanse of continuous fluid. They have been compared with both theories and experiments even for situations in which the conditions of the actual theory or experiment do not match those of the approximate theories. In both of these approximate theories, all the mass transfer resistance is taken to be inside the spherical drop. The concentration at the interface is taken to be equal to the concentration at $r = \infty$ which implies that mass transfer from the drop surface to the bulk of the liquid takes place instantaneously (i.e., the time increment is zero - - a physical impossibility). Furthermore, both theories take all of the solute to be inside the drop for $t \leq 0$. The first of these theories assumes that mass transfer is due entirely to diffusion and the second one assumes that mass transfer is purely convective. Newman (1931) investigated mass transfer out of a drop when $Pe = 0$ and showed that the fractional extraction, as a function of dimensionless time, $\tau \equiv t\mathcal{D}/a^2$, is given by

$$F = 1 - \frac{6}{\pi^2}\sum_{n=1}^{\infty}\frac{1}{n^2}\exp\left(-n^2\pi^2\tau\right). \tag{5.2}$$

Kronig and Brink (1951) investigated mass transfer out of a drop in the limit as $Pe \rightarrow \infty$ and assumed that the flow inside the droplet is described by the well known creeping flow solution due to Hadamard (1911) and Rybczynski (1911) (see, e.g., Chapter 4). They thereby showed that the fractional extraction is given by:

$$F = 1 - \frac{3}{8}\sum_{n=1}^{\infty}A_n^2\exp(-16\lambda_n\tau). \tag{5.3}$$

Kronig and Brink give the first two coefficients A_n and λ_n in their paper. Once a value of $\tau \geq 0.01$ is reached, the first term of the series dominates the expression for the fractional extraction. It is noteworthy that both of these celebrated papers have sidestepped the difficult task of obtaining the velocity field by solving the Navier-Stokes system which, in contrast to the equation governing the transport of mass, is a set of highly nonlinear equations at finite Reynolds number (cf. Chapters 3 and 4).

The predictions of the Newman and the Kronig and Brink models have been compared to experimental measurements in the papers by Johnson and Hamielec (1960), Brounshtein *et al.* (1970), Streicher and Schugerl (1977), and Schugerl and Dimain (1980). These authors have shown that most of the experimental data is bracketed by the Newman solution, valid when $Pe = 0$, and the Kronig and Brink solution, valid when $Pe \rightarrow \infty$. However, in many instances these approximate models disagree with the laboratory measurements since the assumptions of no mass transfer resistance in the continuous phase, or $Pe \rightarrow 0$ or $Pe \rightarrow \infty$, or creeping flow conditions are not usually met in the experiments. Therefore, there is a need to develop accurate theoretical models to predict mass transfer rates from drops even when they are constrained to remain spherical in shape.

Garner and Tayeban (1960) have presented experimental data that indicate that oscillating drops have higher rates of mass transfer than non-oscillating drops. These authors have speculated that wake shedding allows better transport of solute between the droplet and the continuous phase, a point to which we return later on in this chapter. These authors have reasoned that the wake at the rear of the drop imposes yet another interfacial barrier to mass transfer since the solute must diffuse from the wake into the continuous phase.

Rose and Kintner (1966), among a long series of subsequent workers in the field, have chosen to ignore wake shedding and instead have developed a model for mass transfer from oscillating drops based on interfacial stretch. They have proposed that mass transfer occurs across a thin film near the interface where the oscillations cause the film to stretch and thereby increase the interfacial area. These authors have further claimed that oscillations also promote a high degree of mixing with the net result of a well mixed core with a uniform concentration of solute inside the drop.

Angelo *et al.* (1966) have also proposed that surface stretch is the primary reason for mass transfer enhancement from oscillating drops. These authors have used a slightly different approach from that of Rose and Kintner. Their model is based on the assumption that the oscillations of the surface give rise to new elements of the surface to contact the continuous phase since the surface area of the drop increases as it deforms from a sphere to a spheroid. Despite the differences in the models, Angelo *et al.* report that their model and that due to Rose and Kintner agree within about 15%.

Yet another model for mass transfer from oscillating drops is that due to Boyadzhiev *et al.* (1969) who suggest that a fudge factor R' be used to multiply of diffusivity so that $\mathcal{D}$ is replaced by $R'\mathcal{D}$, where R' is allowed to depend on the Reynolds number to take into account changes in the relative importance of convection to diffusion. Of course, a rational basis for predicting the functional form of R' does not exist and this theory too is based entirely on empiricism.

Despite the industrial importance of solvent extraction and the scientific interest in understanding the enhancement of mass transfer brought about by drop oscillations, a fundamentals-based approach to quantifying the effects of fluid convection on mass transfer has heretofore been lacking. The velocity field in and around a drop is unknown *a priori* and standard approximations for determining the flow such as the creeping flow assumption or the boundary layer approximation are limited to vanishingly small and very large Reynolds numbers, respectively (see, e.g., Batchelor 1967). Adoption of the creeping flow assumption at finite Reynolds numbers can be expected to lead to large errors in making mass transfer predictions since it does not allow for the appearance of a wake and previous portions of this thesis have shown that wakes can appear and disappear at relatively low values of the Reynolds number. Plainly, rigorously solving the unsteady mass balance at non-zero Peclet numbers and non-zero Reynolds numbers entails solving the Navier-Stokes equations for fluid flow and then using the velocity field that is thereby obtained in solving the mass balance equation.

Another difficulty in analyzing unsteady mass transfer with many approximate models is that they do not provide information on the concentration profiles in and around the drop at various stages of extraction. A better understanding of the interaction between fluid flow and mass transfer than that currently available requires that the concentration of the solute be known at each point in space for all time. Experimental techniques are unfortunately limited in furnishing such detailed concentration profiles since they generally measure bulk concentrations. Scott (1992) used experimental equipment similar to that described in Chapter 2 (c.f. Figure 2.1) to investigate mass transfer of a fluorescent dye out of a water drop into 2-ethyl-hexanol(2EH). Scott measured the bulk concentration of dye in the water drop as a function of time. However, limits on the experiments precluded determination of concentration as a function of position and the experiment failed to give data on the concentration of dye in the continuous phase. Scott described the finite solubility of water in the organic continuous phase as a significant problem and indicated that he had to develop special techniques to minimize competing transfer of water into the continuous phase. The problems described by Scott are not unique. Clift, et al.(1978) describe difficulties with evaluating experimental mass transfer data between different researchers due to differences in systems chosen for analysis, incomplete reporting of necessary data, effects of contaminants in the experimental systems, and problems associated with reproducing results between different laboratories. Fortunately, computational models of mass transfer can be developed which can determine the required solute concentration data much like the velocity field information obtained in Chapters 3 and 4. The parameters for computational models can be set explicitly and maintained so that the effects of the flow field can be seen without compromising the results due to problems with experimental design and technique.

Numerical methods have been used to solve the equations of mass transfer in situations in which the Peclet number is finite and the resistance to mass transfer in both phases is comparable. When the resistance to mass transfer is finite in both phases, the situation is referred to as the conjugate mass transfer problem. Unfortunately, many of these models are also limited in their applicability since they have adopted the Hadamard–Rybczynski solution for the flow in and around the drops (see, e.g., Ruckenstein, 1967; Abramzon and Borde, 1980; and Brignell, 1975). Moreover, many of these numerical solutions are plagued by additional problems. By way of example, for mass transfer from a spherical drop, Abramzon and Borde have used a numerical method based on the finite difference approximation that has been shown to be unconditionally unstable over part of the domain (Iyengar, 1982). This unstable discretization has later been adopted by Scott and Byers (1988) in their analysis of mass transfer to and from oscillating drops. Moreover, although analysis of a viscous free surface flow as an oscillating drop was a formidable task more than a decade ago, solving such problems has recently become almost routine (see, e.g., Basaran 1992). Without the availability of this recently developed computational machinery, Scott and Byers circumvented the difficult task of solving the Navier-Stokes system and superimposed two solutions — one describing the flow inside an oscillating inviscid spheroid and the other the flow past a viscous spherical drop (i.e., the Hadamard–Rybczynski solution) to approximate the flow in an oscillating drop. Unfortunately, because superimposing several solutions that individually satisfy the Navier-Stokes system is mathematically incorrect unless the Reynolds number is identically zero, the approach adopted by Scott and Byers is invalid in addition to the shortcomings of the numerical method used by these authors.

Not too surprisingly, there also exist solutions involving various degrees of sophistication to the closely related problem of heat transfer to and from drops. Especially noteworthy from the standpoint of the present thesis are the papers by Masliyah and Epstein (1970) and Masliyah (1971). These authors have reported that in the problem of heat transfer from a solid spheroid, the presence of a wake can produce significant changes in the heat transfer coefficient. More recently, Oliver and Chung (1990) examined the closely related problem of conjugate heat transfer from a fluid sphere over the parameter range Reynolds numbers between 0 and 50, viscosity ratios of 0 to 10^7, and ratios of thermal diffusivities of 0.01 to 3.0. Oliver and Chung concluded that fluid motion near the interface can have a significant effect on conjugate heat transfer. The analogies between mass transfer and heat transfer suggest that similar effects should be seen in the problem of conjugate mass transfer.

A major goal of this chapter is to use flow fields computed at values of the parameters appropriate to the problem under consideration as inputs into rigorous computations of transient mass transfer phenomena. To concentrate on the interaction between fluid convection and mass transfer, the problem of a deforming drop boundary is set aside and, in the spirit of earlier chapters on flow past solid and fluid spheres, attention is focused here on the prototypical problem of transient mass transfer from a spherical drop to an ambient fluid. Because such much transfer studies are carried out in finite sized containers in the laboratory (cf. Chapter 2), the drops in this chapter are placed in tubes of finite radii as in Chapters 3 and 4.

Section 5.1 presents the equations, initial conditions, and boundary conditions that govern mass transfer from a fluid sphere in a tube of finite radius. Section 5.2 outlines the Galerkin/finite element technique used for calculation of concentration profiles. Section 5.3 presents concentration profiles and mass transfer coefficients, among others, to build insights into the underlying phenomena. Section 5.4 discusses the relevance and relationship of this work to certain others and lays the groundwork for future studies based on the present analysis.

5.1 GOVERNING EQUATIONS, BOUNDARY CONDITIONS AND INITIAL CONDITIONS

The system is composed of a fluid sphere of radius a that is centrally located in a tube of radius d and is surrounded by an ambient fluid as shown in Figure 5.1. The sphere is either falling or is fluidized by an upflowing fluid in the tube. A solute is present in dilute concentration in both phases and is allowed to transport between the drop and the ambient fluid. Each binary fluid phase is isothermal and the temperature of the two phases are equal. No chemical reactions take place inside or outside the drop. The fluid interior to the sphere is

ORNL DWG 94A–423

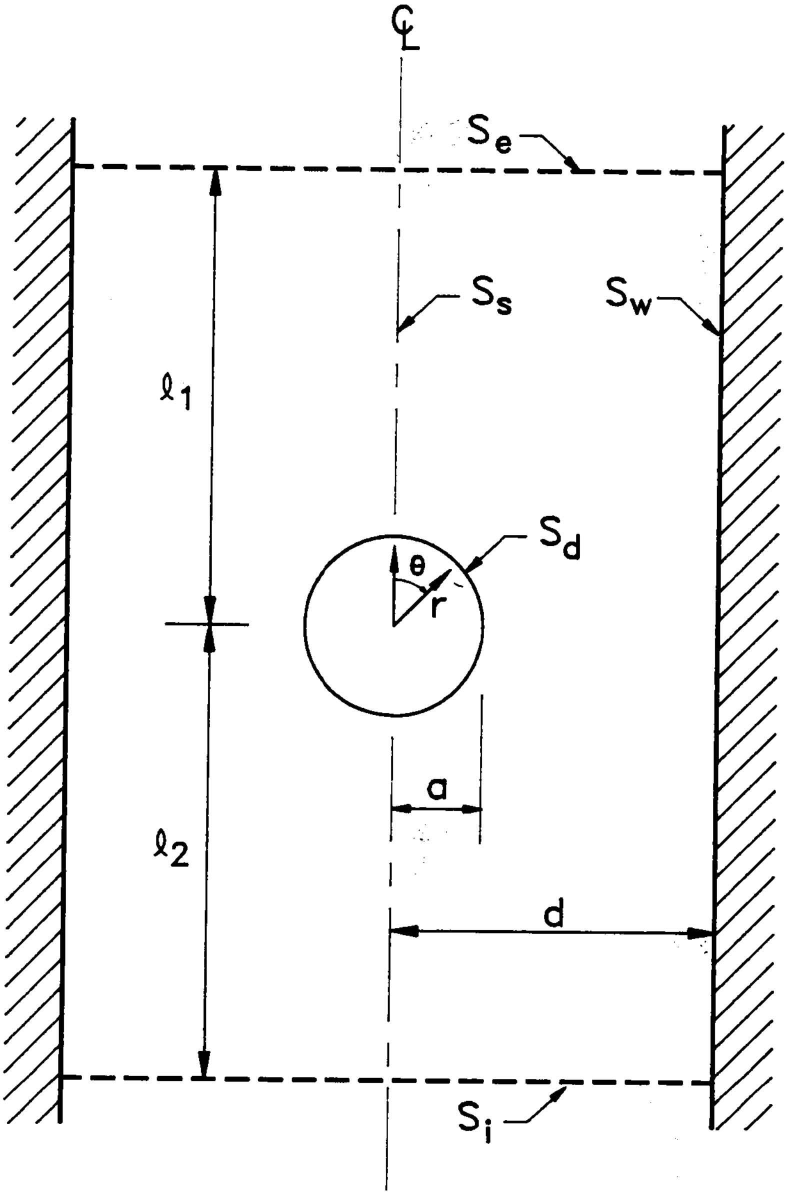

$$\lambda \equiv a/d$$

$$L_1 = \ell_1/a, \; L_2 = \ell_2/a$$

Figure 5.1. Axisymmetric mass transfer from a fluid drop: definition sketch

Newtonian and has constant viscosity $\mu^{(i)}$ and constant density $\rho^{(i)}$. The fluid exterior to the sphere is also Newtonian and has constant viscosity $\mu^{(o)}$ and constant density $\rho^{(o)}$. The diffusivity of the solute in both phases is constant and is given by $\mathcal{D}^{(i)}$ inside the drop and by $\mathcal{D}^{(o)}$ outside it.

Under these conditions, the velocity fields inside and outside the drop, $\underline{\tilde{\mathbf{v}}}^{(i)}$ and $\underline{\tilde{\mathbf{v}}}^{(o)}$, respectively, are identical to those presented in Chapter 4. The transport of the solute in both phases is then governed by the following unsteady mass balance (see, e.g., Bird *et al.*, 1960):

$$\frac{\partial c^{(l)}}{\partial \tau} + Pe^{(i)}\underline{\mathbf{v}}^{(l)} \cdot \nabla c^{(l)} - \mathcal{R}^{(l)}\nabla^2 c^{(l)} = 0\,. \tag{5.4}$$

In equation (5.4), which is already dimensionless, "l" refers to either "i" or "o." In this chapter, a variable with a tilde is dimensional and the same variable without a tilde is dimensionless. Equation (5.4) has been made dimensionless by defining dimensionless time as $\tau \equiv \frac{t\mathcal{D}^{(i)}}{a^2}$, dimensionless concentration inside the drop as $c^{(i)} \equiv \frac{\tilde{c}^{(i)}}{HC}$, and dimensionless concentration outside the drop as $c^{(o)} \equiv \frac{\tilde{c}^{(o)}}{C}$, where C is a characteristic concentration that depends on the problem. Moreover, the Peclet number $Pe^{(i)}$, which is based on the diffusivity of the solute inside the drop, is defined as $Pe^{(i)} = \frac{U_\infty a}{\mathcal{D}^{(i)}}$, where U_∞ is a characteristic velocity, and the coefficient $\mathcal{R}^{(l)}$ is such that $\mathcal{R}^{(i)} = 1$ and $\mathcal{R}^{(o)} = \mathcal{D}^{(o)}/\mathcal{D}^{(i)}$. In the case of a falling sphere, the flow is quiescent sufficiently far upstream and downstream of the sphere, and U_∞ is the steady translational velocity of the falling sphere. In the case of a fluidized sphere, U_∞ is the maximum velocity of the ambient fluid at large distances from the drop center of mass. Finally, $\underline{\mathbf{v}}^{(l)}$ represents the velocity vectors inside and outside the drop with components $v_r^{(l)}$ and $v_\theta^{(l)}$ in a spherical coordinate system (r, θ) based at the center of the sphere, where r is the radial coordinate and θ is the meridional angle (cf. Figure 5.1).

Equation (5.4) inside and outside the drop is to be solved subject to the boundary conditions:

$$\begin{aligned}
S_i : &\quad c^{(o)} = c^{(o)}_{S_i} \\
S_w : &\quad \underline{\mathbf{n}} \cdot \nabla c^{(o)} = 0 \\
S_e : &\quad \underline{\mathbf{n}} \cdot \nabla c^{(o)} = 0 \\
S_d : &\quad c^{(i)} = c^{(o)} \quad \text{and} \quad \underline{\mathbf{n}} \cdot \nabla c^{(i)} = \frac{1}{H} \frac{\mathcal{D}^{(o)}}{\mathcal{D}^{(i)}} \underline{\mathbf{n}} \cdot \nabla c^{(o)} \quad .
\end{aligned} \tag{5.5}$$

In (5.5) $\underline{\mathbf{n}}$ is a unit vector normal to the surfaces bounding the flow domain. In words, (5.4) states that the concentration of the solute is a constant $c^{(o)}_{S_i}$ at the inlet S_i to the flow domain, the mass flux vanishes at the tube walls S_w, infinitely far from the drop the gradient of the concentration normal to the outlet boundary S_e tends to zero, the concentration profile is axially symmetric about the centerline S_s of the tube, and equilibrium exists and no mass accumulates at the sphere surface S_d.

Equation (5.4) is solved subject to initial conditions that the concentration both inside and outside the drop is a specified function of position $\underline{\mathbf{r}}$:

$$c^{(l)}(\tau = 0, \underline{\mathbf{r}}) = c^{(l)}_0(\underline{\mathbf{r}}) \, . \tag{5.6}$$

5.2 GALERKIN/FINITE ELEMENT ANALYSIS

Boundary conditions imposed on both concentration and fluid velocity at the inlet and outlet planes S_i and S_e, respectively, are approached as one moves indefinitely far from the drop center-of-mass. However, because it is impracticable to solve a problem on an infinite domain on a computer, here the outlet and inlet planes are placed at (dimensionless) distances $L_1 \equiv l_1/a$ and $L_2 \equiv l_2/a$ downstream and upstream of the sphere. In this chapter, the axisymmetric material balances (cf. Equation (5.4)) for the dispersed and the continuous fluids are then solved everywhere within the rectangular region $V = \{(x, z) : 0 \leq x \leq D\,, L_1 \leq z \leq -L_2\}$ where $z \equiv r\cos\theta$, $x \equiv r\sin\theta$, and $0 \leq \theta \leq \pi$, and $D \equiv d/a$ is the dimensionless radius of the tube (see Figure 4.1).

The problem domain is tessellated into a set of N_r times N_θ nonuniformly spaced quadrilateral elements, where N_r is the number of elements in the r-direction and N_θ is the number of elements in the θ-direction. Figure 5.2 shows a sample grid or tessellation used in this chapter which contains 4,992 elements and 20,383 nodes.

The unknown concentration field is expanded in a standard set of biquadratic basis functions (Strang and Fix, 1973) ϕ^i as:

$$c^{(l)}(\underline{\mathbf{r}}) = \sum_{i=1}^{I} c_i^{(l)} \phi^i(\underline{\mathbf{r}}) \quad . \tag{5.7}$$

In (5.7) $\underline{\mathbf{r}} \in V$ is the position vector of a point with coordinates (r, θ) and $I \equiv (2N_r + 1)(2N_\theta + 1)$ is the total number of nodes in the finite element mesh, and also equals the total number of concentration unknowns. The coefficients $c_i^{(l)}$ are the unknown coefficients in the finite element approximation of the concentration and $c^{(l)} = (c_1^{(l)}, c_2^{(l)}, \ldots, c_I^{(l)})$ is a vector representing all the unknowns.

The Galerkin weighted residuals of the unsteady mass balance or the transient

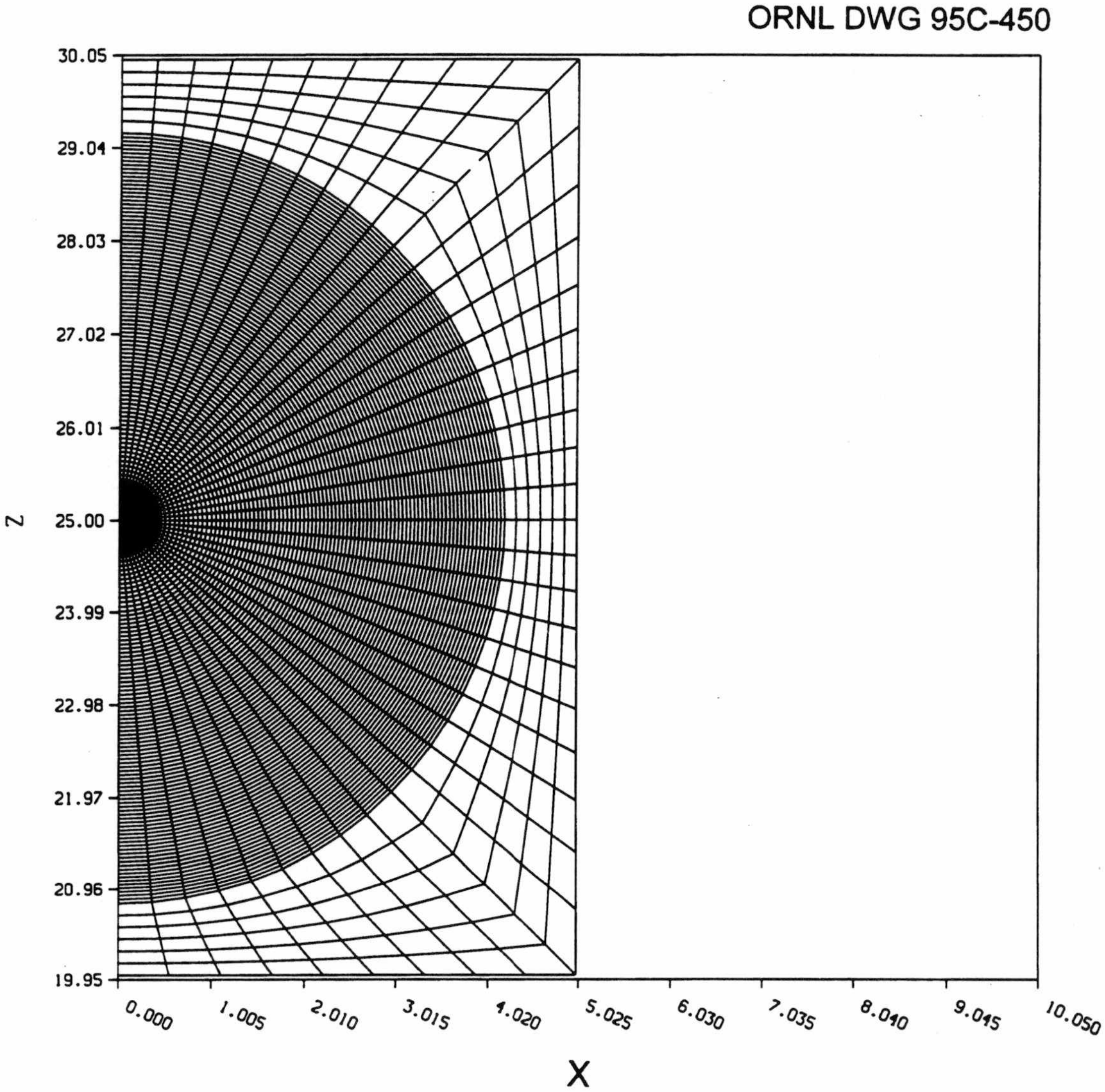

Figure 5.2. Example of a computational grid used in this work.

convection-diffusion (5.4) after integrating the diffusion term by parts is:

$$R_i^{(l)} = \int_{V^{(l)}} \left[\phi^i \left(\frac{\partial c^{(i)}}{\partial \tau} + Pe^{(i)} \underline{\mathbf{v}}^{(l)} \cdot \nabla c^{(l)} \right) + \mathcal{R}^{(l)} \nabla \phi^i \cdot \nabla c^{(l)} \right] dV -$$

$$\int_{S^{(l)}} \phi^i \, \mathcal{R}^{(l)} \, \underline{\mathbf{n}} \cdot \nabla c^{(l)} \, dS = 0, \quad i = 1, \ldots, I \tag{5.8}$$

where $V^{(l)}$ stands for the region inside or outside the drop and $S^{(l)}$ stands for the drop surface such that the unit normal points out of the drop when $l = i$ and into the drop when $l = o$.

Special care must be taken for those nodes that lie along the interface, i.e. the drop surface. The boundary condition on the concentration along the drop surface at (5.5) imply that the dimensionless concentration is continuous along the interface. Therefore, it suffices to use a single concentration node at each mesh point along the interface. The weighted residual equation appropriate for the concentration at each interface node is obtained by adding $\frac{1}{H}$ times the mass balance equation for the outer fluid to the mass balance for the inner fluid. The two surface integral terms that arise from the contributions to the residual from each side of the interface then cancel when use is made of the boundary condition of the continuity of mass flux given in (5.5).

The Galerkin/finite element weighted residuals form a set of time-dependent ordinary differential equations (ODEs). The set of ODEs is solved by a fully implicit predictor-corrector method with automatic time step-size control. Time derivatives are discretized at the pth time step as follows:

$$\frac{\partial c^{(l)}}{\partial \tau}(\tau_p) = \frac{\beta_1}{\Delta \tau_p}[c^{(l)}(\tau_p) - c^{(l)}(\tau_{p-1})] + \beta_2 \frac{\partial c^{(l)}}{\partial \tau}(\tau_{p-1}) \tag{5.9}$$

where $\beta_1 = 1$ and $\beta_2 = 0$ with the backward difference (BD) approximation and $\beta_1 = 2$ and $\beta_2 = -1$ with the trapezoidal rule (TR) . With the first-order accurate BD approximation, a forward difference (FD) predictor is used. With the second-order accurate TR, however, an Adams-Bashforth predictor is employed. The system of algebraic equations the results, in contrast to ones encountered when solving the Navier-Stokes system, is linear and is solved by a direct method using Gaussian elimination.

Initial conditions used need not satisfy exactly the governing equations and the boundary conditions. Four backward difference steps with a fixed time step-size are thus taken to provide the necessary smoothing before the trapezoid rule is used (Luskin and Rannacher, 1982). Thereafter, time step-size is chosen adaptively by requiring the norm of the time truncation error $|d_p|$ to be equal to a prescribed value ξ (Gresho *et al.*, 1979):

$$\Delta\tau_{p+1} = \Delta\tau_p\left(\frac{\xi}{|d_p|}\right)^{\frac{1}{3}} \quad . \tag{5.10}$$

Here a relative error of $\xi = 0.1\%$ is used and an estimate of the local time truncation error is provided by the L_∞ norm of the residuals at the previous time step.

The algorithm was programmed in FORTRAN and the resulting code was run on an IBM RS6000-580H workstation at the Oak Ridge National Laboratory using the arrow solver developed by Thomas and Brown (1987) albeit in the banded matrix solver mode. Moreover, because concentration boundary layers are much thinner than momentum boundary layers at high Peclet and Reynolds numbers, meshes on which the convection-diffusion equations are solved should be finer than ones on which the Navier-Stokes systems are solved. This capability too has been built into the present code.

The correctness of the code was demonstrated by running it under conditions simulating well known standards from the literature including limiting theoretical results and comparing its predictions with those of several well known correlations, as discussed in the paragraphs to follow.

5.3 RESULTS

Section 5.3.1 reports computational results for mass transfer from a solid sphere and compares the predictions made by the new code to well known results for mass transfer by diffusion under both steady and unsteady conditions. Section 5.3.2 compares results obtained with the new code for mass transfer from fluid spheres under unsteady conditions to the well known correlations of Newman (1931) and Kronig and Brink (1951). New results on the problem of conjugate mass transfer from fluid spheres are reported in Section 5.3.3.

5.3.1 Diffusion from a solid sphere

(a) Steady state diffusion

Calculations have been carried out to compare theoretical predictions made with the new algorithm in situations in which mass transfer occurs by diffusion under steady state conditions. In other words, the time derivative and the Peclet number are both set to zero in (5.4). The goals here are to compare computational predictions against an exact analytical solution and to examine the effects of so-called synthetic (Bixler, 1982; Basaran, 1984; Novy *et al.*, 1990, 1991) and/or asymptotic boundary conditions on solution accuracy.

The test problem is one in which mass transfer occurs from a sphere that is maintained at a uniform and constant composition of unity while placed in an infinite expanse of ambient fluid. Thus, (5.4) is solved only in the ambient fluid and the tube walls that are generally present are moved infinitely far from the sphere. Moreover, the concentration of solute goes to zero at infinity in this test problem. It is well known that the Sherwood number, which is the ratio of mass transfer velocity to diffusive velocity (Cussler , 1984) given as $Sh \equiv \frac{\mathcal{K}a}{D}$ equals 2 in this situation (Bird *et al.* 1960). With the Galerkin/finite element method or any other method for solving partial differential equations, the domain outside the spherical drop cannot extend out to infinity but instead must be truncated at some "large" but finite distance r_∞ from the sphere center-of-mass. The radius of this imaginary spherical boundary must be large enough so that the numerical solution is not too sensitive to changes in the value of r_∞, i.e. the boundary condition that strictly applies at infinity is not a bad approximation of reality at a finite distance from the drop center-of-mass. However, the value of r_∞ must also be small enough so that discretization error can be kept below a desired level without having to use an unreasonably large number of elements or mesh points. In practice, r_∞ is determined by computational experiments that test the sensitivity of computed solutions to changes in the value of r_∞ and the amount of physical memory available to the user on the computer on which the simulations are being carried out.

The discretized version of this problem is formulated with three different types of boundary conditions at r_∞. The first is a boundary condition of the first kind or a Dirichlet boundary condition which sets the value of concentration at r_∞ to zero, viz. $c^{(o)}|_{r=r_\infty} = 0$. From the nature of Laplace's equation, it is expected that the slope of the concentration also approach zero as $r \to \infty$. Therefore, the second condition implemented is a boundary condition of the second kind or a Neumann boundary condition which sets the value of the derivative of the concentration or the mass flux to zero, viz. $\underline{\mathbf{n}}\cdot\nabla c|_{r=r_\infty} = 0$. viz. $c^{(o)}|_{r=r_\infty} = 0$. From the nature of Laplace's equation, it is expected that the slope of the concentration also approach zero as $r \to \infty$. Therefore, the second condition implemented is a boundary condition of the second kind or a Neumann boundary condition which sets the value of the derivative of the concentration or the mass flux to zero, viz. $\underline{\mathbf{n}} \cdot \nabla c^{(o)}|_{r=r_\infty} = 0$. The third type of boundary condition implemented here follows once again from the nature of Laplace's equation. This is a boundary condition of the third kind or a Robin boundary condition where the mass flux is set to be proportional to the concentration at r_∞, viz. $\underline{\mathbf{n}}\cdot\nabla c^{(o)}|_{r=r_\infty} = -\frac{kc^{(o)}}{r}|_{r=r_\infty}$. Previous work by Basaran (1984) on the distribution of electrostatic potential fields around charged drops has shown that the Robin boundary condition yields the most accurate solution as compared to Dirichlet and Neumann boundary conditions at the same computational cost (in other words, with the same number of unknowns) while requiring a value of r_∞ on the order of 10. Table 5.1 shows that large errors in concentration profiles and hence Sherwood number are the consequence when the Dirichlet boundary condition is used and the synthetic boundary r_∞ is placed too close to the drop. Indeed, the error in Sh is 25% when $r_\infty = 5$. With the Robin boundary condition, however, the error is 0.1% with $r_\infty = 10$. By contrast, at the same value of r_∞, the error in the solution with the Dirichlet boundary condition is as high as 10%.

Table 5.1

Comparison of Various Boundary Conditions
for Mass Transfer from a Solid Sphere
Pe = 0

r_∞	Type of Boundary Condition	Sh
5	Dirichlet, $c_\infty = 0$	2.5
10	Dirichlet, $c_\infty = 0$	2.22
50	Dirichlet, $c_\infty = 0$	2.04
10	Robin, $\underline{\mathbf{n}} \cdot \nabla c = -\frac{kc}{r}$	2.002

(b) Transient diffusion

Next step transient diffusion was modelled as a test of the unsteady part of the code. In this case, the situation is a sphere in an infinite expanse of fluid where the initial concentration at the surface of the sphere is set equal to unity and remains constant throughout the calculation. The concentration at infinity is set equal to zero and also remains constant throughout the calculation. For this case, there is no convection and the Peclet number was set equal to zero and (5.4), albeit with the time derivative term now present is solved solely in the ambient fluid. In this situation, it is well known that the Sherwood number is given by $Sh = 2(1 + \frac{1}{\sqrt{\pi\tau}})$ (Clift, et al., 1978). Figure 5.3 compares this exact solution (solid curve) with predictions made with the Galerkin/finite element algorithm of this thesis (data points). The numerical solution displayed in Figure 5.3 has been obtained with the Robin boundary condition and a domain radius of $r_\infty = 10$. Except for the first four time steps during which the initial transients are dissipated by the BD method, the two solutions are seen to be in excellent agreement with one another.

5.3.2 Mass transfer from a fluid sphere under limiting conditions

Figure 5.4 compares the predictions made with algorithm developed here (data points) with the Newman (1931) solution (solid curve). Once again, excellent agreement exists between the two solutions.

Next, the predictions of the algorithm are compared with the theory of Kronig and Brink (1950). To simulate the condition of infinite Peclet number, the Pe was set equal to 10,000 in the computer code. Figure 5.5 shows that upon

ORNL DWG 95C-437

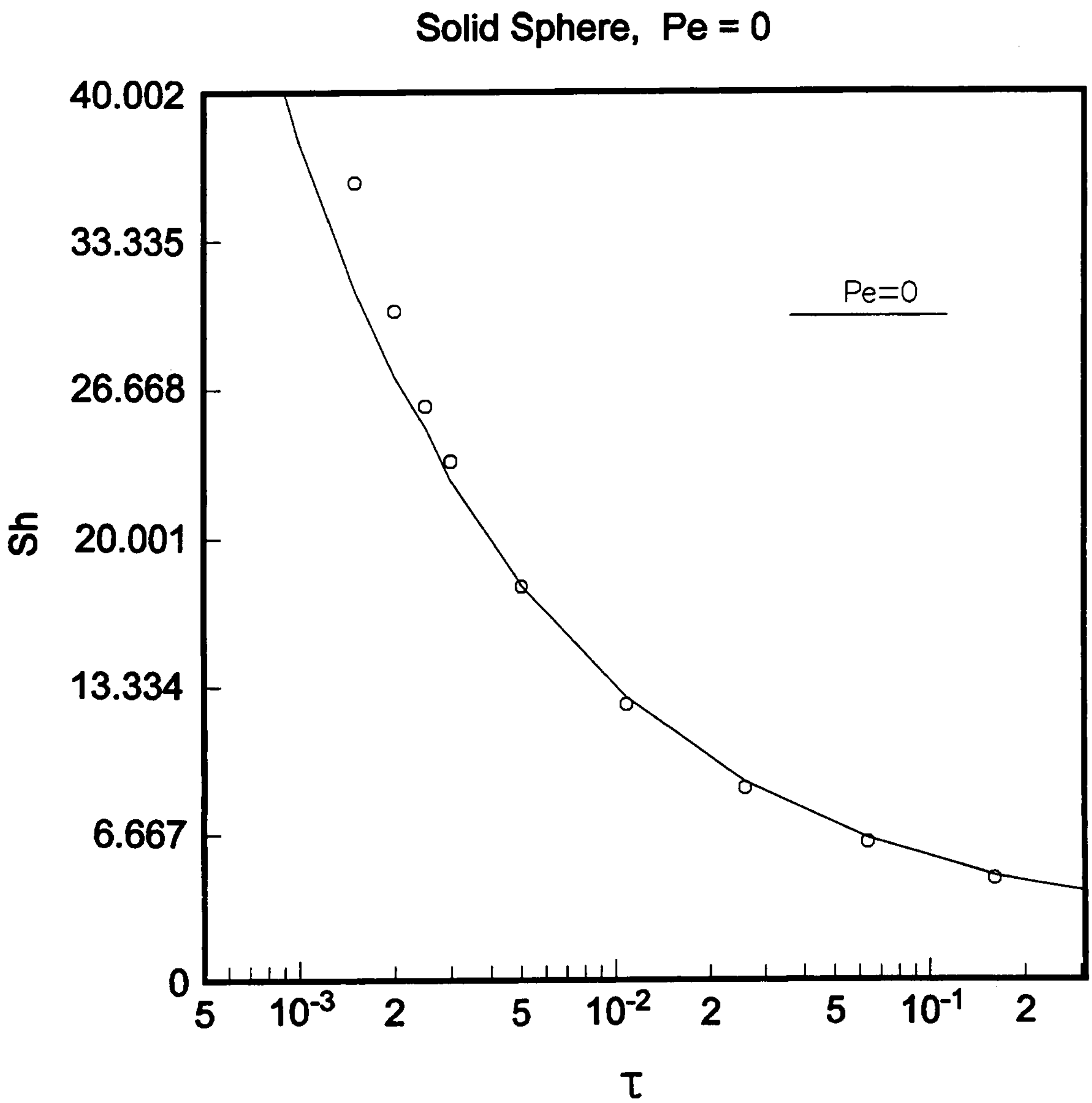

Figure 5.3. Unsteady mass transfer from a solid sphere. The curve is calculated from theory. The points are calculated from this work. Here $Pe = 0$.

ORNL DWG 95C-438

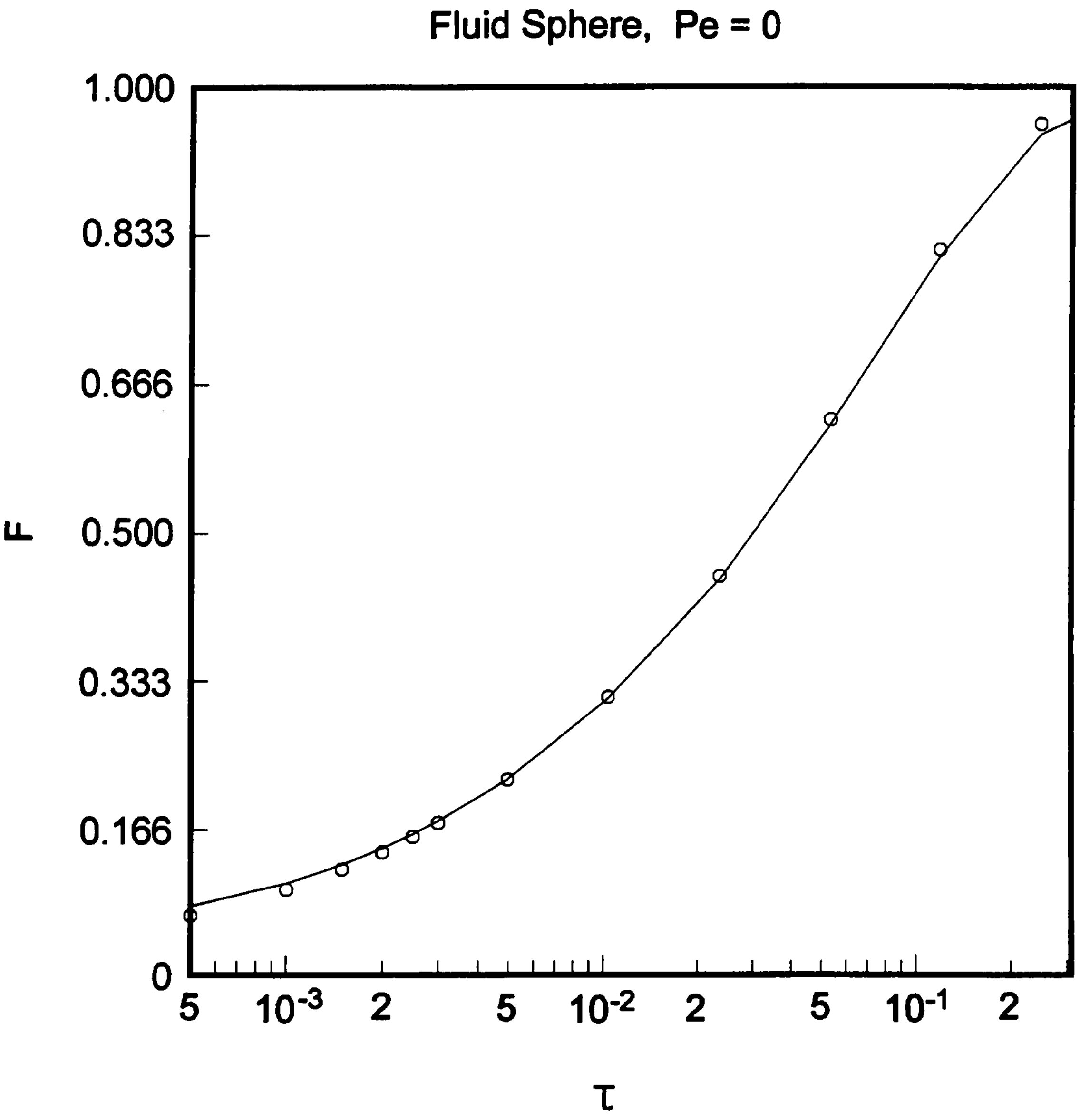

Figure 5.4. Unsteady diffusive mass transfer from a fluid sphere. The curve is calculated from Newman(1931). The points are calculated from this work. Here $Pe = 0$.

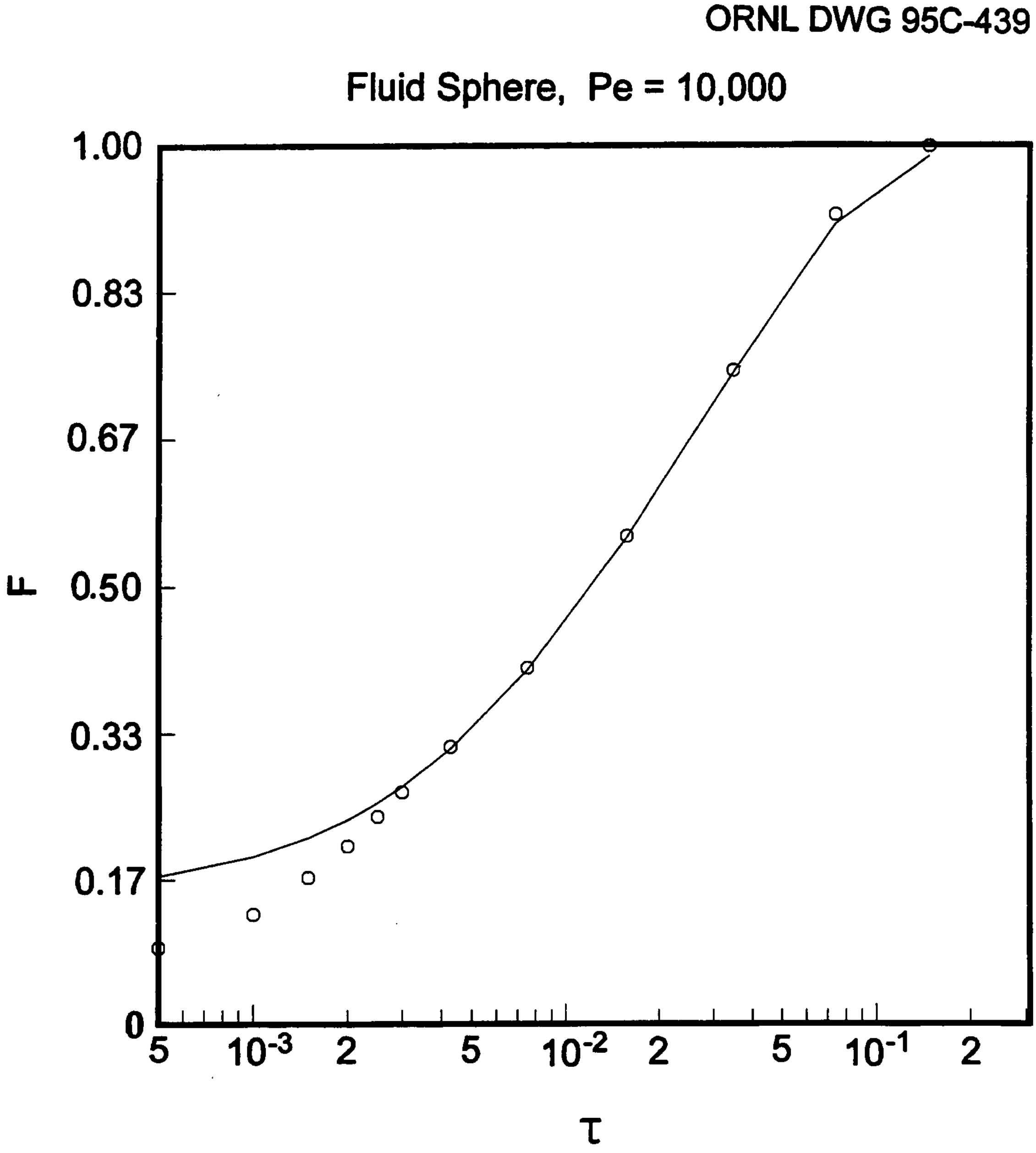

Figure 5.5. Unsteady convective mass transfer from a fluid sphere. The curve is calculated from Kronig and Brink(1951). The points are calculated from this work. Here $Pe = 10,000$.

the decay of the initial transients, the computational results (data points) are in excellent agreement with the analytical theory of Kronig and Brink (solid curve).

5.3.3 Effects of velocity fields on mass transfer

The results presented in the previous sections on mass transfer from solid and fluid spheres placed in an infinite expanse of ambient fluid provide convincing evidence that the algorithm and the computer code developed in this thesis are indeed correct. Therefore, in this section attention is turned to situations in which resistance to mass transfer is not limited to one phase alone and the Peclet number is neither zero nor infinite. Moreover, pioneering computations are carried out for situations in which the drop is suspended in a tube, a far cry from the idealized theories heretofore studied but an excellent model of most laboratory experiments. However, although transient mass transfer calculations have been made for both falling and fluidized drops in tubes, the results presented here are restricted to falling spheres.

A major objective of this section is to gain insights into differences in mass transfer rates from spherical drops when wakes are present with those when wakes are absent. To focus on the physics of wake effects in mass transfer, in all cases, the Peclet number Pe is set equal to 100, the ratio of diffusivities $\frac{D^{(o)}}{D^{(i)}}$ is set equal to 1, the distribution coefficient H is set equal to 1, and the ratio of tube radius to sphere radius $D \equiv \frac{1}{\lambda}$ is set equal to 5. However, the Reynolds number Re and the viscosity ratio κ are allowed to vary (cf. Chapter 4). Six specific cases are considered in what follows to highlight the effects of Re and κ on conjugate mass transfer: (1)$Re = 0$, $\kappa = 1$; (2)$Re = 60$, $\kappa = 1$; (3)$Re = 0$,

$\kappa = 10$; (4)$Re = 60$, $\kappa = 10$; (5)$Re = 60$, $\kappa = 3$; and (6)$Re = 60$, $\kappa = 3.5$.

Figure 5.6 shows concentration contours and velocity vectors in and around a falling drop at several time steps in the situation in which $\kappa = 1$ and $Re = 0$. Each of the subplots in Figure 5.6 depicts the time τ (because the time step-size is chosen adaptively), the instantaneous value of the Sherwood number Sh, and the average concentration of solute remaining inside the drop C_p. Figure 5.6 shows that initially ($\tau \to 0$) the concentration contours are highly symmetric. It is noteworthy that were mass transfer taking place solely by diffusion, concentration contours would be arcs of circles in the plane of the paper, similar to those shown in Figure 5.6 when $\tau = 0.013$. As time advances, for example when $\tau > 0.032$, Figure 5.6 shows that as solute is transferred out of the drop it is then swept to rear of droplet and subsequently swept downstream. Thereafter, the concentration profile and contours become asymmetric since solute is that extracted at the front of the drop by fresh solvent is subsequently swept to the rear of the droplet. Figure 5.6 shows that Sh decreases from a value of 5.32 at $\tau = 0.013$ to a value of 3.78 at $\tau = 0.032$. The decrease in Sh is due to the drop initially containing a uniform concentration of solute which provides a larger overall driving force for $\tau \to 0$. As τ increases, the concentration in the drop decreases and the driving force changes. The net effect is a decrease in the mass transfer coefficient with the attendant decrease in Sherwood number. The slight increase in Sh from $Sh = 3.15$ at $\tau = 0.076$ to $Sh = 3.26$ at $\tau = 0.168$ is due to oscillations in Sh brought about by internal circulation(Clift , et al. 1978).

In Figure 5.6, the concentration contours at $\tau = 0.168$ are asymmetric indicating that solute concentration in the rear of the drop is lower that the concentration in the upstream section of the drop. The asymmetry in concentration

ORNL DWG 94-900

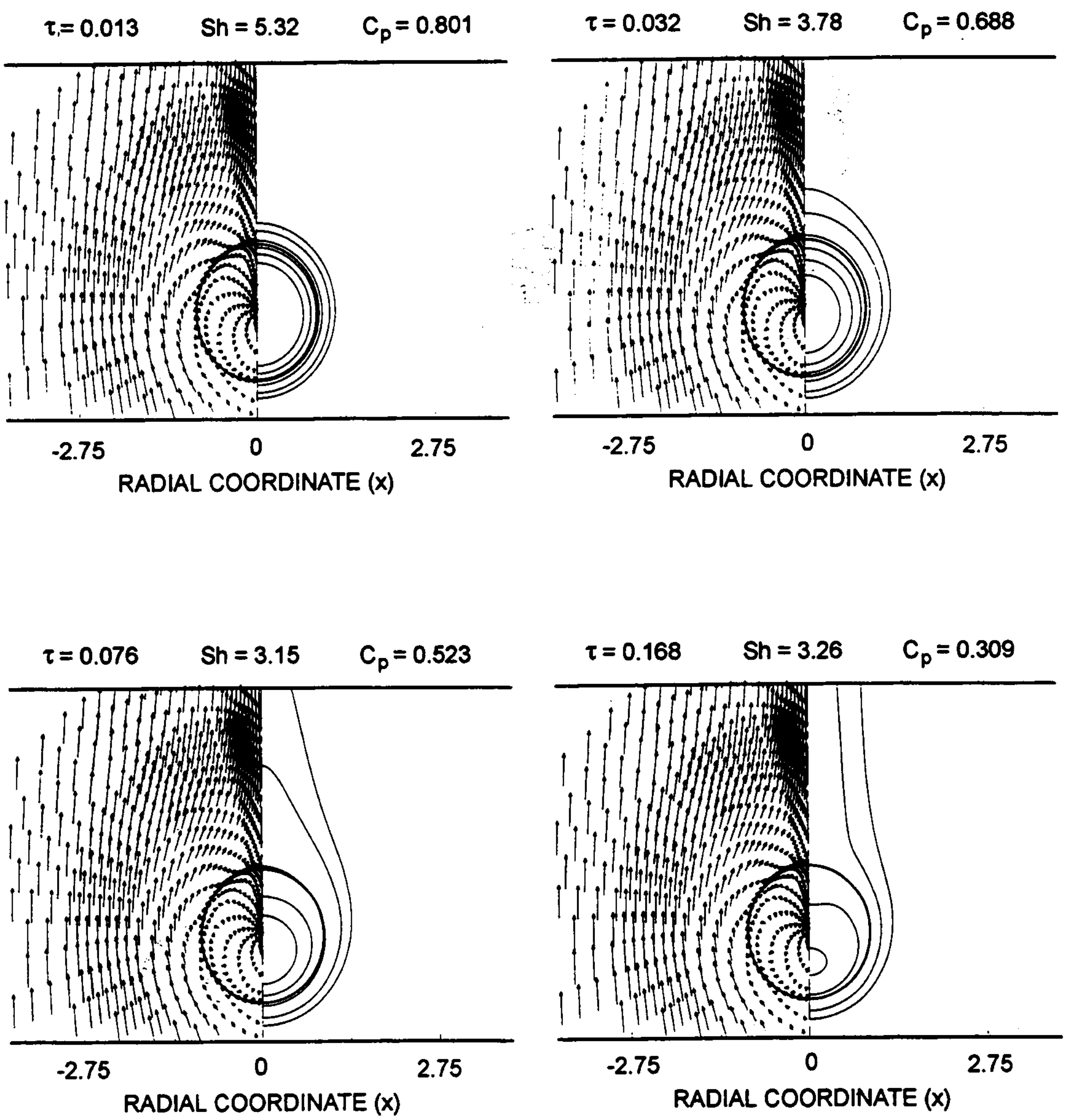

Figure 5.6. Unsteady mass transfer from a fluid sphere. The concentration contours are calculated from this work. Here $Re = 0, \kappa = 1, \frac{1}{\lambda} = 5$, and $Pe = 0$.

contours can be explained by looking both at mass transfer inside the drop as well as outside the drop. Starting on the inside of the drop , a path traversed by the fluid inside the drop as it circulates around the drop takes the fluid through th center of the drop, up to the front stagnation point, around the perimeter of the drop surface and to the rear stagnation point. Solute inside the drop diffuses outward from the internal stagnation point into the circulating fluid. This solute is transferred by convection to the front of the drop where it diffuses across the interface. Diffusion across the interface continues as the fluid containing solute travels parallel to the interface. The concentration decreases as the distance between $\theta = \pi$ to $\theta = 0$ is travelled due to diffusion across the interface. By the time the solvent reaches the rear of the drop, it has been depleted of solute and returns to the center of the drop to begin the cycle again.

Outside the drop the solute transfer is also governed by the competition between diffusion and convection in the continuous phase. At the forward face of the drop , fresh solute comes in from $r = \infty$ and approaches the drop. Convective and diffusive transfer oppose each other at the forward face of the drop and the transfer into to continuous phase is limited to a narrow band as depicted in Figure 5.6. At the rear of the drop, the solute that has transferred into the solvent is convected downstream of the drop since the convective part of the mass transfer is now sweeping the solute downstream.

Further insights into the distortion of the concentration contours can be gained by examining the variation of the local mass transfer coefficient with angular position along the drop surface, as shown in Figure 5.7. Figure 5.7 makes plain that the mass transfer coefficient is highest at the front of droplet, $\theta = \pi$ or 180^o, due to the continual arrival of fresh solvent there. The local mass transfer coeffi-

ORNL DWG 95C-449

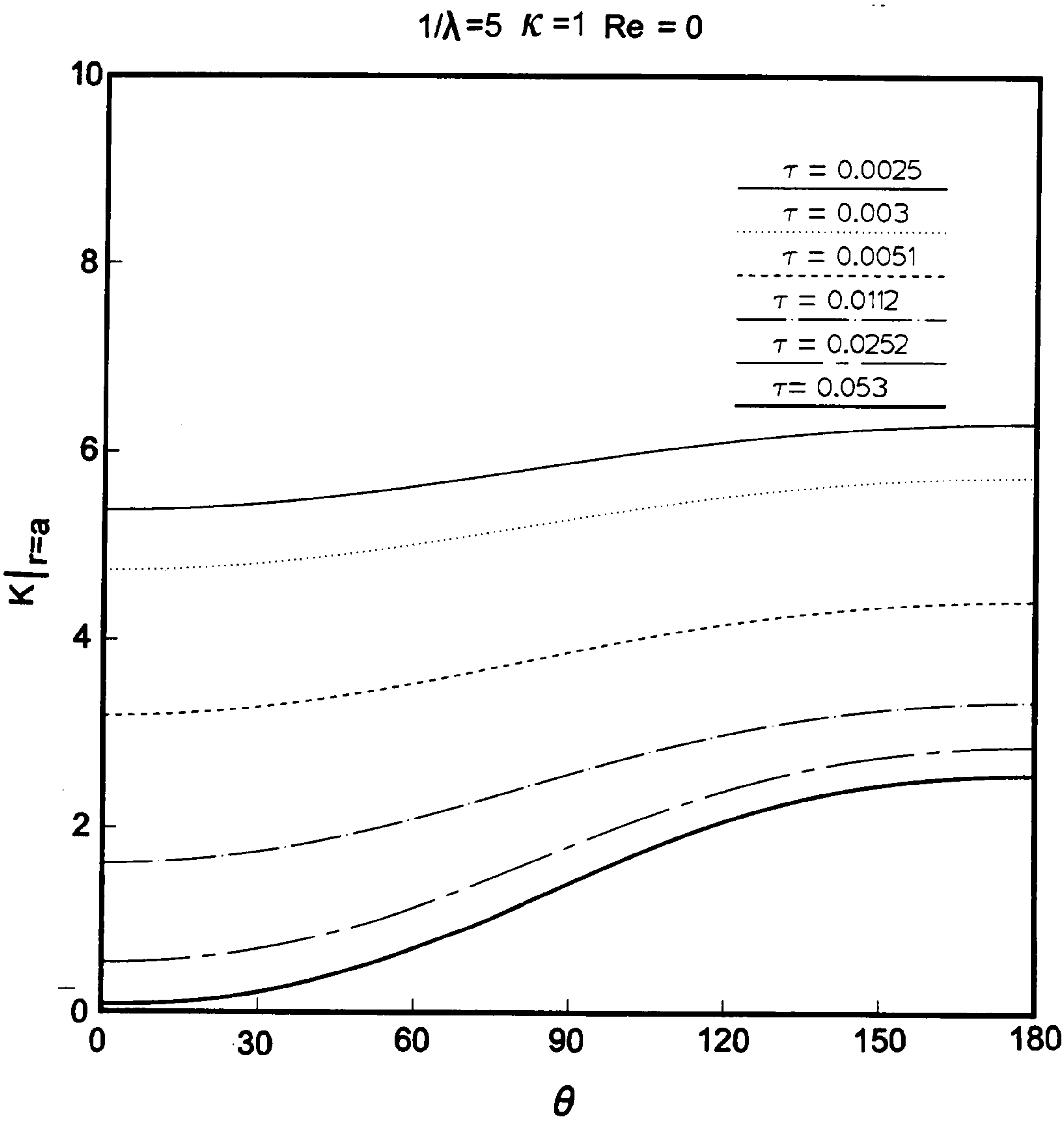

Figure 5.7. Mass transfer coefficient evaluated at the drop surface.Here $Re = 0$, $\kappa = 1$, $\frac{1}{\lambda} = 5$ and $Pe = 0$.

cient is lowest at the rear of the droplet, $\theta = 0$ by the same reasoning. Moreover, Figure 5.7 also shows that the local mass transfer coefficient decreases as time advances due to a reduction in the concentration of solute in the drop over time brought about by the mechanism for mass transfer described previously.

Figure 5.8 shows the variation of concentration of solute with position along the drop surface. That the concentration decreases everywhere on the drop surface as time advances is not surprising because mass is transferring out of the drop. What is more interesting is the fact that the concentration is highest at the front of the drop and is lowest at the rear of the drop. There are two contributing factors for this profile - - (1) transfer of solute out of the drop occurring near the drop surface depletes the solute near the drop surface. (2) the convective $c\underline{v}$ and diffusive $-\nabla c$ contributions to the mass flux in the ambient fluid reinforce each other near the rear of the drop but the two oppose each other near the front of the drop.

Figure 5.9 has been developed in the same format as Figure 5.6. In Figure 5.9 the Reynolds number has been increased to $Re = 60$ wile κ remains equal to 1. For this case, the influence of flow field on concentration contours is more pronounced as evidenced by concentration contours which show a greater degree of asymmetry in the first two contour plots. The change in contours is attributed to the change in velocity field since Pe remains constant between Figure 5.6 and Figure 5.9. The magnitude of velocity close to the drop surface has increased(recall Figure 4.14) and the overall circulation in the interior of the drop has increased(recall $|\psi|$ versus Re from Figure 4.16a). The change in internal circulation changes mass transfer inside the drop due to the increased efficiency of convection in the transfer of solute from the interior of the drop to

ORNL DWG 95C-448

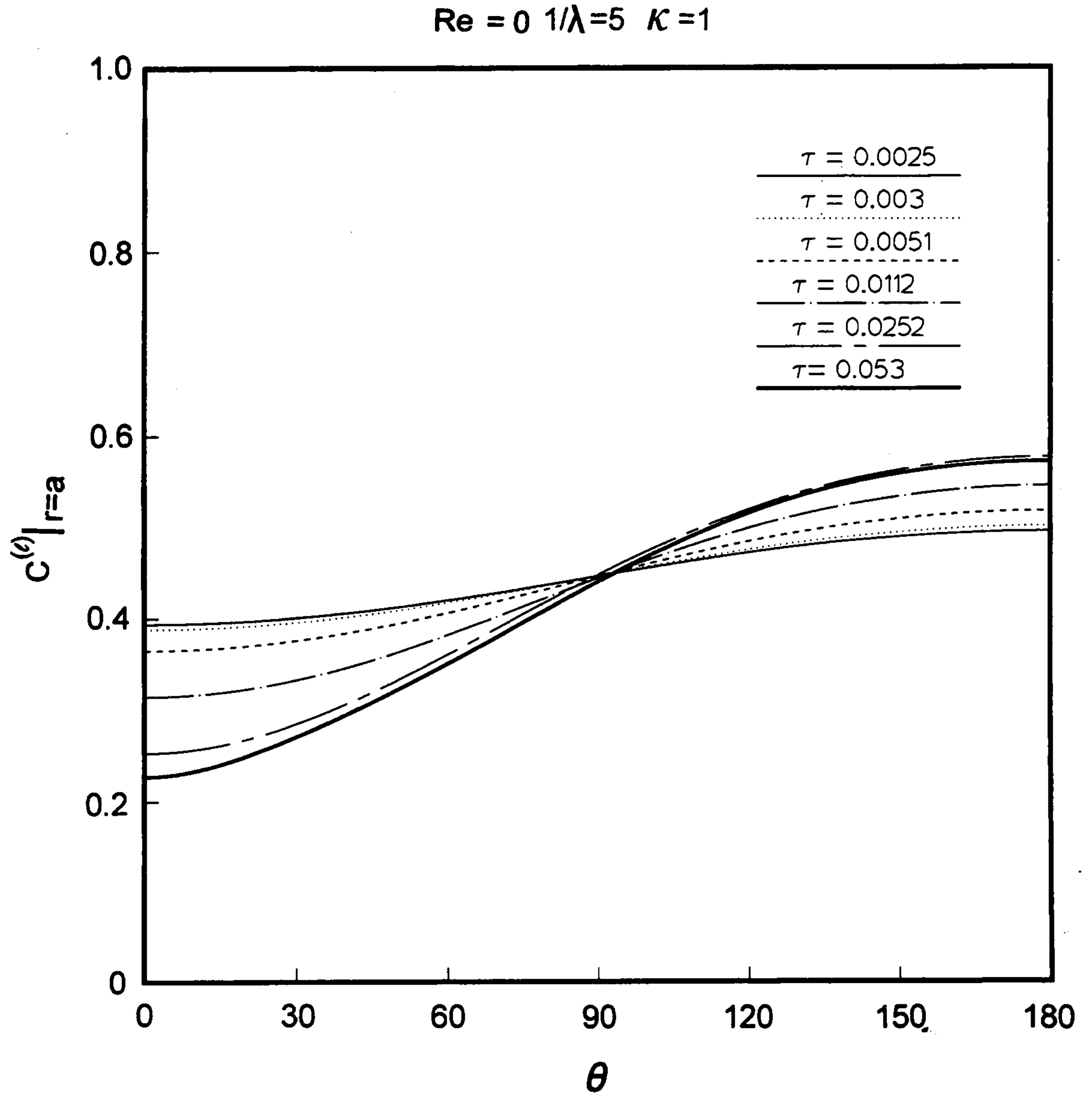

Figure 5.8. Concentration evaluated at the drop surface. Here $Re = 0$, $\kappa = 1$, $\frac{1}{\lambda} = 5$ and $Pe = 0$.

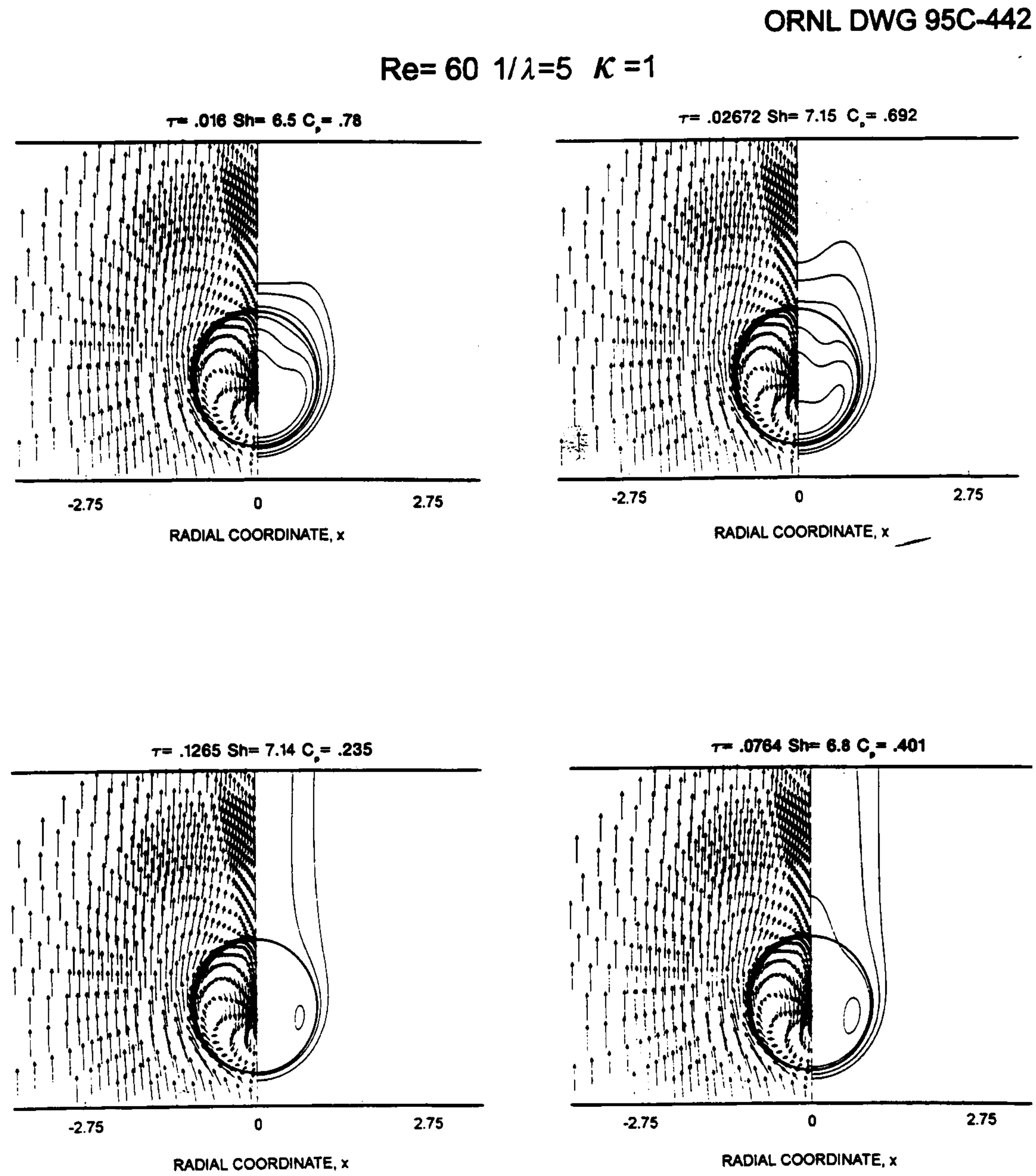

Figure 5.9. Unsteady mass transfer from a fluid sphere. The concentration contours are calculated from this work. Here $Re = 60$, $\kappa = 1$, $\frac{1}{\lambda} = 5$ and $Pe = 0$.

the drop surface where solute can then diffuse across the interface. Comparing the two lower contour plots in Figure 5.9 to the corresponding plots in Figure 5.6, solute swept downstream is dispersed over a larger cross sectional area for $Re = 60$ versus $Re = 0$ indicating that convection outside the drop has become more effective in transporting solute away from the drop. Close examination of the concentration contours for $\tau = 0.02672$ in Figure 5.9 shows that solute accumulates in the region near to $\theta = \frac{\pi}{4}$ prior to formation of a solute trail extending out from downstream face of the drop. The accumulation is due to the change in velocity field occurring downstream of the drop.

Oscillations in Sh can be seen in Figure 5.9 by comparing Sh at the different values of τ. The value of Sh is seen to increase from $Sh = 6.5$ at $\tau = 0.016$ to $Sh = 7.15$ at $\tau = 0.02672$ and then decrease for the remaining values of τ. These changes in Sh are consistent with an increase in oscillation frequency as well as amplitude.

Figure 5.10 shows local mass transfer coefficients versus angular position on the drop surface. Here the effect of changes in velocity fields between those shown in Figure 5.9 and those shown in Figure 5.6 are apparent in the increases in $\mathcal{K}|_{r=a}$(c.f. Figure 5.7 and 5.10). As in Figure 5.7, the highest mass transfer coefficient is at front of droplet. In Figure 5.10, mass transfer coefficients are seen to decrease over time due to lowering in overall driving force as a result of a drop in concentration. Review of the mass transfer coefficients for $\tau > 0.025$ show slight decrease in the mass transfer coefficient at $\theta \approx \frac{\pi}{4}$ reflecting the accumulation of solute seen previously in the concentration contour plots at for $\tau = 0.02672$ in Figure 5.9.

Remarkably, in Figure 5.11 the local concentration at the drop surface remains

ORNL DWG 95C-441

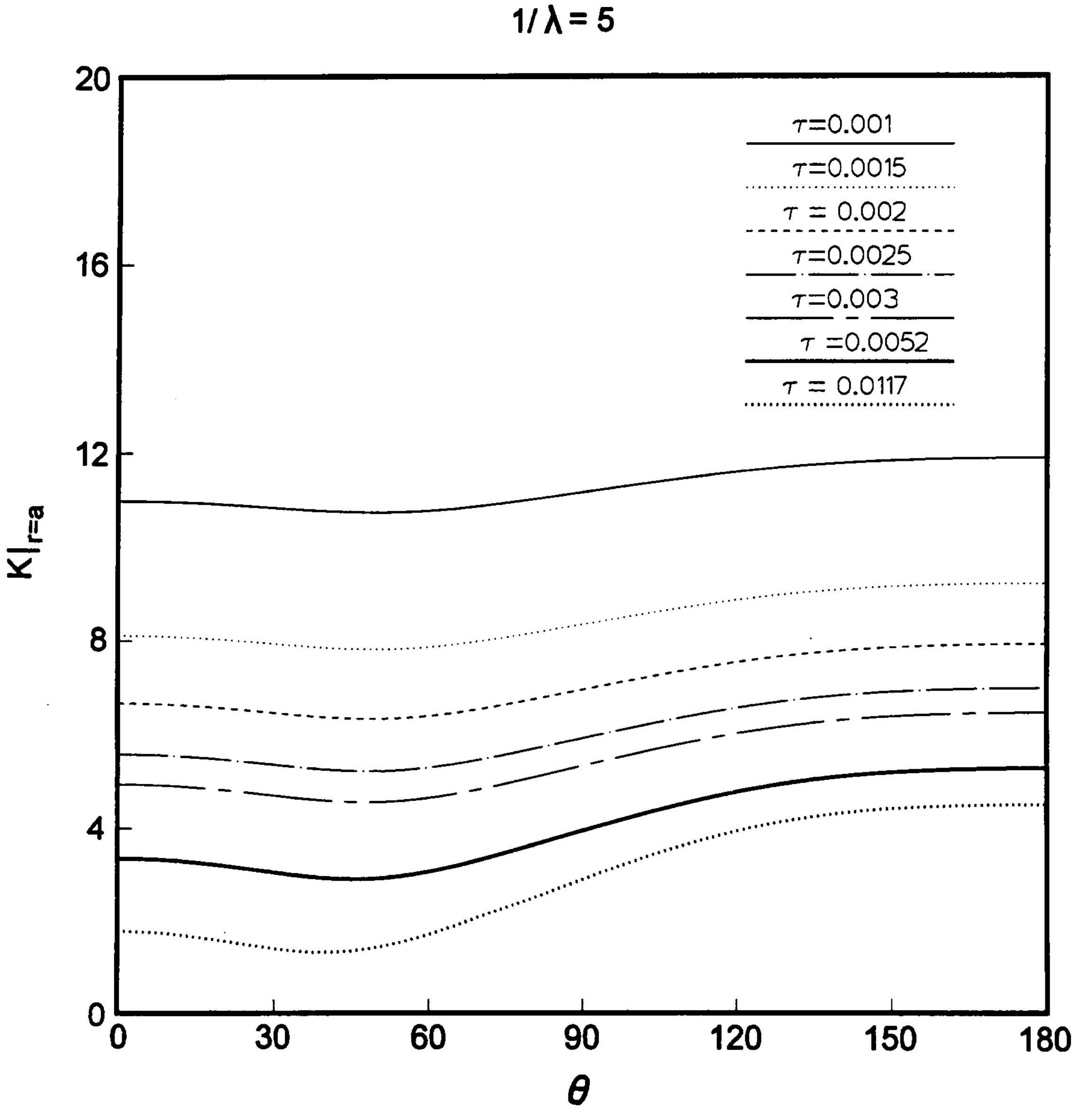

Figure 5.10. Mass transfer coefficient evaluated at the drop surface. Here $Re = 60$, $\kappa = 1$, $\frac{1}{\lambda} = 5$ and $Pe = 0$.

ORNL DWG 95C-440

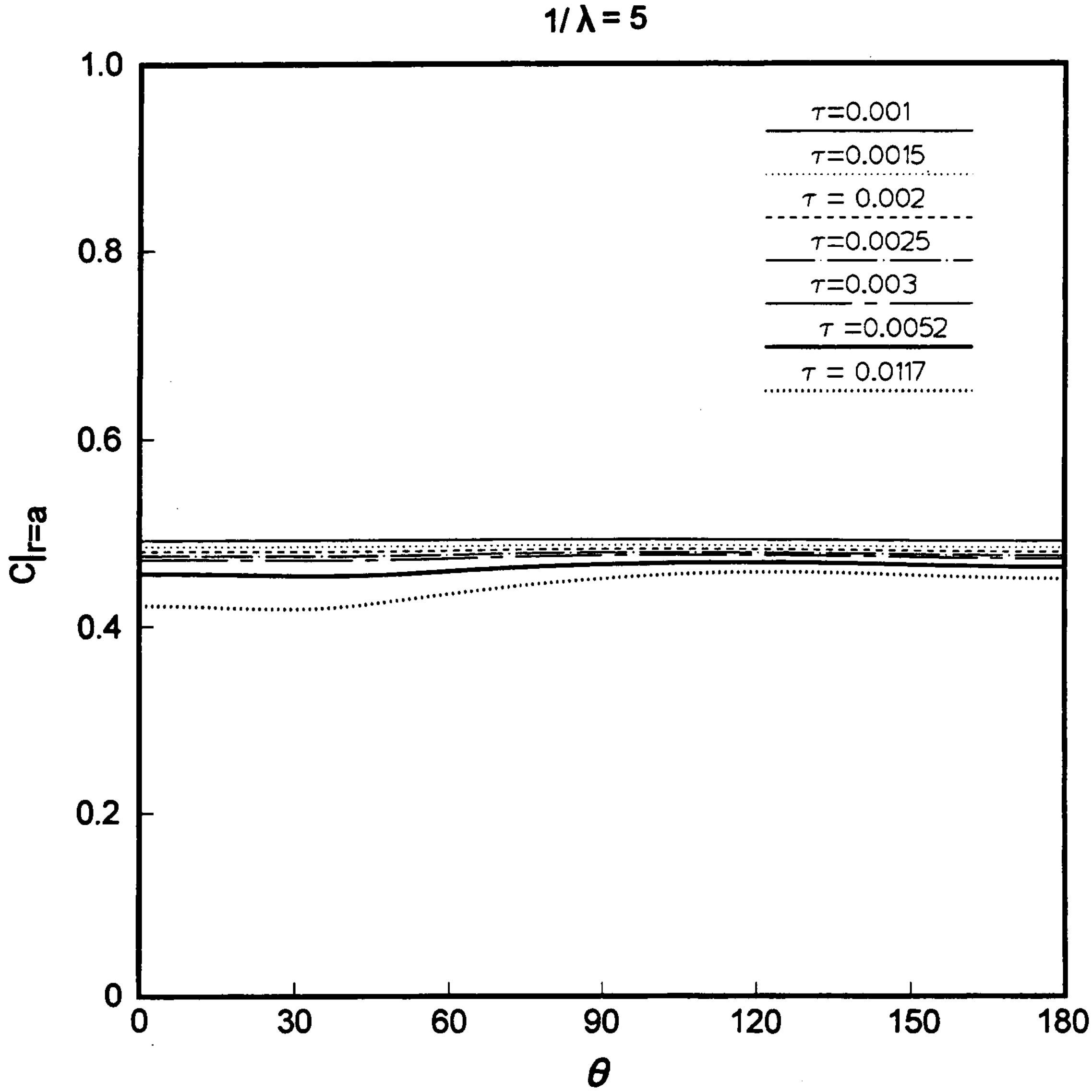

Figure 5.11. Concentration evaluated at the drop surface. Here $Re = 60$, $\kappa = 1$, $\frac{1}{\lambda} = 5$ and $Pe = 100$.

almost constant in sharp contrast to Figure 5.8 where $Re = 0$. The increase in circulation inside the drop at a constant value of the Peclet number, as measured by an increase in $|\psi|$ (c.f. Figure 4.16a) results in the drop concentration becoming more uniform (i.e., more mixing inside the drop). The uniform concentration provides more solute at the interface for transfer across the interface and a higher driving force for mass transfer (c.f. Figure 5.11 and Figure 5.8).

Figure 5.12 presents concentration contours where the value of viscosity ratio has increased to $\kappa = 10$ and Re is set equal to 0. Circulation within the drop is lower than that for the corresponding case of $\kappa = 1, Re = 0$ illustrated in Figure 5.6. The change in circulation can be seen by comparing $|\psi|$ for $\kappa = 1$ to that for $\kappa = 10$ in Figure 4.16a. (Recall that Figure 4.14 shows a significant decrease in interfacial velocity as a function of viscosity ratio.) As was previously illustrated in the Figures 5.6 and 5.9, solute transferring out of the drop is swept to rear of droplet then downstream by the continuous phase.

Figure 5.13 shows mass transfer coefficients evaluated at the drop surface. Here the mass transfer coefficients are slightly higher near the front of the droplet. However, the difference between mass transfer coefficients at the downstream face ($\theta = 0$) and the upstream face ($\theta = \pi$) is not large. The lack of a significant change in mass transfer coefficient can also be seen when looking at the concentration of solute at the interface. Figure 5.14 shows local concentration at the drop surface plotted versus angular position. The concentration at the interface was relatively constant in Figure 5.14. An interesting detail of Figure 5.14 is the increase in concentration in the range of $\theta = \frac{\pi}{4}$ which corresponds to the observed distortion in concentration contours seen in Figure 5.12.

In Figure 5.15, the Reynolds number has increased to 60 while all other vari-

ORNL DWG 95C-443

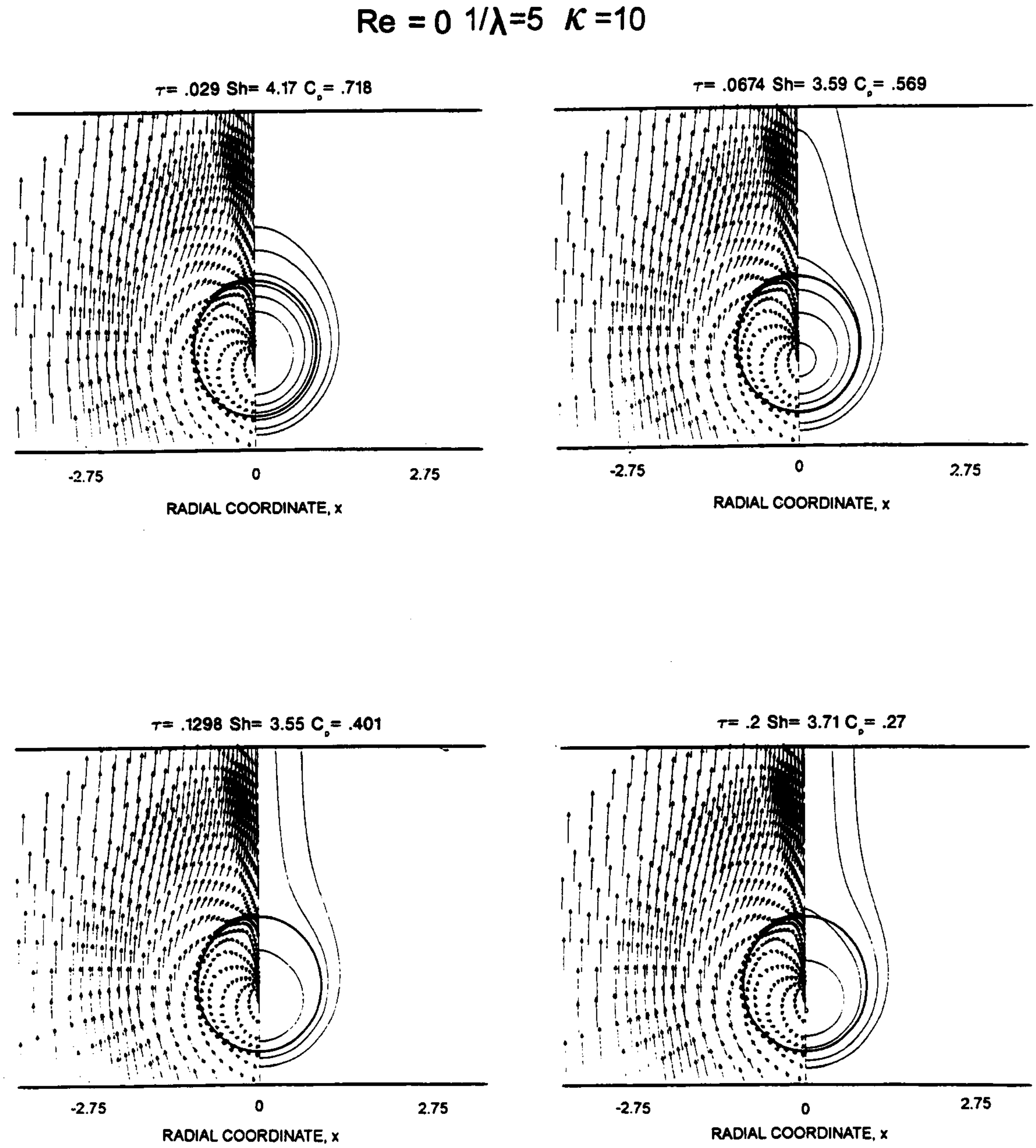

Figure 5.12. Unsteady mass transfer from a fluid sphere. The concentration contours are calculated from this work. Here $Re = 0$, $\kappa = 10$, $\frac{1}{\lambda} = 5$ and $Pe = 100$.

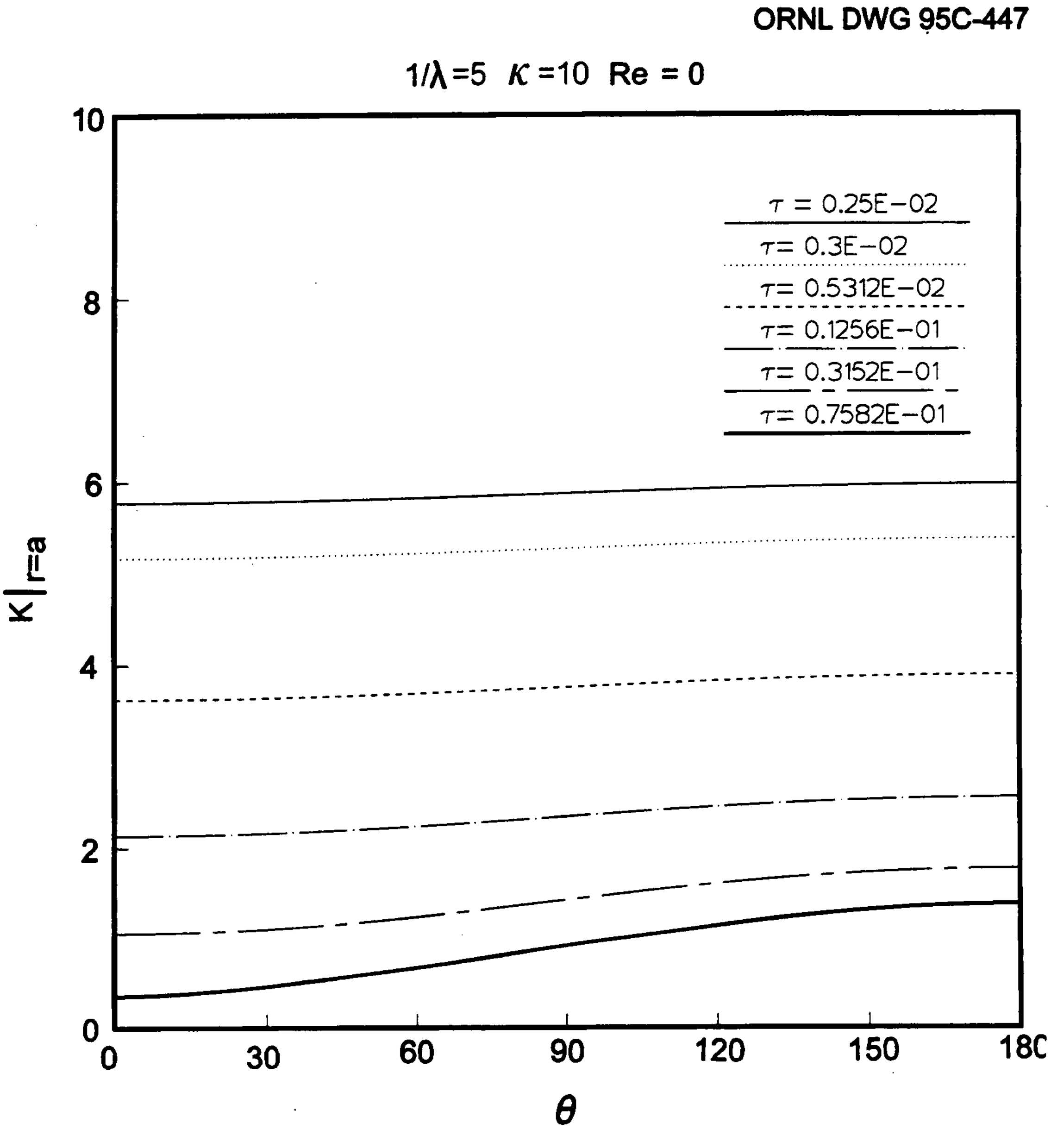

Figure 5.13. Mass transfer coefficient evaluated at the drop surface. Here $Re = 0$, $\kappa = 10$, $\frac{1}{\lambda} = 5$, and $Pe = 100$.

ORNL DWG 95C-444

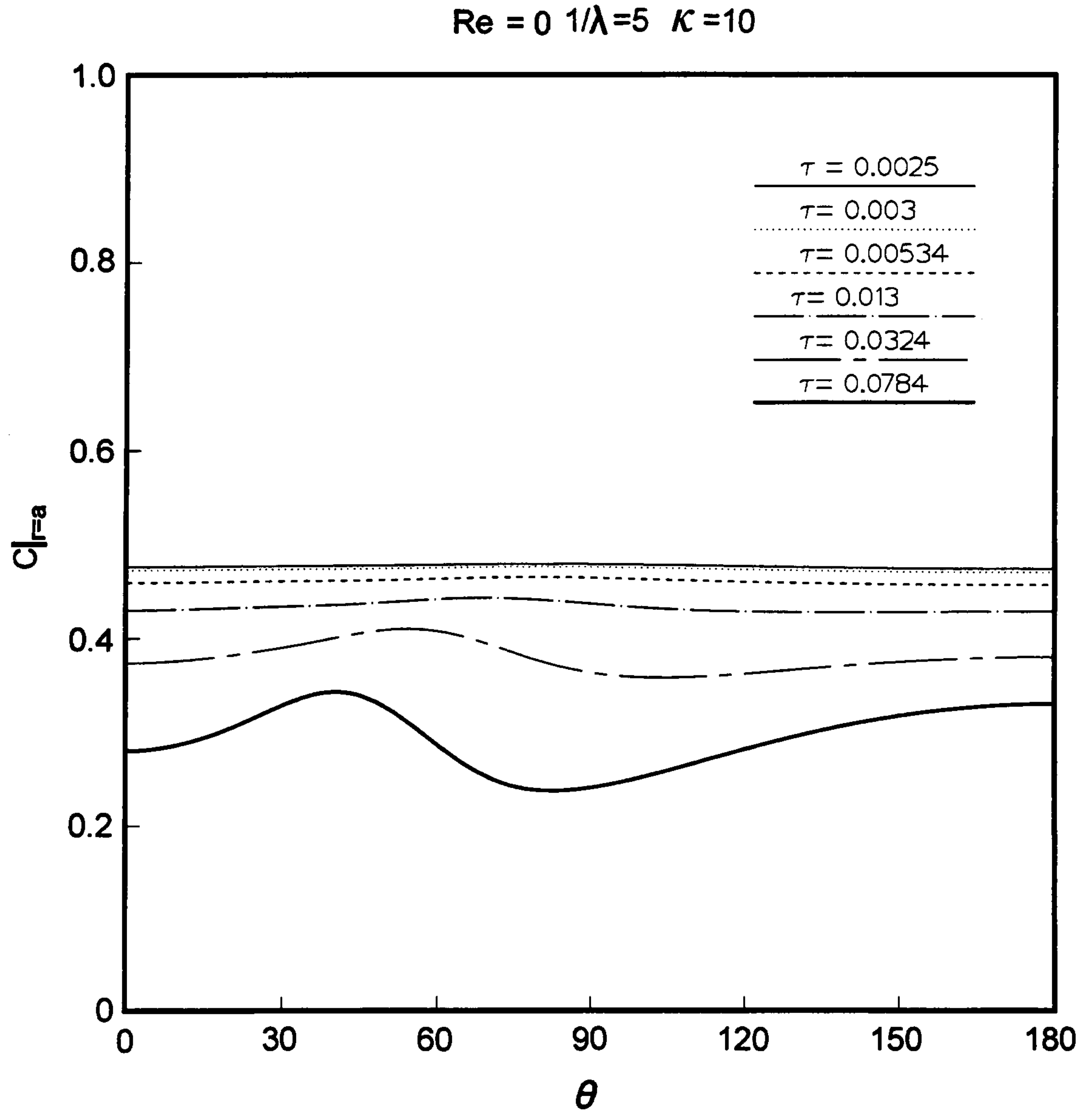

Figure 5.14. Concentration evaluated at the drop surface. Here $Re = 0$, $\kappa = 1$, $\frac{1}{\lambda} = 5$ and $Pe = 100$.

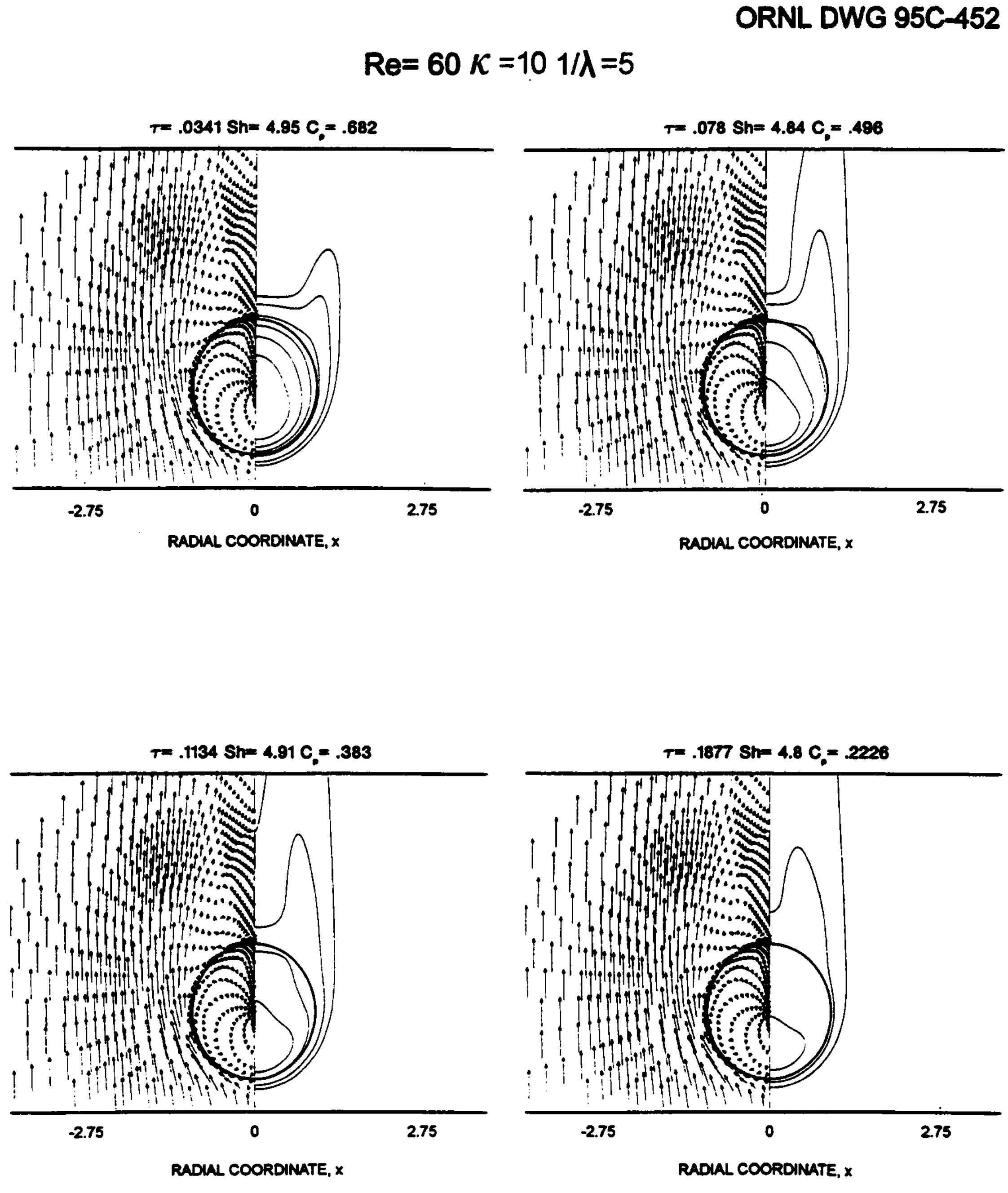

Figure 5.15. Unsteady mass transfer from a fluid sphere. The concentration contours are calculated from this work. Here Re = 60, κ = 10, $\frac{1}{\lambda}$ = 5 and $Pe = 100$.

ables remain identical to those used in Figures 5.12. A significant change has occurred in the velocity field whereas a wake has formed at the rear of the drop (see Figure 4.5). As in Figures 5.6, 5.9 and 5.12, concentration contours in Figure 5.15 depict the continuous phase sweeping the solute to the rear of droplet then downstream. A remarkable result is observed when comparing concentration contours in Figure 5.9 to those in Figure 5.15. The evolution of the concentration contours has changed considerably due to the presence of the wake. The presence of the wake appears to impair solute transport downstream of the drop. That the wake is effecting concentration contours is evident from the concentration contours near the rear of the droplet in the area of the wake. During mass transport at a Reynolds number of 60 and $\kappa = 1$ (c.f. Figure 5.9), solute exiting the drop is swept downstream with no interference as evidenced by the smooth concentration contours downstream of the drop depicted in Figure 5.9. As time increases in Figure 5.9, the length of the solute trail to the rear of the drop continues to increase. Figure 5.15 makes plain that the wake interferes with transport as evidenced by the distortion in concentration contours occurring in the region encompassed by the wake. The explanation of this interference starts with the wake itself. The wake region is enclosed by the streamline $\psi = 0$ meaning that the velocity normal to the $\psi = 0$ streamline is zero. Solute removed by circulation past the rear surface of the drop must transfer by diffusion across the wake interface defined by the $\psi = 0$ streamline. The diffusion process is slower that the combination of diffusion and convection which lowers the overall mass transfer rate. If the wake was not present, mass transport downstream of the drop would be primarily by convection.

In Figure 5.16 the plot of mass transfer coefficient indicates there is a decrease in mass transfer at the drop surface for all values of τ as compared to Figure 5.10 for $Re = 60$ and $\kappa = 1$. These values for mass transfer coefficients are significantly lower than corresponding values of mass transfer coefficients shown in Figure 5.10. In Figure 5.17, the values of concentration at the interface are presented and the concentration values remain relatively constant up for all values of τ.

As further evidence of the effect of wake on concentration profiles, several other values of viscosity ratios are plotted in Figure 5.18. Concentration contours for $\kappa = 1, 3, 3.5, 10$ and $Re = 60$ are shown in Figure 5.18. All of the plots were chosen close to $C_p = 0.5$. Looking at $\kappa = 1$, the concentration contours indicate solute has been swept downstream of the drop with no interference as was the case in Figure 5.9. Turning to $\kappa = 3$, the outer concentration contour indicates solute has not moved as far downstream as the previous $\kappa = 1$ case. A small detached wake is located downstream of the drop for $\kappa = 3$. Increasing viscosity ratio from $\kappa = 3$ to $\kappa = 3.5$ increase the size of the wake at the rear of the drop with the effect of moving the concentration contours closer to the rear of the drop. At $\kappa = 10$, the wake is even closer to the downstream side of the drop as reflected by the concentration contours moving closer to the downstream face of the drop. Another indication of lower mass transfer rate is that the nominal 50% extraction point (at $C_p = 0.5$) occurs at increasingly larger values of τ for increases in κ.

Figure 5.19 depicts the fractional extraction F for $Re = 60, \kappa = 1, 3, 3.5, 10$. The curves for $\kappa = 3, 3.5, 10$ are surprisingly close to each other while a distinct difference can be seen for $\kappa = 1$. This remarkable result indicates that the

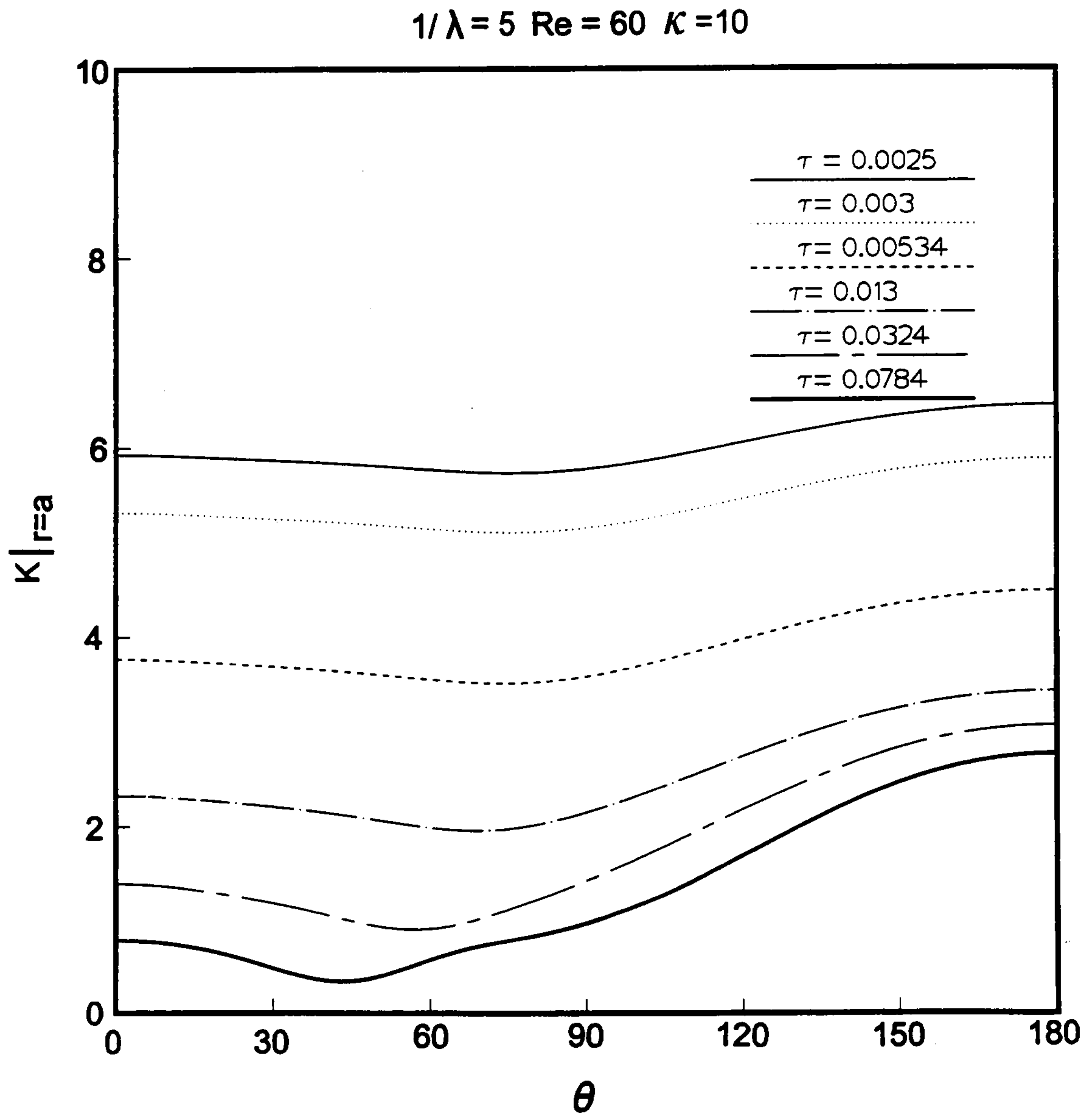

Figure 5.16. Mass transfer coefficient evaluated at the drop surface. Here $Re = 60$, $\kappa = 10$, $\frac{1}{\lambda} = 5$ and $Pe = 100$.

ORNL DWG 95C-446

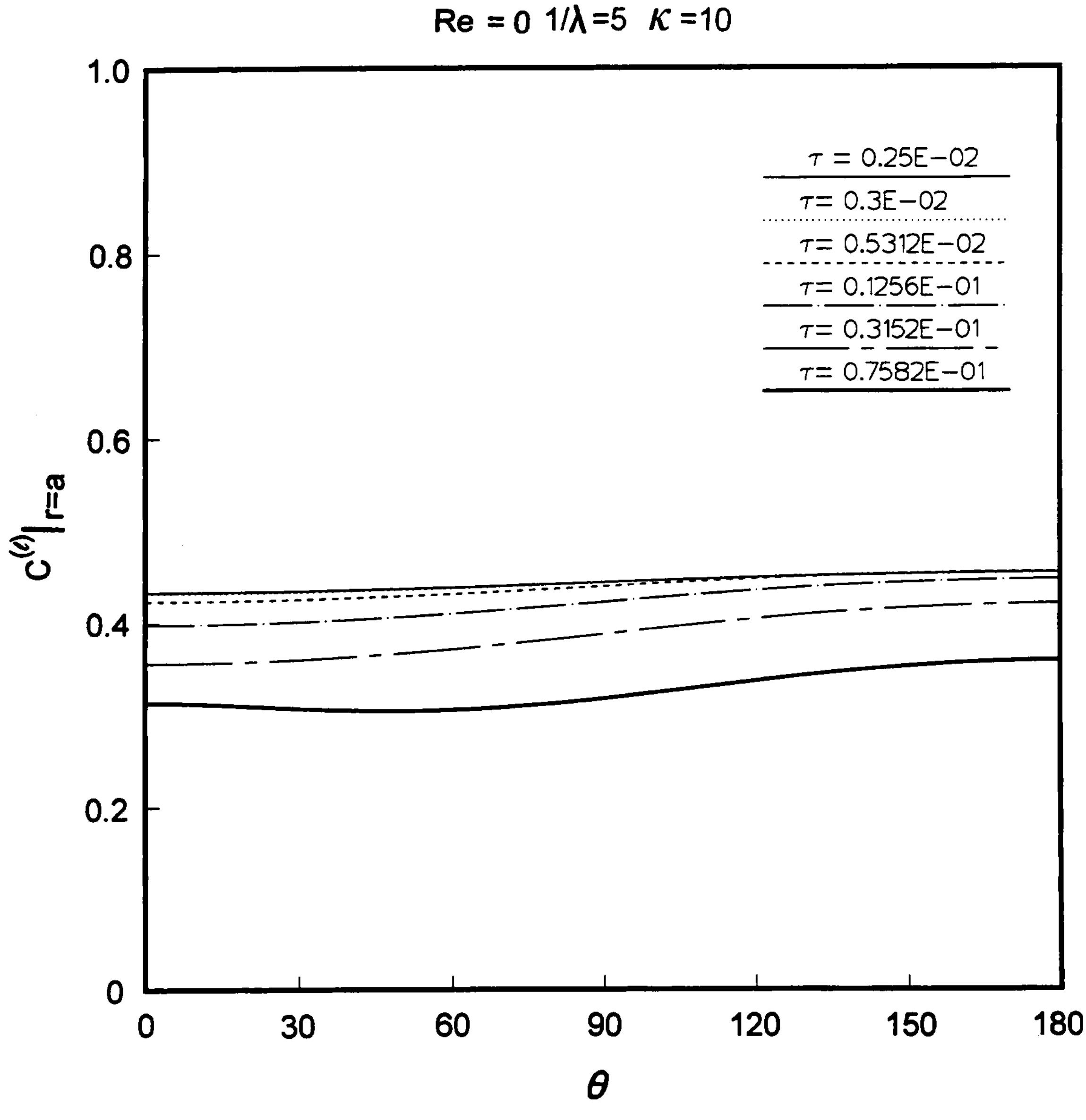

Figure 5.17. Concentration evaluated at the drop surface. Here $Re = 60$, $\kappa = 10$, $\frac{1}{\lambda} = 5$ and $Pe = 100$.

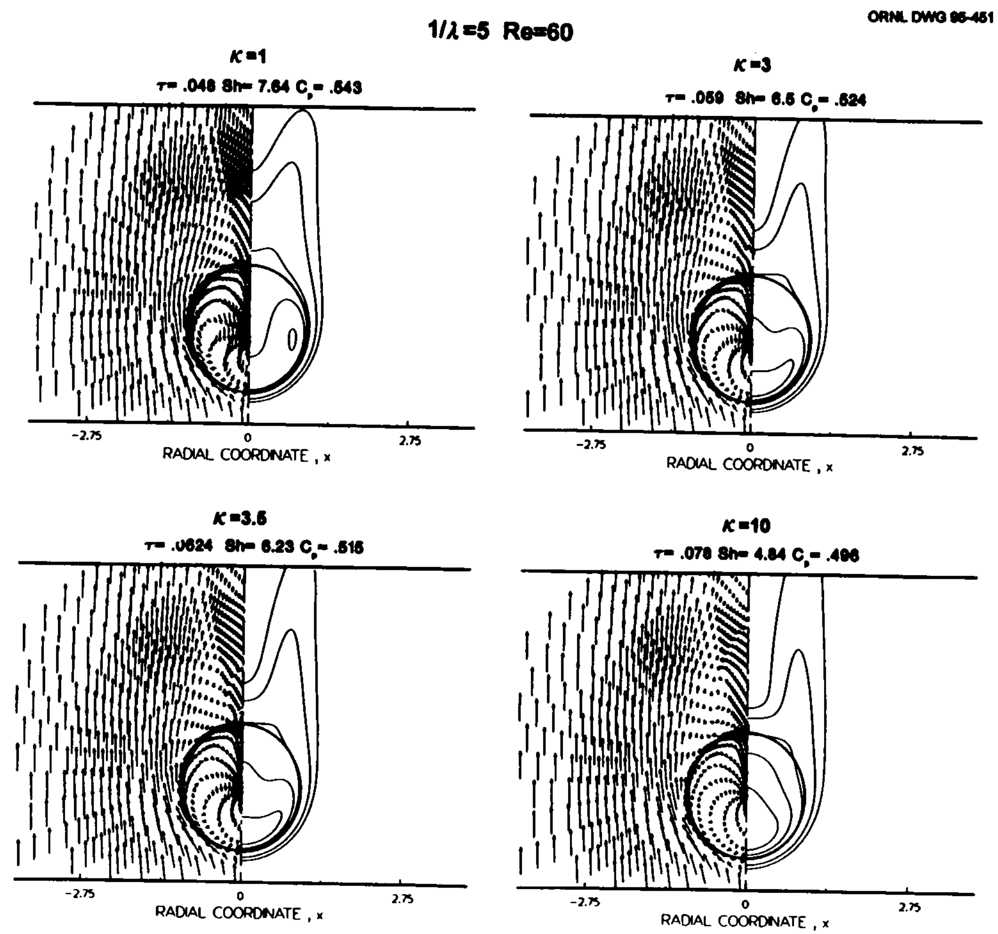

Figure 5.18. Unsteady mass transfer from a fluid sphere. The concentration contours are calculated from this work. Here $Re = 60$, $\kappa = 1, 3, 3.5, 10$, $\frac{1}{\lambda} = 5$ and $Pe = 100$.

ORNL DWG 95C-436

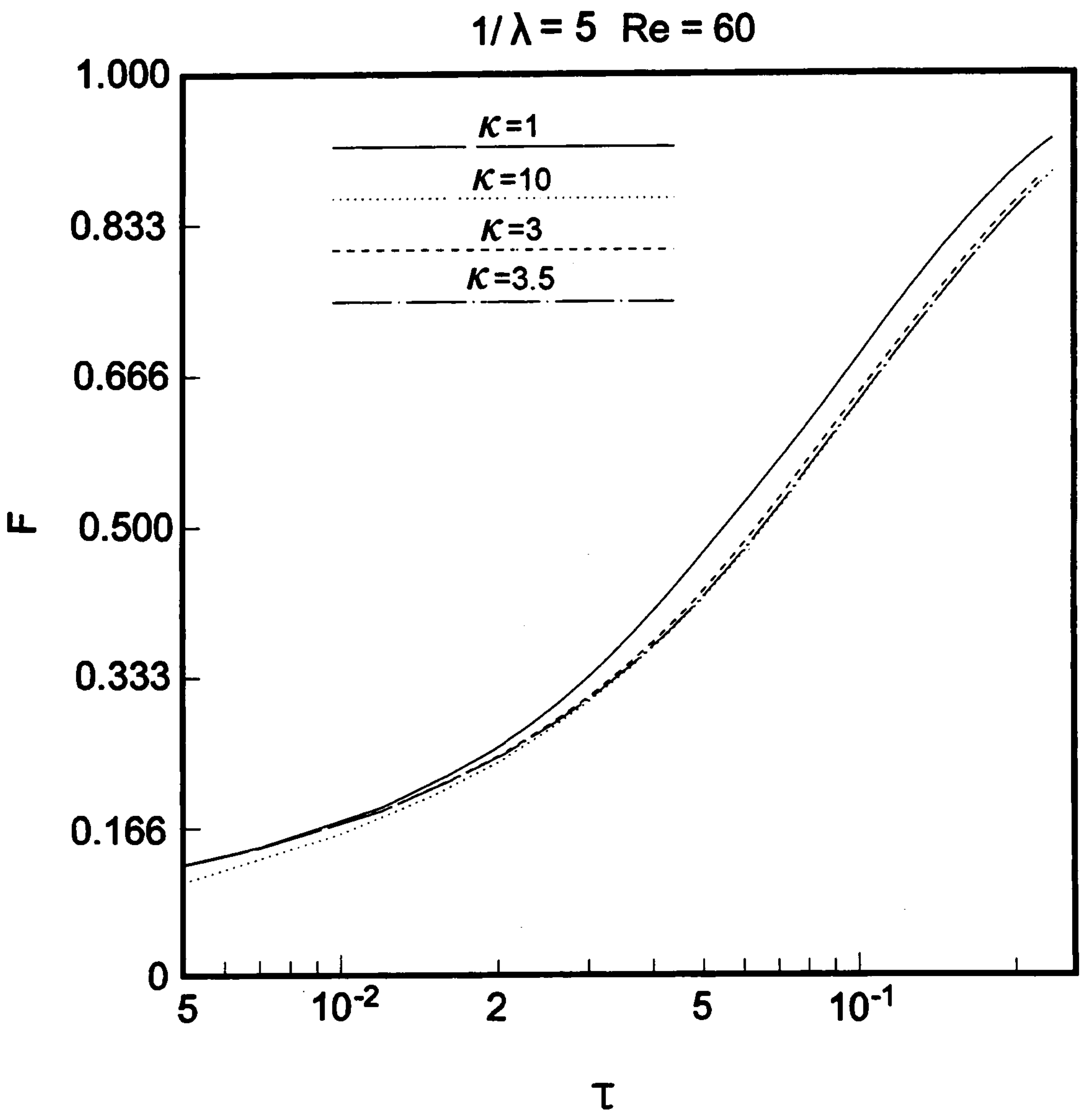

Figure 5.19. Unsteady mass transfer from a fluid sphere. Fractional extraction versus dimensionless time calculated from this work. Here $Re = 60$, $\kappa = 1, 3, 3.5, 10, \frac{1}{\lambda} = 5$ and $Pe = 100$.

presence of even a small wake at $\kappa = 3$ has had a significant effect on mass transfer rate as measured by the fractional extraction of solute, F.

5.4 CONCLUSIONS

The results presented in Section 5.3 depict mass transfer from drops as solute diffuses across the interface, is swept to the rear of the drop, and is then advected downstream. Figures 5.15 and 5.18 make plain that the formation of a wake results in a change in concentration profiles as evidenced by the movement of the concentration contours closer to the drop when $\kappa = 3$, 3.5, and 10. This decrease can be accounted for by noting that regardless of whether a wake is present, the flux of solute out of the drop is solely due to diffusion because the radial component of the velocity vanishes at the spherical interface. When an eddy is present in the continuous phase, it acts like a second barrier to the transport of solute out of the drop - - this is because there can be no velocity component normal to the streamline enclosing the wake. The solute transferring out of the drop and into the wake can only be swept past the drop by the free stream once it diffuses out of the wake, a slow process compared to the convection. The plot of fractional extraction , F, versus dimensionless time , τ, show plainly that the time required for a given degree of extraction increases when a wake is present.

The aforementioned result when coupled to the dominant role played by fluid convection over diffusion at finite Peclet numbers point to the need for developing computational results in order to study mass transfer from oscillating drops.

REFERENCES

REFERENCES

Abramzon, B. and Borde, I. 1980 Conjugate Unsteady Heat Transfer From a Droplet in Creeping Flow. *A.I.Ch.E. Journal* **26**, 536.

Adamson, A. W. 1982 *Physical Chemistry of Surfaces*, Wiley, New York.

Angelo, J. B., Lightfoot, E. N. and Howard, D. W. 1966 Generalization of the Penetration Theory for Surface Stretch: Application to Forming and Oscillating Drops. *AIChE J* **12**,751.

Basaran, O. A., T.W. Patzek, Benner, R.E., and Scriven, L. E. 1995 Non-linear oscillation and breakup of conducting inviscid drops in an externally applied electirc field, *I&E C Research* in print .

Basaran, O. A. 1984 *Electrodynamics of Drops and Bubbles* PhD Thesis University of Minnesota.

Basaran, O. A. and Scriven, L. E. 1989 Axisymmetric shapes and stability of charged drops in an external electric field *Phys. Fluids A* **1**, 799.

Beard, K. V., Ochs, H. T. III, and Kubesh, R. J. 1989 Natural oscillations of small raindrops. *Nature* **342**, 408.

Benedict, M. , Pigford, T., and Levi, H. 1981 *Nuclear Chemical Engineering.* McGraw-Hill, NY, 1981.

Bird, R. B., Stewart, W. E., and Lightfoot, E. N. 1960 *Transport Phenomena.* Wiley, New York.

Boyadzhadhiev, L., Elenkov,D. and Kyuchukov, G. 1969 On Liquid- Liquid Mass Transfer Inside Drops in a Turbulent Flow Field *Can. J. Chem. Engr.* **47**, 42.

Brabston, D. C. and Keller, H. B. 1975 Viscous flows past spherical gas bubbles. *J. Fluid Mech.* **69**, 179.

Brenner, H. and Happel, J. 1958 Slow viscous flow past a sphere in a cylindrical tube. *J. Fluid Mech.* **4**, 195.

Carruthers, J. R. and Testardi, L. R. 1983 Materials processing in the reduced-gravity of space. *Ann. Rev. Mater. Sci.* **13**, 247.

Chang, E. and Maxey, M. 1991 Unsteady flow past a rigid sphere. Paper presented at the 1991 American Physical Society Meeting.

Christodoulou, K. N. and Scriven, L. E. 1992 Discretization of free surface flows and other moving boundary problems. *J. Comput. Phys.* **99**, 39.

Clift, R., Grace, J. R. and Weber, M. E. 1978 *Bubbles, Drops, and Particles.* Academic Press, New York.

Clinton, S. D. 1972 *Mass Transfer of Water from Single Aqueous Sol Droplets Fluidized in a Partially Miscible Alcohol.* ORNL/TM-3771.

Conner, J. M. and Elghobashi, S. E. 1987 Numerical solution of laminar flow past a sphere with surface mass transfer. *Numer. Heat Trans.* **12**, 57.

Dagani, R. 1992 Buoyancy key to new processing method. *Chem. & Eng. News* **70**, 27.

Dandy, D. S. and Leal, L. G. 1986 Bounday-layer separation form a smooth slip surface. *Phys. Fluids* **29**, 1360.

Dandy, D. S. and Leal, L. G. 1989 Bouyancy-driven motion of a deformable drop through a quiescent liquid at intermediate Reynolds numbers. *J. Fluid Mech.* **208**, 161.

Davis, M. H. 1964 Two Charged Spherical Conductors in a Uniform Electric Field: Forces and Field Strength *Quart. J. Mech. Appl. Math.* **17**,499.

Dennis, S. C. R. and Walker, J. D. A. 1971 Calculation of the steady flow past a sphere at low and moderate Reynolds numbers. *J. Fluid Mech.* **48**, 771.

Eaton, B. E. 1983 *The Galerkin Finite Element Method Applied to Viscous Incompressible Flows.* Ph.D. Thesis, Univ. of Colorado, Boulder.

Engelman, M. S., Sani, R. L., Gresho, P. M. and Bercovier, M. 1982 Consistent vs. reduced integration penalty methods for incompressible media using several old and new elements. *Intl. J. Numer. Meth. Fluids* **4**, 25.

Faxen, O. H. 1923 Die bewegung einer starren kugel langs der achse eines mit zaher flussigkeit gefullten rohres. *Ark. Mat. Astron. Fys.* **17**, 1.

Fayon, A. M. and Happel, J. 1960 Effect of a cylindrical boundary on a fixed rigid sphere in a moving viscous fluid. *AIChE J.* **6**, 55.

Flemmer, R. L. C. and Banks, C. L. 1986 On the drag coefficient of a sphere. *Powder Tech.* **48**, 217.

Fornberg, B. 1988 Steady viscous flow past a sphere at high Reynolds numbers.

J. Fluid Mech. **190**, 471.

Francis, A. W. 1933 Wall effect in falling ball method for viscosity. *Physics* **4**, 403.

Freiser, H. and Morrison, G. H. 1959 Solvent Extraction in Radiochemical Separations. *Ann. Rev. Nucl. Sci.* **9**, 221.

Gresho, P. M. 1991 Incompressible fluid dynamics: some fundamental formulation issues. *Ann. Rev. Fluid Mech.* **23**, 413.

Haberman, W. L. and Sayre, R. M. 1958 Motion of rigid and fluid spheres in stationary and moving liquids inside cylindrical tubes. David Taylor Model Basin Report No. 1143.

Hadamard, J. S. 1911 Mouvement permenent lent d'une sphere liquide et visqueuse dans un liquide visqueux. *Compt. Rend. Acad. Sci. (Paris)* **152**, 1735.

Handlos, A.E. and Baron, T. 1957 Mass and Heat Transfer from Drops in Liquid–liquid Extraction. *A.I.Ch.E. Journal* **3** , 127.

Hartman, M., Havlin, V., Trnka, O. and Carsky, M. 1989 Predicting the free fall velocities of spheres. *Chem. Eng. Sci.* **44**, 1743.

Iyengar, S.R.K., Conjugate Unsteady Heat Transfer from a Droplet in Creeping Flow 1982 *A.I.Ch.E. Journal* **28**,700.

Kaji, N., Mori, Y. H., Tochitani, Y. and Komotori, K. 1980 Augmentation of direct contact heat transfer to drops with an intermittent electric field. *Trans. ASME* **102**, 32.

Kang, I. S. 1993 Dynamics of a conducting drop in a time-periodic electric field. *J. Fluid Mech.* **257**, 229.

Kheshgi, H. S. and Scriven, L. E. 1983 Penalty finite element analysis of unsteady free surface flows. In *Finite Elements in Fluids*, Vol. 5, J. T. Oden et al., eds., Wiley, New York.

Kim, S. and Karrila, S. J. 1991 *Microhydrodynamics: Principles and Selected Applications*. Butterworth-Heineman, Boston.

Kim, I. and Pearlstein, A. J. 1990 Stability of flow past a sphere. *J. Fluid Mech.* **244**, 73.

Kronig,R. and Brink, J. C. 1951 On the Theory of Extraction from Falling

Droplets. *Appl.Sci.Res.* **A2**, 142.

Ladenburg, R. 1907 Uber den einfluβ von wanden auf die bewegung einer kugel in einer rebenden flussigkeit. *Ann. Phys. (Leipzig)* **23**, 447.

Leal, L. G. 1989 Vorticity transport and wake structure for bluff bodies at finite Reynolds number. *Phys. Fluids A* **1**, 124.

Loshak, J. 1969 *Forced Oscillation of Drops in a Viscous Medium.* M.S. Thesis, University of Rochester, Rochester, N.Y.

Loshak, J. and Byers, C. H. 1973 Forced Oscillations of Drops in a Viscous Medium. *Chem. Engr. Sci.* **28**, 149.

Macky, W.A. 1930 The deformation of soap bubbles in electric fields *Proc. Camb. Phil. Soc.* **22**, 98.

Masliyah, J.H. 1971 Heat Transfer Mechanism in Recirculating Wakes. *Int. J. Heat Mass Transfer* **14**, 2164.

Masliyah, J.H. and Epstein, N. 1970 Numerical Solution of Heat and Mass Transfer from Spheroids in Steady Axisymmetric Flow. *Progress in Heat and Mass Transfer: Proc. of the International Symposium on Two-Phase Systems* **6** Pergamon Press, 613.

McNown, J. S., Lee, H. M., McPherson, M. B. and Ebgez, S. M. 1948 *Proc. 7th Int. Congr. Appl. Mech.* **2**, 17.

Nakamura, I. 1976 Steady wake behind a sphere. *Phys. Fluids* **19**, 5.

Natarajan, R. and Acrivos, A. 1993 The instability of the steady flow past spheres and disks. *J. Fluid Mech.* **254**, 323.

Newman, A. B. 1931 The Drying of Porous Solids: Diffusion and Surface Emission Equations. *Trans. A.I.Ch.E.* **27**, 310.

Nolan, A. B. 1926 *Proc. Roy. Irish Acad.* **26**,421.

Oliver, D. L. R. and Chung, J.N. 1985 Steady flows inside and around a fluid sphere at low Reynolds numbers. *J. Fluid Mech.* **154**, 215.

Oliver, D. L. R. and Chung, J. N. 1987 Flow about a fluid sphere at low to moderate Reynolds numbers. *J. Fluid Mech.* **177**, 1.

Oliver, D. L. R. and Chung, J. N. 1990 Unsteady Conjugate Heat Transfer from a Translating Fluid Sphere at Moderate Reynolds Numbers. *Int. J. Heat Mass Transfer* **33**, 401.

O'Konski, C.T. and Harris, F. E. 1957, Electric Free Energy and the Deformation of Droplets in Electrically Conducting Systems *J. Phys. Chem.* **61**,1172.

Ptasinski, K. J. and Kerkhof, P. J. A. M. 1992 Electric field driven separations: Phenomena and applications. *Sep. Sci. Technol.* **27**, 995.

Perry, J. H. 1950 *Chemical Engineering Handbook*, 3rd ed. McGraw-Hill, New York.

Ramabhadran, T. E. 1972 *Inference of Dynamic Interfacial Properties from a Study of an Oscillating Drop and Bubble.* Ph.D. Dissertation, University of Rochester, Rochester, N.Y.

Rayleigh, Lord 1882 On the Equilibrium of Liquid Conducting Masses Charged with Electricity. *Phil Mag* **14**, 184.

Rivkind, V. Ya. and Ryskin, G. M. 1976 Flow structure of a spherical drop in a fluid medium. *Fluid Dyn.* **11**, 5.

Rivkind, V. Ia., Ryskin, G. M., and Fishbein, G. A. 1976 Flow around a spherical drop at intermediate Reynolds numbers. *PMM* **40**, 741.

Rose, P. M. and Kintner, R. C. 1966 Mass Transfer from Large Oscillating Drops. *AIChE J* **12**, 530.

Rybczynski, W. 1911 Uber die fortschreitende bewegung einer flussigen kugel in einem zahen medium. *Bull. Acad. Sci. Cracovie* **A**, 40.

Ryskin, G. and Leal, L. G. 1984 Large deformations of a bubble in axisymmetric steady flows. Part 2. The rising bubble. *J. Fluid Mech.* **148**, 19.

SAS Language and Procedures: Usage. 1989 Version 6, First Edition. SAS Institute Inc., Cary, NC.

Scott, T. C. and Wham, R. M. 1988 Surface area generation and droplet size control in solvent extraction systems utilizing high intensity electric fields. U.S. Patent 4,767,515.

Scott, T. C., and Wham, R. M. 1989 An Electrically Driven Multistage Countercurrent Solvent Extraction Device: The Emulsion Phase Contactor. *I & EC Research* **28**,94.

Sherwood, T. K., Pigford, R. L., and Wilke, C. R. 1975 *Mass Transfer*. McGraw-Hill, New York.

Strang, G. and Fix, G. J. 1973 *An Analysis of the Finite Element Method.* Prentice-Hall, Englewood Cliffs, New Jersey.

Stewart, G., and Thorton, J. D. 1967 Charge and Velocity Characteristics of Electrically Charged Drops. Part I Theoretical Considerations. Part II Preliminary Measurements of Droplet Charge and Velocity. *Chem. Engr. Symp. Ser. No. 26* **29**, 27.

Taneda, S., 1956 Experimental investigation of the wake behind a sphere at low Reynolds numbers. *J. Phys. Soc. Jpn.* **11**, 1104.

Tavener, S. J. 1994 Stability of the $O(2)$-symmetric flow past a sphere in a pipe. *Phys. Fluids* **6**, 3884.

Thomas, P. D. and Brown, R. A. 1987 LU-decomposition of matrices with augmented dense constraints. *Int. J. Num. Meth. Eng.* **24**, 1451.

Treybal, R. E. 1963 *Liquid Extraction.* 2nd Edition, McGraw-Hill, New York.

Tritton, D. J. 1988 *Physical Fluid Dynamics.* 2nd Edition, Clarendon Press, Oxford.

Turton, R. and Levenspiel, O. 1986 A short note on the drag correlation for spheres. *Powder Tech.* **47**, 83.

Wakiya, S. 1957 Viscous flows past a spheroid. *J. Phys. Soc. Japan* **12**, 1130.

Waterman, L.C. 1965 Electrical Coalescers *Chem. Engr. Prog.* **61** , 51.

Weaver,B. 1974 Solvent Extraction in the Separation of Rare Earths and Trivalent Actindes. **6**, Marcel Dekker , NY.

Wham, R. M., Basaran, O. A., and Byers, C. H. 1995 Wall effects on flow past solid spheres at finite Reynolds number. Submitted to *I&EC Research.*

Wham, R. M., Basaran, O. A., and Byers, C. H. 1995 Wall effects on flow past fluid spheres at finite Reynolds number. Submitted to *Chem. Engr. Science* .

Wham, R. M. and Byers, C. H. 1987 Mass Transport from Single Drops in Imposed Electric Fields. *Separation Science and Technology*, 447.

Zhang, X. , Basaran, O. A. and Wham, R. M. 1995 Theoretical Prediction of

Electric Field-Enhanced Coalescence of Spherical Drops. *AIChE J* **41**, 1629.

VITA

Robert M. Wham was born in Springfield, Illinois on September 5, 1957. He attended schools in the public school system of Springfield, Illinois where he graduated from Springfield High School in June, 1975. He entered University of Illinois at Champaign-Urbana in August of 1975 where in December, 1978 he received a Bachelor of Science in Chemical Engineering graduating as a James Scholar with distinction in the curriculum. He accepted a position with the Oak Ridge National Laboratory (ORNL) working in the Chemical Technology Division in February, 1979. In May, 1979 he entered University of Tennessee, Knoxville where in May, 1983 he received a Masters degree in Chemical Engineering.

He continued his studies at the University of Tennessee and obtained a doctoral degree in May, 1996.

He is presently the manager of the Radiochemical Engineering Development Center which is operated by the Chemical Technology Division at ORNL.